



Swansea University
Prifysgol Abertawe



Swansea University E-Theses

Synthesis and photochemical characterisation of luminescent gold complexes for technological applications.

Pichereau, Jeremie Guillaume

How to cite:

Pichereau, Jeremie Guillaume (2008) *Synthesis and photochemical characterisation of luminescent gold complexes for technological applications.* thesis, Swansea University.
<http://cronfa.swan.ac.uk/Record/cronfa42464>

Use policy:

This item is brought to you by Swansea University. Any person downloading material is agreeing to abide by the terms of the repository licence: copies of full text items may be used or reproduced in any format or medium, without prior permission for personal research or study, educational or non-commercial purposes only. The copyright for any work remains with the original author unless otherwise specified. The full-text must not be sold in any format or medium without the formal permission of the copyright holder. Permission for multiple reproductions should be obtained from the original author.

Authors are personally responsible for adhering to copyright and publisher restrictions when uploading content to the repository.

Please link to the metadata record in the Swansea University repository, Cronfa (link given in the citation reference above.)

<http://www.swansea.ac.uk/library/researchsupport/ris-support/>

**Synthesis and Photochemical Characterisation
of Luminescent Gold Complexes
for Technological Applications**

by

Jérémie Guillaume Pichereau

A thesis submitted to the Swansea University in partial fulfilment of the requirements
for the degree of Doctor of Philosophy in Chemistry

**Department of Chemistry
School of Engineering
Swansea University
September 2008**

ProQuest Number: 10798172

All rights reserved

INFORMATION TO ALL USERS

The quality of this reproduction is dependent upon the quality of the copy submitted.

In the unlikely event that the author did not send a complete manuscript and there are missing pages, these will be noted. Also, if material had to be removed, a note will indicate the deletion.



ProQuest 10798172

Published by ProQuest LLC (2018). Copyright of the Dissertation is held by the Author.

All rights reserved.

This work is protected against unauthorized copying under Title 17, United States Code
Microform Edition © ProQuest LLC.

ProQuest LLC.
789 East Eisenhower Parkway
P.O. Box 1346
Ann Arbor, MI 48106 – 1346



Declaration

This work has not previously been accepted in substance for any degree and is not being concurrently submitted in candidature for any degree.

(Signature of candidate)

.....
11th / 03 / 2009
.....

(Date)

Statement 1

This thesis is the result of my own investigations, except where otherwise stated. Other sources are acknowledged by footnotes giving explicit references. A bibliography is appended.

.....
(Signature of candidate)

.....
11th / 03 / 2009
.....

(Date)

Statement 2

I hereby give consent for my thesis, if accepted, to be available for photocopying and for inter-library loan, and for the title and summary to be made available to outside organisations.

.....
(Signature of candidate)

.....
11th / 03 / 2009
.....

(Date)

To my family and friends.

« On ne peut bien voir qu'avec le cœur, l'essentiel est invisible aux yeux »

Antoine de Saint-Exupéry, "Le petit Prince"

« Courage is to look for the Truth and to tell it »

Jean Jaurès

Acknowledgements

During these years of research, I have met great people and have lived in a wonderful country where I have been warmly welcomed.

The person who has shared all these years most intimately is Marya Vrba. There are no words to express the deep recognition I have towards you for supporting me in the darkness and in the light, and for having been the strong oak stick I could lean on when I needed it. Finishing this PhD would have been a lot more difficult without your ever welcome advice, insight, unconditional support and immense love. You have been and will always be a bright and warm light in my life.

To my father Dominique, my brother Bastien and my sister Emmanuelle: we followed too many roads together to say a simple thank you - that wouldn't be enough. We are together for eternity. The Vrba family has a very warm place in my heart for their constant presence and wonderful welcome in Arizona.

I would then like to thank a very special man, Peter Douglas, whose bright mind and high spirits always drive people to go further than they think they can. His imagination, allied with an inimitable sense of humour, and the depth of his analyses and thoughts are some of the numerous joys of speaking science with him. I would like to express my deepest thanks to him for giving me a chance to return to science and for his support in good and bad times.

I have also met another great man: Chris Morley. He has a deep knowledge of chemistry and is always ready to challenge your mind. The assistance he provided during these years was unbelievable. I always thought that he and Peter formed a "dream team" of supervisors. Thank you so much to you both.

Chris Winscom from Kodak also deserves a good share of thanks for his bright ideas, his consistently clear mind and his broad knowledge of applications. I will miss our meetings.

During the last moments of the chemistry department at Swansea University, some people continued to provide laughter and support. Thank you Vic, Hans, Rachel, Karen, Steve, Des, and Brendan for all the good times.

I would like to thank the ERASMUS programme for funding a three-month placement of research training, experience and development at the Chemistry Department of the University of Coimbra, Portugal, where Hugh Burrows welcomed me warmly. I met wonderful and brilliant people there, especially Dan, Licinia, and Luisa. Licinia performed the calculations on gold complexes and Luisa did some of the ^{31}P NMR spectroscopy.

I also would like to thank Massimo Di Vaira for providing the crystal structures and their analyses, and Bill for his precious help with the DFT calculations. The labs were kept in good working order thanks to the great work of Stan. The NMRs were run by Ian Matthews. Thanks also to John Tregembo for his skills as an engineer and rugbyman.

I thank the EPSRC National Mass Spectrometry Service Centre in Swansea for performing the mass spectrometry work.

This research has been funded by Kodak UK Ltd, for which I am very grateful. Some of the gold precursor KAuCl_4 was generously provided by Johnson Matthey.

I would also like to thank all the friends I made in Swansea through salsa dancing, especially Gorka, who brought us all together. I met people from all over the world, and my special thoughts go to Emiliano, Yorgos, Carlos, Regina, Lisi, Benjamin, Nicolas, Ann, Nick, Claire, Ben, Sally, Bella, Asad, Emad, Maria, Martina, Layla, Agostino, TR, and to all the others I am certainly forgetting - please forgive me.

And last but not least, my old friends, with whom everything started: Xavier, Astrid, Severine, Zor, Sammy, David, Sophie, Marjolaine, Elodie, Tugdual, Kristell, Yoann, Olivier, Titi, Yann, Ann, Fabien Marion, Sébastien, Laurence and Thomas. Un grand merci à vous!! Tant que je vivrais, vous ne mourrez pas.

And why chemistry? Because it is fun:

“Evans boldly put 50 ATM of ethylene in a cell with 25 ATM of oxygen. The apparatus subsequently blew up, but luckily not before he obtained the spectra shown in figure 8”

Merer A.J., Mulliken R.S., Chem. Rev. 69 (1969) 64

Summary

Two new precursors of dithiolate ligands, 2,6-dimercaptopyrazine (DMPA) and 2,6-dimercaptopicotinic acid (ADMN) have been synthesised and characterised. Their photochemical properties have been studied along with those of other known N-heterocyclic thiol compounds namely: (4,6-dimercaptopyrimidine (46PYRI), 2,4-dimercaptopyrimidine (24PYRI), 5,6-diamino-2,4-dimercaptopyrimidine (NPYRI) and 2,6-dimercaptopyridine (DMP)). All these compounds can be in a tautomeric equilibrium between thiol and thione forms, and it has been shown that in polar media the thioketone is the dominant species. All emit in a glass at 77 K and room temperature, but only 24PYRI and 46PYRI give phosphorescence at 77 K ($\tau = 380 \mu\text{s}$ and $57 \mu\text{s}$ respectively). The presence of a thiol group effectively quenches the phosphorescence and only fluorescence is observed for the other compounds. They all have an irreversible electrochemistry. The crystal structure of 46PYRI is reported for the first time.

Twenty-five new binuclear gold(I) phosphine derivatives of these dithiolate ligands have been synthesised: *i.e.* with bis(diphenylphosphino)methane, bis(diphenylphosphino)ethane, bis(diphenylphosphino)propane and bis(diphenylphosphino)butane, for annular complexes, or with triphenylphosphine for open ring compounds. A mononuclear triphenylphosphinegold(I) complex with DMP is also reported. Gold-gold interactions were absent from the two crystal structures obtained. All these compounds show phosphorescence in the solid state at RT and in a glass at 77 K, but only complexes with DMP as dithiolate emit in solution at RT (through phosphorescence also). The origin of the luminescence is thought to be from a mixture of LMCT or ILCT excited states. Complexes with electron-withdrawing groups (e.g. ADMN) on the thiolate promote the ILCT excited state whereas electron-donating groups (e.g. NPYRI) promote the LMCT excited state. All complexes studied gave irreversible electrochemistry.

Ab initio studies on the dithiols confirm the greater stability of the thioketone form in polar solvents. Structural simulations of the binuclear gold(I) complexes confirm both the absence of an aurophilic interaction and the origin of luminescence.

Conventions and abbreviations

These abbreviations have been used through the thesis to describe the degree of splitting of NMR signals:

s, singlet; d, doublet; t, triplet; m, multiplet.

These abbreviations have been used through the thesis to describe the peaks intensity in infrared spectra:

vw (very weak) < w (weak) < m (medium) < s (strong) < vs (very strong)

The following abbreviations have been used throughout the thesis:

24PYRI:	2,4-Dimercaptopyrimidine
46PYRI:	4,6-Dimercaptopyrimidine
ADMN:	2,6-Dimercaptonicotinic acid
a.u.:	Arbitrary units
CIS:	Configuration interactions singlet
Cl-DMB:	4-Chloro-1,3-dimercaptobenzene
CV:	Cyclic voltammetry
D:	Debye
DCM:	Dichloromethane
DFT:	Density functional theory
DMB:	1,3-Dimercaptobenzene
DMF:	Dimethylformamide
DMP:	2,6-Dimercaptopyridine
DMPA:	Dimercaptopyrazine
DMSO:	Dimethylsulfoxide
dppb:	1,4-Bis(diphenylphosphino)butane
dppe:	1,2-Bis(diphenylphosphino)ethane
dppet:	1,2- <i>cis</i> -Bis(diphenylphosphino)ethene
dppf:	1,1'-Bis(diphenylphosphino)ferrocene
dpph:	1,6-Bis(diphenylphosphino)hexane

dppm:	Bis(diphenylphosphino)methane
dppp:	1,3-Bis(diphenylphosphino)propane
DPV:	Differential pulse voltammetry
ECP:	Effective core potential
EI/CI MS:	Electron impact/chemical ionisation mass spectrometry
EL:	Emissive layer
EPA:	Diethyl ether : isopentane : ethanol (5 : 5 : 2 in volume)
ES MS:	Electrospray ionisation mass spectrometry
ETL:	Electrons transport layer
EtOH:	Ethanol
FAB MS:	Fast atomic bombardment mass spectrometry
FWHM:	Full width at half maximum
GTT:	triphenylphosphine(2-mercaptopyridine)gold(I)
Har:	Hartree, 1 hartree = 627.5 kcal mol ⁻¹
HE:	High energy
HF:	Hartree-Fock
HOMO:	Highest occupied molecular orbital
HTL:	Holes transport layer
IR:	Infrared
ITO:	Indium tin oxide
K:	Kelvin
LE:	Low energy
LED:	Light emitting device
LLCT:	Ligand to ligand charge transfer
LMCT	Ligand to metal charge transfer
LMMCT	Ligand to metal-metal charge transfer
LUMO:	Lowest unoccupied molecular orbital
MC:	Metal centred
Me:	Methyl
MeOH:	Methanol
MLCT:	Metal to ligand charge transfer

MP:	Møller-Plesset
MS:	Mass spectrometry
NMR:	Nuclear magnetic resonance
NPYRI:	5,6-Diamino-2,4-dimercapto-pyrimidine
OLED:	Organic light emitting device
OTF:	Trifluoromethanesulfonate (or triflate)
PCM:	Polarisable continuum model
PFMCH:	Perfluoromethylcyclohexane
Ph:	Phenyl
PLED:	Phosphorescence light emitting device
PPh ₃ :	Triphenylphosphine
ppm:	Part per million
TD-DFT:	Time dependent density functional theory
TEOA:	Tetraethylorthoacetate
THF:	Tetrahydrofuran
THT:	Tetrahydrothiophene
TMOA:	Tetramethylorthoacetate
TPA:	1,3,5-triaza-7-phosphaadamantane
UV:	Ultraviolet
ZPE:	Zero point energy
μ :	Micro (10^{-6})
$^{\circ}\text{C}$:	Degree Celsius
Φ :	Quantum yield
λ :	Wavelength (in nm)
ν :	Frequency (s^{-1} or hertz)
δ :	Chemical shift in ppm
τ :	Lifetime

Contents

Declaration	ii
Dedication	iii
Acknowledgements	iv
Summary	vi
Conventions and abbreviations	vii
Contents	x

Chapter 1: *Introduction*

1.1 Introduction to the OLED technology	2
1.1.1 Description of an OLED device	3
1.1.2 Influence of the electrodes on the device performance	5
1.1.3 Hole transport layer (HTL)	6
1.1.4 Electron transport layer (ETL)	7
1.1.5 Emissive Layer	7
1.1.5.1 Phosphorescent or fluorescent emitters?	8
1.1.5.2 Charge transfer from the hostmatrix to the dopant	9
1.1.5.3 Triplet emitters for OLEDs	10
1.1.6 Efficiency	11
1.2 Photophysical processes of organic molecules	12
1.2.1 Creation of an excited state	12
1.2.1.1 Absorption of a photon	12
1.2.1.2 Rules regulating the transition	13
1.2.2 Characteristics of an excited state	14
1.2.2.1 Multiplicity	14
1.2.2.2 Configuration	
1.2.2.2.1 Configuration in aromatic hydrocarbons	14
1.2.2.2.2 Configuration in metal complexes	13
1.2.3 Deactivation of the excited state	16

1.2.4 Energy transfer	16
1.2.5 Charge transfer in OLEDs	19
1.2.6 Factors governing the non-radiative decay	19
1.3 Gold complexes as possible emissive dopants in OLEDs	20
1.4 Introduction to gold chemistry	21
1.4.1 Gold coordination	22
1.4.1.1 Gold complexes with gold in the oxidation state –I	23
1.4.1.2 Gold complexes with gold in the oxidation state +I	23
1.4.1.2.1 Mononuclear gold(I) complexes	23
1.4.1.2.2 Binuclear gold(I) complexes	25
1.4.1.2.3 Multinuclear gold(I) complexes	27
1.4.1.3 Gold complexes with gold in the oxidation state +III	28
1.4.1.4 Gold complexes with gold in the oxidation state +V	28
1.4.1.5 Hypothetical gold complexes with gold in higher oxidation state	28
1.4.2 Luminescence of gold complexes	29
1.5 Strategy for designing a potentially efficient blue emitter based on a gold(I) derivative	32
1.6 Thesis overview	33
References for Chapter 1	34

Chapter 2: *Experimental Techniques*

2.1 Introduction	44
2.2 Chemical synthesis and characterisation	44
2.2.1 Reaction techniques and chemicals	44
2.2.1.1 Schlenk techniques and dry solvents	44
2.2.1.2 Reaction in liquid ammonia	44
2.2.1.3 Chemicals	45
2.2.2 ^1H , ^{13}C , ^{31}P NMR spectroscopy	45
2.2.3 Mass spectrometry	45

2.2.4 Infrared spectroscopy	46
2.2.5 UV-Vis absorption spectroscopy	46
2.2.6 Electrochemistry	46
2.2.7 X-ray diffraction crystallography	46
2.3 Luminescence studies	47
2.3.1 Steady state emission and excitation studies	47
2.3.1.1 Emission and excitation spectra measurements	47
2.3.1.2 77 K measurements	47
2.3.1.3 Correction factor for Perkin-Elmer MPF-44E fluorimeter	48
2.3.1.4 Quantum yield at 77 K	49
2.3.2 Time resolved studies	49
2.3.2.1 Phosphorescence lifetime measurements	49
2.3.2.2 Fluorescence single photon counting	50
2.3.2.3 Flash photolysis	50
2.4 Molecular modelling	51
2.4.1 Ligands	51
2.4.2 Gold(I) complexes	51
2.5 Error calculations	51
References for Chapter 2	52

Chapter 3: *Syntheses, photochemistry and electrochemistry of some thiol-substituted heterocycles*

3.1 Introduction	54
3.1.1 Compounds studied	54
3.1.2 Review of their known properties	55
3.1.2.1 Synthesis and chemical properties of N-heterocyclic thiols	55
3.1.2.2 Photophysical properties of thiones	59
3.1.2.3 Applications for these compounds	60
3.2 Syntheses	61
3.2.1 Synthesis of 2,6-dimercaptonicotinic acid ADMN and its sodium salt	61

3.2.1.1 Synthesis	61
3.2.1.2 Characterisation	61
3.2.1.3 Crystal structure of the sodium salt of ADMN	62
3.2.1.3.1 Crystal packing	62
3.3.1.3.2 Sodium coordination	62
3.2.1.3.3 Molecular structure	65
3.2.2 Synthesis of 2,6-dimercaptopyrazine, DMPA	67
3.2.2.1 Synthesis	67
3.2.2.2 Characterisation	67
3.2.2.3 Effect of pH	67
3.2.3 Syntheses of 2,6-dimercaptopyridine (DMP), 2,4-dimercaptopyrimidine (24PYRI), and 4,6-dimercaptopyrimidine (46PYRI)	68
3.2.3.1 Synthesis of 4,6-dimercaptopyrimidine (46PYRI)	68
3.2.3.1.1 Crystal structure of $C_4H_4N_2S_2 \cdot H_2O$	69
3.2.3.1.2 Crystal packing	69
3.2.3.1.3 Molecular structure	69
3.2.3.2 Synthesis of 2,4-dimercaptopyrimidine (24PYRI)	73
3.2.3.3 Synthesis of 2,6-dimercaptopyridine (DMP)	74
3.2.4 Conclusion on syntheses	75
3.3 Photochemistry	76
3.3.1 Absorption spectra	76
3.3.1.1 Comparison between compounds	76
3.3.1.2 Solvatochromism	80
3.3.1.3 Absorption spectra at different pH	86
3.3.1.4 Photodegradation of the compounds	90
3.3.2 Emission and excitation spectra at 77 K	92
3.3.2.1 Pyridine derivatives	92
3.3.2.2 Pyrazine derivatives	94
3.3.2.3 Pyrimidine derivatives	95
3.3.2.4 Conclusion from the study of emission spectroscopy at 77 K	99
3.3.3 Photoluminescence and excitation at room temperature	101

3.3.4 Conclusion	106
3.4 Electrochemistry	107
3.4.1 Introduction	107
3.4.2 Results	109
3.4.3 Interpretation and conclusion	112
3.5 Conclusion	113
References for Chapter 3	114

**Chapter 4: Syntheses, photochemistry and electrochemistry
of neutral binuclear gold complexes with phosphine and bridging
N-heterocyclic dithiolate ligands**

4.1 Introduction	119
4.2 Syntheses of binuclear gold(I) phosphine thiolate complexes	122
4.2.1 Introduction	123
4.2.2 Synthesis of precursors	123
4.2.2.1 Dithiol ligands	123
4.2.2.2 Syntheses of the gold(I) precursors used	123
4.2.2.3 Other gold(I) precursors synthesised	124
4.2.3 Syntheses of gold(I) complexes	124
4.2.3.1 Formation of a mononuclear gold(I) complex triphenylphosphine(2,6-dithiolato-pyridine)gold(I) (4f)	125
4.2.3.1.1 Synthesis	125
4.2.3.1.2 Analyses	125
4.2.3.1.3 Crystal structure of [Au(S ₂ C ₅ H ₄ N)(PPh ₃)] (4f)	125
4.2.3.2 Formation of binuclear gold(I) complexes	129
4.2.3.2.1 Syntheses with all dithiolate ligands except ADMN	129
4.2.3.2.1.1 With chloro(triphenylphosphine)gold(I)	129
4.2.3.2.1.2 With chlorogold(I) complexes of bridging diphosphines	130
4.2.3.2.2 Syntheses with ADMN as dithiolate ligand	130
4.2.3.2.2.1 With chloro(triphenylphosphine)gold(I)	130

4.2.3.2.2 With chlorogold(I) complexes of bridging diphosphines	131
4.2.3.2.3 Characterisation of the open ring complexes	131
4.2.3.2.4 Characterisation of the closed ring complexes	133
4.2.3.2.5 Crystal structure of $[\text{Au}_2(\mu\text{-}2,6\text{-S}_2\text{C}_5\text{H}_3\text{N})(\text{PPh}_3)_2]$ (4a)	141
4.2.4 Discussion	145
4.2.4.1 NMR studies	145
4.2.4.2 Mass spectrometry	148
4.2.4.3 IR spectroscopy	148
4.2.4.4 Possible reasons which drive the reaction toward annular compounds	149
4.2.5 Conclusions from synthetic work	150
4.3 Photoluminescence	151
4.3.1 Absorption spectroscopy	154
4.3.1.1 Compounds with a benzene thiolate (7a and 8a)	154
4.3.1.2 Compounds with a pyrimidine thiolate	155
4.3.1.3 Compounds with a pyridine thiolate	158
4.3.1.4 Compounds with a pyrazine thiolate	163
4.3.1.5 General conclusion from the absorption study	164
4.3.2 Photoluminescence studies	165
4.3.2.1 Experimental	165
4.3.2.2 Binuclear gold phosphine series with 24PYRI as dithiolate	165
4.3.2.3 Binuclear gold phosphine series with NPYRI as dithiolate	173
4.3.2.4 Binuclear gold phosphine series with 46PYRI as dithiolate	176
4.3.2.5 Binuclear gold phosphine series with DMPA as dithiolate	179
4.3.2.6 Binuclear gold phosphine series with DMP as dithiolate	183
4.3.2.7 Binuclear gold phosphine series with ADMN as dithiolate	192
4.3.2.8 Binuclear gold phosphine series with DMB or Cl-DMB as dithiolate	196
4.3.3 Discussion	198
4.3.3.1 Influence of the phosphine (length, charge)	198
4.3.3.2 Influence of the thiolate	200

4.3.4 Conclusion on photochemistry	201
4.4 Electrochemistry	202
4.5 Conclusion	203
References for Chapter 4	204

Chapter 5: *Computational studies of some N-heterocyclic dithiolate and their binuclear gold(I) phosphine complexes*

5.1 Introduction	209
5.1.1 Description of the basis set	210
5.1.2 Description of methods used in computational chemistry	210
5.2 Computational studies of N-heterocyclic dithiolates	211
5.2.1 Introduction	211
5.2.2 Geometry optimisation and most stable tautomer	212
5.2.2.1 Determination of the most stable tautomer of 2,4-dimercaptopyrimidine (24PYRI)	214
5.2.2.2 Determination of the most stable tautomer of 4,6-dimercaptopyrimidine (46PYRI) in different media	214
5.2.2.3 Determination of the most stable tautomer of 2,6-dimercaptopyrazine (DMPA) in different media	218
5.2.2.4 Determination of the most stable tautomer of 2,6-dimercaptopyridine (DMP) in different media	220
5.2.2.5 Determination of the most stable tautomer of 2,6-dimercaptonicotinic acid (ADMN) in different media	222
5.2.2.6 Conclusion on the geometry optimisation	227
5.2.3 Studies of infrared spectra	228
5.2.3.1 46PYRI infrared spectra	228
5.2.3.2 DMPA infrared spectra	230
5.2.3.3 DMP infrared spectra	231
5.2.4 HOMO-LUMO localisation and transition estimation via TDDFT	232
5.2.4.1 TDDFT for 2,6-dimercaptopyridine (DMP)	232

5.2.4.2 TDDFT for 2,6-dimercaptonicotinic acid (ADMN)	235
5.2.4.3 TDDFT for 2,6-dimercaptopyrazine (DMPA)	238
5.2.4.4 TDDFT for 4,6-dimercaptopyrimidine (46PYRI)	240
5.2.4.5 Conclusions from TDDFT calculations	242
5.2.5 Conclusion for the <i>ab initio</i> simulation of N-heterocyclic dithiols	243
5.3 Computational studies of binuclear gold(I) phosphine dithiolate complexes	244
5.3.1 Introduction	244
5.3.2 Structure optimisation	245
5.3.3 Localisation of the HOMO and LUMO	248
5.3.4 Relative charge calculation	254
5.3.5 Conclusion	255
5.4 General conclusions from <i>ab initio</i> studies	256
References for Chapter 5	257
Chapter 6: Conclusions	
6.1 Future work on the new dithiols synthesised	261
6.2 Future work with the binuclear gold(I) complexes synthesised	262
6.3 Future <i>ab initio</i> calculations	263
References for Chapter 6	264
APPENDIX A: List of chemicals used and purification if needed	266
APPENDIX B: Attempts to synthesise different dimercaptopyridines	269
Drawing and abbreviations of the molecules	277

Chapter 1

Introduction

1.1 Introduction to OLED technology

One great achievement of humankind has been the creation of tools and devices to control his surroundings.

In former ages, the two dominant light sources were the sun or the fire. A relatively recent development has been the ability to create light from different sources e.g. light (photoluminescence), electricity (electroluminescence), pressure (piezoluminescence), and chemical reactions (chemiluminescence). There has been a great deal of research into electroluminescence, and, since the creation of the first incandescent light bulb in 1802 attributed to Sir Humphry Davy, many new light emitting devices have been developed such as discharge tubes, and most recently light emitting diodes (LED) and plasma screens.

We use electroluminescence for general lighting, imaging, and displays. In electronic display technology, the cathode ray tube is widely used; it gives a good image quality but is not easily portable, and recent technological improvements in flat screen displays have made these devices highly competitive in the display market. In these thin panel devices, the luminescence can originate from inorganic materials (LEDs), organic materials (OLEDs and PHOLEDs) or excited noble gases (plasma screens). Liquid crystal technology is also widely used in flat screens where a fluorescent backlight, or a mirror reflecting the incident light, is the primary light source.

The development of OLEDs began in 1963 when Pope *et al.* [1] reported the first organic electroluminescent cell operating in dc mode. Soon after, in 1967, a device using an emissive polymer was created by Hartman and co-worker [2]. With the discovery in 1987 of an efficient multilayer film device based on the green luminescence of the complex tris(8-hydroxyquinolato)aluminium by Tang and Van Slyke from Kodak [3], research and corporate interest increased dramatically, to lead to the first display using this technology [4], and to take us to the point where now many companies have commercialised this technology in the screens of many consumer devices. Indeed it could be argued that it was the development of this technology which allowed the development of many of the consumer devices which rely on displays, such as mobile phones, digital cameras, and portable computers.

These devices are self-emitting, so there is no need for another light source as required in a liquid crystal display. This makes the device lighter, thinner and easier to use, and OLEDs also have a better viewing angle and higher contrast than LCD displays. Also there is a tremendous gain in energy efficiency from this device as it emits from the required pixel only, and not from the whole panel. Furthermore, the OLED display can “refresh” faster than traditional LEDs (almost 1000 times faster) and so it can display information almost in real time. OLEDs can be deposited on flexible or rigid substrates, opening the route to the creation of flexible displays which can be used in many areas such as: architecture, clothes design, etc.

A tremendous amount of effort has been applied to improving the efficiency, lifetime, and optical qualities of OLEDs. To better understand these developments we need to describe the OLED structure, the physics associated with this technique and the chemistry of the compounds used in its construction.

1.1.1 Description of an OLED device

A schematic of a multilayer OLED device is shown in figure 1.1.

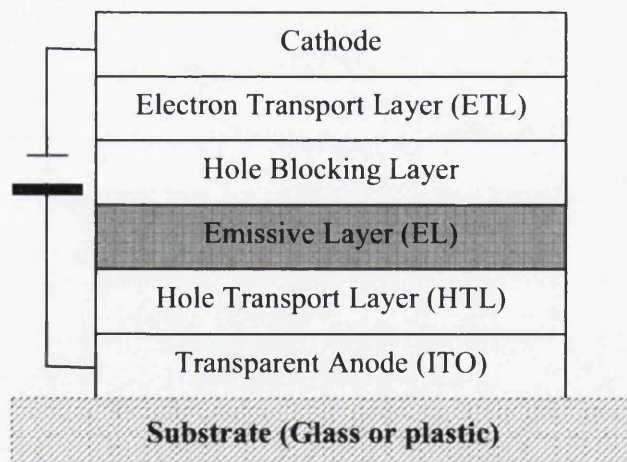


Figure 1.1: Basic structure of a multilayer OLED

An OLED is made up of different organic layers sandwiched between a transparent anode and a metallic cathode. The cathode is a metal with a low workfunction (such as Ca, Al, Mg) to enhance electron injection into the LUMO of the electron transport layer. The anode is a conduction layer usually made of indium tin oxide (ITO) which has a LUMO lying at a low energy level and therefore can easily capture the electrons coming from the HOMO of the hole transport layer.

When a current is applied, charge begins to migrate inside the device. Electrons (e^-) are injected into the ETL-cathode interface when holes (h^+) are created in the HTL-anode interface. Driven by the electric field, they migrate inside their respective layer by a hopping process until they reach the Emissive Layer, EL. (For further details on the transport of the charge carriers, which is beyond the scope of this thesis, the reader is referred to the books of Shinar [5] or to the paper of Forrest [6] or Kalinowski [7]). The hole-blocking layer is made up of an organic material with a high HOMO but a LUMO low enough to let the electrons pass through to the EL. This hole-blocking layer can be used to control the electroluminescence in certain designs [8].

The first OLEDs had only one layer [3] between the two electrodes. This layer was based on fluorescent organic dyes. The introduction of different specialised layers had greatly improved the external quantum yield [9]. The two transport layers allow a better charge injection at the electrode interfaces, and they introduce a better control of the e^-h^+ recombination.

Current OLEDs emitting in the green or red region have a lifetime of up to 230,000 hours. The remaining challenge is to find a stable blue OLED, since current blue OLEDs have a much reduced lifetime. In May 2008, Merck KGaA launched a blue singlet emitter with an external quantum efficiency of 7 % with a lifetime of 36,000 hours [10].

The development of a white emitting OLED is under way, with the ultimate aim to replace classic lighting systems. This white OLED can be obtained from either iridium(III) complexes using a multilayer architecture [12, 13], or a multiply doped emissive layer [14], or a semiconducting polymer blend [15]. The complex

architecture required can be difficult to produce, so the trend is to synthesise new molecules which have a broad emission spectrum and high quantum yield [16, 17]. White OLEDs, their architecture and their challenges have recently been reviewed by D'andrade [18] and by Raja [19].

1.1.2 Influence of the electrodes on the device performance

Choice of the electrode material is important in maximising device efficiency. The HOMO energy of the hole transport layer should be slightly above the work function of the anode. A good connection is necessary between the anode and the injection layer, therefore specific cleaning of the electrode surface with an oxygen plasma or UV or ozone is required [20]. Also a coating can smooth the surface, and coating the anode with Pt or poly(ethylenedioxythiophene) doped with polystyrenesulfonic acid can enhance the injection by a factor of 100 relative to an uncoated electrode [21, 22, 23]. The most common material used as anode is ITO, but Pt [21], ZnO [5], or polyaniline [24] have also been used.

The LUMO energy of the electron transport layer should be slightly below the workfunction of the material used as cathode. A low workfunction metal such as Ca, Al or $Mg_{0.9}Ag_{0.1}$ can be deposited at the ETL surface. Diffusion of the metal into the organic layer can reduce the global efficiency of the device [5]. It is important to maintain a balance in the flux of charge carriers injected in the device.

Both organic transporting layers have quite a low conductivity. The typical mobility of h^+ in the HTL is 10^{-7} - 10^{-3} $cm^2 (Vs)^{-1}$ and the e^- mobility in ETL is typically lower by a factor of 10-100. This low conductivity associated with an efficient charge injection can produce charge accumulation in the organic film. This charge accumulation effectively quenches the luminescence. So we can extend the criteria for an efficient device to include a balanced charge injection in conjunction with the mobility of these charges in the HTL and ETL.

1.1.3 Hole transport layer (HTL)

The hole transport layer is usually an aromatic amine or some polymer such as polyaniline [25, 26] or polythiophene [28]. Some commonly used polymers are shown in figure 1.2. Their glass transition temperature T_g , should be high to avoid the formation of any crystals during processing. Crystallisation reduces the lifetime of the device dramatically and can be avoided by adding a guest molecule such as rubrene [27].

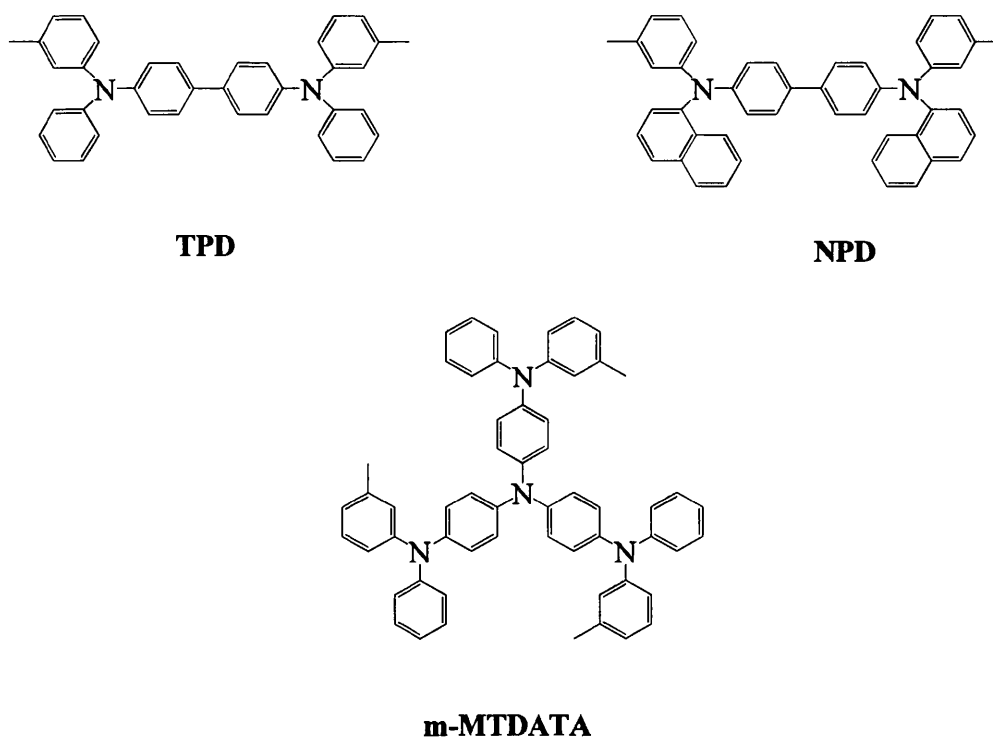


Figure 1.2: Molecules commonly used as HTL in OLED devices: **TPD** [29] (*N,N'*-diphenyl-*N,N'*-bis(3-methylphenyl)-1,1'-biphenyl-4,4'-diamine), **NPD** [28] (*N,N'*-diphenyl-*N,N'*-bis(1-naphthylphenyl)-1,1'-biphenyl-4,4'-diamine), **m-MTDATA** [29] (4,4',4''-tris(*m*-tolylphenylamino)triphenylamine)

1.1.4 Electron transport layer (ETL)

In some structures, the ETL was also the emissive layer. Tris(hydroxyquinolato)aluminium (Alq_3) is the classic example. The ETL material should not be a strong electron acceptor as it will efficiently quench the luminescence. Some commonly used molecules for the ETL are oxadiazoles (such as butyl-PBD), or distyrylarylenes such as DPVBi (see figure 1.2). Triazoles [29] or triazines can also be used as ETL. Commonly used polymers are poly(N-vinylcarbazole) or polyfluorene.

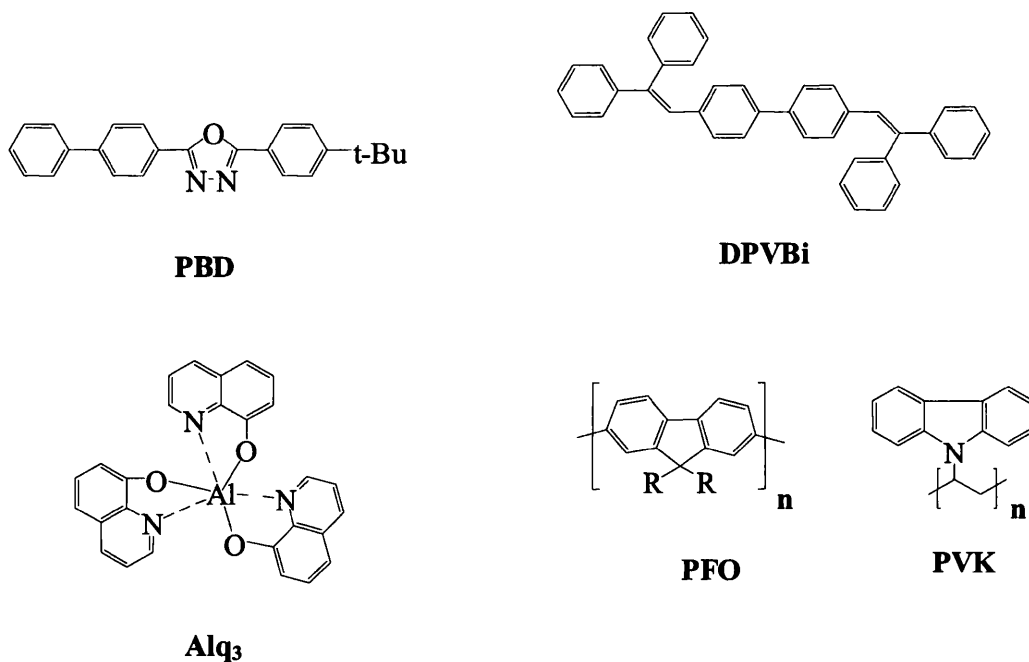


Figure 1.3: Polymers commonly used as ETL in OLED devices: **PBD** [30] (2-(4-biphenyl)-5-(4-tert-butylphenyl)-1,3,4-oxadiazole), **DPVBi** [28] (4,4'-bis(2,2'-diphenylvinyl)-1,1'-biphenyl), **Alq₃** (tris(8-hydroxyquinolato)aluminium), **PFO** (polyfluorene), **PVK** (poly(N-vinyl carbazole))

1.1.5 Emissive Layer

As we have seen before the ETL can also play the role of emissive layer, but this design is less efficient than using a specific layer dedicated to luminescence. A good emissive dopant should be thermally stable and have a very high quantum yield in the solid state. Experiments have proven that the emission is dopant-localised by comparing the emission of the OLED with the solid state emission of the different organic layers and the dopant. With a high enough concentration of dopant, the

matrix emission is totally quenched and electroluminescence arises from the dopant only [31, 32].

1.1.5.1 Phosphorescent or fluorescent emitters?

The emission is due to the formation of an exciton localised on the dopant through charge recombination. According to spin statistics this charge recombination can produce three triplet states and one singlet excited state. If both processes occur with the same kinetics, the probability of getting a triplet state is three times higher than that for a singlet state [33, 34]. A fluorescent material emits from the singlet excited state, so when the excited states of the dopant molecule are populated, 75% of the electron recombinations will be non-emissive [35], see figure 1.4.

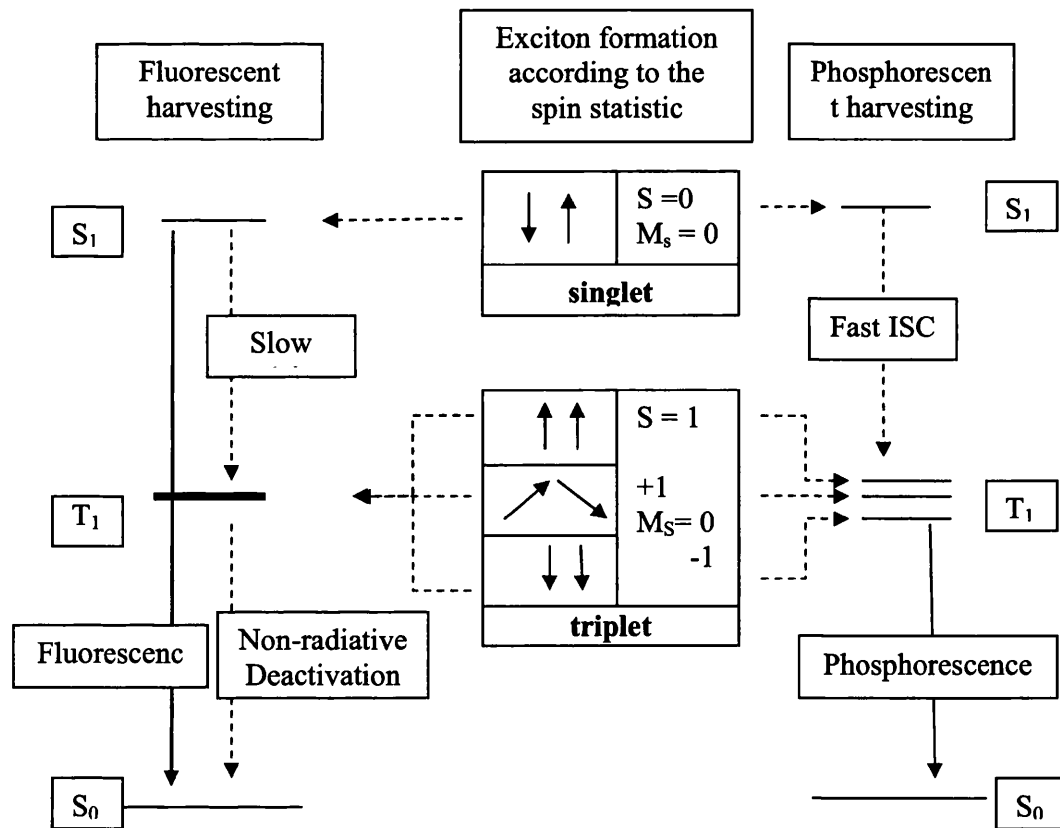


Figure 1.4: Scheme explaining the process of harvesting the exciton by the dopant molecule. Dotted lines represent non-radiative processes

When using a phosphorescent molecule, the excited singlet state can deactivate to the triplet excited state through rapid intersystem crossing, and therefore 100% of the charge recombinations can emit light. This theoretical 100% internal efficiency is

certainly harder to achieve than the theory suggests, as triplet-triplet annihilation or exciplex formation with the host matrix will quench the luminescence [36]. This theoretical approach has led to the development of the phosphorescent OLED [37] where the emitting dopant is a phosphorescent material. At the moment, commercial OLEDs are based on fluorescent materials, but the search for even better and more efficient devices continues and it is anticipated that phosphorescent light emitting devices will play an important role in this.

1.1.5.2 Charge transfer from the host matrix to the dopant

To explain conduction in an organic charge-carrier layer, the conduction band or the delocalization of orbitals in the material should be considered. In an inorganic host, the overlap of the orbitals of atoms forming the lattice leads to the formation of energy bands which allow the movement of charge through the material. In organic materials the hopping motion of a polaron is used to explain the conductivity of such materials. It is thought that the charge conductivity inside OLEDs lies somewhere in between these two processes.

The movement of charge is thermally activated. The electron transfer between an ionized species and its neutral neighbour is energetically neutral, but kinetically limited. This limitation in oxidation (hole transfer) or reduction (electron transfer) is explained by the Frank-Condon restriction: the electron transfer process should not change the total energy of the system [38]. Therefore, the ionized species and the neutral species should first be in the right configuration before the charge transfer can occur; this limitative reorganization step is related to the energy gained by the ionic species to get into the excited state from the neutral state.

Energy transfer occurs via the migration of an exciton. Two types of exciton have been defined:

- 1) Frenkel exciton, where the electron-hole is localised on the same molecule, and which requires large coulombic interaction over a small distance;
- 2) Charge-transfer exciton, where the hole and the electron are localised on two neighbouring molecules of the matrix and they transfer their energy to the dopant.

Three processes of energy transfer are in competition: Förster, Dexter and charge trapping and their relative importance depends on the lifetime of the exciton, the thickness of the film and charge mobility [35].

1.1.5.3 Triplet emitters for OLEDs

Since the aim of the work presented in this thesis was the synthesis of efficient triplet emitters, we will not describe the singlet emitters existing in the literature [11, 39]. Nevertheless, coumarin (green emission) [40], pyran based materials (red emission) [41] or distyrylarenes (blue emission) [42] can be given as examples of fluorescent molecules which cover the visible spectra.

The emitting layer can be of a number of different types: small molecules [43], organometallic polymers [44, 45, 46, 47] or dendrimers [48, 49].

The advantage of using small molecules is the localisation of the exciton on one molecule acting as a trap in the system, which prevents the diffusion of charge and allows better control of the luminescence properties.

A review from Evans *et al.* [43] assesses the recent discoveries and trends in research on triplet emitters. Third row organometallic compounds are perfect candidates for phosphorescence properties as the heavy atom effect will promote triplet excited state formation. An extensive survey of the photochemistry and photophysics of coordination compounds regrouped by metal types has recently been published [50, 51] and this is a gold mine for further reading, and references on any specific metal. Generally, iridium complexes are the best known phosphorescent emitters, followed by some platinum derivatives.

Red emitters

Early red emitters were based on Pt(II)-octaethylporphine [44] or europium complexes [53], but had a low efficiency. Some recent research on the iridium complex of 2-benzo[b]thiophen-2-ylpyridine [54] or phenylisoquinolines derivative [55] gives a better yield. Some pyridyl-azotale osmium, ruthenium or iridium complexes also look interesting as red emitters [56].

Green emitters

Classic green emitters are [Ir(ppy)₃], (ppy = 2-(2-pyridyl)phenyl) and related derivatives [57, 58]. Benzoimidazole [59] or 2-phenylbenzothiazole [60] iridium complexes are other highly efficient green emitters.

Blue emitters

A first challenge for the design of blue emitters is to find the right host. The LUMO-HOMO gap of a blue emitter is by nature the largest of the emitting compounds and to get an efficient recombination the design of a new host has been necessary. Therefore arylsilane materials such as diphenyldi(*o*-tolyl)silane have been created [61]. A second challenge is to find a stable lumophore with a high enough triplet state to correspond to a blue emission. Stability is one of the main problems as this high energy triplet state is relatively long-lived. This is why the use of blue phosphorescent emitters in OLED devices falls far behind their fluorescent counterparts.

Just a few blue phosphorescent emitters have been tested into OLED devices and they have very short lifetimes (300 hours). Proposed blue emitters include some cyclometalated Ir(III) complexes with pyrazolyl or picolinate ancillary ligands [62,63].

1.1.6 Efficiency

The OLED external efficiency η_{ext} is given by:

$$\eta_{ext} = \eta_{int} \times \eta_{ph} = \gamma \eta_{ex} \Phi_L \eta_{ph} \quad \text{Equation 1.1 [64]}$$

where η_{int} is the internal efficiency and η_{ph} is the light-out coupling efficiency. η_{int} is made up of η_{ex} , which is the fraction of total exciton formed which will effectively populate an emitting excited state (η_{ex} is 0.25 for a fluorescent molecule and 1 for a phosphorescent molecule), γ is the ratio of electrons to holes injected from opposite contacts and Φ_L is the intrinsic quantum yield for radiative decay, which includes both phosphorescence and fluorescence.

1.2 Photophysical processes of organic molecules

When a molecule absorbs a quantum of light energy, it goes into an excited state. From this excited state, it will relax to the ground state through different processes: radiative (phosphorescence or fluorescence) or non-radiative (intersystem crossing (ISC), vibrational deactivation, internal conversion, energy transfer).

1.2.1 Creation of an excited state

A molecule in the ground state has its electrons filling the orbitals in such a way that the total energy of the molecule is a minimum. When a quantum of energy is absorbed by the molecule, the lowest electronic configuration of the molecule changes to promote an electron into a molecular orbital of higher energy, which creates an excited configuration. One of the most common ways to generate an excited state is by absorption of a single quantum of light energy, a photon.

1.2.1.1 Absorption of a photon

Light can be described as an electromagnetic wave or a stream of particles in movement called photons. The strength of the interaction of the electromagnetic wave with a molecule will determine the amount of light absorbed by such molecules. In solution, the absorbance is directly linked to the concentration by the Beer-Lambert law:

$$A = \epsilon \times c \times l \quad \text{Equation 1.2}$$

where ϵ is the molar extinction coefficient in $\text{dm}^3 \text{mol}^{-1} \text{cm}^{-1}$, c is the concentration in mol dm^{-3} and l the cell path length in cm.

1.2.1.2 Rules regulating the transition

A transition is a very abrupt event. The electronic transition occurs a lot faster than any nuclear vibration, therefore it is assumed that the nuclear positions in the molecule are the same during a transition (Franck-Condon principle [38]).

The transitions between two electronic states are governed by two selection rules which indicate their feasibility in term of quantum numbers. They arise from the fact that the total angular momentum is conserved during a transition:

1) Laporte's rule [65]:

Electronic transitions which conserve either symmetry or asymmetry relative to an inversion centre are forbidden (e.g., g→g or u→u transitions are forbidden).

2) Spin selection rule:

A transition should conserve the electron spin or $\Delta S = 0$, where S = spin quantum number. All transition between two states of different multiplicity should be forbidden in a first order approximation.

These selection rules give an idea about which transitions may or may not occur. However, the triplet to singlet transition (phosphorescence) or symmetry forbidden transitions ($n \rightarrow \pi^*$) are frequently observed. The breaking down of the spin selection rule (phosphorescence notably) can be explained by the interaction between the orbital angular momentum and the spin orbital momentum (known as spin-orbit coupling), or to a weaker extent the interaction between the spin of two different electrons (spin-spin coupling). The intensity of the spin-orbit interaction depends on the size of the molecular orbitals and the relative orientation of the two angular momenta. The greater the nuclear charge, the greater is the electron orbital angular momentum and the greater the spin-orbit coupling. Coupling constants in heavy atoms are of the order of magnitude of an electronic transition ($\sim 80 - 125 \text{ kJ mol}^{-1}$) [38]. This phenomenon is called the "heavy atom effect" where the spin-forbidden process is enhanced by the presence of an atom of high atomic number. So when excited in its S_n state, the heavy atom effect will lead to an efficient intersystem crossing from the singlet excited state to the triplet manifold. Furthermore, the spin-forbidden nature of the $T_1 \rightarrow S_0$ radiative transition will be partially removed and this may result in intense phosphorescence.

1.2.2 Characteristics of an excited state

1.2.2.1 Multiplicity

The excited state of a molecule is characterised by its total spin S , which gives the multiplicity ($2S + 1$). When all the electron spins are paired ($S = 0$), the multiplicity equals 1, and the state is called a singlet. These excited states are denoted S_n . If two electron spins are unpaired ($S = 1$), the multiplicity equals 3 and the state is a triplet. These excited states are denoted T_n . States of higher multiplicity are also possible, and are important in the photochemistry of some transition metals, and even more so in the lanthanides.

1.2.2.2 Configuration

The energy states are related to the molecular orbitals (MOs) of which they are composed. The photophysical properties of any molecule are also related to these MOs.

1.2.2.2.1 Configuration in aromatic hydrocarbons

The linear combination of the atomic orbitals can give two bonding orbitals (σ and π), a non bonding orbital (n) and two anti-bonding orbitals (σ^* and π^*). Their relative energies are ordered:

$$\sigma < \pi < n < \pi^* < \sigma^*$$

1.2.2.2.2 Configuration in metal complexes

Metal complexes generally do not have their frontier molecular orbitals delocalised uniformly across the molecule but often preferentially localised on the metal or the ancillary ligand. When excited, an electronic transition between the occupied and unoccupied frontier orbitals will take place. Therefore the nature of the excited state can change according to the nature of the metal and the ligand; this induces versatile photophysical properties which can be exploited in OLED technology. Different types of transitions can occur.

Metal to ligand charge transfer (MLCT)

This type of transition often occurs when the metal is in a low oxidation state, mostly with metals belonging to the middle or late transition elements. It involves an

electronic transition from the metal d orbital to the ligand π^* orbital [66]. Since the π^* orbital is usually delocalised, a minimal geometrical distortion occurs in the molecule upon excitation, and this can enhance the radiative relaxation of the excited state.

Ligand to metal charge transfer (LMCT)

Ligand to metal charge transfer occurs from the filled ligand orbitals to an empty metal orbital. The metal should be in a high oxidation state to be able to act as a reductive species, and is typically from the early transition metals. However, Cu(I), Ag(I) and Au(I) also give this type of transition, and due to the heavy effect atom, this can lead to phosphorescence radiative decay.

Intraligand charge transfer (ILCT)

Intraligand charge transfer occurs between π orbitals localised on the same ligand. If the metal perturbation of the ligand is minimal, the emission could be very similar to that exhibited by the free ligand. The heavy atom effect can enhance the spin-orbit coupling and in consequence the phosphorescence properties of the ligand.

Metal centred transitions (MC)

Metal centred transition occurs between the filled d_{π} non-bonding orbital of the metal and the d_{π^*} antibonding orbital of the metal. These transitions are Laporte forbidden and, as a result, are generally of low intensity. This transition is due to the splitting of the d orbital of the metal upon coordination. The difference in energy is quite small and therefore this absorption band is generally observable in the visible. With late transition metals, having a strong-field ligand, this MC transition can be shifted to higher energy.

1.2.3 Deactivation of the excited state

When in the excited state, the molecule tends to release the excess energy and go back to the ground state. Different pathways may contribute to this relaxation: by emitting a photon (a radiative pathway) or by any non-emissive ways. The two radiative pathways are:

- 1) fluorescence which occurs from a state of the same multiplicity as the ground state ($S_n \rightarrow S_0$) and therefore is spin-allowed;
- 2) phosphorescence which occurs from a state of different multiplicity from the ground state and therefore is spin forbidden (usually $T_n \rightarrow S_0$).

As the fluorescence transition is allowed, this process is quick (typically 10^{-12} to 10^{-6} s). As phosphorescence is spin forbidden, the deactivation process is longer (typically 10^{-6} to 10^{-1} s).

The principal non-radiative pathways from an excited state are:

- 1) internal conversion, which is radiationless energy transfer between states of the same multiplicity;
- 2) inter system crossing, which consists of radiationless energy transfer between states of different multiplicity;
- 3) energy transfer between different molecules. This charge transfer is the basis of the OLED technology. However, this can lead to the quenching of the luminescence (the quenching of the triplet state by singlet oxygen is a typical example).

1.2.4 Energy transfer

The energy transfer between two excited states is a deactivation pathway which in most applications needs to be prevented for efficient luminescence. However in OLED technology it is required to create the excited state.

Schematically, an excited donor entity D^* will transfer its energy to the ground state of an acceptor entity A, which will be promoted to its excited state A^* , when the donor will go back to its ground state D following the scheme 1.1.

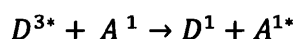
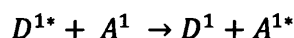


This energy transfer can only occur when the energy difference between the ground state and the excited state of A and D is the same. The entities can interact in three

ways: Coulombic interaction (Förster type, long distance), exchange interaction (Dexter type, short distance) or by charge trapping.

Förster energy transfer [67]

The coulombic interaction involves the coupling of the magnetic moments or dipole-dipole interaction through space ($\approx 40-100 \text{ \AA}$) between the donor and the acceptor (see fig. 1.5). No direct contact between the centres is needed as the interaction is due to electromagnetic forces through space. The acceptor excited state should be the product of an allowed transition, and because of this in general this mechanism involves the generation of singlet states.



The rate of energy transfer k_{ET} has been evaluated to be as follows.

$$k_{ET}(\text{Förster}) = k \frac{\kappa^2 k_D^0}{R_{DA}^6} J(\epsilon)$$

The rate is proportional to: the spectral overlap, $J(\epsilon)$, of the acceptor absorption with the donor emission; R_{DA}^{-6} where R_{DA} is the distance between the donor and the acceptor; κ , representing the dependence of the interaction on the relative orientation of the dipoles; the radiative rate of the donor k_D^0 , and k , representing an experimental constant depending on the concentration and the refractive index of the solvent.

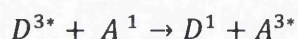
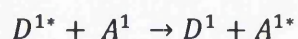
Dexter energy transfer [68]

The Dexter energy transfer is a short distance transfer due to the spatial overlap of electron clouds. This takes place on a scale of one to two molecular distances (10 \AA). The rate constant for electron exchange k_{ET} has been proposed by Dexter to be as follows

$$k_{ET}(\text{Dexter}) = K J e^{-\frac{2R_{DA}}{L}}$$

K is related to their specific orbital interaction, J is the normalized spectral overlap, R_{DA} is the distance between the donor and the acceptor relative to the van der Waals radii, L.

An immediate difference between the Dexter and the Förster theory is that triplet-triplet energy transfer (with a very weak oscillator strength) is spin allowed in the electron transfer (Dexter) theory.



A second difference is the relation between the energy transfer rate constant and the interaction distance: in the dipole interaction mechanism the rate is proportional to R_{DA}^{-6} and can occur over distances of up to 100 Å. In the orbital overlap mechanism, the rate is proportional to the exponential of $(-R_{DA}/L)$ and therefore will decrease drastically with distance, and the effect can only be short range up to 10 Å. A Dexter mechanism will be localised between two molecules, and will be slow between molecules which are not neighbours.

Both mechanisms are dependent on the extent of spectral overlap between the donor D^* emission and the acceptor A absorption.

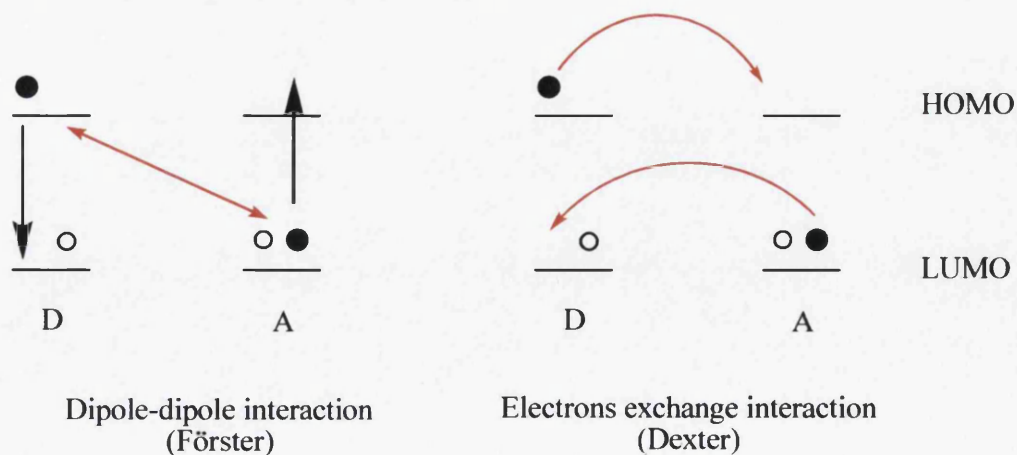


Figure 1.5: Electronic transitions in the two different energy transfer mechanisms

Charge trapping

A third process can occur in which the guest molecule traps a charge and generates an exciton by recombination with an opposite charge on a neighbouring molecule. This mechanism allows triplet-triplet charge transfer.

1.2.5 Charge transfer in OLEDs

When an exciton transfers its energy to the guest emitting molecules, it will do so via one of the three processes previously described. The competition between the three processes depends on the concentration of the dopant, on the mobility of the charge carrier, the lifetime of the exciton and the thickness of the layers. Charge transfer to a singlet excited state can be done through all three processes, but the Förster one will dominate as it is a long distance interaction and will be less dependent on exciton migration than the others.

Charge transfer to a triplet can also be achieved through the three mechanisms. However, the Förster charge transfer process will not populate the triplet state, a spin flip of the electron is necessary. Dexter transfer and charge trapping populate directly the triplet state and therefore will be the main mechanism for generation of the excited triplet state in OLEDs.

1.2.6 Factors governing the rate of non-radiative decay

The probability of a transition is proportional to the overlap of the vibrational wavefunctions of the initial and final states of the transitions. The larger the difference in vibrational quantum numbers, the smaller the probability of the transition. The transition probability also depends on the relative geometry of the excited state and ground state molecule. If the two geometries are alike, the transition will occur between states of the same quantum number, if the geometry is different the transition will take place where the overlap of wavefunctions will be the greatest. A radiationless transition transforms electronic energy into heat or kinetic energy. To occur, it needs to be successively a vertical and a horizontal transition. Therefore this transition will occur between states having a small difference in vibrational number. In the case of a compound with different geometry in the excited and ground state, there is a possible overlap of the wavefunction which will promote this radiationless transition.

1.3 Gold complexes as possible emissive dopants in OLEDs

Evan's review [43] points out the small amount of study on gold complexes as potential emitting dopants. To our knowledge, only three devices have been reported in the literature which use gold complexes: $[\text{Au}_2(\text{dppm})_2]\text{Cl}_2$ [69], $[\text{Au}_2\text{Cl}_2(\text{dppm})]$ [70] and a phosphole gold(I) complex [71]. Gold has one of the largest spin-orbit coupling constants among metals, ($\zeta_{\text{Au}} = 5104 \text{ cm}^{-1}$) [72], and many gold organometallic derivatives show phosphorescence in the solid state or in solution. The emission can be easily tuned by ligand variation and/or by metal-metal interactions, and the emission wavelengths can span the whole visible spectrum [43]. However their electrochemistry is often irreversible, so their redox stability could be a problem for OLEDs.

1.4 Introduction to gold chemistry

When we think about gold, the first thought is of a malleable noble metal with a characteristic beautiful yellow colour. Its cultural symbolism and physical properties are a universal attraction and chemists do not escape from its seduction.

Since antiquity gold has found numerous applications in technology, crafting and medicine. A gold(I) derivative of thioglucose constitutes the major medication for early rheumatoid arthritis (Auranofin). Its biochemistry, notably its cyto-toxicity towards cancer cells and anti-arthritic activity, has been recently reviewed by Shaw III [73, 74]. Its unique malleability, stability, high boiling point and the large colour range of its alloys are inestimable presents for jewellers and craftsmen. More recently, its high electrical and thermal conductivity, its chemical inertia towards heat, air, most corrosive agents and moisture made it an ideal candidate for high precision and reliable electronic devices and connections (as in spacecraft). Some recent studies show a promising role as a heterogeneous or homogeneous catalyst [166, 167]. Also, despite its noble character, it has a rich chemistry and organo-gold complexes often have luminescent properties which could be used for example in the sensing industry.

With an atomic mass of 197 and an atomic number of 79, gold has only one naturally occurring stable isotope: ^{197}Au . Its electron configuration is $[\text{Xe}] 4f^{14} 5d^{10} 6s^1$. Oxidation states can vary between $-I$ and $+V$, with common oxidation states of $+I$ or $+III$. Its electronegativity on the Pauling scale is 2.54, very close to those of sulphur (2.58) and selenium (2.54). It has a high electron affinity (223 kJ mol^{-1}), which explains the stability of the $-I$ oxidation state. Its two first ionisation energies are 890 kJ mol^{-1} and 1980 kJ mol^{-1} .

Gold presents some unique behaviour which can be explained by two phenomena working together, [76]

- Relativistic effects, which are the highest among atoms with atomic number below 100. This relativistic effect is attributed to the speed of the s or p outer-shell electrons of heavy atoms, which approaches the speed of light. A mass increase will lead to an energy stabilisation and a contraction of the orbitals. This orbital

contraction shields the d or f orbital from the nuclear attraction and therefore the radius of these orbitals expands.

- the lanthanide contraction, which is the effect of filling the 4f orbital on the 6s and 6p orbitals.

The theory of these effects in gold has been the life work of Pyykö and the reader is referred to the following references for a more detailed description: [75, 76, 77, 78]. Some of the consequences of the lanthanide contraction are the smaller size of the gold atom compared to silver, and short Au-L distances.

The relativistic effects are at the origin of a very peculiar behaviour: two or more gold(I) cations can form a bond with an energy of *ca* 30-50 kJ mol⁻¹ [79-82] which is comparable to that of a strong hydrogen bond. This Au-Au bond length can be as short as 270 pm but is usually to be found around 300 pm, clearly shorter than the sum of the van der Waals radius (370 nm). This specific type of bonding has been baptised by Schmidbaur in 1989 as “aurophilicity” and has been the source of numerous investigations in a range of studies including: polymers, self-assembly, sensors, luminescence, and theoretical studies. Aurophilicity orients molecules in crystals, governs the properties of certain polymers based on gold(I) derivatives, and has a strong influence on luminescence properties.

1.4.1 Gold coordination

The gold atom can be found in the following oxidation states -I, 0, +I, +II, +III, + V, but the coordination chemistry of gold is largely dominated by the +I and +III state. It is a “soft” atom which prefers to bind with large polarisable ligands. The softness of gold has been proven by using ambidentate ligands where the gold atom tends to bind preferentially to the softer end of the ligand [83]. For example complexes with SCN are S-bonded rather than N-bonded, NCO complexes are N-bonded rather than O-bonded. There are numerous gold complexes, connected to different atoms: halogens, chalcogens (mainly S, although some examples of Se-bonded or O-bonded species will be reported), group 15, and carbon. Compounds with coordination number 2, 3 or 4 are quite common. The following brief overview of the rich chemistry of gold is presented according to oxidation state.

The fragment $[\text{Au-PR}_3]^+$ is isolobal with H^+ ; this is used to predict the reactivity of certain heteronuclear metal-gold complexes. An example of this isolobality analogy is illustrated by the gold-carborane cage complex which forms a trigonal coordination at gold upon hydrogen substitution [114]. When two or more of these fragments are vicinal, the analogy disappears because of the aurophilicity (and the tendency to form gold(I)-gold(I) bonding).

1.4.1.1 Gold complexes with gold in the oxidation state -I

Gold has the highest electron affinity of all metals. This is due to the relativistic effect on the 6s orbital. Therefore the lowest oxidation state for gold is -I: for example CsAu [84], CsAu-NH_3 [85], RbAu , KAu or $(\text{Me})_4\text{NAu}$ [86] have been reported.

1.4.1.2 Gold complexes with gold in the oxidation state +I

In the oxidation state +I, its electron configuration is $[\text{Xe}] 4f^{14} 5d^{10} 6s^0$. When two ligands are used, it has the tendency to coordinate in a linear mode with both ligands in *trans* positions. It can also adopt a three- or four-coordinated geometry.

1.4.1.2.1 Mononuclear gold(I) complexes

Mononuclear gold(I) complexes can have coordination numbers 2, 3 or 4. Some usual precursors to obtain gold derivatives are $[\text{AuCl}(\text{THT})]$ (THT = tetrahydrothiophene) [87], $[\text{AuC}_6\text{F}_5(\text{THT})]$ [88], $[\text{Au}(\text{THT})_2]\text{ClO}_4$ [89], $[\text{AuCl}(\text{SMe}_2)]$ [90] and different chlorogold(I) phosphine complexes [91]. The coordination number depends on the proportion and the nature of the starting material, as is nicely illustrated by the work on gold(I) dppf complexes [92].

When its coordination number is 2, gold(I) adopts a linear geometry. For example we can see the well known series of mononuclear gold(I) phosphine thiolate complexes. When possible, the crystal structure of the members of this series always shows a short gold-gold distance in the range of 2.9-3.3 Å. A series of complexes $[\text{Au}(\text{S-2,4-6-C}_6\text{H}_2\text{R}_3)(\text{PPh}_3)]$ with $\text{R} = \text{H}, \text{Me}, \text{Et}$ or *i*-Pr shows that only the complex with $\text{R} = \text{H}$ forms a dimer, proving the importance of steric effects in the presence of the aurophilic interaction [93]. The small cone angle phosphine TPA has been used by

Figure 1.6: Examples of four- or three-coordinated mononuclear gold(I) complexes. Four-coordinated mononuclear gold(I) complexes adopt a tetrahedral geometry, e.g. $[\text{Au}(\text{PPh}_3)_4]\text{BF}_4$ [119], and $[\text{Au}(\text{TPA})_4]\text{Cl}$ [120]. With bidentate ligands such as dppe [115], the tetrahedral geometry is disturbed due to steric effects.

1.4.1.2.2 Binuclear gold(I) complexes

Binuclear gold(I) complexes involve in coordination with the same ligand types as the mononuclear ones. They can exist in either open or ring structures. An important feature for these compounds is the possibility of intra-molecular gold(I)-gold(I) interactions. The steric effect imposed by the ligand plays an important role as has been shown by the elegant design of the three compounds shown fig 1.7 [121]. Compounds A and B allow intramolecular gold-gold interactions in the solid state ($d_{\text{Au-Au}} = 300 \text{ pm}$) whereas C allows only intermolecular gold-gold interactions.

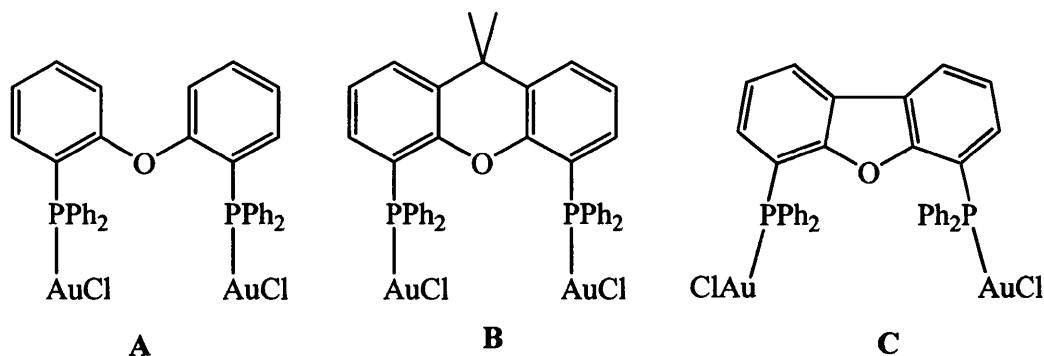
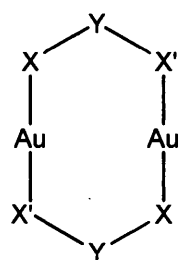


Figure 1.7: Example of a series of binuclear gold(I) complexes used to illustrate the influence of the aurophilicity on the luminescence

Aurophilicity influences the geometry of the molecules in the crystal packing. For example open ring dinuclear complexes having a bidentate diphosphine ligand $\text{PPh}_2(\text{CH}_2)_n\text{PPh}_2$ with $n \geq 2$ have the tendency to have their gold moieties in an *anti* configuration [80, 122-124]. However, when dppm is used the two gold moieties are in a relative *syn* position [125,126] even if the other ligand is bulky [127]. If a dithiolate is the bridging ligand, a short distance between the two gold-anchoring groups will also promote the *syn*- conformation so that the gold atoms can interact with each other [128].

Annular binuclear gold complexes have been quite extensively studied. Eight-membered rings (see fig 1.8) were the first synthesised. Then Bruce et al. [80] extended the number of atoms in the ring by using larger dithiolates and diphosphines as bridging ligands, and studied their luminescence.



(Charge omitted)

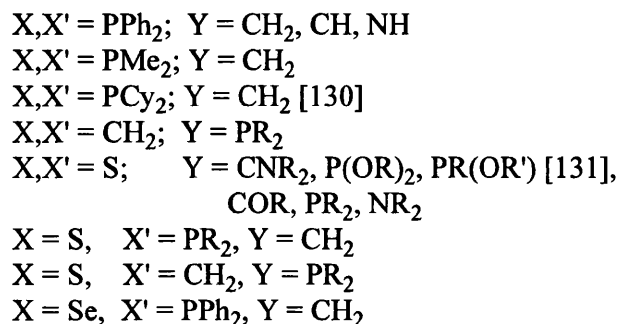


Figure 1.8: different annular gold complexes, from reference 129 except if annotated

The coordination number can go up to three for binuclear gold complexes. $[Au_2(dmpm)_3]^{2+}$ is an example [132], as is the bis(triphenylphosphinegold(I) dithiolate [133] in which one of the gold atoms can be considered as three-coordinated.

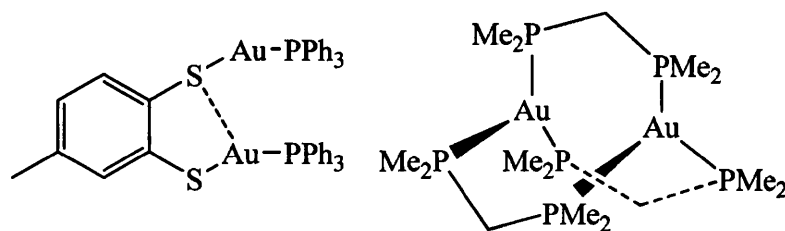


Figure 1.9: Binuclear gold(I) compounds having a coordination number of 3

1.4.1.2.3 Multinuclear gold(I) complexes

Multinuclear gold(I) complexes can be divided into small molecules and polymeric structures.

Small molecules

Some triphosphine compounds have been used to synthesise trinuclear gold(I) complexes: for example $\text{CH}(\text{PPh}_2)_3$ [135], bis(dimethylphosphinomethyl)methylphosphine [136] or bis(diphenylphosphinomethyl)phenylphosphine [137].

Some tetragold(I) complexes with N-Au-P bonds have also been synthesized by using some amidinate complexes [138] to form the structure A in figure 1.10, where gold(I) atoms are in a plane forming a square. By choosing carefully the building block, Lin and *al.* have synthesised a luminescent gold rectangle which can be used for molecular recognition (structure B, figure 1.10) [139].

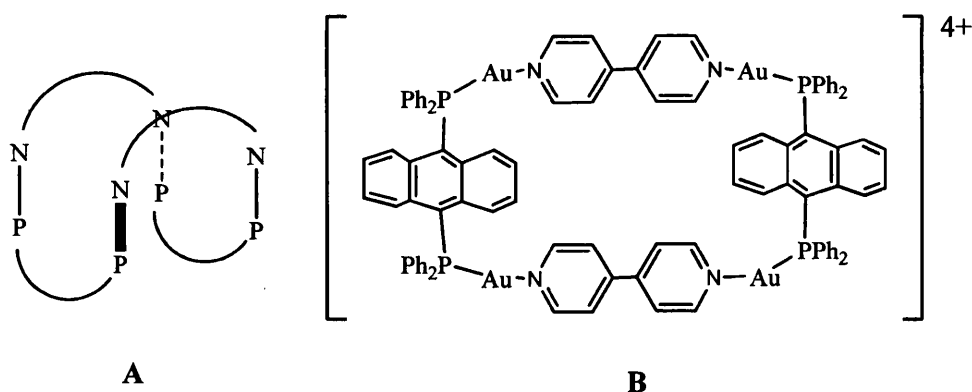


Figure 1.10: Some tetranuclear gold(I) complexes

Polymers

The aurophilic interaction has been used to build one- or two-dimensional supramolecular networks [140]. 4,4'-Bipyridyl has also been used with (diphenylphosphino)alkanes to build long polymer chains [142] and Puddephatt studied the equilibrium between the annular form and the polymeric form of different gold(I) complexes [143-145]. These polymers can emit light and possibly could be used as functional new materials [146]. Finally some functionalised calixarenes give

tetranuclear gold(I) complexes which phosphoresce, and which can be used as molecular sensors [147].

1.4.1.3 Gold complexes with gold in the oxidation state +III

In the oxidation state +III, the electron configuration is $[\text{Xe}] 4f^{14} 5d^8 6s^0$. Gold(III) coordination is essentially square planar as illustrated in figure 1.11 with a gold(III) bis(pyrazine-2,3-diselenolate) complex [148].

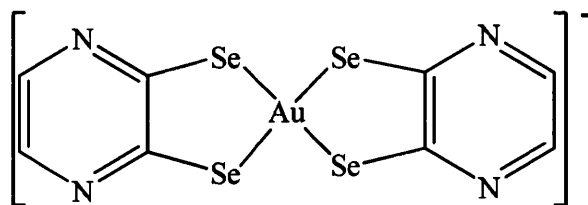


Figure 1.11: Typical square planar coordination for Au(III)

Luminescent gold(III) complexes are rare, and therefore we will not describe gold +III complexes further. Except to note that the gold(III) complexes created by Buckley $[\text{Au}(\text{N}^{\wedge}\text{C})\text{X}_2]$ ($\text{N}^{\wedge}\text{C} = o\text{-C}_6\text{H}_4\text{CH}_2\text{NMe}_2$, $\text{X} =$ monodentate anionic ligand or $\text{X}_2 =$ bidentate dianionic ligand) [149] opened the route to a variety of compounds which have been tested for cytotoxicity and antitumour activities [150, 151].

1.4.1.4 Gold complexes with gold in the oxidation state +V

The only reported gold(V) complexes are AuF_5 and the anion AuF_6^- . In the solid state, gold(V) fluoride is dimeric Au_2F_{10} [152]. The monoanionic hexafluoroaurate(V) AuF_6^- has been synthesised with the counter cations $[\text{Xe}_2\text{F}_{11}]^+$, Cs^+ , $[\text{O}_2]^+$ and $[\text{KrF}]^+$ [153].

1.4.1.5 Hypothetical gold complexes with gold in higher oxidation state

A recent computational study [154] contradicts the report made in the 1980s of the formation of AuF_7 which has not subsequently been reproduced. According to the calculation, AuF_7 is expected to be easily decomposed into F_2 and AuF_5 in an exothermic process, which contradicts the claim made of a stable compound at room temperature [155, 156]. Higher oxidation states than +V are unlikely for Au.

1.4.2 Luminescence of gold complexes

Gold(III) complexes are usually non-luminescent. This could be explained by the presence of low lying d-d ligand field states which will quench the luminescence by thermal equilibration or energy transfer [157]. Recently Yam synthesised the first luminescent gold(III) complex which is based on a (C[^]N[^]C) pincer ligand (figure 1.12). [158, 159]. Gold is connected to a strong σ -donor acetylide ligand which should increase the d-d energy gap and reduce the quenching. The emission is believed to originate from a LLCT excited state.

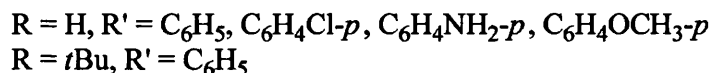
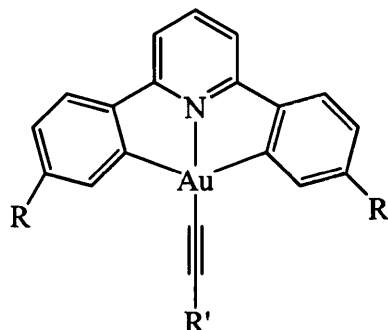


Figure 1.12: Room temperature luminescent Au(III) complexes

Of all its oxidation states, gold(I) complexes present the richest luminescent properties. When they emit, it is always through a spin-forbidden transition (phosphorescence) which is strongly allowed by the heavy atom effect of the gold atom. The luminescence of gold(I) complexes has been attributed to ligand centred [112], metal centred [116], and LMCT [94, 160] states, or a combination of these excited states [161]. The excited state is influenced by the ligands and by changing the ligand electron density it is possible to tune the emission of the gold complexes.

Laguna recently synthesized a series of pentachlorophenylgold pyridine complexes $[\text{Au}(\text{C}_6\text{Cl}_5)(4\text{-R-C}_5\text{H}_4\text{N})]$ ($\text{R} = \text{MeO}, \text{Me}, t\text{Bu}, \text{H}, \text{COOMe}, \text{CN}$) and studied their photoluminescence properties, showing the importance of having a more electron-donating group on the pyridine for tuning the maximum emission wavelength towards the blue [98]. The origin of the luminescence is attributed to a LLCT (ligand to ligand charge transfer).

In gold phosphine thiolates, the origin of the luminescence is usually attributed to a LMCT $^3[\text{S} \rightarrow \text{Au}]$ excited state [120, 125, 162] and therefore an electron rich gold(I) having a stronger σ -donor phosphine (like dcpm instead of dppm) or electron-withdrawing groups on the thiolate should blue-shift the emission [120].

An important feature in gold chemistry is the aurophilicity and it plays an important role in the photochemistry of these derivatives. If we take the z axis along the Au-Au vector, and x axis along the S-Au-P bond, the energy of the orbitals without any gold-gold interaction lie in the following order: $\text{Au}(6p_z) > \text{S}_p > \text{Au}(5d_{z^2}) \geq \text{Au}(5d_{x^2-y^2}) > \text{Au}(5d_{xy}) \geq \text{Au}(5d_{xz})$, with S_p being the HOMO and $6p_z$ the LUMO. When the two gold are close enough, the $5d_{z^2}$ and $5d_{x^2-y^2}$ orbitals will be the most affected by the interaction [80]. The sulphur orbital will also be destabilised as the repulsion between the lone pairs on sulphur will increase when getting closer. This will reduce the HOMO-LUMO gap and is responsible for a red-shift in the emission (see figure 1.13).

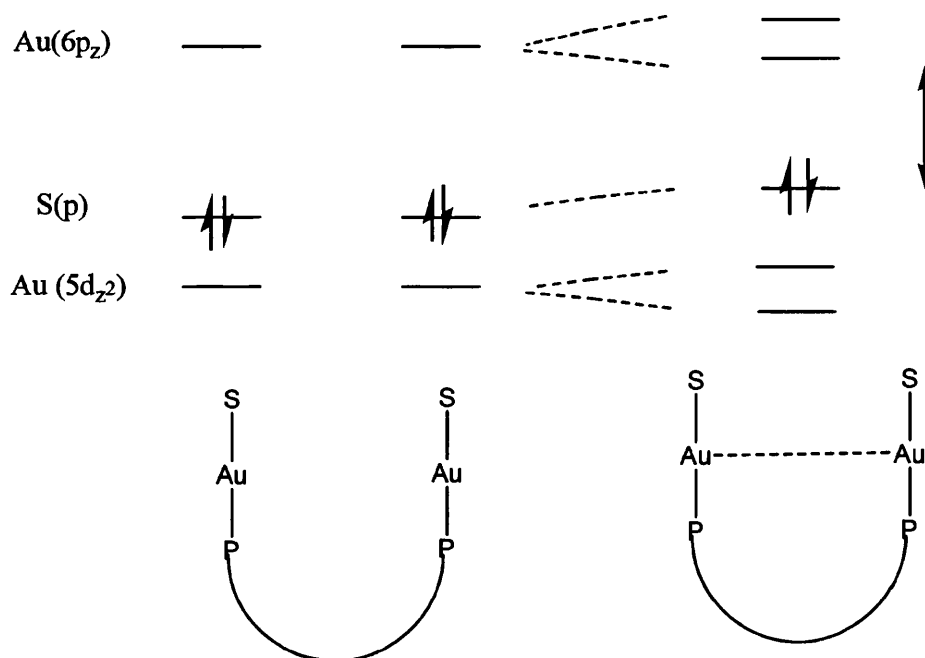


Figure 1.13: Molecular orbital diagram showing the influence of the gold-gold interaction on the luminescence

A study on monogold(I) phosphine thiolates [94, 163] shows that Au-Au interactions play an important role in the luminescence of this kind of compound. But it is not a necessary condition for an emitting species.

Fackler and co-workers have synthesised a series of binuclear gold(I) dithiophosphonate complexes and related their structure to their luminescence properties. There is a clear relation between a longer gold-gold distance and an emission at higher energy [131]. This is explained by the extent of aurophilicity in the molecule; the shorter the distance the stronger will be the gold-gold interaction and the more destabilised will be the HOMO, red-shifting the emission. Yam [157] used this property to design some chemo-sensing materials based on two benzo-15-crown thiolates bonded to a $[\text{Au}_2(\text{dppm})]$ moiety. When a cation interacts with the two crownethers, it brings the two gold atoms to a distance where they can interact, and a drastic redshift in emission is observed.

Tuning of the emission by changing ligand electronic properties will be illustrated by two examples. Gold acetylenic compounds emit from a $^3(\pi, \pi^*)$ excited state based on the ligand [166-168]. By using $[(\text{AuX})_2(\text{dppa})]$ (dppa = bis(diphenylphosphino)acetylene), Laguna's group tuned the room temperature solid state luminescence from 470 nm ($\text{X} = \text{Cl}$) to 516 nm ($\text{X} = \text{C}_6\text{F}_5$) and 598 nm ($\text{X} = \text{S}_2\text{CN}(\text{CH}_2\text{Ph})_2$). The room temperature solid state emission of a series of monogold(I) phosphine thiolate complexes $[\text{Au}(\text{SC}_6\text{H}_4\text{X})(\text{P})]$ has been tuned from 413 nm ($\text{P} = \text{PPh}_3$, $\text{X} = \text{H}$) to 702 nm ($\text{P} = \text{TPA}$, $\text{X} = m\text{-Cl}$) by changing the ligand substituent and the extent of the aurophilicity [94].

The luminescence properties of gold(I) complexes have been the subject of hundreds of studies and the following references are useful reviews: 6, 51, 157, 164. Due to the complexity of the origin of the emission, and the development of more reliable orbital occupancy simulations, the use of *ab initio* calculations to determine the occupancy of the LUMO and HOMO are being used as an aid to the interpretation of the results.

1.5 Strategy for designing a potentially efficient blue emitter based on a gold(I) derivative

The aim of this work is to explore the synthesis chemistry and photochemistry of some novel binuclear gold complexes with a mind to the synthesis of new efficient and stable triplet emitters for display applications. Binuclear gold(I) complexes were selected from the series of potential emitters reviewed by Evans [43].

The deposition of the dopant being by vapour deposition, it is necessary to have a product with a low sublimation point which is thermally stable during the sublimation process. Ionic species have a higher sublimation point than their neutral counterparts and also they can react with the charge circulating in the OLED host layer. Therefore it has been decided to concentrate on neutral gold(I) complexes such as gold(I) phosphine thiolates.

To enhance the luminescence efficiency, a rigid ligand and a rigid molecule are preferred. So annular binuclear gold(I) complexes were selected for investigation. The dithiolates selected for investigation were N-heteroring based, and were to be connected to digold(I) complexes of bridging diphosphines (annular geometry) or to two triphenylphosphine gold(I) moieties (open ring geometry). Due to the presence of two gold heavy atoms, and as gold phosphine thiolates mostly emit from LMCT triplet states, phosphorescence emission was anticipated.

As the aurophilic interaction will red shift the emission, it should be avoided to get an emission in the blue. A dithiolate supported by a rigid backbone having the two thiolates in a meta position should sterically pull the two gold atoms apart and hinder the aurophilic interaction.

1.6 Thesis overview

This work will present a study of some gold(I) complexes, with a goal to synthesise new phosphorescent emitting dopants for OLED devices. Gold complexes are a promising category for this purpose, as their emission is always phosphorescence. Their emission wavelength can be tuned by judicious choice of ligands and by changing the gold(I)-gold(I) distance. Despite the recent interest in the chemistry of N-heterocycle monothione with gold(I) and their interesting properties, N-heterocyclic dithiolates have generally been neglected in the literature. Therefore it has been chosen to study some digold(I) complexes connected to some rigid N-heterocyclic dithiolates.

After describing the techniques used during the thesis, in chapter two, chapter three describes the syntheses, the luminescence and the electrochemistry of some new and known N-heterocycle dithiolate ligands. They are used for the synthesis of some neutral binuclear gold(I) phosphine thiolate complexes as described in chapter four. Their luminescent properties at 77 K in a frozen matrix, at room temperature in solution, and the solid state are reported as well as their electrochemistry. Their luminescent properties are discussed according to four main variables: the relative electronic contribution of the ligands, the relative position of the nitrogen in the ring of the thiolate, a closed ring or open structure, and the length of the diphosphine ligands (and therefore the gold-gold distance). Some simulations of the geometry of the ligands and the relative energies of their tautomers are given in chapter five. The geometries of some binuclear gold(I) complexes have also been optimised to assess the gold(I)-gold(I) distance and the degree of any aurophilic interaction. The LUMO and HOMO of these molecules are given and used to support the assignment of an LMCT and ILCT origin of luminescence. Finally, in chapter six, some conclusions are drawn from this work together with an assessment of whether or not these new compounds could be of use in OLED technology.

References for Chapter 1

- [1] Pope M., Kallmann H.P., Magnate P., *J. Chem. Phys.* 38 (1963) 2042-2043
- [2] Hartman W.A, Armstrong H.L, *J. Appl. Phys.* 38 (1967) 2393-2395
- [3] Tang C.W., Van Slyke S.A., *Appl. Phys. Lett.* 51 (1987) 913-915
- [4] Borchardt J.K., *Mater. Today* 7 (2002) 42
- [5] Shinar J., in “*Organic Light Emitting Devices: a survey*” (Ed: Shinar, J.) Springer, 2003
- [6] Sibley S, Thompson M.E., Burrows P.E., Forrest S.R., in “*Optoelectronic Properties of Inorganic Compounds*” (Ed: Roundhill D.M., Facker Jr. J.P.) Plenum Press, 1999
- [7] Kalinowski J., in “*Organic Electroluminescent Materials and Devices*” (Ed: Miyata S., Nalwa N.S) Gordon & Breach, 1997
- [8] Mori T., Masumoto Y., Itoh T., *J. Photo. Sci. Tech.* 21 (2008) 173-180
- [9] Adachi C., Tokito S., Tsutsui T., Siato S., *Jpn. J. Appl. Phys.* 28 (1988) L269
- [10] Biebel A., Merck News Release, 20 may 2008
- [11] “*Organic Light-Emitting Materials and Devices*” (Ed: Li Z., Meng H.) Taylor & Francis Group, 2007
- [12] D’Andrade B.W., Thompson M.E., Forrest S.R., *Adv. Mater.* 14 (2002) 147-149
- [13] Tokito S., Iijima T., Tsuzuki T., Sato F., *Appl. Phys. Lett.* 83 (2003) 2459-2460
- [14] D’Andrade B.W., Holmes R.J., Forrest S.R., *Adv. Mater.* 16 (2004) 624-628
- [15] Gong X., Ma W., Ostrowski J.C., Bazan G.C., Moses D., Heeger A.J., *Adv. Mater.* 16 (2004) 615-619
- [16] Yan B.P., Cheung C.C.C., Fui S.C.F., Xiang H.F., Roy V.A.L., Xu S.J., Che C.M., *Adv. Mater.* 19 (2007) 3599-3603
- [17] Liu J., Cheng Y.X., Xie Z.Y., *Adv. Mater.* 20 (2008) 1357-1360
- [18] D’Andrade B.W., Forrest S.R., *Adv. Mater.* 16 (2004) 1585-1595
- [19] Raja I.U., Lee J.Y., Kim I.T., *Monat. Chemie* 139 (2008) 725-737
- [20] Wang X., Rundl P., Bale M., Mosley A., *Synth Met.* 137 (2003) 1051-1055
- [21] Malliaras G.G., Shen Y., Scott J.C, in “*Organic Light-emitting Materials and Devices IV*”, (Ed: Kafafi Z.H.) Proc. SPIE 4105, 2000
- [22] Kawamura Y., Yanagida S. Forrest S.R., *J. Appl. Phys.* 92 (2002) 87-93
- [23] Lee C.L., Lee K.B., Kim J.J., *Appl. Phys. Lett.* 77 (2000) 2280-2282

- [24] Gustafsson G., Cao Y., Treacy M., Klavetter F., Colaneri N., Heeger A.J., *Nature* 357 (1992) 447-448
- [25] Antoniadis H., Hueschen M.R., McElvain J., Miller J.N., Moon R.L., Roitman D.B., Sheats J.R., *Polymer Prep.* (1997) 383-387
- [26] Yang Y., Heeger A.J., *J. Appl. Phys.*, 64 (1994) 1245
- [27] Murata H., Merritt C.D., Kafafi Z.H., *IEEE Journal of Selected Topics in Quantum Electronics* 4 (1998) 119-122
- [28] Adachi C., Tsutsui T, in “*Organic Light Emitting Devices: a survey*” (Ed:Shinar J.) Springer, 2003
- [29] Ma Y., Che C.M., Chao H.Y., Zhou X., Chan W.H., Shen J., *Adv. Mater.* 11 (1999) 852-857
- [30] Tang C.W., *Appl. Phys. Lett.* 48 (1986) 183-185
- [31] Gong X., Robinson M.R., Ostrowski J.C., Moses D., Bazan G.C., Heeger A.J., *Adv. Mater.* 14 (2002) 581-583
- [32] O’Brien D.F., Giebeler C., Fletcher R.B., Vadby A.J., Palilis L.C., Lidzey D.G., Lane P.A., Bradley D.C.C., *Synth. Met.* 116 (2001) 379-383
- [33] Baldo M.A., Thompson M.E., Forrest S.R., *Pure Appl. Chem.* 71 (1999) 2095-2106
- [34] Burshtein A.I., Neufeld A.A., Ivanov K.L., *J. Chem. Phys.* 115 (2001) 10464-10471
- [35] Yersin H., *Top. Curr. Chem.* 241 (2004) 1-26
- [36] Pope M., Swenberg C.E., in “*Electronic Processes in Organic crystals*” Oxford University Press, 1982
- [37] Baldo M.A., O’Brien D.F., You Y., Shoustikov A., Sibley S., Thompson M.E., Forrest S.R., *Nature* 395 (1998) 151-152
- [38] Turro N.J., in “*Modern Molecular Photochemistry*” (Ed: Turro N. J.), University Science Books, 1991
- [39] “*Organic Light-Emitting Devices: Synthesis, Properties and Application*” (Ed: Muller K., Scherf U.) Wiley, 2006
- [40] Li J., Lui D., Li Y., Lee C., Kwong H., Lee S., *Chem. Mater.* 17 (2005) 1208-1212
- [41] Chen C.H., Klubek K.P., Shi J., (1999) US Patent 5,908,581
- [42] Hosokawa C., Higashi H., Nakamura H., Kusumoto T., *Appl. Phys. Lett.* 67 (1995) 3853-3855

- [43] Evans R.C., Douglas P., Winscom C.J., *Coord. Chem. Rev.*, 250 (2006) 2093-2126
- [44] Wilson J.S., Dhoot A.S., Seeley A.J.A.B., Khan MS., Koelher A., Friend R.H., *Nature* 413 (2001) 828-831
- [45] Lee C.L., Kang N.G., Cho Y.S., Lee J.S., Kim J.J., *Opt. Mater.* 21 (2002) 119-123
- [46] Tokito S., Suzuki M., Sato F., *Thin Solid Films* 445 (2003) 353-357
- [47] Furuta P.T., Deng L., Garon S., Thompson M.E., Frecher J.M.J, *J. Am. Chem. Soc.* 126 (2004) 15388-15389
- [48] Zhou G., Wong W.-Y., Yao B., Xie Z., Wang L., *Angew. Chem.* 119 (2007) 1167-1169
- [49] Anthopoulos T.D., Markham J.P.J, Nmabas E.B., Samuel I.D.W, Lo S.C., Burn P.L., *Appl. Phys. Lett.* 82 (2003) 4824-4826
- [50] "Photochemistry and Photophysics of Coordination Compound I" (Ed: Balzani V., Campagna S.) Springer, 2007
- [51] "Photochemistry and Photophysics of Coordination Compound II" (Ed: Balzani V., Campagna S.) Springer, 2007
- [52] Baldo M.A., Thompson M.E., Forrest S.R., *Nature* 403 (2000) 750-753
- [53] Adachi C., Baldo M.A., Thompson M.E., Forrest S.R., *J. Appl. Phys.* 87 (2000) 8049-8055
- [54] Adachi C., Baldo M.A., Forrest S.R., Lamansky S., Thompson M.E., Kwong R.C., *Appl. Phys. Lett.* 78 (2001) 1622-1624
- [55] Li C.-L., Su Y.-J., Tao Y.-T., Chou P.-T., Chien C.-H., Cheng C.-C., Liu R.-S., *Adv. Funct. Mater.* 15 (2005) 387-395
- [56] Chou P.T., Chi Y., *Chem. Eur. J.* 13 (2007) 380-395
- [57] Baldo M.A., Lamansky S., Burrows P.E., Thompson M.E., Forrest S.R., *Appl. Phys. Lett.* 75 (1999) 4-6
- [58] King K.A., Spellane P.J., Watts R.J., *J. Am. Chem. Soc.* 107 (1985) 1431-1432
- [59] Ma B., Knowles D.B., Brown C.S., Murphy D., Thompson M.E., *PCT Int. Appl.* (2004) WO 045001 A1
- [60] Chang W.-C., Hu A.T., Duan J.-P., Rayabarapu D.K., Cheng C.H., *J. Organomet. Chem.* 689 (2004) 4882-4888
- [61] Ren X., Li J., Holmes R.J., Djurovich P.I., Forrest S.R., Thompson M.E., *Chem. Mater.* 16 (2004) 4743-4747

- [62] Li J., Djurovich P.I., Alleyne B.D., Tsyba I., Ho N.N., Bau R., Thompson M.E., *Polyhedron* 23 (2004) 419-428
- [63] Han E., Luy Y.Y., Lee T.W., Lyun L., Kwon O., Tikhonovski A., Kwon Y., Park G.S., Das R.R., *J. Nano. Nanotech.* 8 (2008) 2990-2995
- [64] Adachi C., Baldo M.A., Thompson M.E., Forrest S.R., *J. Appl. Phys.* 90 (2001) 5048-5051
- [65] Laporte O., Meggers W.F., *J. Opt. Soc. Am.* 11 (1925) 459-460
- [66] Vlcek Jr. A., *Coord. Chem. Rev.* 177 (1998) 219-256
- [67] Förster T., *Disc. Faraday Soc.* 27 (1959) 7-12
- [68] Dexter D.L., *J. Chem. Phys.* 21 (1953) 836
- [69] Ma Y., Che C.-M., Chao H.-Y., Zhou X., Chan W.-H., Shen J., *Adv. Mater.* 11 (1999) 852-857
- [70] Ma Y., Zhou X., Shen J., Chao H.-Y., Che C.-M., *Appl. Phys. Lett.* 74 (1999) 1361-1363
- [71] Fave C., Cho T.-Y., Hissler M., Chen C.W., Luh T.Y., Wu C.-C., Reau R., *J. Am. Chem. Soc.*, 125 (2003) 9254-9255
- [72] Montalti M., Credi A., Prodi L., Gandolfi M.T., "Handbook of Photochemistry" Taylor and Francis, Boca Raton, 2006
- [73] Shaw III C.F., *Chem. Rev.* 99 (1999) 2589-2600
- [74] "Gold, Progress in Chemistry, Biochemistry and Technology" (Ed: Schmidbaur H.) Wiley New York, 1999, 259-308
- [75] Desclaux J. P., Pyykkö P., *Chem. Phys. Lett.* 39 (1976) 300-303
- [76] Pyykkö P., *Angew. Chem. Int. Ed.* 43 (2004) 4412-4456
- [77] Pyykkö P., *Inorg. Chim. Acta* 358 (2005) 4113-4130
- [78] Schmidbaur H., Cronje S., Djordjevic B., Schuster O., *Chem. Phys.* 311 (2005) 151-161
- [79] Dziwok K., Lachmann J., Wilkinson D.L., Müller G., Schmidbaur H., *Chem. Ber.* 122 (1990) 423-427
- [80] Narajanaswamy R., Young M.A., Parkhurst E., Ouelette M., Kerr M.E., Ho D.M., Elder R.C., Bruce A.E., Bruce M.R.M., *Inorg. Chem.* 31 (1993) 2506-2517
- [81] Puddephatt R.J., Vittal J.J., in "Encyclopedia of inorganic chemistry" Vol. 3 (Ed.: King R.B.), Wiley, Chichester 1994 1320-1331
- [82] Schmidbaur H., Graf W., Muller G., *Angew. Chem. Int. Ed.* 27 (1988) 417-419

- [83] Burgmeister J.L., De Stefano N.J., *Inorg. Chem.* 10 (1971) 998-1003
- [84] Biltz W., Weibke F., *Z. Anorg. Allg. Chem.* 236 (1938) 12-14
- [85] Mudring A.V., Jansen M., Daniels J., Kraemer S., Mehring M., Ramalho J.P.P., Romero A.H., Parrinello M., *Angew. Chem. Int. Ed.* 41 (2002) 120-124
- [86] Holleman A.F., Wiberg E., "*Inorganic Chemistry*" Academic Press San Diego, 2001
- [87] Allen E.A., Wilkinson W., *Spectrochim. Acta Part A*, 28 (1972) 2257-2259
- [88] Uson R., Laguna A., Vicente J., *J. Chem. Soc., Chem. Commun* (1976) 353-354
- [89] Uson R., Laguna A., Laguna M., Jimenez J., Gomez M.P., Sainz A., Jones P.G., *J. Chem. Soc. Dalton Trans.* (1990) 3457-3463
- [90] Vicente J., Herrero-Gonzales P., Garcia-Sanchez Y., *Inorg. Chem.* 43 (2004) 7516-7531
- [91] McAuliffe C.A., Parish R.V., Randall P.D., *J. Chem. Soc. Dalton Trans.* (1979) 1730-1735
- [92] Gimena M.C., Laguna A., Sarroca C., Jones P.G., *Inorg. Chem.* 32 (1993) 5926-5932
- [93] Nakamoto M., Hiller W., Schmidbaur H., *Chem. Ber.* 126 (1993) 605-610
- [94] Forward J.M., Bohmann D., Fackler Jr. J.P., Staples R.J., *Inorg. Chem.* 34 (1995) 6330-6336
- [95] Nunokawa K., Onaka S., Tatematsu T., Ito M., Sakai J., *Inorg. Chim. Acta* 322 (2001) 56-64
- [96] Ho S.Y., Cheng E.C.-C., Tiekink E.R.T., Yam V.W.-W., *Inorg. Chem.* 45 (2006) 8165-8174
- [97] Lui C.H., Kui S.C.F., Sham I.H.T., Chui S.S.Y., Che C.-M., *Eur. J. Inorg. Chem.* (2008) 2421-2428
- [98] Henderson W., Nicholson B.K., Tiekink E.R.T., *Inorg. Chim. Acta* 359 (2006) 204-214
- [99] Miranda S., Vergara E., Mohr F., De Vos D., Cerrada E., Mendía A., Laguna M., *Inorg. Chem.* 47 (2008) 5641-5648
- [100] Fernandez E.J., Laguna A., Lopez-de-Luzuriaga M.P, Mongel M., Montiel M., Olmos E., Perezand J., Rodríguez-Castillo M., *Gold Bull.* 40 (2007) 172-183

- [101] Lin J.C.Y., Tang S.S., Vasam Shekar C., You W.C., Wo T.W., Huang C.H., Sun B.J., Huang C.Y., Lee C.S., Hwang W.S., Chang A.H.H., Lin I.J.B., *Inorg. Chem.* 47 (2008) 2543-2551
- [102] Kim P.S.G., Hu Y., Brandys M.-C., Burchell T.J., Puddephatt R.J., Sham T.K., *Inorg. Chem.* 46 (2007) 949-957
- [103] Bonati F., Burini A., Pietroni B.R., Bovio B., *J. Organomet. Chem.* 408 (1991) 271-280
- [104] Jothibasu R., Huynh H.V., Koh L.L., *J. Organomet. Chem.* 693 (2008) 374-380
- [105] Rios D., Pham D.M., Fettinger J.C., Olmstead M.M., Balch A.L., *Inorg. Chem.* 47 (2008) 3442-3451
- [106] Barnard P.J., Wedlock L.E., Baker M.V., Berners-Price S.J., Joyce D.A., Skelton B.W., Steer J.H., *Angew. Chem. Int. Ed.* 45 (2006) 5966-5970
- [107] Ray L., Katiyar V., Raihan M.J., Nanavati H., Shaikh M.M., Ghosh P., *Eur. J. Inorg. Chem.* (2006) 3724
- [108] Mueller T.E., Choi S.W.-K., Mingos D.M.P., Murphy D., Williams D.J., Yam V. W.-W., *J. Organomet. Chem.* 484 (1994) 209-224
- [109] Yam V. W.-W., Choi S. W.-K., Cheung K.K., *Organometallics* 35 (1996) 1734-1739
- [110] Lu W., Xiang H.F., Zhu N., Che C.-M., *Organometallics* 21 (2002) 2343-2346
- [111] Packheiser R., Jakob A., Ecorchard P., Walfort B., Lang H., *Organometallics* 27 (2008) 1214-1226
- [112] Watase S., Nakamoto M., Kitarama T., Kanehisa N., Kai Y., Yanagida S., *J. Chem. Soc., Dalton Trans.* (2000) 3585-3590
- [113] Bardaji M., Caldhorda M.J., Costa P.J., Jones P.G., Laguna A., Perez M.R., Villacampa M.D., *Inorg. Chem.* 45 (2006) 1059-1068
- [114] Gimeno M.C., Laguna A., *Chem. Rev.* 97 (1997) 511-522
- [115] Bates P.A., Waters J.M., *Inorg. Chim. Acta* 81 (1984) 151-156
- [116] King C., Khan M.N.I., Staples R.J., Fackler Jr. J.P., *Inorg. Chem.* 31 (1992) 3236-3238
- [117] Forward J.M., Fackler Jr. J.P., Staples R.J., *Organometallics* 14 (1995) 4194-4198
- [118] Uson R., Laguna A., Navarro A., Parrish R.V., Moore L.S., *Inorg. Chim. Acta* 112 (1986) 205-210
- [119] Jones P.G., *J. Chem. Soc., Chem. Commun.* (1980) 1031-1033

- [120] Forward J.M., Assefa Z. Staples R.J., Fackler Jr. J.P., *Inorg. Chem.* 35 (1996) 16-22
- [121] Lagunas M.C., Fierro C.M., Pintado-Alba A., De La Riva H., Betanzos-Lara S., *Gold Bull.* 40 (2007) 135-141
- [122] Tzeng B.-C., Zank J., Schier A., Schmidbaur H., *Z. Naturforsch. B* 54 (1999) 825-831
- [123] Maspero A., Kani I., Mohamed A.A., Omary M.A., Staples R.J., Fackler Jr. J.P., *Inorg. Chem.* 42 (2003) 5311-5319
- [124] Onaka S., Yaguchi M., Yamauchi R., Ozeki T., Ito M., Sunahara T., Sugiura Y., Shiotsuka M., Nunokawa K., Horibe M., Okazaki K., Iida A., Chiba H., Inoue K., Imai H., Sako K., *J. Organomet.Chem.* 690 (2005) 57-68
- [125] Yam V. W.-W., Chan C.-L., Cheung K.-K., *J. Chem. Soc., Dalton Trans.* (1996) 4019-4022
- [126] Tzeng B.-C., Liao J.-H., Lee G.-H., Peng S.-M., *Inorg. Chim. Acta* 357 (2004) 1405-1410
- [127] Yam V. W.-W., Li C.-K., Chan C.L., *Angew. Chem. Int. Ed.* 37 (1998) 2857-2859
- [128] Davila R.M., Elduque A., Grant T., Staples R.J., Fackler Jr. J.P., *Inorg. Chem.* 32 (1993) 1749-1755
- [129] Schmidbaur H., Eschenbach J.E., Kumberger O., Mueller G., *Chem. Ber.* 123 (1990) 2261-2265
- [130] Fu W.-F., Chan K.-C., Miskowski V.M., Che C.M., *Angew. Chem. Int. Ed.* 38 (1999) 2783-2785
- [131] Van Zyl W.E., Lopez-de-Luzuriaga J.M., Mohamed A.A., Staples R.J., Fackler Jr. J.P., *Inorg. Chem.* 41 (2002) 4579-4589
- [132] Yam V.W.-W., Lee W.K., *J. Chem. Soc., Dalton Trans.* (1993) 2097-2100
- [133] Gimeno M.C., Jones P.G., Laguna M., Laguna A., Terroba R., *Inorg. Chem.* 33 (1994) 3932-3938
- [134] Yip H.K. Shier A., Riede J., Schmidbaur H., *J. Chem. Soc. Dalton Trans.* (1994) 2333-2334
- [135] Fernandez E.J., Lopez de Luzuriaga J.M., Monge M., Olmos E., Laguna A., Villacampa M.D., Jones P.G., *J. Cluster Sci.* 11 (2000) 153-167
- [136] Yam V.W.-W., Lai T.-F., Che C.M., *J. Chem. Soc., Dalton Trans.* (1990) 3747-3752

- [137] Laguna A., Bardaji M., Jones P.G., Fischer A.K., *Inorg Chem.* 39 (2000) 3560-3566
- [138] Abdou H.E., Mohamed A.A., Lopez-de-Luzuriaga, Fackler Jr. J.P., *J. Cluster Sci.* 15 (2004) 397-411
- [139] Lin R., Yip J.H.K., Zhang K., Koh L.L., Wong K.Y., Ho K.P., *J. Am. Chem. Soc.* 126 (2004) 15852-15869
- [140] Awaleh M.O., Baril-Robert F., Reber C., Badia A., Brisse F., *Inorg. Chem.* 47 (2008) 2964-2974
- [141] Hunks W.J., Jennings M.C., Puddephatt R.J., *Inorg. Chim. Acta* 359 (2006) 3605-3616
- [142] Brandys M.C., Jennings M.C., Puddephatt R.J., *J. Chem. Soc., Dalton Trans.* (2000) 4601-4606
- [143] Puddephatt R.J., *Chem Comm.* (1998) 1055-1062
- [144] Puddephatt R.J., *Coord. Chem. Rev.* 216 (2001) 313-332
- [145] Barndys M.C., Puddephatt R.J., *Chem. Comm.* (2001) 1280-1281
- [146] Brandys M.C., Puddephatt R.J., *J. Am. Chem. Soc.* 123 (2001) 4839-4840
- [147] Yip S.K., Cheng E.C.C., Yuan L.H., Zhu N., Yam V.W.-W., *Angew. Chem. Int. Ed.* 43 (2004) 4954-4957
- [148] Morgado J., Duarte M.T., Alcaer L., Santos I.C., Henriques R.T., Almeida M., *Synth. Metals* 86 (1997) 2187-2188
- [149] Buckley R.G., Elsome A.M., Fricker S.P., Henderson G.R., Theobald B.R.C., Parish R.V., Howe B.P., Kelland L.R., *J. Med. Chem.* 39 (1996) 5208-5214
- [150] Shaw III C.F., *Chem. Rev.* 99 (1999) 2589
- [151] Casini A., Cinellu M. A., Minghetti G., Gabbiani C., Coronello M., Mini E., Messori L., *J. Med. Chem.* 49 (2006) 5524-5531
- [152] Hwang I.-C., Seppelt K., *Angew. Chem. Int. Ed.* 40 (2001) 3690-3693
- [153] Mohr F., *Gold Bull.* 37 (2004) 164-169
- [154] Riedel S., Kaupp M., *Inorg. Chem.* 45 (2006) 1228-1234
- [155] Timakov A.A., Prusakov V.N., Drobyshevskii Y.V., *Dokl. Akad. Nauk SSSR* 291 (1986) 125-128
- [156] Ostropikov V.V., Rakov E.G., *Izv. Vyssh. Uchebn. ZaVed., Khim. Khim. Tekhnol.* 32 (1989) 3-17
- [157] Vogler A., Kunkely H., *Coord. Chem. Rev.* 219-221 (2001) 489-507

- [158] Yam V.W.-W., Choi S.W.K., Lai T.F., Lee W.K., *J. Chem Soc. Dalton Trans.* (1993) 1001-1006
- [159] Yam V.W.-W., Wong K. M.C., Hung L.L., Zhu N., *Angew. Chem. Int. Ed.* 44 (2005) 3107–3110
- [160] Tang S.S., Chang C.P., Lin I.J.B., Liou L.S., Wang J.C., *Inorg. Chem.* 36 (1997) 2294-2300
- [161] Lee Y.A., Mc Garrah J.E., Lachicotte R.J., Eisenberg R., *J. Am. Chem. Soc.* 124 (2002) 10662-10663
- [162] Li C.K., Lu X.X., Wong K.M.C., Chan C.L., Zhu N., Yam V.W.-W., *Inorg. Chem.* 43 (2004) 7421-7430
- [163] Jones W.B., Yuan J., Narayanaswamy R., Young M.A., Elder R.C., Bruce A.E., Bruce M.R.M., *Inorg. Chem.* 34 (1995) 1996-2001
- [164] Yam V.W.-W., Chan C.L., Li C.K., Wong K.M.C., *Coord. Chem. Rev.* 216-217 (2001) 173-194
- [165] Mansour M.A., Connick W.B., Lachicotte R.J., Gysling H.J., Eisenberg R., *J. Am. Chem. Soc.* 120 (1998) 1329-1330
- [166] Kovacs G., Ujaque G., Lledos A., *J. Am. Chem. Soc.* 130 (2008) 853-864
- [167] Zhang G., Huang X., Li G., Zhang L., *J. Am. Chem. Soc.* 130 (2008) 1814-1815

Chapter 2

Experimental Techniques

2.1 Introduction

The materials and methods used in this work are briefly described here. The detailed syntheses of the different compounds used in this work will be given in the appropriate chapters: the ligands and their precursors in chapter three; gold phosphine complexes with thiolate ligands in chapter four. The computational methods for molecular modelling are described in more detail in chapter five.

2.2 Chemical synthesis and characterisation

2.2.1 Reaction techniques and chemicals

2.2.1.1 Schlenk techniques and dry solvents

For reactions requiring an inert atmosphere of dry nitrogen, standard Schlenk techniques were used [1]. Solvents were dried following standard procedures [2]: THF by reflux over potassium after filtration on a column; toluene by reflux over sodium; and DCM by reflux over CaH_2 , all under an inert atmosphere of dry nitrogen.

2.2.1.2 Reaction in liquid ammonia

The synthesis of 1,3-bis(diphenylphosphino)benzene and some of its derivatives (see appendix B) required the use of liquid ammonia. A diagram of the arrangement is given in figure 2.1.

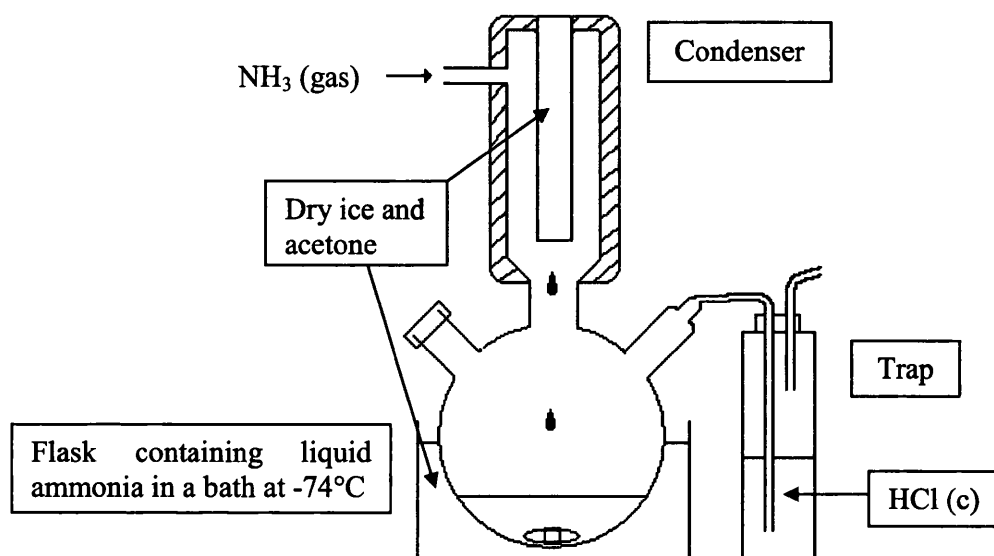


Figure 2.1: Set-up for a reaction in liquid ammonia

2.2.1.3 Chemicals

The list of chemicals and solvents used is given in appendix A.

Potassium tetrachloroaurate(III) was provided by Johnson Matthey under their loan scheme.

2.2.2 ¹H, ¹³C, ³¹P NMR spectroscopy

The ¹H, ¹³C and some of the ³¹P NMR spectra were recorded on a 400 MHz Bruker AC NMR spectrometer at Swansea University. The rest of the ³¹P NMR spectra were measured by Luisa Ramos, at the Universidade de Coimbra, using a Varian Unity-500 NMR spectrometer. ¹H and ¹³C chemical shifts were determined using the principal resonance due to the solvent as internal standard. 85% phosphoric acid was used as external standard for ³¹P.

2.2.3 Mass spectrometry

Fast atom bombardment (FAB) and electrospray ionisation (ES) mass spectra were recorded by the EPSRC Mass Spectrometry Service Centre located at Swansea University. Results will be presented in the following format: *m/z*, assignment, relative abundance.

2.2.4 Infrared spectroscopy

IR spectra were recorded on a Perkin-Elmer “Spectrum one” FTIR spectrometer, using an attenuated total reflection (ATR) sampling accessory.

2.2.5 UV-Vis absorption spectroscopy

UV-Vis absorption spectra were recorded with 1 cm or 4 cm path length quartz cells on a Hewlett Packard HP8452A single beam diode array spectrophotometer. All UV-Vis spectra were measured against the appropriate reference. Absorption spectra for the measurement of quantum yields at 77 K were recorded on a Shimadzu 2100 spectrometer at the Chemistry Department, Universidade de Coimbra, Portugal.

2.2.6 Electrochemistry

Cyclic voltammograms were recorded on a PGSTAT30 potentiostat system at Cardiff University. Samples were dissolved in MeCN containing 0.1 M [Bu₄N][PF₆] as the supporting electrolyte. Solutions were gently purged with dry nitrogen prior to each scan. A three-electrode system was employed using a platinum working and counter electrode, and an Ag/Ag⁺ reference electrode (0.01 M AgNO₃ and 0.1 M [Bu₄N][PF₆] in MeCN). The scan rate used for the results reported in this thesis was 0.1 V s⁻¹. The ferrocene-ferrocenium couple was used as a standard ($E^0 = 0.42$ V versus standard calomel electrode).

2.2.7 X-ray crystallography

X-ray diffraction analyses were carried out by Prof. Massimo Di Vaira at the University of Florence. Crystals were mounted on a glass fibre and analysed using an Oxford Diffraction Xcalibur 3 CCD diffractometer, using graphite-monochromated MoK α radiation. Intensities were corrected for absorption by the multi-scan ABSPACK routine, part of the CrysAlisPRO RED Oxford Diffraction software.

2.3 Luminescence studies

2.3.1 Steady state emission and excitation studies

2.3.1.1 Emission and excitation spectra measurements

The measurements were carried out using a Perkin-Elmer MPF-44E fluorescence spectrometer with an Oriel 150 W Xenon arc lamp as an excitation source.

Room temperature measurements were carried out using sealed 10 mm quartz cells. Where necessary, solutions were degassed with dry nitrogen for at least 20 minutes before measurements were taken.

Solid state measurements were carried out by putting the sample in a 4 mm width quartz tube and using a quartz Dewar as holder. The signal was collected at an angle of 90° from the excitation light source.

77 K measurements were carried out by putting a 3 mm width NMR tube with the desired solution of products in a quartz Dewar holder containing liquid nitrogen.

Correction factors for the wavelength dependent variation in excitation intensity and emission sensitivity were obtained as described in section 2.3.1.3.

2.3.1.2 77 K measurements

Some 77 K emission and excitation spectra were recorded in the Chemistry Department, Universidade de Coimbra, Portugal, using a Fluorolog-3 fluorescence spectrometer, with a 150 W Xenon arc lamp as excitation source. The samples were in a 4 mm width quartz tube in a quartz Dewar filled with liquid nitrogen. The solvents used were either EPA or a mixture of DCM/MeOH 1/1 [5] and were carefully checked to ensure they formed a glass without cracks before each measurement. All spectra recorded with this instrument were automatically corrected with the correction files provided by the manufacturer.

2.3.1.3 Correction factor for Perkin-Elmer MPF-44E fluorimeter

Excitation spectra were corrected according to the intensity of the excitation lamp at different wavelengths using the method described by Demas and Crosby [3]. Rhodamine B (4 g dm^{-3}) in glycerol was used as quantum counter to determine the wavelength dependence of the photon output of the excitation lamp $PO(\lambda)$. The detector response of the instrument, $S(\lambda)$, also depends on the wavelength. This was determined by using barium sulphate as diffuse reflectance standard and scanning with the emission and excitation monochromators simultaneously. The barium sulphate plate being used as reference for the diffuse reflectance apparatus, the scatter is considered to be the same at all wavelengths. By varying the excitation and the emission monochromator at the same time with the diffuse reflectance standard in place as a scattering sample, we obtain $S(\lambda)PO(\lambda)$, and since $PO(\lambda)$ is known from the quantum counter response we obtain $S(\lambda)$.

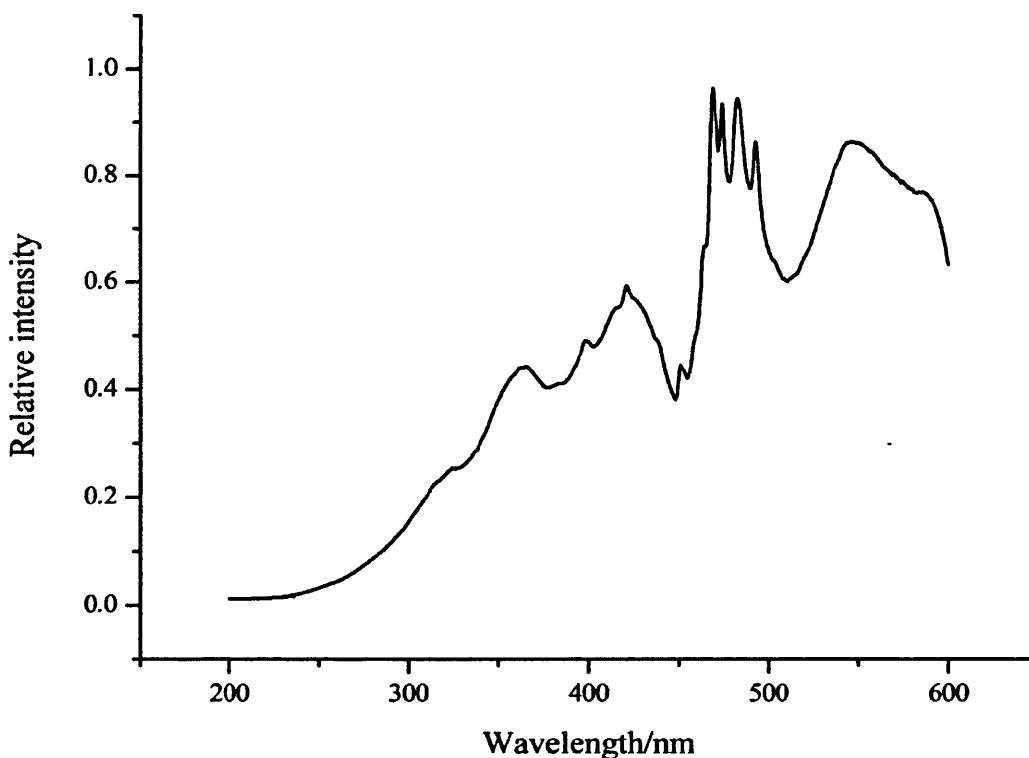


Figure 2.2: Relative intensity output of the excitation 150 W Xenon lamp using rhodamine B quantum counter

2.3.1.4 Quantum yield at 77 K

77 K quantum yield measurements were carried out using the Fluorolog-3 fluorescence spectrometer with the sample held in an NMR tube of 4 mm diameter. The reference used was benzophenone with a phosphorescence quantum yield of 0.94 [5] in DCM/MeOH. The probe and the reference were dissolved in the same solvent: DCM/MeOH (1/1 v/v). Absorption of the sample and the reference was carefully measured so the difference would be less than 0.01 at the excitation wavelength. Solutions were reasonable optically dilute (less than 0.15 in absorbance in a 10 mm quartz square cell at the excitation wavelength). Each measurement was carried out three times for the sample and for the reference. The position of the tube and the absence of any visible cracks in the glass were checked each time.

The quantum yield at 77 K of a sample P is determined by comparing it to the quantum yield of a known reference material R. It can be obtained by the following formula:

$$\Phi_P = \Phi_R \cdot \frac{A_R}{A_P} \cdot \frac{W_R}{W_P} \cdot \frac{I_P}{I_R} \cdot \left(\frac{\eta_P}{\eta_R}\right)^2 \cdot \frac{c_P}{c_R}$$

where Φ is the quantum yield, A the absorbance of the compound at the excitation wavelength, W is the power of the excitation light, I is the integral of the corrected emission intensity, c the contraction factor of the solvent and η its refractive index. P and R stand for the sample and reference respectively.

2.3.2 Time resolved studies

2.3.2.1 Phosphorescence lifetime measurements

Phosphorescence decays were measured using an Applied Photophysics Laser Kinetic Spectrometer with the third harmonic of an Nd/YAG Spectron pulsed laser (355 nm) as an excitation source. Signals were recorded using a Hamamatsu R928 photomultiplier tube having an emission monochromator fitted with a grating blazed at 500 nm with a reciprocal dispersion of 4.65 nm/cm, coupled through a variable resistor to a LeCroy 9304AM Quad 200 MHz digital storage oscilloscope. Resistance termination can be chosen between 50, 100, 500, 1k, 5k, 10k ohms. The number of

laser shots (minimum 16) averaged to get the final decay curve was chosen to give a signal to noise ratio superior to 100.

2.3.2.2 Fluorescence single photon counting

Room temperature fluorescence decays of dimercapto N-heteroring ligands were measured in the Chemistry Department by J. Pina, Universidade de Coimbra, Portugal using a custom built time correlated single photon counting (TCSPC) instrument with an IBH NanoLED (373 nm) excitation source, Jobin-Yvon excitation and emission monochromators, Philips XP2020Q photomultiplier, and Canberra Instruments time-to-amplitude and multi-channel analyser. The detection time limit is 150 ps. The fluorescence decays were analysed using the modulating functions method of Stricker with automatic correction for the photomultiplier “wavelength shift” [4].

2.3.2.3 Flash photolysis

The flash photolysis apparatus in the Chemistry Department, Universidade de Coimbra, Portugal was also used to determine some low temperature lifetimes, as a complementary technique. The experimental set-up consists of an Applied Photophysics laser flash photolysis apparatus pumped by a Nd/YAG laser (using the third harmonic at 355 nm). The signal was collected by a HP digital analyser and transferred to an IBM RISC computer.

2.4 Molecular modelling

2.4.1 Ligands

Molecules were drawn using Gaussview 3.0 and the Gaussian(R)03W program, version 6.1 revision C-02. The program was run on a windows-NT operating system installed on a desktop having 128 Mb of random access memory (RAM). The calculations were performed with one processor and the maximum available memory (128 Mb).

2.4.2 Gold(I) complexes

Geometry optimisation calculations for the gold(I) complexes were performed with the GAMESS program, using four processors and 1 Gb of memory. They were carried out in the home-made cluster "Milipeia" of the Centre for Computational Physics of the Universidade de Coimbra, Portugal.

2.5 Error calculations

The error estimates are the \pm standard deviation (σ), which is the square root of the standard variance (see equation 2.1) of n observations of the sample:

$$\sigma = \sqrt{\frac{\sum_{i=1}^n (x_i - \bar{x})^2}{(n-1)}} \quad \text{equation 2.1}$$

where \bar{x} is the mean value.

The propagation of systematic errors related to any exterior variables or calculated errors, is calculated according to equation 2.2 for addition or subtraction, or to equation 2.3 for multiplication/division:

$$y = \sqrt{(a^2 + b^2)} \quad \text{equation 2.2}$$

$$y = \sqrt{\left(\frac{a}{A}\right)^2 + \left(\frac{b}{B}\right)^2} \quad \text{equation 2.3}$$

where y is the error, a and b the errors related to the variables A and B respectively.

References for Chapter 2

- 1) Müller A., Diemann E., in "*Comprehensive Coordination Chemistry*" (Ed.: Wilkinson G.) Pergamon, Oxford. **1988**
- 2) Riddick J.A., Bunger W.B., Sakano T.K., in "*Organic Solvents, 2nd edition*) John Wiley and Sons, **1986**
- 3) Demas J.N., Crosby G.A., *J. Phys. Chem.*, **75** (1971) 991-1024
- 4) Stricker G., Subramaniam V., Seidel C.A.M., Volkmer A.J., *J. Phys. Chem. B* **103** (1999) 8612
- 5) Murov S., Chermichael I., Hug G.L., in "*Handbook of Photochemistry*" (Ed.: Marcel Dekker) New York, **1993**

Chapter 3:

Syntheses, photochemistry and electrochemistry of some thiol-substituted heterocycles

3.1 Introduction

3.1.1 Compounds studied

Studies of syntheses of some N-heterocyclic ring compounds (pyrimidine, pyrazine, pyridine) disubstituted by thiol groups, and their photochemical and electrochemical properties, are presented in this chapter. In choosing compounds both the number of nitrogens in the ring and their relative position have been changed in order to study the influence of these factors on the photochemical properties of their gold(I) derivatives (see Chapter 4).

Specifically, this chapter deals with the synthesis and properties of the following compounds (for structures see Fig 3.1):

- two pyridine dithiols: 2,6-dimercaptopyridine (DMP) and 2,6-dimercaptopyridine-3-carboxylic acid (ADMN)
- one pyrazine dithiol: 2,6-dimercaptopyrazine (DMPA)
- three pyrimidine dithiols: 2,4-Dimercaptopyrimidine (24PYRI), 4,6-Dimercaptopyrimidine (46PYRI), and 2,4-diamino-5,6-diaminopyrimidine (NPYRI).

For comparison purposes, some properties of 1,3-dimercaptobenzene (DMB) and 4-chloro-1,3-dimercaptobenzene (Cl-DMB) have also been investigated. In addition, appendix A gives details of unsuccessful attempts to synthesize a disubstituted dimercaptoisoquinoline and other substituted dimercaptopyridines.

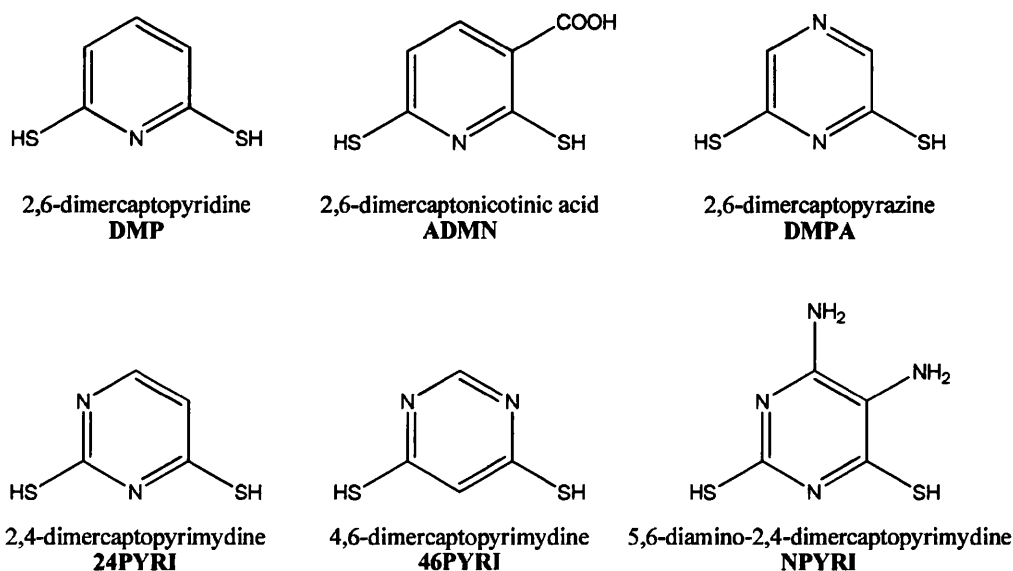


Figure 3.1: Structures of the compounds discussed in this chapter

3.1.2 Review of their known properties

N-heterocyclic thiols have a rich chemistry, and this will be described first, along with the different synthetic routes investigated in the literature; then, the general photochemical properties of thiones will be described.

3.1.2.1 Synthesis and chemical properties of N-heterocyclic thiols

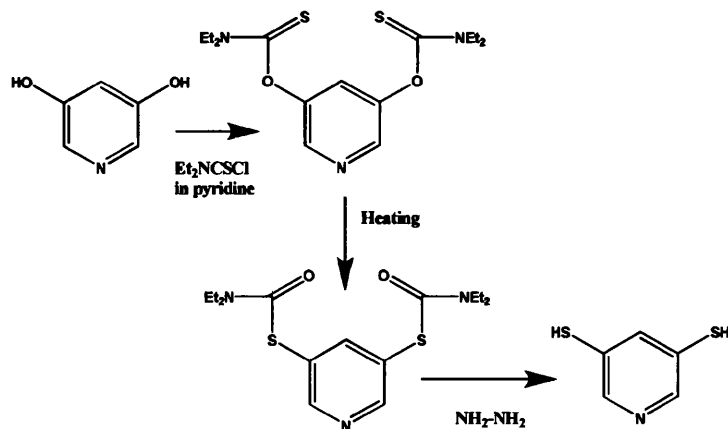
Existing paths for synthesising thiol-substituted N-heterocycles will first be described, then some specific chemical properties such as tautomerism, aggregation, and disulphide formation will be examined; a discussion of their coordination with different metals will conclude this section.

Pyrimidine

The syntheses of different pyrimidine thiols have been investigated thoroughly by Koppel *et al.* [1], in complementary work to the research of Boarland *et al.* [2]. Two leaving groups can be used: a hydroxyl or chloro-group. Substitution of a hydroxyl group requires the use of purified phosphorus pentasulphide [1]. As direct substitution of a hydroxyl group is not always possible, POCl_3 can be used to substitute the hydroxyl group by a chloride before the thiol substitution. In 1899, pyrimidine thiols were obtained by treating chloropyrimidine with alkali metal hydrosulphides under drastic conditions, but with a poor yield [3]. In 1951, an improvement in the yield (and smell) has been achieved by treating chloropyrimidine with thiourea in hot ethanol [2] or with sodium hydrosulphide in ethylene glycol [1]. This method provides the thione derivative in a good yield (70-90%) under mild conditions.

Pyridine

Nucleophilic aromatic substitutions on pyridine are favoured for C2 or C4. Therefore to obtain 3,5-dimercaptopyridine, an indirect route has been chosen by Krowicky [4].



For the 2,4-, 3,4-, or 2,3-isomers [5-9] the N-oxide halo-derivative has been used as starting material, with the pyridine N-oxide being more reactive than pyridine itself. The sulphur donor reagent can be thioacetamide or sodium hydrosulphide.

Finally, a direct pathway for obtaining the 2,6-isomer has been discovered by Pappalardo [10] which uses the dichloropyridine and sodium hydrosulphide in boiling DMF.

Pyrazine

2-Mercaptopyrazine has been obtained by reaction of thiourea and 2-chloropyrazine in acidic conditions [11]. As for pyrimidine, phosphorus pentasulphide can be used as a sulphur donating agent for hydroxyl derivatives [11]. Halogen substitution in 2,3-dichloropyrazine by sodium hydrosulphide gives 2,3-dimercaptopyrazine [12].

Tautomerism

This class of compounds can easily tautomerise (see Fig 3.2). An extensive literature [13, 14] can be found on this characteristic phenomenon, particularly with: pyrimidine-4-thione [15], 2,4-Dimercaptopyrimidine [16, 17, 71], pyridine-2-thione [18,19,20,21], pyridine-4-thione [20], quinoline-2-thione [22], 6-thiopurine [23], pyrazine-2-thione [22] or pyrazine-3-thione [15]. As a general rule, the thiol form is predominant in the gas phase or apolar solvents, whereas the thione form is more stable in polar solvents. For example, 2-mercaptopyridine (2TP) is predominantly in the thiol form (2TPSH) in the gas phase, but predominantly in the thione form (2TPNH) in a polar solution [14, 18]. This is due to the stabilisation effect of the solvent on 2TPNH. The effect of water on the stabilisation of 2TPNH has been

recently theoretically studied by Fu and colleagues [24]. This clearly confirms the strong influence of the medium on the tautomeric equilibrium of this compound and more generally on this kind of conjugated N-ring thione. The tautomerisation involves proton transfer. The exact mechanism depends on the relative position of the substituent on the ring. For example 2-hydroxy- (and 2-mercapto-) pyridine has both dissociative (*i.e.* deprotonation and protonation) and non-dissociative (*i.e.* solvent mediated, intramolecular, dimeric) isomerisation proton-transfer, while for 4-hydroxy- (and 4-mercapto-) pyridine only the dissociative steps are available due to the long distance between the donor and acceptor sites [25, 26, 27].

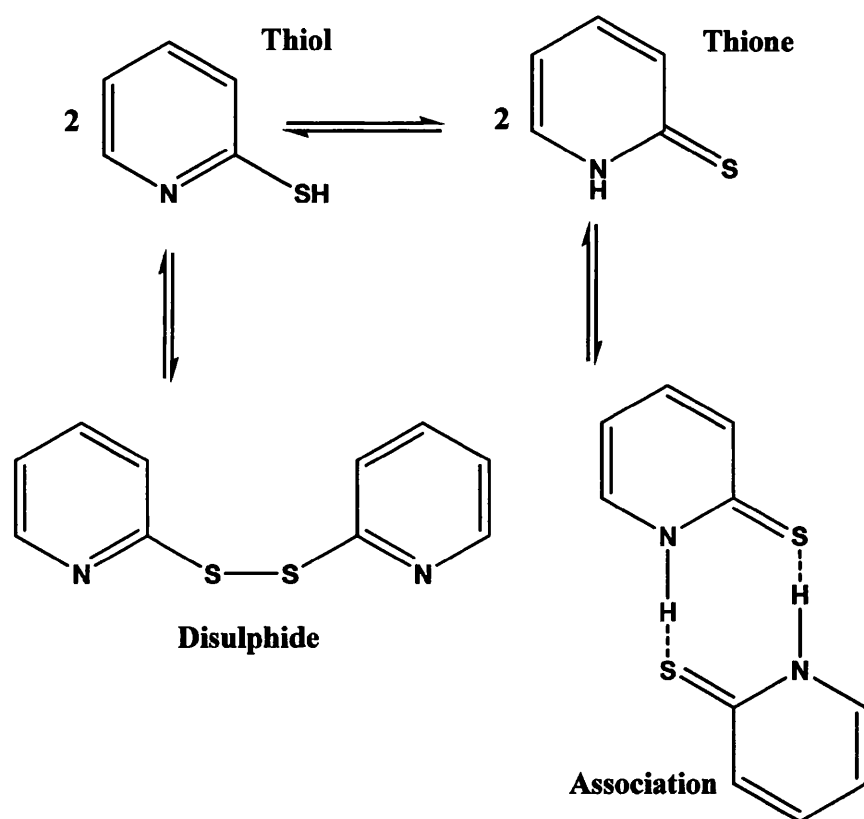


Figure 3.2: Tautomers for N-heterocyclic thiols

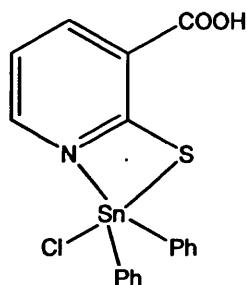
Another feature shown in fig 3.2 for N-heterocyclic thiols is the formation of aggregates when in the thione form, or the formation of disulphide bridges when the thiol is exposed to light. These phenomena have been studied via UV-vis absorption spectrometry by Stoyanov *et al.* [28] and Beak [14, 25, 29, 30] and once again, clearly show the influence of the nature of the solvent proticity and polarity, temperature, light, and concentration on the relative abundance of these species. At

high concentration, the thione dimer predominates; this disappears upon dilution which restores the tautomeric equilibrium. When exposed to daylight, the thiol is oxidised to the disulphide and eventually all the thione is consumed to form the disulphide bridged compound.

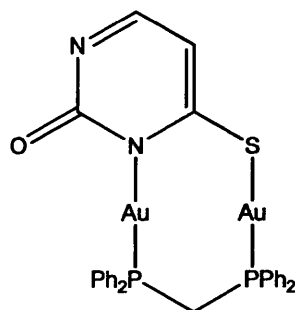
The series studied in the present work features compounds that are dithiol-substituted on each side of nitrogen, to extend the SH conjugation and tautomerisation, but both thiol and thione groups could also be present simultaneously.

Metal coordination

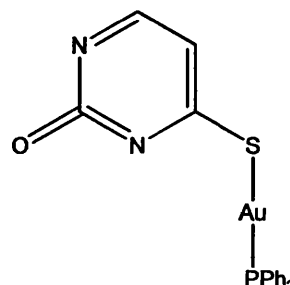
These molecules have two different donor sites: S atom or N atom, and can therefore chelate numerous metals, for example: Sn(II) with 2-mercaptopyridine-3-carboxylic acid [31], Ni(II) or Cu(II) with pyridine-N-oxide-2-thione [32], Co(II), Ni(II), Zn(II) Cd(II), Hg(II), Pt(II), Bi(III), Sn(II) [33], Ir(I) [34] with 2-mercaptopyridine, and Co(III), Ni(II), Cu(I), Ag(I) with silylated 2-mercaptopyridine [35]. Using 24PYRI as complexing agent with different metals [36] demonstrates its coordination versatility: it acts as monodentate ligand in Ag(I) complexes, as bidentate in Co(II) and Tl(I) complexes, as tridentate in Cu(II) complexes, as a tetradentate ligand in Cd(II), Ni(II), or Pb(II) complexes, and can coordinate with one or more (Au(III)) metal ions simultaneously. Pyridine, and pyrimidine monothiols [37,39], and 24PYRI [39] have been used with triphenylphosphinegold(I), which binds preferentially to the sulphur atom. Digold phosphine fragments such as $[Au_2(dppm)]$ are connected to thiouracil through both N-Au and S-Au links [40].



Ref: [31]



Ref:[40]



Ref: [38]

Figure 3.3: Examples of metal coordination to N-heterocyclic thiolate ligands

3.1.2.2 Photophysical properties of thiones

A brief introduction to thione photochemistry is presented here; for further reading, some very good reviews on the photochemistry of thiones can be found [41, 42, 43]. Electronic transitions in sulphur containing chromophores are induced by the absorption of light at longer wavelengths than required for their oxygen containing homologues. An intense allowed transition ($S_0 \rightarrow S_2$) generally occurs in the 250-350 nm region (with $\epsilon \approx 10^4 \text{ dm}^3 \text{ mol}^{-1} \text{ cm}^{-1}$) and a weak forbidden transition ($S_0 \rightarrow T_1$) can be observed at longer wavelengths ($> 530 \text{ nm}$, with $\epsilon \approx 10\text{--}100 \text{ dm}^3 \text{ mol}^{-1} \text{ cm}^{-1}$).

The emissions in oxygen-free inert solvent from thione compounds at room temperature are fluorescence, $S_2 \rightarrow S_0$, and phosphorescence, $T_1 \rightarrow S_0$. The energy gap $S_1\text{--}T_1$ is small, allowing an efficient intersystem crossing with a high quantum yield for the transition between the two states. No fluorescence is observed from the $S_1 \rightarrow S_0$ transition, even if the thione is directly excited into the S_1 state by the $S_0 \rightarrow S_1$ absorption band or into some higher singlet energy levels, which relax to the S_1 state. This also indicates a very efficient and rapid intersystem crossing. The T_1 or S_2 excited states of aromatic thiones have a generally high reactivity and can react with solvents, oxygen or with a neighbouring thione. The $T_1(n,\pi^*)$ state of thiones can be efficiently self-quenched by the ground state thione (rate constant of self quenching $k_q \approx 10^{10} \text{ dm}^3 \text{ mol}^{-1} \text{ s}^{-1}$) and therefore to study their luminescence a low concentration (10^{-6} M) should be used [44, 45 and refs therein].

As 2,4-Dimercaptopyrimidine (24PYRI) is structurally very similar to both the nucleosides uracil found in RNA and 4-thiouridine found in tRNA of *escherichia coli* [46, 47], an extensive literature on the photochemistry [48, 49, 50] and the photophysics [16, 17] of this pyrimidine derivative has been produced. In 24PYRI, an oxygen atom of thiouracil has been replaced by a sulphur atom. The first effect of this is a noticeable red shift of the singlet-singlet ($\pi \rightarrow \pi^*$) absorption band from 330 nm to 376 nm. The second effect is a decrease in both the lifetime and yield of phosphorescence. Because it has two thione groups, 24PYRI has a very efficient ($S_0\text{--}S_2$) absorption transition and noticeable phosphorescence at 482 nm in EPA at 77 K ($\tau = 390 \text{ }\mu\text{s}$, $\Phi_p = 0.10$) [48]. Phosphorescence deactivation is thought not to be induced by the weak "heavy" atom effect of sulphur, but by the sulphur (d)-orbital contribution to the π delocalised orbitals on the pyrimidine ring [48, 51].

Luminescence of thione groups is usually self-quenched. For 4-thiouracil it has been found that the two major processes of excited state T_1 deactivation (in the absence of oxygen) are firstly self-quenching, and secondly solute-solvent interactions [52, 53].

Finally this N-heterocyclic dithiol shows phototautomerisation as the Lapinski group demonstrated using 2,4-Dimercaptopyrimidine [16, 17] and 4-thiouracil [54, 55] isolated in an inert gas matrix at 10 K. The thione form of 24PYRI has been proven to be the most stable form in the solid state and in the gas phase, but when excited by UV light ($\lambda > 355$ nm) the dithiol form is predominant.

Another photochemical process is the formation of the disulphide from the thiol, as shown in fig 3.2. This process is reversible when the solution is put in the dark. An apolar solvent and low concentration favours the thiol and therefore promotes disulphide formation [56].

The species studied here are thiol-substituted derivatives of already known compounds (i.e. 2,6-dithiopyridine is a derivative of the 2-thiopyridine). DMP, ADMN, DMPA should give both thiol and thione in a polar solvent, and therefore must be protected from light to avoid any daylight induced photoreaction. The pyrimidine derivatives seem to be more stable in solution, but throughout this work they also have been protected from light when made up in solution.

3.1.2.3 Applications for these compounds

Compounds containing a 2-pyridyl disulphide unit can be used to introduce thiol groups into certain proteins to form a reversible protein-protein linkage [70]. Pyridine thiols also enhance antifungal or anti-inflammatory activity of several important drugs [57] and have, themselves, antibacterial and anti-cancer activities [56, 58, 59, 60, 61]. Also, the presence in otherwise natural t-RNA of a nucleic acid with a sulphur atom substituted instead of an oxygen atom is of interest for investigation [46]. These classes of thione can also be used as ligands with different metals, and can be used in analytical methods based on surface enhancement and detection [62].

These numerous biological and chemical applications make N-heterocyclic thiols worthy of investigation.

3.2 Syntheses

3.2.1 Synthesis of 2,6-dimercaptopicotinic acid (2,6-dimercaptopyridine-5-carboxylic acid), ADMN and its sodium salt

A method derived from the synthesis of 2,6-dimercaptopyridine discovered by Pappalardo [10] was used. The final product was a yellow powder, stable in the air and light. Recrystallisation from a basic water solution gave greenish crystals of a salt in which the anion is the mono-deprotonated derivative.

3.2.1.1 Synthesis

Sodium hydrosulphide (7 g, 0.12 mol) was dissolved in hot DMF (70 mL). The solution was cooled to room temperature, and 2,6-dichloronicotinic acid (2 g, 10.5 mmol) was added. The solution was boiled for 8 h, and then cooled down to room temperature. Distilled water (80 mL) was added and the solution turned yellow. Dilute HCl solution (10 %) was added until the solution began to be turbid. The yellow precipitate which formed overnight was collected by filtration (180 mg). Conc. HCl (10 mL) was added to the filtrate and more yellow precipitate (580 mg) was formed. This second precipitate was collected by filtration. The two precipitates were re-dissolved together in a minimum of 1 M sodium hydroxide solution and re-precipitated by acidifying the solution with 10% HCl. The resulting solid was collected by filtration and dried under vacuum (710 mg, 3.8 mmol, yield = 35 %). Slow evaporation of a solution of the product in 1 M sodium hydroxide gave green crystals, the crystal structure of which is described in part 3.3.1.3.

3.2.1.2 Characterisation

$^1\text{H NMR}$ (d_6 -DMSO): 6.68 (d, 1H, C-H aromatic), 7.74 (d, 1H, C-H aromatic),
12.03 (b, 1H, N-H), 14.25 (b, 1H, COO-H)

$^{13}\text{C NMR}$ (d_6 -DMSO): 114 (C-H), 122 (C-H), 137 (C-COO), 167 (COO), 170,
181(C-S)

MS (ES^+): 187 $[\text{M}]^+$ (25%), 169 $[\text{M} - \text{H}_2\text{O}]^+$ (30%), 143 $[\text{M} - \text{COO}]^+$ (45%)

Melting point: 160°C

Crystals of the sodium salt have been used for IR measurements.

IR (cm^{-1}): 2982, 2854 (w), 1676 (s), 1574 (vs), 1543 (s), 1436 (s), 1386 (m), 1284 (s), 1154, 1141 (s), 1192 (m), 1058 (s), 948 (vw), 896 (w), 831 (s), 769 (vs), 699 (m), 661 (s), 557 (vs), 430 (vs)

The ^{13}C and ^1H NMR spectra are consistent with those in the literature for 2-mercaptonicotinic acid [63].

3.2.1.3 Crystal structure of the sodium salt of ADMN

Thick green needle-like crystals were obtained. Figure 3.4 gives the crystal packing. The distances and angles relating to the coordination of the sodium cations are collected in table 3.1 and are shown in figures 3.5.a and 3.5.b. The structure of the anion with atom labelling and the relevant distances is given in figure 3.6. Crystal data and refinement details are reported table 3.2.

3.2.1.3.1 Crystal packing

The product crystallises in a monoclinic space group, and each unit cell contains 8 formula units, with two successive layers of anionic-cationic species along the (a, b) plane. For each layer the four anions are stacked two by two through π - π interactions with the carboxylic group facing opposite directions. Each anion has one equivalent of Na^+ in two different positions, each with 0.5 occupancy. A water molecule is intercalated between each layer and forms two H-bonds through hydrogen atoms: one connected to the carbonyl of the carboxylic acid group of an anion, the other to the thione substituent on the pyridine ring of another anion; and the oxygen interacts with a sodium cation.

3.3.1.3.2 Sodium coordination

The sodium counterion is coordinated by two ADMN anions through the oxygen of the carboxylic acid group (ADMN-O), two ADMN anions through the sulphur in the 1-position (ADMN-S), and two water molecules, in two different octahedral configurations (type I and type II) (see fig 3.5a and 3.5b).

In type I, each pair of ligands of the same type is in trans positions. The octahedral configuration is slightly distorted, the S-Na-OH₂-O(ADMN) dihedral angle being 84°. The distance Na-S is greater than both Na-O distances, reflecting the higher electronegativity of O.

In type II, the two ADMN-O are in trans positions and compared with the type I their distance to the sodium is shorter by 18 pm. The Na-(ADMN-S) distance is longer than the sum of the van der Waals radii for Na and S (305 pm). It is nevertheless convenient to describe the Na coordination environment as octahedral. The water molecules are at the same distance from the cation in each type.

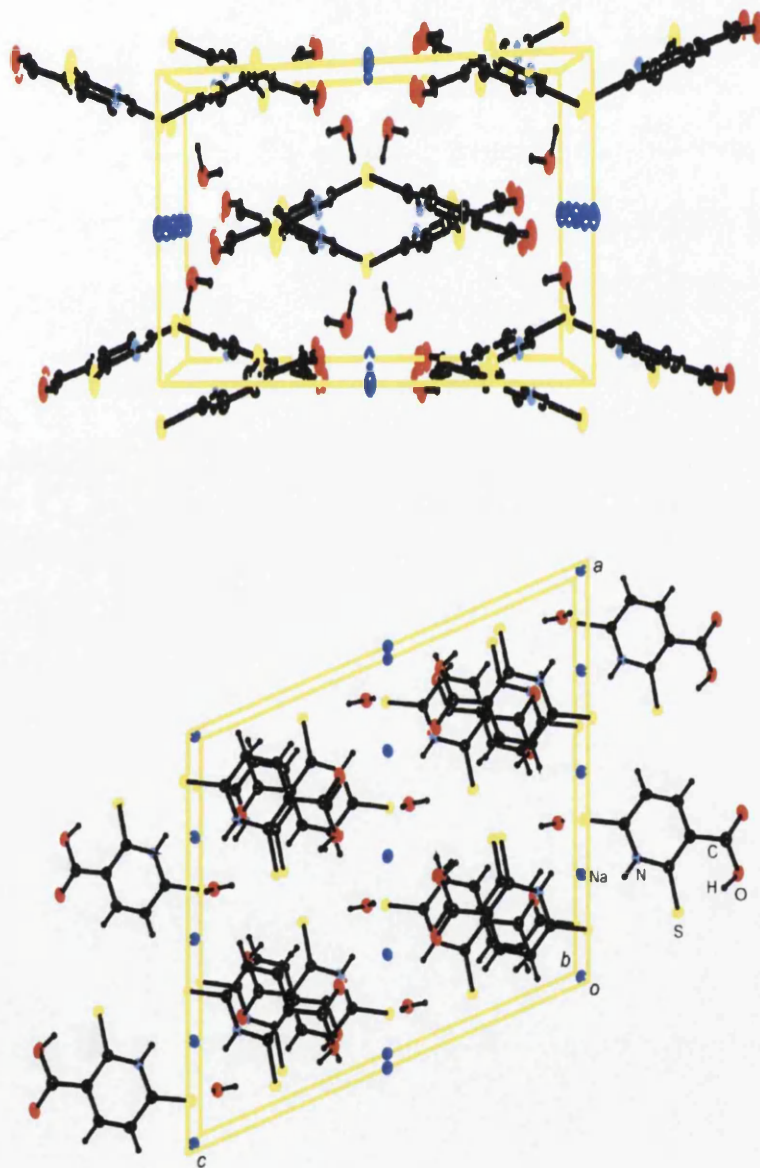


Figure 3.4: Representation of crystal packing for $[\text{ADMN} - \text{H}^+] \text{Na}^+ \cdot \text{H}_2\text{O}$. Top: cell along “a” axis. Bottom: cell along “b” axis with atoms labelled

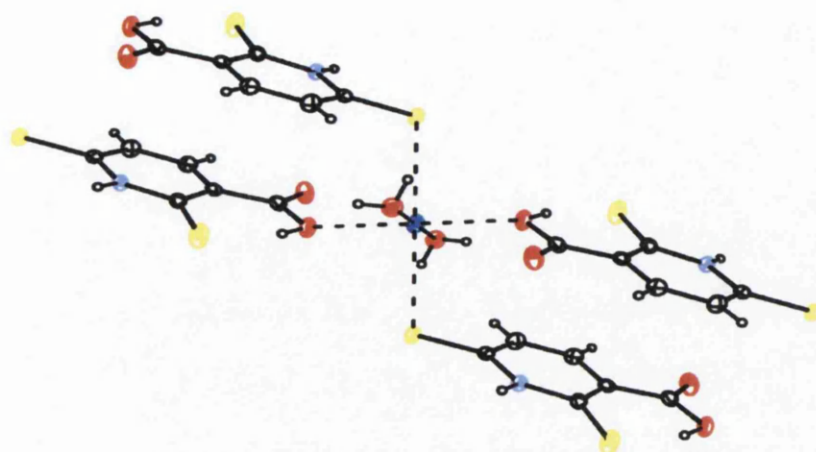


Figure 3.5a: Sodium coordination Type I

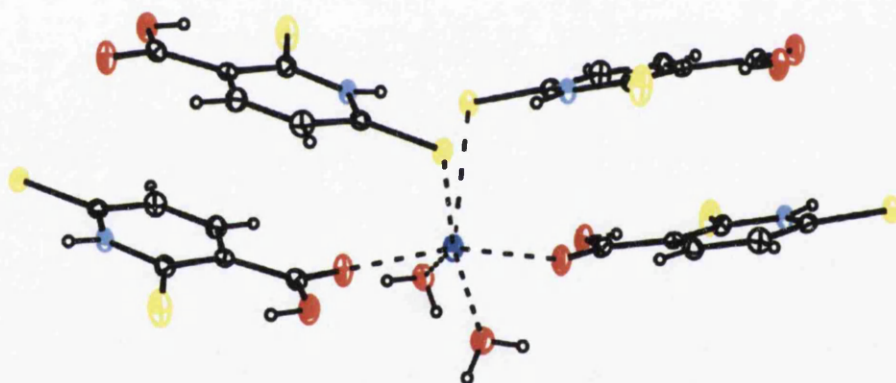


Figure 3.5b: Sodium coordination Type II

	Type I	Type II
<u>Distance (in pm)</u>		
Na-(ADMN-S)	298(3)	311(3)
Na-OH ₂	242(2)	244(2)
Na-(ADMN-O)	244(2)	226(2)
<u>Angle (°)</u>		
S-Na-S	180.0(1)	80.4(1)
H ₂ O-Na-OH ₂	180.0(1)	122.6(2)
O-Na-O (for ADMN)	180.0(2)	162.2(2)

Table 3.1: Selected distances and angles for the two types of sodium coordination

3.2.1.3.3 Molecular structure

As the ^1H NMR spectrum in solution suggests, the nitrogen in the ring is bonded to a hydrogen atom. The carboxylic acid group is non-dissociated and forms an intramolecular hydrogen bond with one of the sulphur atoms (S1). Therefore the atoms of the carboxylic acid group are in the plane of the pyridine ring. Neither of the sulphur-carbon bond lengths (figure 3.6) fits clearly in the expected range for a thiol (≈ 175 pm) or for a thione (160 - 168 pm) [64], suggesting that the sulphur is present in an intermediate form, with both sulphurs carrying a negative charge (see figure 3.7) and that the nitrogen rings have a partial deficit in electron density.

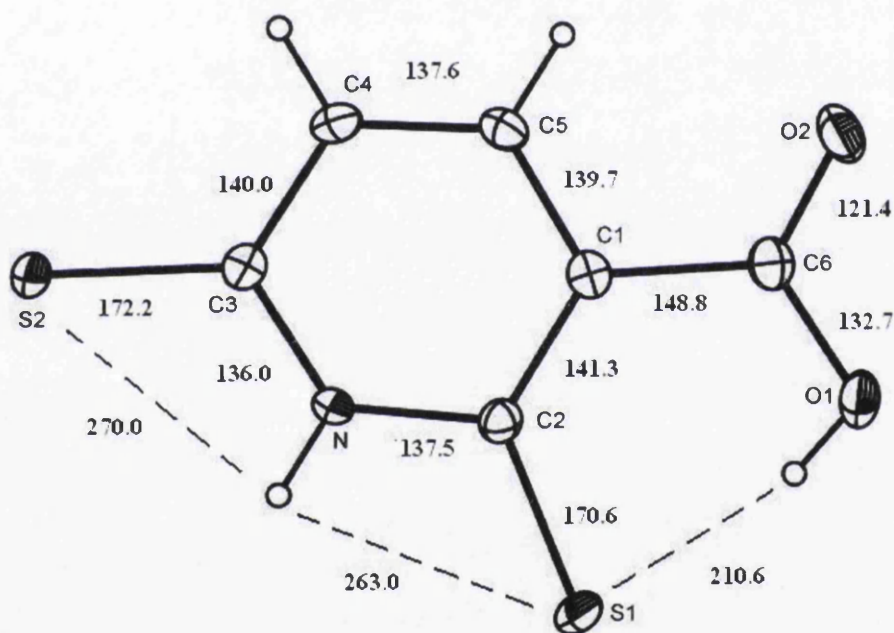


Figure 3.6: Structure and distances in pm of the monoanion of 2,6-dimercaptopyridine

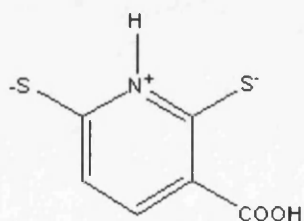


Figure 3.7: Partition of charge deduced from the crystal structure

Empirical formula	NaC ₆ H ₄ NO ₂ S ₂ ·H ₂ O
Formula weight	227.23
Temperature (K)	172 (2)
Crystal system	monoclinic
Space group	I2/a
<i>a</i> /Å	15.363(1)
<i>b</i> /Å	6.749(3)
<i>c</i> /Å	18.116(1)
α /°	90.00
β /°	110.35(1)
γ /°	90.00
Volume/Å ³	1761.3(17)
Z	8
<i>D</i> _{calc} (g cm ⁻³)	1.714
Absorption coefficient (mm ⁻¹)	5.77
<i>F</i> (000)	928
Crystal dimensions (mm)	0.80 × 0.24 × 0.12
Reflections collected	6753
Independent reflections	1706 (<i>R</i> _{int} = 0.031)
θ Range for data collection(°)	4.7-72.1
Absorption correction	multi-scan ABSPACK in CrisAlisPro RED
<i>T</i> _{min} / <i>T</i> _{max}	0.161/1.000
Reflections with <i>I</i> ≥ 2σ(<i>I</i>)	1688
No. of parameters	141
Final R values [<i>I</i> ≥ 2σ(<i>I</i>)]	0.031, <i>wR</i> ₂ ^a = 0.098
ρ _{fin} (min/max) (e.Å ⁻³)	-0.38/0.43

^a: $wR_2 = \{[w(F_o^2 - F_c^2)^2]/[w(F_o^2)^2]\}^{1/2}$, $w = 1/[\sigma(F_o^2) + (ap)^2 + bp]$, $p = (F_o^2 + 2F_c^2)/3$
a,b 0.0631, 2.6696

Table 3.2: Crystal data and structure refinement for NaC₆H₄NO₂S₂·H₂O

3.2.2 Synthesis of 2,6-dimercaptopyrazine, DMPA

3.2.2.1 Synthesis

Sodium hydrosulphide (8.5 g, 150 mmol) was dissolved in hot DMF (80 mL), and the solution allowed to cool to room temperature. Then 2,6-dichloropyrazine (2.5 g, 17 mmol) was added. The solution was heated at 60 °C for 2 h, and then allowed to cool to room temperature. Distilled water (50 mL) was added and the solution was acidified with 10% HCl solution (40 mL). A red precipitate was collected and washed with water. The red solid was dissolved in 1 M aqueous sodium hydroxide, to give a yellow solution. By acidifying the solution with 10% HCl solution, filtering, and drying under vacuum a red product was obtained (1.43 g, yield = 54%; m.p. 190 °C, decomposed).

This red product was hard to identify clearly because of its low solubility. Therefore half of it was dissolved in a minimum volume of 1M aqueous sodium hydroxide, the solution was filtered through diatomaceous earth and the water was removed to give the sodium salt, which is highly soluble in any polar solvent, and which was used for characterisation.

3.2.2.2 Characterisation

$^1\text{H NMR}$ (d_4 -MeOH): 7.72 (s); (D_2O); 7.71 (s)

$^{13}\text{C NMR}$: 139 (C-H), 169 (C-S) (in both solvents)

MS (ES+): 144 $[\text{M}]^+$

IR (cm^{-1}): 3342-3198 (m), 1639 (m), 1544 (m), 1461 (s), 1383 (s), 1173 (s),
1134(s), 996 (m), 850 (m), 827 (s), 550, 470, 449 (vs)

Melting point: 320 °C (decomposed)

3.2.2.3 Effect of pH

pH has a major effect on the properties of the product. The acidic form is red, with a low solubility in protic polar solvents. The basic form is yellow, with a very high solubility in protic polar solvents and photodegrades quickly.

3.2.3 Syntheses of 2,6-Dimercaptopyridine (DMP), 2,4-Dimercaptopyrimidine (24PYRI), and 4,6-Dimercaptopyrimidine (46PYRI)

2,6-Dimercaptopyridine [10], 2,4-Dimercaptopyrimidine [2], 4,6-Dimercaptopyrimidine [1] are known compounds which have been synthesised previously. However, to the best of our knowledge, MS, and IR spectroscopy of 2,6-Dimercaptopyridine and 4,6-Dimercaptopyrimidine have not been described previously. The crystal structure and ^1H , ^{13}C NMR spectra of 4,6-Dimercaptopyrimidine are also presented here for the first time.

3.2.3.1 Synthesis of 4,6-dimercaptopyrimidine (46PYRI)

By following the literature method [1], a mixture of monothiol-substituted and dithiol-substituted pyrimidine is obtained. The separation of the two products was not possible by column chromatography with different eluents. Elemental analysis is the only characterisation of the products in the references [1, 2], of H found is slightly lower than the one calculated. It could be possible that a mixture was also obtained. However, by using DMF instead of ethanol and carefully acidifying the resulting mixture, crystallisation of the desired product can be achieved. It has been characterised by ^1H NMR, ^{13}C NMR, MS and IR.

Method

4,6-Dichloropyrimidine (1.5 g, 10 mmol) was suspended in DMF (50 mL). Sodium hydrosulphide (5.6 g, 0.1 mmol) was added and the mixture was boiled for 2 h. The solution was cooled to room temperature, and became brown-orange when distilled water (100 mL) was added. After filtration, 0.1 M HCl (20 mL) and concentrated H_2SO_4 (5 mL) were added, and the mixture left overnight to yield a mixture of brown crystals (see the crystal structure, section 3.2.3.1.3) and amorphous precipitate. The solids were collected by filtration and dried under vacuum, after which the crystals were separated manually.

Characterisation

^1H NMR (d_6 -DMSO) : 6.8 (s, 1H), 8.5 (s, 1H), 14.1 (2H, N-H, broad)

^{13}C NMR (d_6 -DMSO): 127 (C-C-C), 146 (N-C-N), 173 (C=S)

(Starting material gives peaks at 162, 159 and 122 ppm)

MS (ES^+) = 145 $[\text{M}+\text{H}]^+$

Melting point: 250 °C (250-252 °C in the literature [1])

IR (cm⁻¹): 2689 (vw), 1579 (m), 1531 (m), 1385 (w), 1358 (m), 1241 (w), 1202 (w), 1180 (m), 1050 (m), 970 (m), 847 (m), 813 (s), 714 (m), 531 (s), 451 (vs), 410 (vs)

3.2.3.1.1 Crystal structure of C₄H₄N₂S₂·H₂O

Thick brown needle-like crystals were obtained. Figure 3.8 depicts the crystal packing. The structure, with atom labelling and relevant distances, is given in figure 3.9. Crystal data and refinement details are reported in table 3.3.

3.2.3.1.2 Crystal packing

The molecules crystallise in a monoclinic space group with four molecules in each cell. A row of 4,6-Dimercaptopyrimidine dimers and a row of water molecules alternate along the b axis, the dimer forming a zigzag pattern along the b axis with an angle of 45°. Each strand is bound to each other by the π - π interaction of pyrimidine rings, and the distance between two dimer units is 506 pm. The structure is stabilised by a network of H-bonds. Two 4,6-Dimercaptopyrimidine s (X = A, B) forming a dimer unit are linked by two intermolecular H bonds between one thione and a protonated nitrogen (NH_B→S_A, NH_A→S_B, 244pm), S_X and NH_X being neighbours. The other S_X, NH_X couple forms two H bonds, each with one water molecule (NH_X-O = 198 pm, S_X-HO = 249 pm).

The competition between intramolecular H bonds (S-H_{intra} = 273pm) and intermolecular H bonds (S-H_{inter}(H₂O) = 249 pm, S-H_{inter}(NH) = 244 pm) is in favour of intermolecular bonding.

3.2.3.1.3 Molecular structure

The molecule could tautomerise into three different species: the dithiol, thiol-thione or dithione form. The presence of the protonated nitrogen and the S=C distance of 169 pm show that the dithione form is preferred in the solid state, this form being stabilised by numerous H-bonds as described before. The symmetry of the molecules is, not surprisingly, perturbed by the crystal packing forces.

This result is consistent with the extensive study done on 24PYRI. This pyrimidine derivative, which is very similar to 46PYRI, has been proven to crystallise in the

dithione form [65], and the energy calculation done by Leszczyński and Lammertsma at the MP2/6-31G**//3-21G(d) level shows an energy gap of 28 kJ mol⁻¹ between the most stable dithione form and the others [66, 72]. We will show similar results for our compounds in chapter 5.

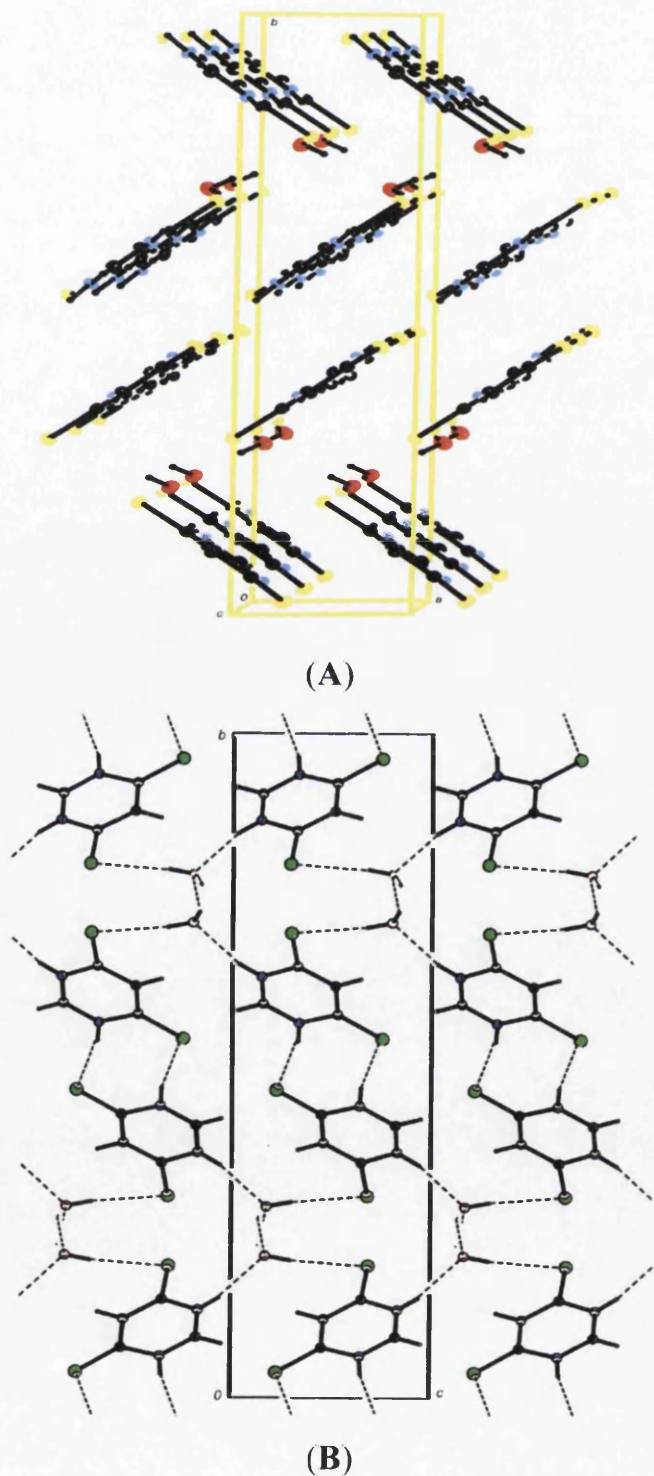


Figure 3.8: Crystal packing of 46PYRI along the c axis (A) and b axis (B)

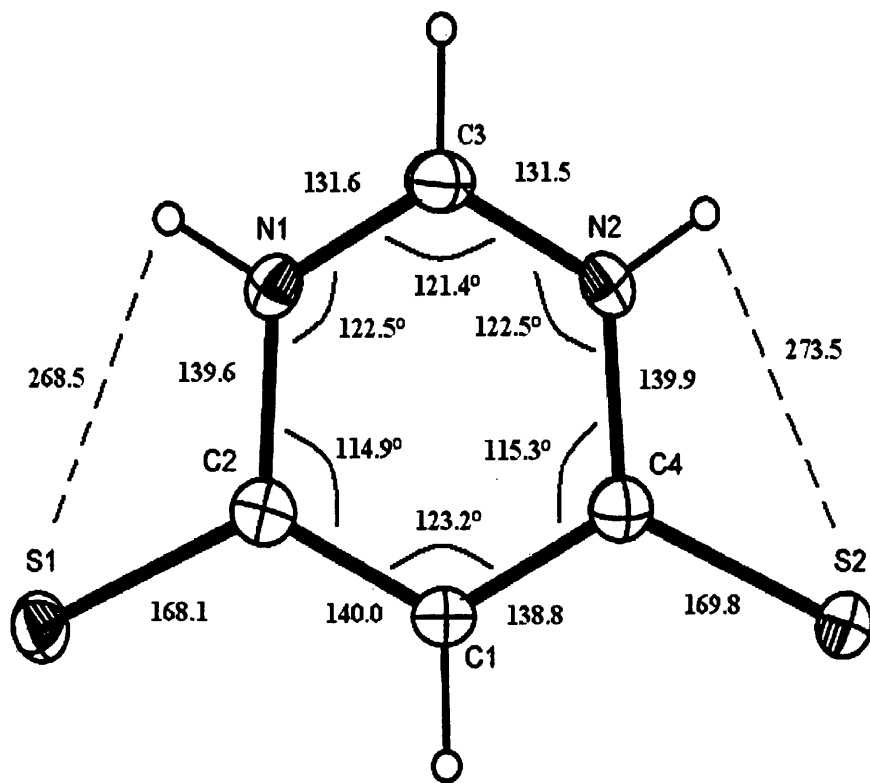


Figure 3.9: Structure, bond distances (pm) and angles (°) of 46PYRI from X-ray diffraction

Empirical formula	C ₄ H ₄ N ₂ S ₂ .H ₂ O
Formula weight	162.33
Temperature (K)	149 (2)
Crystal system	monoclinic
Space group	P2 ₁ /a
<i>a</i> /Å	5.036(1)
<i>b</i> /Å	21.605(4)
<i>c</i> /Å	6.649(3)
α /°	90.00
β /°	110.13(3)
γ /°	90.00
<i>V</i> /Å ³	679.2(3)
<i>Z</i>	4
<i>D</i> _{calc} (g cm ⁻³)	1.586
Absorption coefficient(mm ⁻¹)	0.70
<i>F</i> (000)	336
Crystal dimensions (mm)	0.80 × 0.40 × 0.03
Reflections collected	6420
Independent reflections	1392 (<i>R</i> _{int} = 0.029)
θ Range (°)	3.8 - 26.4
Absorption correction	multi-scan ABSPACK in CrisAlisPro RED
<i>T</i> _{min} / <i>T</i> _{max}	0.545/1.000
Reflections with <i>I</i> ≥ 2σ(<i>I</i>)	1187
No. of parameters	103
Final <i>R</i> values [<i>I</i> ≥ 2σ(<i>I</i>)]	0.031, <i>wR</i> ₂ ^a = 0.083
ρ _{fin} (min/max) (e.Å ⁻³)	-0.25/0.38

$$^a: wR_2 = \{[w(F_o^2 - F_c^2)^2]/[w(F_o^2)^2]\}^{1/2}, w = 1/[\sigma(F_o^2) + (ap)^2 + bp], p = (F_o^2 + 2F_c^2)/3$$

$$a, b \quad 0.0495, 0.2615$$

Table 3.3: Crystal data and structure refinement for C₄H₄N₂S₂.H₂O

3.2.3.2 Synthesis of 2,4-Dimercaptopyrimidine (24PYRI)

This compound has been extensively studied and can also be purchased, at somewhat lower purity than obtained here, from Aldrich [2].

Synthesis

2,4-Dichloropyrimidine (2.5 g, 16.8 mmol) and thiourea (5 g, 65 mmol) were dissolved in ethanol (50 mL). The solution was boiled for 2 h and turned slowly yellow. After cooling to room temperature, a yellow precipitate was isolated by filtration. The precipitate was re-crystallised from boiling water to provide yellow needles of 2,4-Dimercaptopyrimidine .

Characterisation

$^1\text{H NMR}$ (d_6 -DMSO): 6.45 (d, $J = 12\text{Hz}$, 1H), 7.25 (d, $J = 12\text{Hz}$, 1H),

13.24 (b, 2H, N-H)

$^{13}\text{C NMR}$ (d_6 -DMSO): 117, 137, 173, 188 [39]

MS (ES^+): 145 $[\text{M}+\text{H}]^+$

Melting point: 300 °C (decomposition) [1]

IR (cm^{-1}): 3000 (w), 1608 (m), 1560 (m), 1249 (m), 1208 (m), 1120 (s), 790 (m),
463 (s), 444 (s) [67]

All characteristics are in accordance with the literature, and the product obtained has a cleaner $^1\text{H NMR}$ spectrum than the one bought.

3.2.3.3 Synthesis of 2,6-dimercaptopyridine (DMP)

This compound has been synthesised following the literature method [10]

Synthesis

Sodium hydrosulphide (22.2 g, 0.40 mol) was dissolved in boiling DMF (75 mL). The resulting blue solution was cooled to room temperature, 2,6-Dichloropyridine (7.35 g, 0.05 mol) was added and the solution refluxed (136 °C) for 8 h. The solution was cooled to room temperature, and filtered. Distilled water (100 mL) was added and the solution turned yellow. When 10% aqueous HCl (150 mL) was added, a precipitate of yellow needles appeared and this was isolated by filtration. For purification, the precipitate was dissolved in a minimum amount of 1 M sodium hydroxide and the solution then acidified with 10% aqueous HCl giving bright yellow needles of 2,6-Dimercaptopyridine (3.7 g, 0.026 mol, yield = 52%).

Characterisation

$^1\text{H NMR}$ (CDCl_3): 6.9 (1H, d, $J = 12$ Hz), 7.2 (1H, t, $J = 12$ Hz)

$^{13}\text{C NMR}$ (CDCl_3): 122, 139, 161 (C=S)

MS (ES^+): 144 $[\text{M}+\text{H}]^+$

Melting point: 140 °C

IR (cm^{-1}): 2815 (m), 1932 (m), 1568 (s), 1360 (s), 1237 (s), 1158 (s), 1128 (s),
1019 (m), 973 (w), 870 (s), 850 (s), 815 (s), 750 (vs), 703 (vs), 657 (s),
447 (vs), 427 (vs), 409 (vs)

(The IR spectrum of 2-Mercaptopyridine was generally used to confirm the identity of the product [19]). The IR peak for SH is generally very weak and hard to detect at room temperature.

Both NMR spectra are generally consistent with results published by Perez-Torrente [68] except that they reported a peak at 9.56 ppm in the $^1\text{H NMR}$ spectrum in CDCl_3 corresponding to the hydrogen carried by both thiol groups which is absent from our data. No peak is present in the NH region in our spectra. A hydrogen exchange quicker than the time detection of the NMR could explain the absence of the SH and NH peak.

3.2.4 Conclusion on syntheses

The reaction of sodium hydrosulphide with the chloro-derivative of the N-heterocycle gives the desired product in a modest yield of around 50% after purification. The substitution of the halogen by a thiol group is supported by the NMR results and the IR spectrum.

- The shift of the ^{13}C peak allocated to the supporting C to lower field (usually from around 150 to around 170 ppm).
- The shift of the ^1H peak allocated to the vicinal hydrogen to higher field (from 7.2 to 6.8). This effect is consistent with the weaker electron withdrawing effect of the thiolate substituent compared with the chlorine atom.
- In the IR spectrum of the product, a peak at $1100\text{-}1150\text{ cm}^{-1}$ consistent with the vibrational band associated with the C=S bond of a thione appears. The IR peak around 1560 cm^{-1} is due to C=C stretching of the ring and is very sensitive to the sulphur substitution [69].

3.3 Photochemistry

The absorption spectra in different solvents as well as the influence of acid or base on the solution properties are presented first. Results on the photodegradation of two compounds are then presented. Finally, emission and time-resolved measurements at low temperature and room temperature are described.

For consistency, the results and discussion in each sub-chapter have been grouped according to the type of N-heterocycle.

3.3.1 Absorption spectra

Absorption spectra of all the dimercapto-N-heterocycles have been measured in a quartz cell with 1 cm pathlength as described in section 2.2.5. Solvents used were spectroscopic grade. Solutions were permanently protected from light, as oxidation of product can occur in the presence of light and oxygen.

These N-heterocyclic thiols are interesting to study because of the different possible processes as shown in figure 3.2. The possibility of aggregation was studied first, then the influence of the properties of the medium (solvent polarity, pH) on the tautomerisation has been studied, and finally the photodegradation of some products was examined.

3.3.1.1 Comparison between compounds

The solvent used for this study was a mixture of DCM and MeOH (1:1). Absorption spectra are shown in figure 3.10 and the value of the maximum absorption wavelengths (λ_{\max}) with their associated absorption coefficients (ϵ_{\max}) are reported in table 3.4. The absorption coefficients were calculated using the least squares method from a Beer-Lambert plot, for concentrations between $1-150 \times 10^{-6} \text{ mol dm}^{-3}$. The Beer-Lambert plot shows a linear regression along the range of concentration for each compound, showing the absence of aggregation of the species present at these concentrations. This is supported by previous work on the UV-Vis of 2-mercaptopyridine which does not show any aggregation up to $10^{-3} \text{ mol dm}^{-3}$ [25].

As a general experimental rule, 2-mercapto-N-heterocycles are commonly found in the thione form in polar solvents and in the thiol form in the gas phase or in apolar

solvents [13, 20, 26, 73], and thiol tautomers rarely absorb at wavelengths higher than 330 nm in ethanol [14]. All the excitation spectra for any emission wavelength fit the absorption spectrum of the compound, indicating only one absorbing species (see section 3.3.2), and the observation of absorption bands at wavelengths longer than 330 nm suggests that it is the thione tautomer which is present in DCM:MeOH (1:1) solution.

The absorption bands of all the compounds lie at longer wavelengths than those of their chlorinated starting material, the lowest $(\pi\text{-}\pi^*)^1$ and $(n\text{-}\pi^*)^1$ transitions of thiocarbonyls being at lower energy. A general pattern can be identified with a relatively low energy absorption band around 380-400 nm ($S_0\rightarrow S_2$) and a higher energy absorption band around 290 nm ($S_0\rightarrow S_3$). They all have high absorption coefficients, ruling out non-allowed transitions. Both bands are attributed to $(\pi\text{-}\pi^*)^1$ transitions [20, 26, 41, 42]. Usually thiones show no significant $(\pi\text{-}\pi^*)^3$ transition, and in keeping with this we did not observe any such bands even at higher concentration. This transition is usually very weak in intensity and could well be hidden inside the intense $(\pi\text{-}\pi^*)^1$ transition

Pyridine derivatives

Beak [14] measured the absorption spectrum of 2-mercaptopyridine in ethanol (λ_{max} at 287 nm and 362 nm, with ϵ_{max} 10200, 4860 $\text{dm}^3 \text{mol}^{-1} \text{cm}^{-1}$ respectively) and Alam's group [20] measured it in THF (λ_{max} at 250 nm, 293 nm and 385 nm, with ϵ_{max} 10300, 11200 and 2900 $\text{dm}^3 \text{mol}^{-1} \text{cm}^{-1}$ respectively); all of the bands were attributed to $(\pi\text{-}\pi^*)^1$ transitions. If a $(n\text{-}\pi^*)^1$ transition should exist, it should be hidden in the strong band at 385 nm [20]. DMP has two bands at 292 nm and 392 nm ($\epsilon_{\text{max}} = 10300$ and 8100 $\text{dm}^3 \text{mol}^{-1} \text{cm}^{-1}$ respectively) each corresponding to a $(\pi\text{-}\pi^*)^1$ transition. ADMN presents four bands at 274 nm, 320 nm, 390 nm and 400 nm ($\epsilon_{\text{max}} = 9200, 12700, 12400, 14300 \text{ dm}^3 \text{mol}^{-1} \text{cm}^{-1}$ respectively). When comparing the absorption spectrum of ADMN to that of DMP, red shifts in the absorption maxima of $\approx +30$ nm for two high energy bands (320 nm to 292 nm, the band corresponding to the 274 nm absorption in ADMN is out of range) and $\approx +10$ nm for the lower energy one (400 nm to 390 nm) are observed. An electron-withdrawing carboxylic acid substituent should stabilise the LUMO of the molecule. For ADMN, two very close peaks can be observed in the 400 nm region. This could

potentially be explained by the position of the carboxylic acid group in the ring which breaks the C_{2V} symmetry of the DMP. ADMN has the possibility of intramolecular hydrogen bonding which could also perturb the orbital energy.

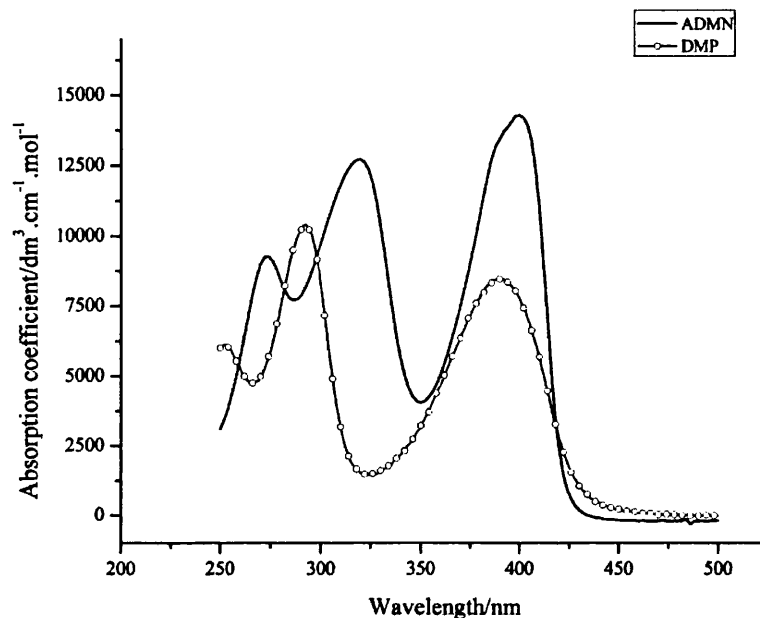


Figure 3.10: Absorption coefficient for pyridine derivatives in DCM:MeOH (1:1)

Pyrimidine derivatives

The spectrum of 24PYRI is the same as in the literature; the two bands at 284 nm and 354 nm ($\epsilon_{\max} = 19700$ and $7500 \text{ dm}^3 \text{ mol}^{-1} \text{ cm}^{-1}$ respectively) have been assigned to $(\pi \rightarrow \pi^*)^1$ transitions [3, 70].

46PYRI has a strong absorption band at 380 nm ($\epsilon_{\max} = 30000 \text{ dm}^3 \text{ mol}^{-1} \text{ cm}^{-1}$) and two weaker bands at higher energy: 290 and 260 nm ($\epsilon_{\max} = 13000$ and $8000 \text{ dm}^3 \text{ mol}^{-1} \text{ cm}^{-1}$ respectively). By comparison with the absorption spectra of the 24PYRI isomer, we assume that the higher absorption coefficient of the low energy band in 46PYRI is due to the presence of the two equivalent thione groups in 46PYRI.

NPYRI has two relatively strong absorption bands at 258 and 287 nm, and a broad absorption band at 369 ($\epsilon_{\max} = 9200, 13000$ and $11000 \text{ dm}^3 \text{ mol}^{-1} \text{ cm}^{-1}$ respectively). The two amino groups extend the number of isomers available through tautomerisation and polar solvent interactions which could explain the breadth of the absorption band at 369 nm.

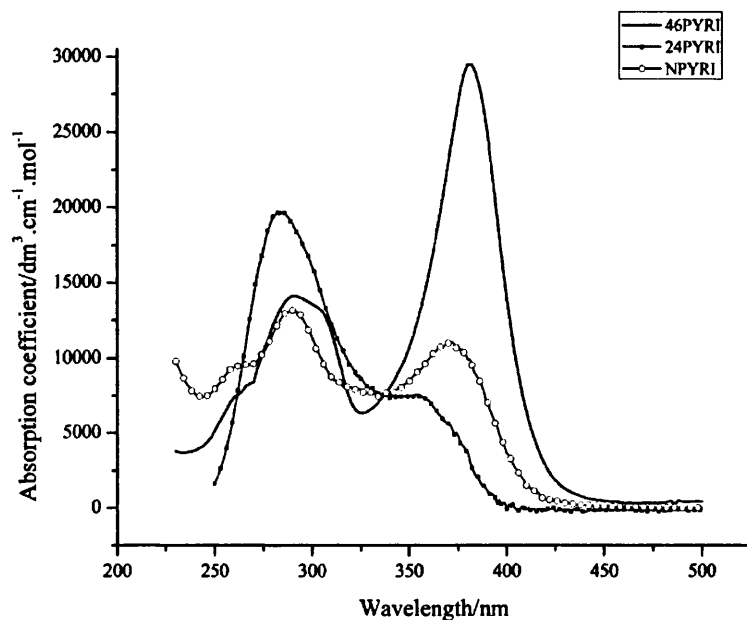


Figure 3.11: Absorption coefficient for pyrimidine derivatives in DCM:MeOH (1:1): 46PYRI (plain), 24 PYRI (filled figures), NPYRI (hollow figures)

Pyrazine derivatives

The sodium salt of DMPA has three absorption bands at 252, 290 and 433 nm ($\epsilon_{\max} = 8100, 5700$ and $6200 \text{ dm}^3 \text{ mol}^{-1} \text{ cm}^{-1}$ respectively). The red shift in the lowest energy bands is mainly due to the pyrazine ring.

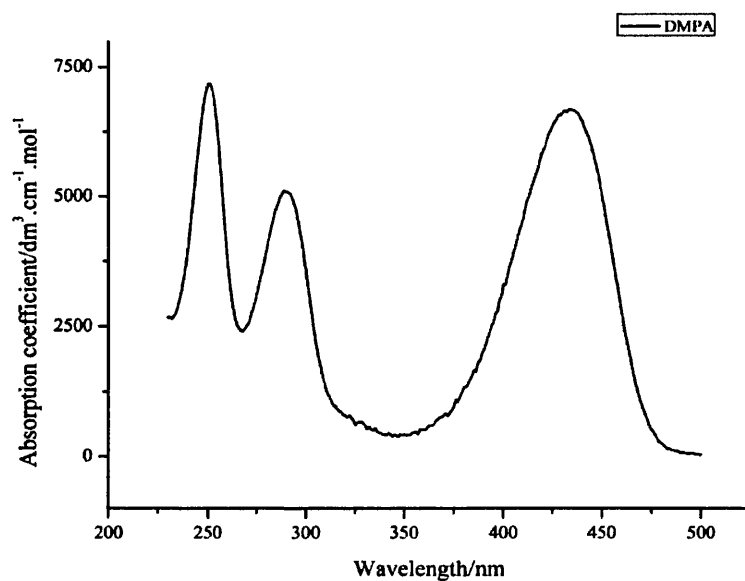


Figure 3.12: Absorption coefficient for the sodium salt of DMPA in DCM:MeOH (1:1)

Product	λ_{\max}/nm	$\epsilon_{\max}/\text{dm}^3 \text{ cm}^{-1} \text{ mol}^{-1}$
DMP	292	10300 (± 400)
	392	8100 (± 300)
ADMN	274	9200 (± 200)
	320	12700 (± 300)
	390	12400 (± 300)
	400	14300 (± 500)
sodium salt of DMPA	252	8100 (± 300)
	290	5700 (± 200)
	433	6200 (± 200)
24PYRI	284	19700 (± 400)
	354	7500 (± 300)
	375	4800 (± 200)
46PYRI	260	8000 (± 850)
	290	13000 (± 1300)
	380	30000 (± 3200)
NPYRI	258	9200 (± 300)
	287	13000 (± 400)
	369	11000 (± 400)

Table 3.4: Values of the wavelengths of maximum absorption and their corresponding absorption coefficients in DCM:MeOH (1:1) solution. The errors for 46PYRI are higher due to the small amount of compound available

3.3.1.2 Solvatochromism

Solvent effects on UV-vis absorption spectra can provide us with information on the nature of the transition. For N-heterocyclic thiols, the relative abundance of thione/thiol tautomers can also change according to the solvent and the phase.

Molecules in excited states can have different geometries from those in the ground state, and also have a different electronic distribution. The electronic properties of the solvent, as measured by its polarity and its dielectric constant, can modify the absorption spectra. If μ_e and μ_g are respectively the dipole moment of the molecule in the excited state and in the ground state, a more polar solvent will have a greater

stabilisation effect on both states, and if $\mu_e > \mu_g$, the more polar excited state will be more solvated and a red shift will be observed.

Therefore it is generally possible to distinguish between a $\pi \rightarrow \pi^*$ transition and a $n \rightarrow \pi^*$ transition by changing the polarity of the solvent. An n orbital is localised on one atom in the molecule, but a π^* orbital is delocalised, so a $n \rightarrow \pi^*$ transition will lead to a less polar excited state compared to the ground state.

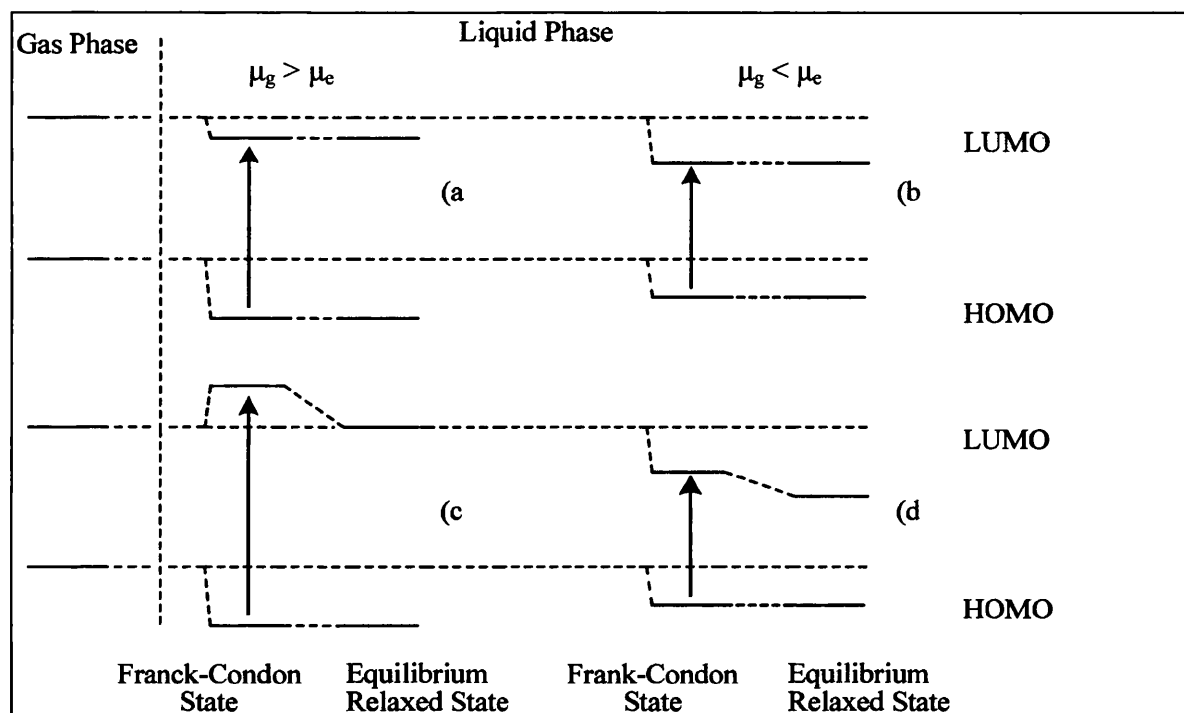


Figure 3.13: Energy diagram of solvatochromic shift for:
 polar solute and non polar solvent: a) ($\mu_g > \mu_e$); b) ($\mu_g < \mu_e$)
 non- polar solute and polar solvent: c) ($\mu_g > \mu_e$); d) ($\mu_g < \mu_e$)

Solvent	Water	MeCN	MeOH	THF	Dioxane
Dielectric constant	80	37	33	7.5	2.3
Dipole moment (D)	1.85	3.92	1.70	1.63	0.45
Polarity index [81]	10.2	5.8	5.1	4	4.8

Table 3.5: Dielectric constant, dipole moment, polarity index of solvents used

Therefore a more polar solvent will have a greater stabilisation effect on an n orbital than on a π^* orbital, and one can conclude that a more polar solvent will have a hypsochromatic (blue shift) effect on an $n \rightarrow \pi^*$ absorption band and a bathochromatic (red shift) effect on a $\pi \rightarrow \pi^*$ absorption band (see figure 3.13). As the compounds studied here only dissolve properly in relatively polar solvents, their absorption spectra have been measured in the following solvents: methanol, tetrahydrofuran, dioxane, water and acetonitrile (dipole moments and dielectric constants are given in table 3.5).

The tautomerisation equilibrium is also shifted according to solvent properties, and this also needs to be considered. The protomeric equilibrium constants in different solvents for 2-Mercaptopyridine have been calculated by Beak [26, 73] and it has been confirmed that the thiol isomer is preferred in the gas phase or an apolar solvent, while the thione isomer is predominant in a polar solvent (for further information, an extensive review on the tautomerism of six-membered heterocycles has recently been published [13]).

Figure 3.15 presents the normalised absorption obtained in different solvents for one representative of each type of ring. The pyridine and pyrazine derivatives have not been measured in dioxane, because of their instability in this solvent.

Pyridine derivatives

The energy of absorption transitions for ADMN and DMP can be classified from the lowest to the highest according to the solvent used: THF < MeCN < MeOH < H₂O. As for the pyridine thiol [18, 50], the DMP absorption peaks are blue-shifted, with a higher absorption coefficient in MeOH compared to THF. When small portions of methanol were added to a DMP acetonitrile solution, the absorption spectrum shifted to fit the one measured in pure methanol, which illustrates important hydrogen bonding interactions between protic solvents and the molecule. The absorption spectra in dioxane show that there is a rapid degradation of the compound, probably due to disulphide formation, and therefore indicates that the thiol tautomer is predominant in this solvent.

Acetonitrile has the highest dipole moment of the solvents used and the second highest dielectric constant. The absorption bands were expected to be the most shifted (either way) in this solvent; however there is no clear connection between the electronic properties of the solvent and the position of the absorption bands. So the differences in absorption can be explained by the presence of different species in equilibrium. The presence of aggregation has been ruled out by the linearity of the Beer-Lambert plot. The disulphide bridges do not absorb light at this wavelength and the other study excluded them from being present. So, now we will consider the equilibrium between the thione, thiol and zwitterion (fig 3.14).

As previously reported, the thione form is predominant in more polar solvents. New insight might be given by considering the zwitterion in the equilibrium. In a protic polar solvent, this tautomer is even more stabilised. Water has the highest hydrogen bonding capability of all the solvents used, and its greater interaction with the zwitterion explains the absorption shift in water compared with other solvents.

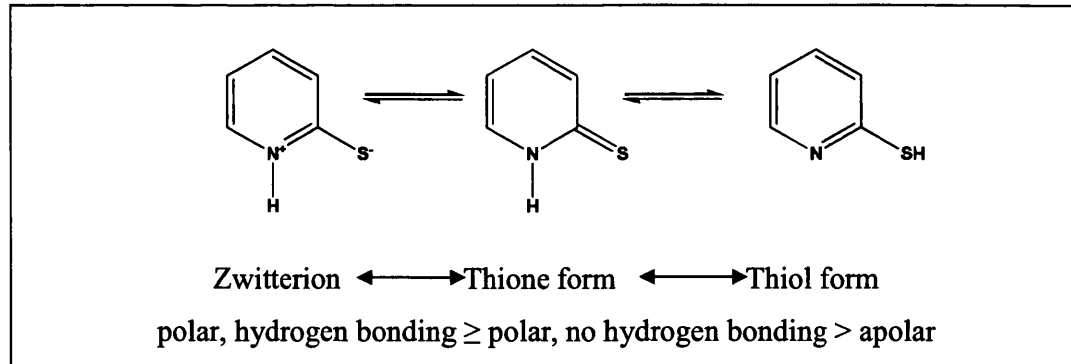


Figure 3.14: Different isomers of 2-Mercaptopyridine

Pyrimidine derivatives

Absorption spectra of 24PYRI in water [50] and EPA [48] have been reported. Our absorption spectra are consistent with the literature, and they do not vary much in other solvents.

The lowest energy absorption band at 380 nm of NPYRI and 46PYRI in the more polar aprotic solvents THF and MeCN is red-shifted compared with that in dioxane, confirming the ($\pi \rightarrow \pi^*$) nature of this transition. No noticeable changes in the

absorption of the pyrimidine in dioxane were observed during the time of experimentation. 46PYRI shows different spectral shapes in the 250-300 nm region, corresponding to the pyrimidine ring absorption. These changes are attributed to the different tautomers present in solution. The dithione is expected to be predominant in a protic polar solvent. When solvents with lower dipole moment are used, the proportion of mono-thiol increases, and this is believed to be responsible for the appearance of the band at 260 nm.

Pyrazine derivatives

DMPA is unstable in dioxane and THF, and degrades very quickly in the presence of light. This is indicative of a very high rate of disulphide formation and suggests a predominance of the thiol form in solvents with lower dipole moment. Protic and polar solvents stabilise the thione tautomer.

Conclusion from solvatochromic study

In conclusion, the solvatochromatic study shows the strong influence of the medium on the particular species present in it. In general in polar protic solvents the predominant form is either the zwitterion or the thione, whereas in aprotic apolar solvents the thiol form predominates, but this degrades via disulphide formation. The occurrence of tautomerisation and degradation makes it difficult to use the solvent effects on absorption spectra to determine the (n,π^*) or (π,π^*) nature of the transitions involved. Further studies in this chapter will use protic solvents to ensure the presence of only one tautomer: the thione form.

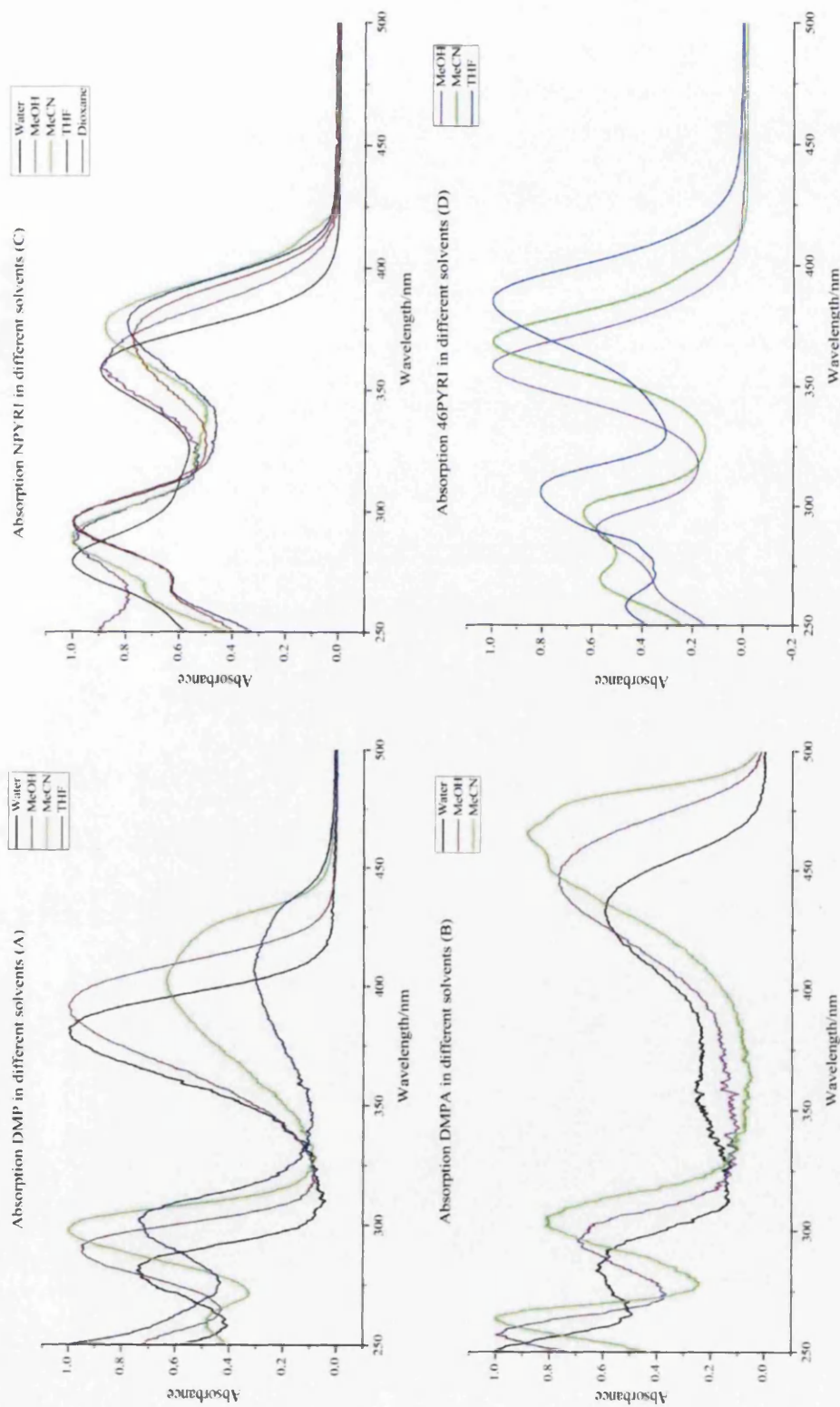


Figure 3.15: Normalised absorption spectra for DMP (A), DMPA (B) NPYRI (C) and 46PYRI (D) in different solvents at room temperature. (water in black, MeOH in violet, MeCN in green, THF in blue and dioxane in red)

3.3.1.3 Absorption spectra at different pH

To measure the variation in absorption spectra at different pH, 3 mL of a DCM:MeOH (1:1) solution of the desired compound were placed in a 1 cm path length quartz cell; then, to decrease the pH 10, 20, 30, 40 or 50 μL of CF_3COOH in methanol ($7.7 \times 10^{-2} \text{ mol dm}^{-3}$) were added, and to increase the pH 10, 20, 30, 40 or 50 μL of tetraoctylammonium hydroxide (20%) in methanol was added. The results are summarised in table 3.6 and the corresponding spectra are given in figure 3.16.

Such a study has been already reported by Psoda for 24PYRI [50] and our results are similar to those. They proved that the anionic form **A** (figure 3.16) is predominant in water by comparing the absorption spectra of the N-methyl substituted compounds to those of the N-hydrogen substituted compound. The form **B** has its absorption spectra blue-shifted compared with **A**.

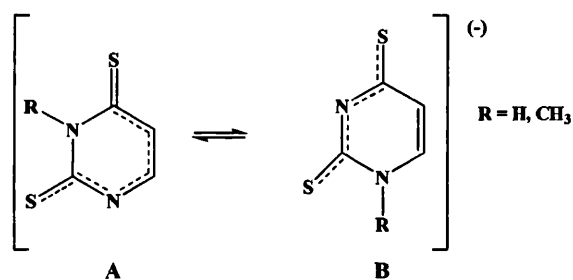


Figure 3.16: Possible anionic forms of 24PYRI derivatives in water

Theoretical studies on 24PYRI excited states via DT-DFT calculations suggest that the NH group could be deprotonated in water or acetonitrile [74]. However, we do not observe in water, nor in acetonitrile, any difference in absorption spectrum which could correspond to a corresponding deprotonated species. If a deprotonated species is present, it must be in a very small amount. By adding base, a blue shift in the lowest energy absorption band of 46PYRI and NPYRI from 380 and 370 nm to 325 and 355 nm respectively was observed.

The anionic 1-Methyl-2,4-dimercaptopyrimidine absorption spectrum [50] is similar to the anionic 46PYRI one, which is not surprising considering the absence of extended conjugation in 46PYRI which results in a mono-anion corresponding to the **B** form. For NPYRI, in basic media, the two electron donating amino groups in positions 4 and 5 will enhance the formation of the **B** tautomer. The blue shift in the

absorption band is also indicating the preference for the **B** form of the mono anionic form.

It was not possible to study the effect of pH on the spectrum of DMPA, as only the deprotonated form is soluble: there was no change when further base was added; when acid was added, the solution turned red and a precipitate appeared. ADMN shows only one peak at 400 nm when base is added.

Compound	DMP	ADMIN	Sodium salt of DMPA	24PYRI	46PYRI ^a	NPYRI
Acid added	292 (10300) 385 (7300)	274 (9200) 320 (12700) 390 (10500) 400 (11100)	Insoluble	No Change	295 310 385	287 (13000) 340 (7900)
Base added	292 (9800) 400 (10100)	300 (12700) 400 (13500)	No change	267 (15500) 290 (16400) 380 (13600) 390 (12500)	280 325	Broad shoulder < 300 nm 355 (16500)
Normal	292 (10300) 392 (8100)	274 (9200) 320 (12700) 390(12400) 400 (14300)	252 (8100) 290 (5700) 433 (6200)	284 (19700) 354 (7500) 375 (4800)	260 (8000) 290 (13000) 380 (30000)	258 (9200) 287 (13000) 315 (8000) 370 (10800)

^a: ϵ_{\max} not measured due to the small amount of compound available

Table 3.6: Influence of acid or base on the UV-Vis absorption bands of the N-heterocyclic dithiols in a solution of DCM:MeOH (1:1). Value of λ_{\max} reported in nm and ϵ_{\max} in $\text{dm}^3 \text{mol}^{-1} \text{cm}^{-1}$

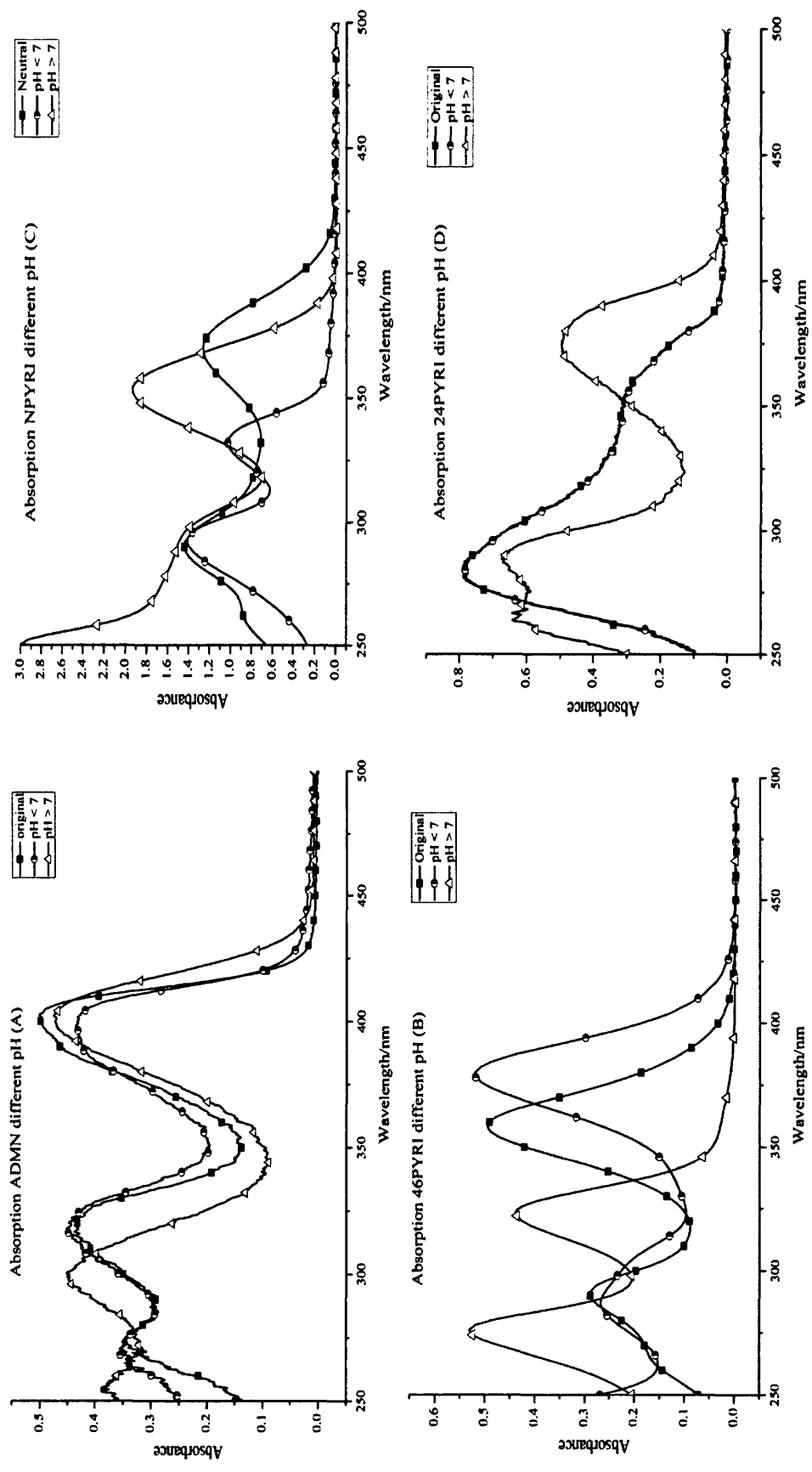


Figure 3.16: Absorption spectra of ADMN (A), 46PYRI (B), NPYRI (C) and 24PYRI (D) in DCM:MeOH (1:1) at different pH

3.3.1.4 Photodegradation of the compounds

Early on in this work it was observed that, in certain circumstances with certain compounds, there was decolouration of the solution after a varying amount of time. It has been shown by others that thiones or thiols can photodegrade to their oxo analogues in air in daylight or even in the dark (e.g. thiobenzophenone to benzophenone [75]). Also the thiol can be oxidised to give a disulphide [43]. A study by Stoyanov [28] on different 2-mercaptopyridines or pyrimidines gives the kinetics of this photodegradation. Light and/or dioxane seem to significantly catalyse the thiol-disulphide process. Some similar results were obtained for our compounds.

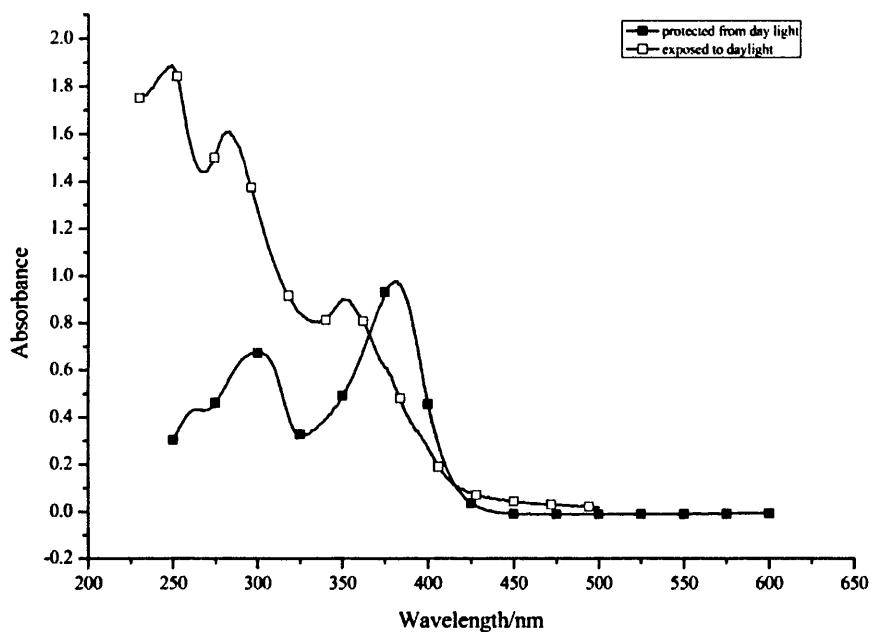


Figure 3.17: Absorption of a DCM:MeOH(1:1) solution of 46PYRI after 72 h exposed to daylight (empty squares) or protected from light (filled squares)

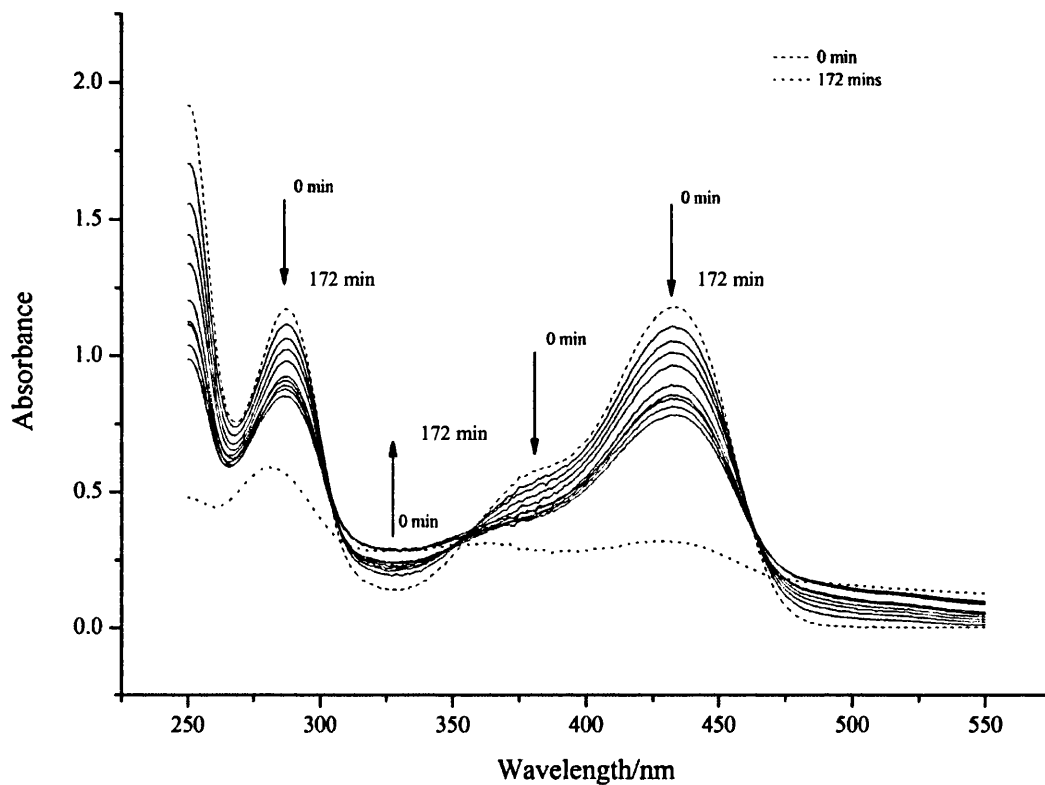


Figure 3.18: Changes in absorption with time of a water solution of sodium salt of DMPA exposed to daylight for three hours

A photoelectrochemical study of the oxidation of 2-thiouracil in water provided similar absorption results [76] and the disulphide has been identified as an intermediate of the reaction.

We assume a similar process occurs in our compounds, and therefore they should be protected from light when in solution.

3.3.2 Emission and excitation spectra at 77 K

The emission spectra at 77 K have been measured in a transparent glass of DCM:MeOH (1:1) or the less polar EPA. Care has been taken to check for the absence of cracks in the glass. The absence of molecule aggregation at the concentrations used was demonstrated by the invariance of the luminescence spectral shape compared with a more dilute solution. The excitation spectra are the same for any emission wavelength. They are analogous to the absorption spectra (a slight spectral shift occurs due to the temperature), indicating the presence of only one emitting species (as an example, see figure 3.19).

When accessible, the time-resolved data were collected on the apparatus described in section 2.3.2.1 at the emission maximum (λ_{\max}) and two other wavelengths: usually $\lambda_{\max} + 10$ nm and $\lambda_{\max} + 20$ nm. When measuring at the maximum emission wavelength, the intensity of the irradiating pulse was varied to ensure the absence of multi-photon absorption. The emission spectra at 77 K in EPA and DCM:MeOH (1:1) of the compounds studied in this chapter are depicted in figures 3.20 to 3.25.

3.3.2.1 Pyridine derivatives

The maximum emission at 77 K in glassy ethanol of 2-Mercaptopyridine (2TP) is reported at 479 nm [20] and originated from a $^3(\pi, \pi^*)$ triplet state; no fluorescence was observed. For the pyridine derivatives studied here emission spectra show two series of peaks with some vibrational structure (406, 416, 430 nm and 475, 485, 502 nm for ADMN 412, 423 nm and 470, 498 nm for DMP). We believe this emission originates from singlet states as:

- 1) the emission occurs within the time scale of our ns laser system (*ca.* 50 ns);
- 2) there is a overlap of the excitation and the emission spectra (a (0-0) band) at 405 nm in DCM:MeOH (1:1) for ADMN and DMP (figures 3.20 and 3.21);
- 3) no emission is detected at room temperature in N₂-saturated solution (see next section).

The highest energy peak originates probably from a ($S_2 \rightarrow S_0$) transition and the lowest energy peak from a ($S_1 \rightarrow S_0$) transition. A radiative deactivation originating from the S_1 state for a thione is a rare feature as $k_{nr}(S_1 \rightarrow T_1)$ is usually very high (up to 10^8 s^{-1}). This is even more striking considering that 2TP gives only a long-lived phosphorescent emission. In thiones, the T_1 and S_1 excited states are very close in

energy. The presence of an additional thiol group in the α -position of the pyridine ring seems to effectively quench the triplet state formation. It is also possible that emission is due to a very short-lived emitting T_1 state, although thione triplets are generally reasonably long lived.

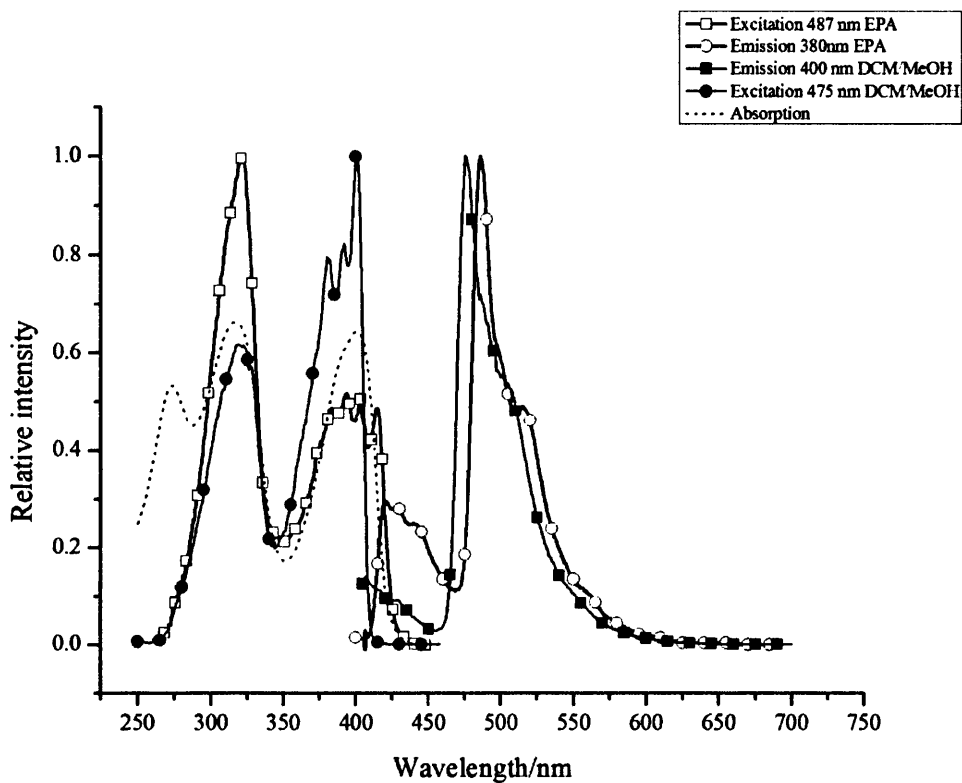


Figure 3.20: Emission and excitation spectra of ADMN at 77 K in EPA (hollow figures) and in DCM:MeOH (1:1) (filled figures)

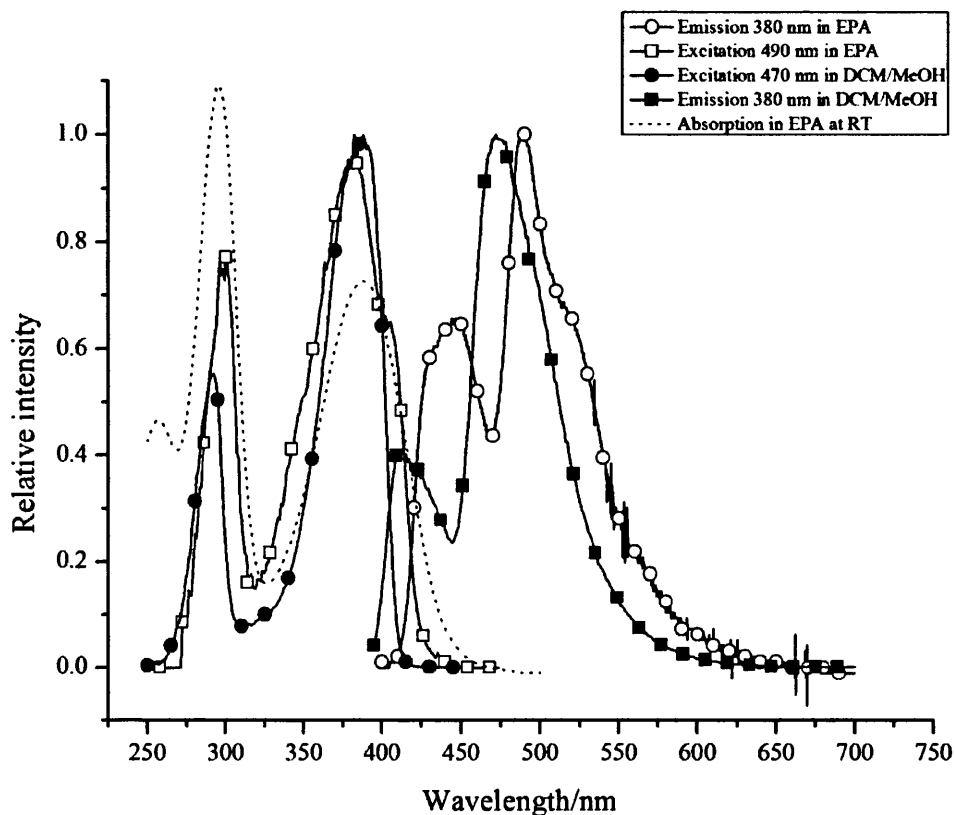


Figure 3.21: Emission and excitation spectra of DMP at 77 K in EPA (hollow figures) and in DCM:MeOH (1:1) (filled figures)

3.3.2.2 Pyrazine derivatives

The maximum emission wavelength is 487 nm in EPA and 491 nm in DCM:MeOH (1:1). The emission from the sodium salt of DMPA has a well-resolved vibrational structure in EPA, this solvent being less polar and interacting less with the deprotonated DMPA molecules. This photoluminescence originates from a singlet excited state as:

- 1) the emission occurs within the time scale of our ns laser system (*ca.* 50 ns);
- 2) there is a overlap of the excitation and the emission spectra (a (0-0) band) band at 470 nm in DCM:MeOH (1:1) (figure 3.23);
- 3) no peak appears at room temperature in N_2 -saturated solution (see next section).

The bathochromic shift in the more polar solvent indicates that the nature of the transition is $^1(\pi^*,\pi)$. As for the pyridine analogue, no phosphorescence is detectable, which is consistent with the presence of two thiol groups in the α -positions of the ring. But in this case, due to the absence of two patterns in the emission spectra

(unlike the pyridine), we can assume that the origin of the luminescence arises from the S_2 excited state only.

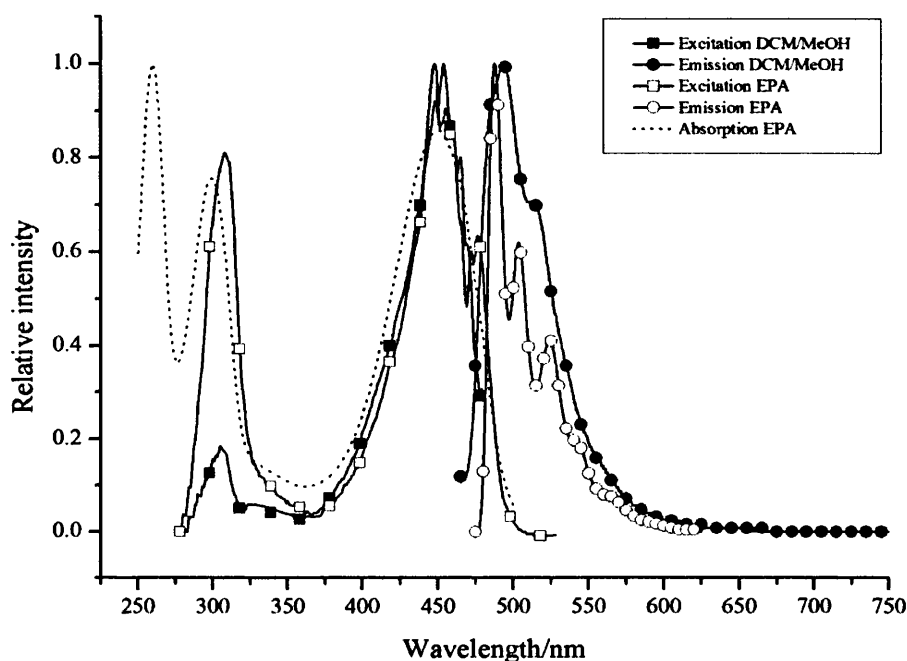
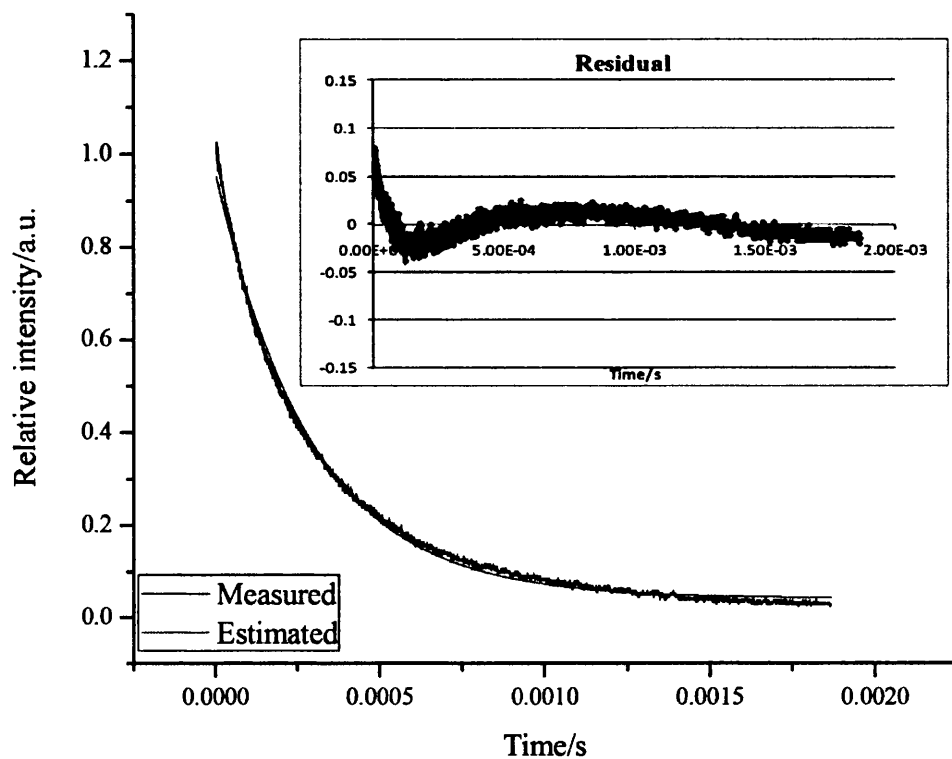


Figure 3.25: Emission and excitation spectra of DMPA at 77 K in EPA (hollow figures) and in DCM:MeOH (1:1) (filled figures)

3.3.2.3 Pyrimidine derivatives

24PYRI has already been studied at 77 K in EPA [20] and a maximum emission at 482 nm with a mono-exponential decay of 390 μ s lifetime was reported. Our measurements generally confirm the data found, with the exception of the time-resolved study. Curve fitting the time-resolved decay of 24PYRI in EPA at 490 nm gives a best fit for a double exponential with a process at 422 (± 5) μ s and another at a faster process of 133 (± 3) μ s. The longer lifetime is consistent with the lifetime obtained in reference [20] but the faster process has not been reported. The fitting of lifetime measurements data for a single exponential or a double exponential is shown in figure 3.22. The origin of the faster decay is not understood. As reported, the origin of the emission comes from triplet states having a relatively long lifetime due to the spin forbidden transition to S_0 . The maximum phosphorescence emission wavelengths do not vary much when using a more polar solvent (there is a slight hypsochromism of 5 nm), which confirms the assignment made of the transition to originate from a $^3(\pi,\pi^*)$ excited state.



A: fitting to a single exponential

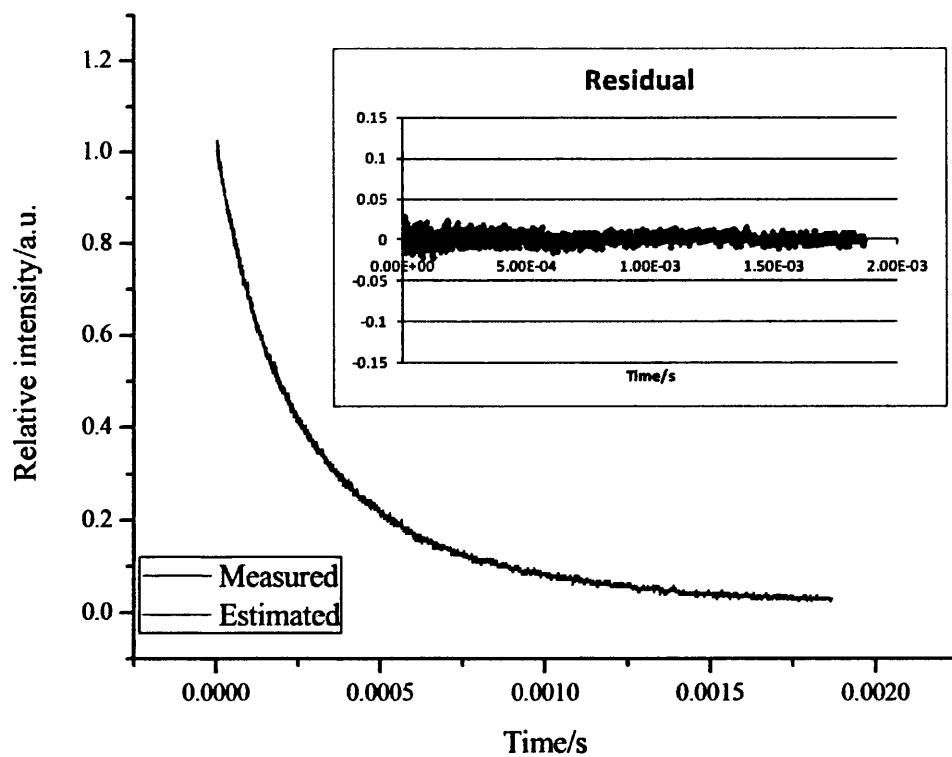
B: fitting to a double exponential (422 μ s (60 %) and 133 μ s (40 %))

Figure 3.22: Time resolved measurements for 24PYRI in glassy EPA at 77 K and curve fitting (A single exponential; B double exponential)

46PYRI shows emission maxima at 464 nm and 471 nm in DCM:MeOH (1:1) and EPA respectively. Emission in both glasses shows a tail featuring some vibrational bands. The deconvolution of the time-resolved decay gives also a best fit for a double exponential with lifetimes of $60 (\pm 4) \mu\text{s}$ and $11 (\pm 2) \mu\text{s}$. As for 24PYRI, the emission originates from a $^3(\pi, \pi^*)$ excited state.

NPYRI gives a broad emission which is not well-resolved in any solvent, with a maximum emission wavelength at 426 nm and 431 nm in DCM:MeOH and EPA respectively. The lifetime is shorter than *ca.* 100 ns and there is also a (0-0) band around 411 nm, which indicates that this emission originates from a singlet state *i.e.* $^1(\pi, \pi^*)$. The presence of the two amino groups on the ring should effectively quench the triplet states through internal vibration, even in a glassy medium. These two electron donating groups shift the emission wavelength by ≈ -64 nm compared with 24PYRI. The HOMO is probably located on the thione groups; its energy level should not vary much by substitution on the rings, and this large shift in energy suggests that the LUMO is destabilised by both electron donating groups and is therefore probably located on the ring. This will be confirmed later by the DFT calculations discussed in chapter 5.

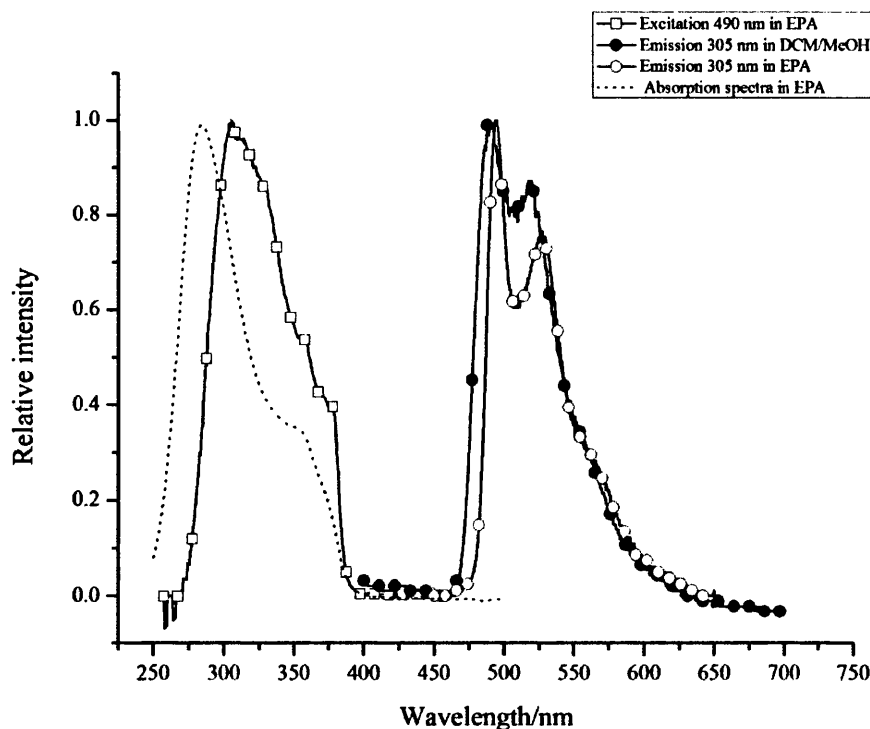


Figure 3.23: Emission and excitation spectra of 24PYRI at 77 K in EPA (hollow figures) and in DCM:MeOH (1:1) (filled figures)

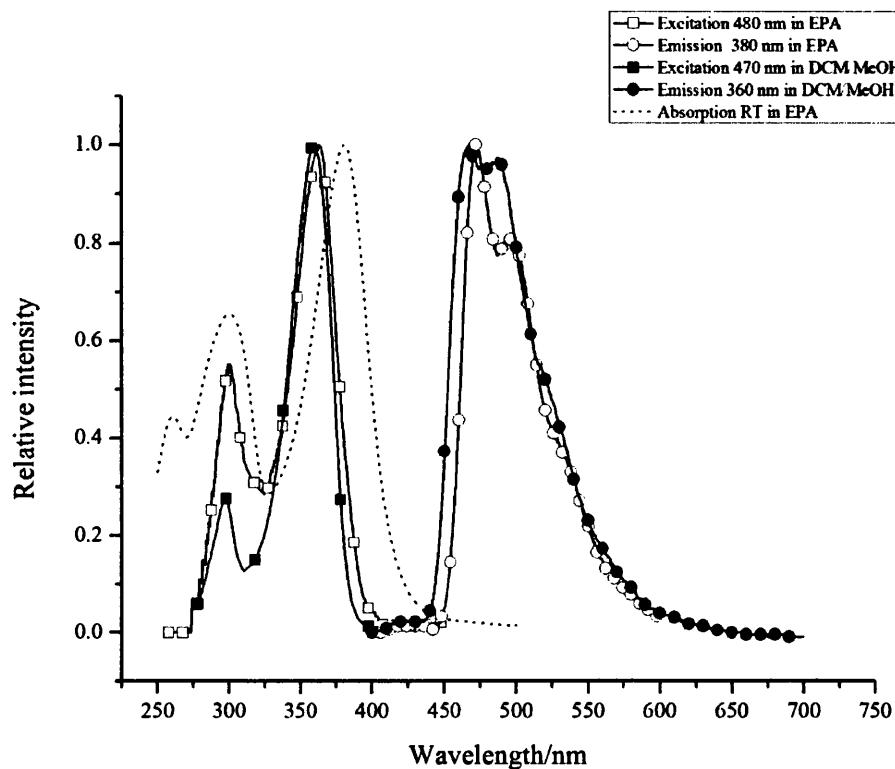


Figure 3.24: Emission and excitation spectra of 46PYRI at 77 K in EPA (hollow figures) and in DCM:MeOH (1:1) (filled figures)

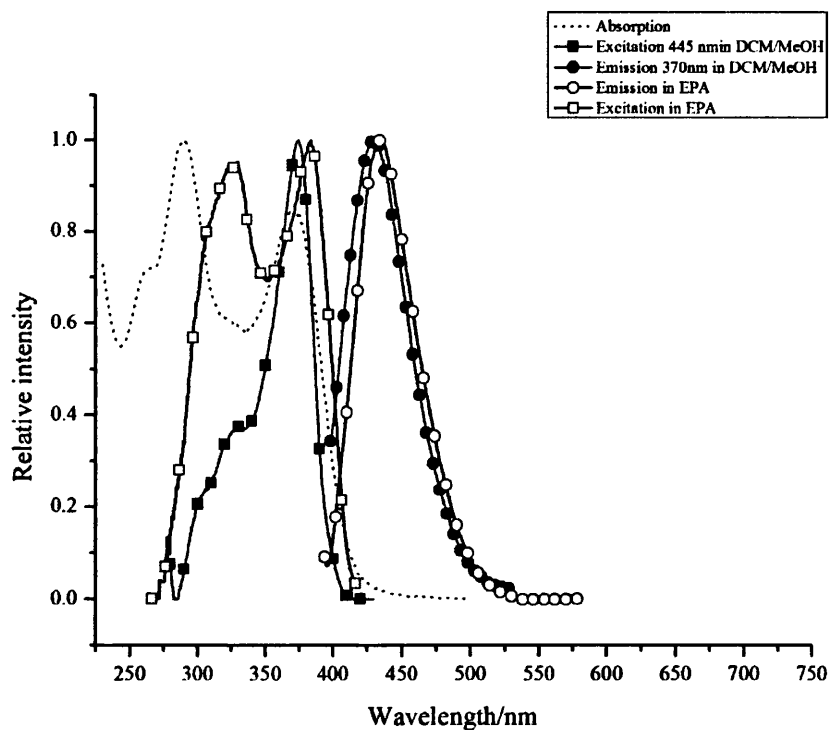


Figure 3.25: Emission and excitation spectra of NPYRI at 77 K in EPA (hollow figures) and in DCM:MeOH (1:1) (filled figures)

3.3.2.4 Conclusion from the study of emission spectroscopy at 77 K

This 77 K study provides us with determinant results on the nature and origin of the different emissions. All the emissions arise from a $(\pi,\pi^*)\rightarrow S_0$ transition. Only some of the pyrimidine rings, when not substituted, phosphoresce. The 2,6-Dimercaptopyridine and 2,6-Dimercaptopyrazine fluoresce and do not show any phosphorescence at 77 K. This fluorescence seems to originate from the S_2 and S_1 states for the pyridine derivative, but from only one state (S_2) for the pyrazine derivative.

Compound	DCM:MeOH(1:1)	EPA	
	Emission wavelength (nm)	Emission wavelength (nm)	Lifetime (μ s)
DMP	412	426	ND
	422	448	
	470 (max)	486 (max)	
	498	517	
ADMN	406	422	ND
	416	432	
	430	442	
	475 (max)	487 (max)	
	485	501	
	502	518	
Sodium salt of DMPA	491	487 (max)	ND
	511	502	
		522	
		542	
		562	
24PYRI	488 (max)	493 (max)	422 (\pm 20) 60% 133 (\pm 4) 40%
	516		
	558	526	
		564	
46PYRI	464 (max)	471 (max)	60 (\pm 4) 49% 11 (\pm 2) 48%
	487		
	520	498	
	570	533	
		580	
NPYRI	426	431	ND

Table 3.7: Emission wavelengths at 77 K in a polar and relatively non-polar glass. When measurable, the lifetime is also reported (ND stands for non-detectable)

3.3.3 Photoluminescence and excitation at room temperature

The 77 K study shows that spectra in EPA are better defined, due to less interaction between the solvent and solute. To minimize the deactivation of the excited state through solvent interaction, and also allow comparison between room temperature and 77 K data we chose this solvent for the room temperature photoluminescence study. To minimize possible self-quenching of the thione, solutions with an optical density of 0.1 or less at the excitation wavelength were used. The absence of aggregates was also checked by comparing emission spectra of solutions of differing concentration: when any of the solutions was diluted (absorbance from *ca.* 0.3 to *ca.* 0.12) there was no change in the shape of the emission spectrum. A first measurement was done under nitrogen and then, after 45 minutes in air, a second measurement was carried out. Careful attention was paid to ensure no significant change in concentration between the two measurements. The absorption and excitation spectra match well for all the compounds studied. Emission and excitation spectra in EPA at room temperature are reported in figures 3.26 to 3.30. Maximum emission wavelengths are reported in table 3.8.

Results

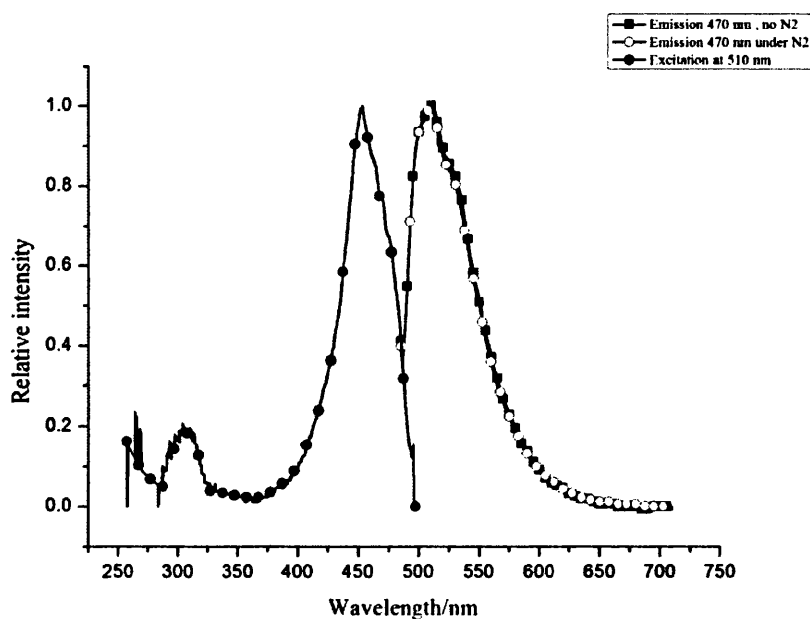


Figure 3.26: Emission and excitation spectra of sodium salt of DMPA at room temperature in EPA under N₂ (hollow figures) or in air (filled figures)

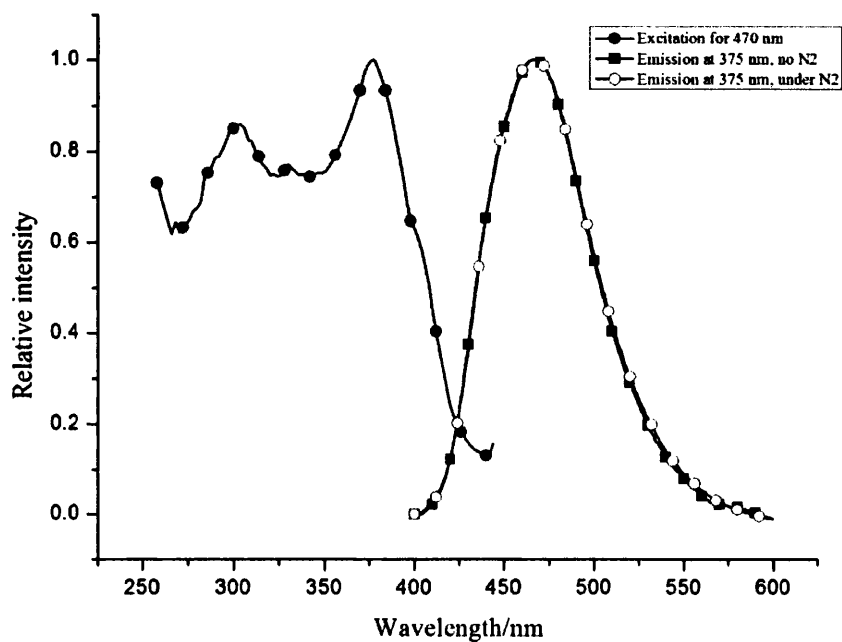


Figure 3.27: Emission and excitation spectra of NPYRI at room temperature in EPA under N₂ (hollow figures) or in air (filled figures)

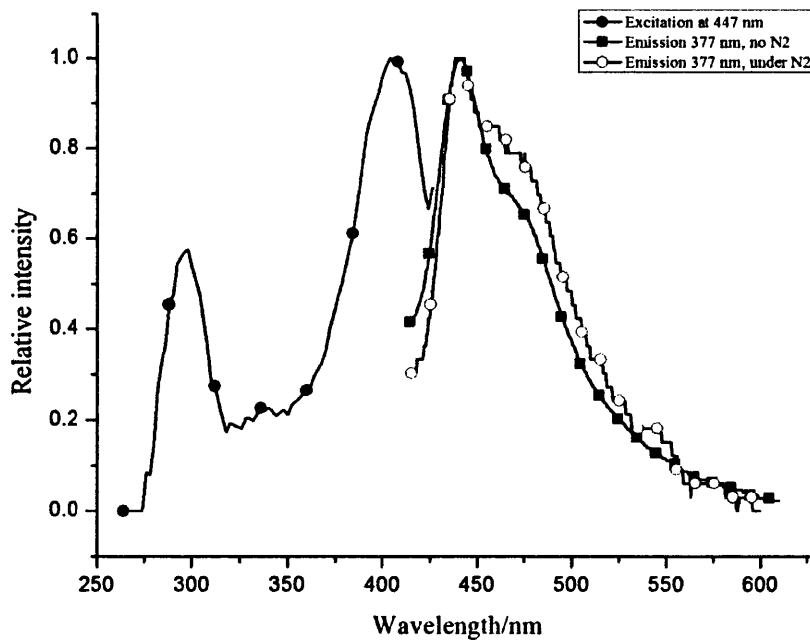


Figure 3.28: Emission and excitation spectra of 46PYRI at room temperature in EPA under N₂ (hollow figures) or in air (filled figures)

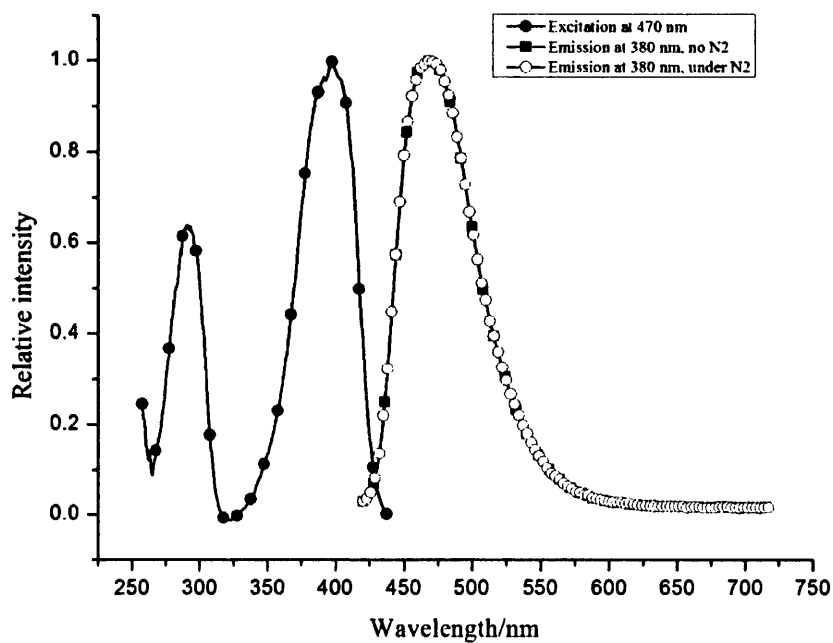


Figure 3.29: Emission and excitation spectra of DMP at room temperature in EPA under N_2 (hollow figures) or in air (filled figures)

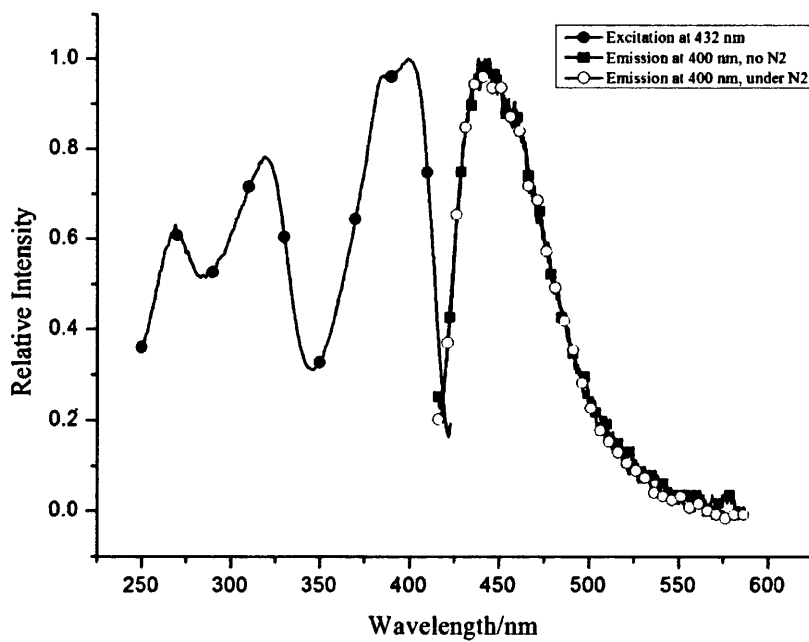


Figure 3.30: Emission and excitation spectra of ADMN at room temperature in EPA under N_2 (hollow figures) or in air (filled figures)

Compound	Emission λ_{\max} (nm) under nitrogen	Emission λ_{\max} (nm) in air
DMP	465	465
ADMN	450	450
24PYRI	430	430
46PYRI	455, 490 (shoulder)	455
NPYRI	462	462
Sodium salt of DMPA	506	506

Table 3.8: Emission maxima at room temperature in aerated and nitrogen purged EPA solution

For all the compounds except 46PYRI, the emission spectra under inert atmosphere match the ones in aerated conditions. In this solvent there is indication of phosphorescence for 46PYRI only.

For 46PYRI and 24PYRI, the 77 K measurements show phosphorescent emission. The T_1 excited state of 4-thiouridine is primarily efficiently self-quenched (the self-quenching rate constants approaching the diffusion rate constant of the products) and secondarily by a solvent effect (the lifetime in the inert solvent perfluoromethylcyclohexane (PFMCH) is 5.3 ms, compared with 3.6 μ s in CCl_4 or 0.2 μ s in water) [52]. So the absence of phosphorescence bands for 24PYRI is certainly due to a combination of these two highly efficient non-radiative processes.

24PYRI and 46PYRI present a weak fluorescence at room temperature at 430 nm and 455 nm respectively. At 77 K, this emission was not detected. When emission intensity at 77 K at a specific time after a laser pulse irradiation is plotted for different wavelengths, a curve similar to the steady-state emission is obtained. So the weakness of the fluorescence compared to the highest triplet emission ($\Phi_P = 0.1$ in glassy EPA [20]) could explain the non-detection of this peak. However, 46PYRI has a weak phosphorescence band at 490 nm, red shifted by 20 nm compared with the measurement at 77 K. The blue shift upon cooling in emission is common.

The time-resolved measurements on DMP, sodium salt of DMPA, ADMN solutions under nitrogen using the single-photon counting technique described in part 2.3.2.2 with a time limit detection of 150 ps do not provide any signal, confirming the singlet excited states of these species. As no phosphorescence is observed for 24PYRI in this medium at room temperature, it would be surprising to observe any for the other products. Therefore it is impossible to confirm through this room temperature study whether DMP and ADMN are emitting from two singlet states only or from a S_2 and a very short-lived ($\leq 1\mu\text{s}$) T_1 state.

The maximum emission wavelengths for the sodium salt of DMPA in different solvents (table 3.9) stay more or less the same. For the other rings, the substituent electronic effect also shows that the excited states should be localised on an N-heterocycle π orbital. These results confirm that the emitting transition should originate from a $^1(\pi,\pi^*)$ excited state for all the compounds studied.

	MeCN (Exci. 470 nm)	MeOH (Exci. 450 nm)	EPA (Exci. 460 nm)
Emission (nm)	506, 524	505	506, 522

Table 3.9: Maximum emission wavelength (in nm) for the sodium salt of DMPA in different solvents, with excitation wavelengths given in brackets

3.3.4 Conclusion

Because of their photoreactivity and their potential for tautomerisation and dimerisation, these N-heterocyclic dithiols are an intriguing subject for photochemical characterisation.

The absorption study gave results consistent with the literature in that there is an intense $S_0 \rightarrow S_2$ absorption in the 350-400 nm region. The solvent study has confirmed that a solvent with a higher dipole moment will stabilise the thione tautomer whereas a less polar solvent will shift the equilibrium towards the thiol and therefore promote the photo-oxidation of the latter to a disulphide, as shown in the degradation study. Theoretical studies of the relative energies of the different tautomers in gas, polar or apolar solvent will be described in the chapter 5.

Pyridine dithiols seem to present an unusual feature for a thione: an intense $S_1 \rightarrow S_0$ emission band and a less intense $S_2 \rightarrow S_0$ emission band, although there is still some doubt about the true nature of the less energetic band at 77 K, as it could originate from a short-lived T_1 state. A room temperature study in an inert solvent such as PFMCH could resolve this issue.

2,6-Dimercaptopyrazine has only one emitting band originating from an S_2 state.

At 77 K emission from 24PYRI and 46PYRI is predominantly from a T_1 excited state. In room temperature fluid solution this phosphorescence is quenched almost completely, and a much weaker fluorescence can then be detected.

Emission of NPYRI is of a fluorescent nature, the two amino groups efficiently quenching any radiative deactivation of any triplet state.

3.4 Electrochemistry

3.4.1 Introduction

Cyclic voltammetry (CV) and differential pulse voltammetry (DPV) have been carried out in MeCN with 0.1M Bu₄NPF₆ as supporting electrolyte, using Ag⁺/Ag as a reference electrode (with 0.1 M Bu₄NPF₆ and 0.01 M AgNO₃) and Pt working and counter electrodes. The solutions were purged with nitrogen for 10 minutes before measurements. The scan rates were generally 100 mV s⁻¹ for CV, 72 mV s⁻¹ for DPV. The potentials of the current peaks (E_A and E_C for anodic and cathodic peak respectively) are quoted relative to the half-wave (E_{1/2}) potential of the internal reference [77] ferrocene/ferrocenium (Fc/Fc⁺ = 0 mV), which typically was +0.85 V under the conditions employed.

For each compound studied four scans were run: a scan towards the oxidation process, a second towards the reduction process, and then two full scans, one starting towards the oxidation, the other one towards the reduction. The difference between the two scans which were run in different directions is interesting. Fig 3.31 shows this for the sodium salt of DMPA. If the scan runs through the oxidation cycle first, then on the reverse wave there is an irreversible reduction peak (fig 3.31B). This is absent in the scan which runs through the reduction cycle first (fig 3.31A). It is known that upon oxidation, thiols form disulphides [76, 78, 79], and we assign the irreversible reduction in fig 3.31B to the reduction of the disulphide formed in the initial oxidation cycle. The potentials for this disulphide reduction wave for DMP, ADMN, and sodium salt of DMPA are given in table 3.10.

Compound	DMP	ADMN	sodium salt of DMPA
E _C (V)	-0.60	-0.59	-1.35

Table 3.10: Reduction potential E_C of disulphide product formed during the previous oxidative sweep

Full scans, started towards reduction to avoid the disulphide wave, for all the compounds studied are given in figures 3.31 (pyrazine derivatives) 3.34 (pyrimidine derivatives) and 3.35 (pyridine derivatives).

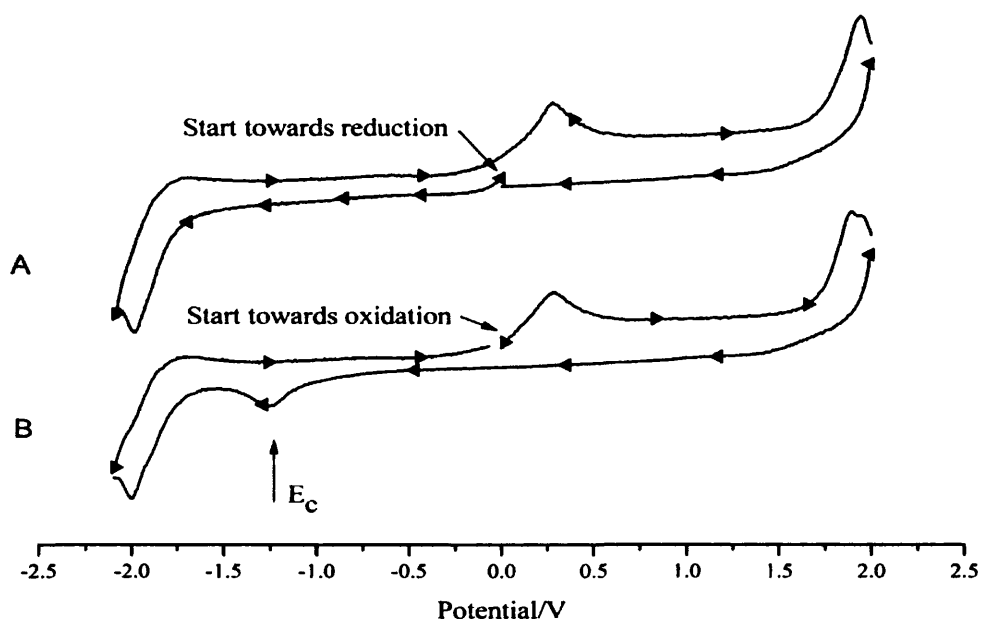


Figure 3.31: CV at 0.1 V s^{-1} for sodium salt of DMPA starting initially towards negative potential (A) or towards positive potential (B). The currents in A are shifted by $+10 \mu\text{A}$ to allow easy comparison

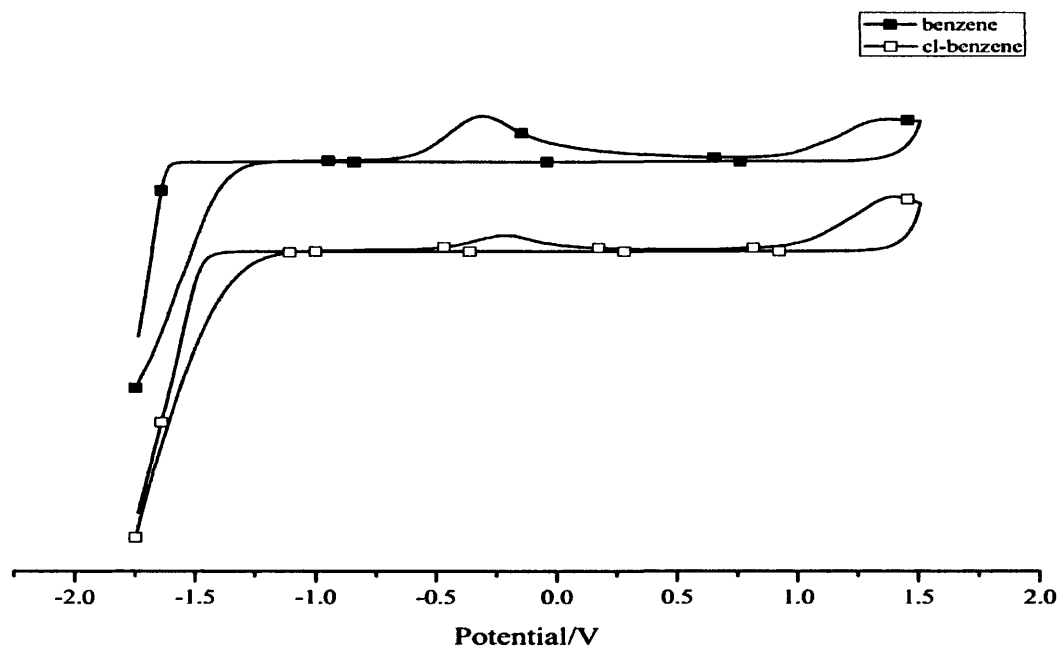


Figure 3.32: CV at 0.5 V s^{-1} for 1,5-dimercaptobenzene (filled squares) and 4-chloro-1,5-dimercaptobenzene (hollow squares) in deaerated MeCN. The 1,5-dimercaptobenzene voltammogram is shifted by $+14 \mu\text{A}$ to allow easy comparison

3.4.2 Results

Benzene derivatives

For comparison the CVs of 1,5-dimercaptobenzene (DMB) and 4-chloro-1,5-dimercaptobenzene (Cl-DMB) in MeCN were recorded (figure 3.32). They show no reduction peaks, and two oxidation waves: $E_A = -0.53$ V and 1.08 V for DMB, $E_A = -0.46$ V and 1.15 V for Cl-DMB.

Pyridine derivatives

The CVs of both compounds are similar (figure 3.33). When reduced, two peaks appear around -1.02 and -1.29 V. They also appear on the DPV. Then a wave at $E_{1/2} = -1.80$ V corresponding to a quasi-reversible process appears. On the reverse oxidation, a succession of irreversible oxidative processes occurs. The reaction potentials are collected in table 3.11.

By changing the maximum reduction potential of the CV, we noticed that the oxidation wave at -0.42 V in DMP appears only if the first reduction at -1.02 V occurs. Therefore this peak involves the species formed by reduction of DMP.

All the other peaks appear if we use either only positive or only negative potentials for the scans, so they seem to be independent of oxidised or reduced by-products.

Pyrimidine derivatives

The CVs of the pyrimidine derivatives show only waves corresponding to irreversible processes (figure 3.34).

As expected 46PYRI and 24PYRI have similar voltammograms, showing low intensity and broad oxidation peaks at 0.19 V and 0.11 V respectively (values taken from the top of the slope), and reduction peaks at -1.27 V and -1.52 V respectively. The DPVs of 46PYRI and 24 PYRI show only one peak around -1.3 V and -1.6 V respectively.

NPYRI gives three oxidation peaks, at 0.62 V, 0.00 V and -0.43 V. The amino group is an electron donating substituent and therefore should facilitate oxidation. As aniline shows an oxidation of the amino-group at +0.70 V (*vs* Ag/AgCl) [80], we attribute the two other peaks to oxidation processes involving the amino-groups. NPYRI shows a reduction peak at -1.65 V.

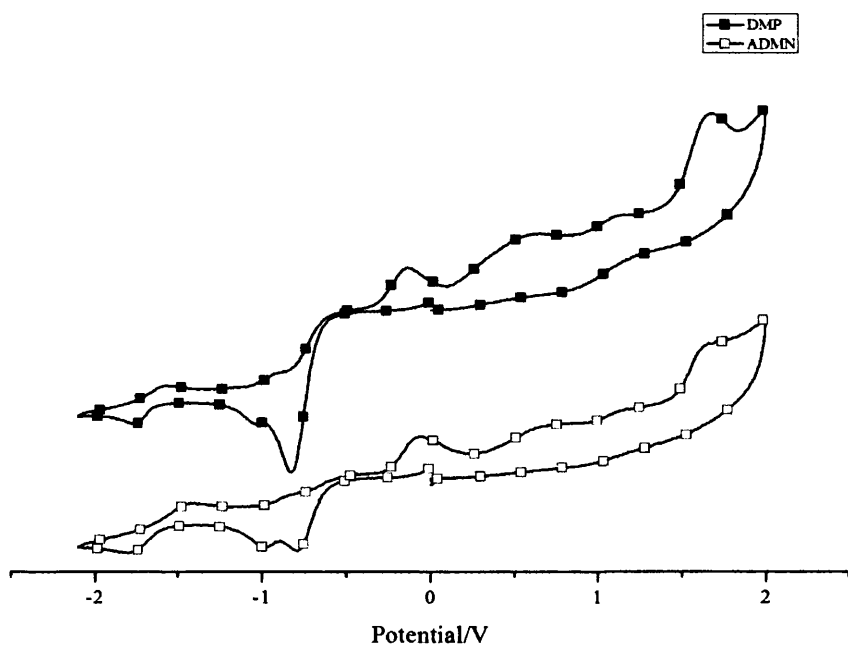


Figure 3.33: CV at 0.1 V s^{-1} for DMP and ADMN in deaerated MeCN; DMP voltammogram is shifted by $+20 \mu\text{A}$ to allow comparison

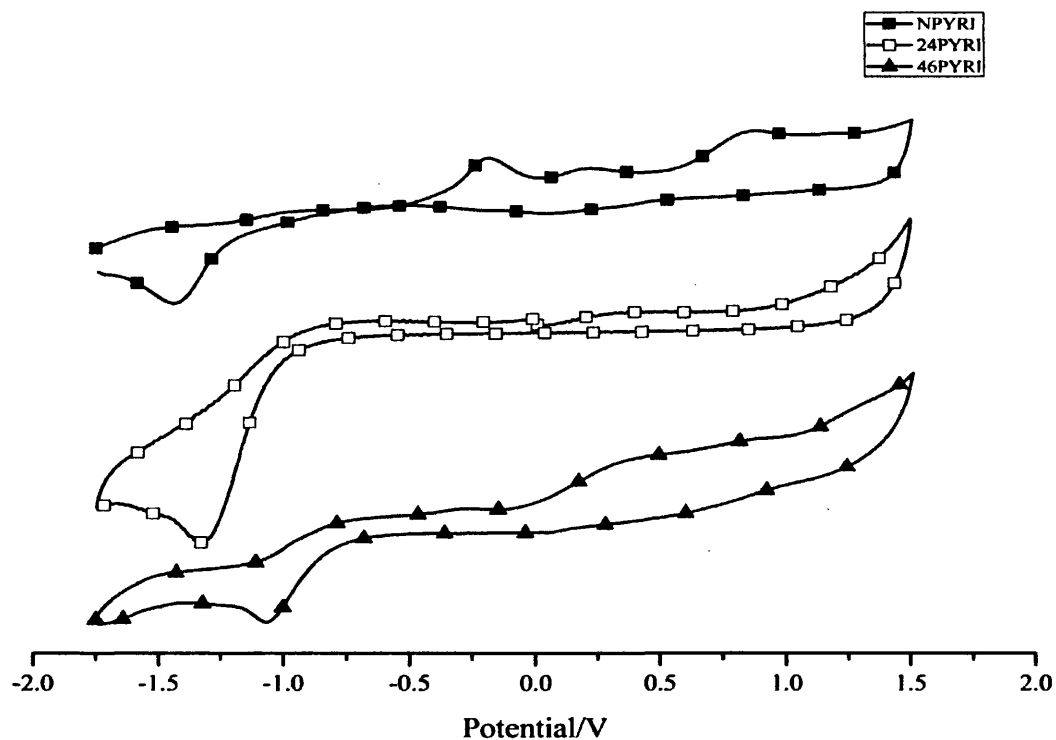


Figure 3.34: CV at 0.1 V s^{-1} for 24PYRI (hollow squares), 46PYRI (triangles) and NPYRI (filled squares). The currents of NPYRI and 46PYRI are shifted by $+6 \mu\text{A}$ and $+10 \mu\text{A}$ to allow comparison on the same graphic

Pyrazine derivatives

Deprotonated DMPA has been studied. Interestingly, and in contrast to the other compounds examined, there are no reduction peaks in the -1 V to -1.8 V range. We have an oxidation peak at 0.03 V and one at 1.65 V. When only positive potentials were used for running the CV, both peaks are still present. Therefore the oxidative processes responsible for these do not involve any potential reduced species created during the reductive sweep.

Product	DMP	ADMN	24PYRI	46PYRI	NPYRI(*)	DMPA(d)
E _A (V)	1.45	1.38	0.11	0.19	0.62	1.65
	0.90	0.83			0	0.03
	0.35	0.41			-0.43	
	-0.42	-0.36				
E _C (V)	1.20	0.70	-1.52	-1.27	-1.65	-2.26
	0.72	-1.02	-2.12	-2.01		
	-1.02	-1.23				
	-1.29	-2.00				
	-1.95					

Table 3.11: Cathodic potential (E_C) and anodic potential (E_A) measured in MeCN referred to Fc/Fc⁺.

*: NPYRI has been measured between -1.75 V and +1.5 V only

3.4.3 Interpretation and conclusion

All the compounds studied present irreversible CV waves in MeCN. When a thiol group is present, disulphide formation takes place upon oxidation, and this can be reduced back.

The reduction peak potentials of the pyrimidine derivatives show that the easiest to reduce is 46PYRI then 24PYRI and NPYRI. The two electron donating amino groups are responsible for the shift of NPYRI towards more negative reduction potential. The difference between 24PYRI and 46PYRI is probably due to the greater extent of the tautomerisation of the former, which renders it harder to reduce.

The two reduction peaks around -1.02 V and -1.19 V for DMP and ADMN could be the reduction of the thiol substituent and then the thione, the latter being a bit more electron rich than the thiol. The oxidation peak at -0.36 V (ADMN) or -0.42 V (DMP) is attributed to the oxidation of this reduced thiol/thione. The oxidation is a bit harder for ADMN due to the electron-withdrawing effect of the carboxylic acid group. The oxidation peaks at 1.45 V and 0.9 V for DMP, 1.38 V and 0.83 V for ADMN are attributed to the oxidation of the nitrogen of the pyridine ring. This attribution has been suggested by the study of adsorbed pyridine or nicotinic acid on a Pt surface [83]. The oxidation potentials of ADMN and DMP are shifted to higher potential than those of pyridine and nicotinic acid due to the presence of the two thiol groups.

3.5 Conclusion

Two new compounds have been synthesised and characterised: 2,6-dimercaptopyridine and 2,6-dimercaptopyrimidine. The relatively easy reaction of NaSH with the halogeno-derivative in boiling DMF allowed the production of the majority of desired compounds with reasonable yield.

The crystal structure of 4,6-dimercaptopyrimidine has been determined.

The compounds described here can adopt at least two tautomeric forms: a thiol or thione. The relative concentrations of these tautomers depends on the medium: a more polar solvent promotes the thione form, whereas an apolar solvent promotes the thiol form.

Dimercaptopyrimidine and dimercaptopyridine derivatives have been shown to emit from singlet states, with no evidence of phosphorescence detected, and this lack of phosphorescence is believed to be due to the presence of the thiol groups. An interesting feature discovered during this study is the emission from the S_1 state at 77 K for both pyridine derivatives.

Both dimercaptopyrimidines emit principally from the T_1 state at 77 K, and show weak singlet emission in room temperature fluid solution; 46PYRI shows weak room temperature phosphorescence. However when amino-groups are present on the ring as in NPYRI, they promote a rapid non-radiative deactivation through vibrations and therefore only a weak emission from a singlet state is detectable.

These compounds were chosen and synthesised for use as ligands in gold complexes as will be discussed in the following chapters. However, they may have uses in a number of different applications: surface enhanced spectroscopy, and as ligands for other metals such as Rh, Ru, Pd, Pt, for example. It is also anticipated that they will show some biological activity, and their possible antifungal activity may well be worth investigating [81, 82].

References for Chapter 3

- [1] Koppel H.C., Springer R.H., Robins R.K., Cheng C.C., *J. Org. Chem.* 26 (1961) 792-803
- [2] Boarland M., McOmie J. F. W., *Chem. Soc.* (1951) 1218-1221
- [3] Gabriel J., Colman H., *Chem Ber.* 32 (1899) 2921
- [4] Krowicky K., *Polish J. Chem.* 53 (1979) 503-506
- [5] Krowicky K., *Polish J. Chem.* 50 (1976) 1785-1789
- [6] Vogtle F., Effler A.H., *Chem. Ber.* 102 (1969) 3071
- [7] Krowicky K., Nantka-Namirsky P., *Polish J. Chem.* 51 (1977) 1785-1789
- [8] Krowicky K., *Polish J. Chem.* 52 (1978) 2039-2042
- [9] Puszko A., Talik Z., *Polish. J. Chem.* 65 (1991) 377-380
- [10] Bottino F., Cosentino S., Cunsolo S., Pappalardo S., *J Heterocycl. Chem.* 18 (1981) 199-200
- [11] Barlin G.B, Brown D.J, Cronin B.J., Ngu M., *Aust. J. Chem.* 39 (1986) 69-75
- [12] Papavassiliou G.C., Yiannopoulos S.Y., Zambounis J.S., *Chem. Scripta* 27 (1987) 265-268
- [13] Stanovnik B., Tisler M., Katritzky A.R., Denisko O.V., *Adv. Hetero. Chem.* 91 (2006) 1-134
- [14] Beak P., Fry F.S., Lee J., Steele F., *J. Am. Chem. Soc.* 98 (1976) 171-179
- [15] Nowak M. J., Lapinski L., Fulara J., Les A., Adamowicz L., *J. Phys. Chem.* 95 (1991) 2404-2411
- [16] Lapinsky L., Nowak M.J., Kolos R., Kwiatkowski J.S., Leszczyński J., *Spectro.Chim. Acta Part A* 54 (1998) 685-693
- [17] Khvorostov A., Lapinski L., Rostkowska H., Nowak M.J., *J. Photochem. Photobiol. A : Chem.* 184 (2006) 322-330
- [18] Moran D., Sukcharoenphon K., Puchta R., Schaefer III H. F., Schleyer P., Hoff C. D., *J. Org. Chem.* 67 (2002) 9061-9069
- [19] Lapinski L., Rostkowska H., Nowak M. J., Leś A., Adamowicz L., *J. Phys. Chem.* 94 (1990) 7406-7414
- [20] Alam M. M., Fujitsuka M., Watanabe A., Ito O., *J. Chem. Soc., Perkin Trans.* (1998) 817-824
- [21] Kwiatkowski J. S., Leszczyński J., *J. Mol. Struct.* 376 (1996) 325-342
- [22] Prusinowska D., Lapinski L., Nowak M. J., Adamowicz L., *Spectrochim. Acta A* 51 (1995) 1809-1826

- [23] Lapinski L., Nowak M. J., Kwiatkowski J. S., Leszczynski J., *J. Phys. Chem. A* 103 (1999) 280-288
- [24] Fu A., Li H., Du D., *J. Mol. Structure: THEOCHEM* 767 (2006) 51-60
- [25] Beak P., Covington J.B., Smith S.G., White J.M., Zeiger J.M., *J. Org. Chem.* 45 (1980) 1354-1362
- [26] Beak P., Covington J.B., White W.M., *J. Org. Chem.* 45 (1980) 1347-1353
- [27] Aveline B. M., Redmond R.W., *J. Am. Chem. Soc.* 121 (1999) 9977-9985
- [28] Stoyanov S., Petkov I., Antonov L., Stoyanov T., *Can. J. Chem.* 68 (1990) 1482-1490
- [29] Beak P., Covington J.B., Smith S.G., *J. Am. Chem. Soc.* 98 (1976) 8284
- [30] Beak P., *Acc. Chem. Res.* 10 (1977) 186-192
- [31] Xanthopoulou M.N., Hadjikakou S.K., Hadjiliadis N., Kubicki M., Karkabounas S., Charalabopoulos K., Kourkoumelis N., Bakas T., *J. Organometallic Chem.* 691 (2006) 1780-1789
- [32] Lobana T.S., Paul S., *Trans. Metal Chem.* 21 (1996) 300-304
- [33] Kennedy B.P., Lever A.B.P., *Can. J. Chem.* 50 (1972) 3488-3507
- [34] Ogata K, Toyota A, *J. Organometallic Chem.* 692 (2007) 4139-4146
- [35] Garcia-Vasquez J.A., Romero J., *J. Chem. Soc., Dalton Trans.* (2000) 559-567
- [36] Dwivedi J.S., Agarwala U., *Ind. J. Chem.* 10 (1972) 652-656
- [37] Cookson P.D., Tiekink E.R.T., *J. Chem. Soc. Dalton Trans.* (1993) 259-263
- [38] Harker C.S.W., Tiekink E.R.T., Whitehouse M.W., *Inorganica Chim. Acta* 181 (1991) 23-30
- [39] Stocco G., Gattuso F., Isab A.A., Shaw III C.F., *Inorg. Chim. Acta* 209 (1993) 129-135
- [40] Beak Lee Y.A., Eisenberg R., *J. Am. Chem. Soc.* 125 (2003) 7778-7779
- [41] Ramamurthy V., Steer R. P., *Acc. Chem. Res.* 21 (1988) 380-387
- [42] Maciejewski A., Steer R. P., *Chem. Rev.* 93 (1993) 67-98
- [43] Ramamurthy V., in "Organic Photochemistry Vol. 7", (Ed: Dekker J.)chapter 4, p.231-338, 1985
- [44] Gilbert A., Baggott J., "Essentials of Molecular Photochemistry", Blackwell Science Ltd, 1991
- [45] Kozlowski J., Maciejewski A., Szymanski J. M., *J. Chem. Soc., Faraday Trans.* 88 (1992) 557
- [46] Lipsett M.N., *J. Biol. Chem.* 240 (1965) 3975-3978

- [47] Yaniv M., Barrel B.G., *Nature* 222 (1969) 278-279
- [48] Pownall H.J., Schaffer A.M., Becker R.S., Mantulin W.W., *Photochem. Photobiol.* 27 (1978) 625-628
- [49] Taherian M.R., Maki A.H., *Chem. Phys.* 55 (1981) 85
- [50] Psoda A., Shugar D., *Acta Biochim. Pol.* 26 (1979) 55-72
- [51] Lancelot G., *Mol. Phys.* 31 (1976) 241-254
- [52] Taras-Goślińska K., Wenda G., Skalski B., Maciejewski A., Burdzinski G., Karolczak J., *Photochem. Photobiol.* 75 (2002) 448-456
- [53] Taras-Goślińska K., Wenda G., Skalski B., Maciejewski A., Burdzinski G., *J. Photochem. Photobiol. A : Chem.* 168 (2004) 226-233
- [54] Wenska G., Taras-Goślińska K., Skalski B., Maciejewski A., Burdziński G., Karolczak J., *J. Photochem. Photobiol. A : Chem.* 181 (2006) 12-18
- [55] Khvorostov A., Lapinski L., Rostkowska H., Nowak M.J., *Photochem. Photobiol.* 81 (2005) 1205-1211
- [56] Albert A., in “*Selective Toxicity: The Physico-Chemical Basis of Therapy*” 7th edition, (Ed: Chapman and Hall), London, 1985
- [57] Arnoldi A., Drasso S., Meinardi G., Merlini L., *Eur. J. Med. Chem.* 23 (1978) 49
- [58] Shaw E., Bernstein J., Loser K., Lott W. A., *J. Am. Chem. Soc.* 72 (1950) 4362
- [59] Kontoghiorghes G. J., Piga A., Hoffbrand A. V., *Hematol. Oncol.* 4 (1986) 195
- [60] Adam W., Cadet J., Dall’Acqua F., Ramaiah D., Saha-Moller C. R., *Angew. Chem.* 107 (1995) 91-97
- [61] Shaw III C.F, Beery A., Stocco G.C., *Inorg. Chim. Acta* 123 (1986) 213-216
- [62] Pinheiro L.S., Temperini M.L.A., *Surface Science* 601 (2007) 1836–1843
- [63] Grimee R., Gelbcke M., *Bull. Soc. Chim. Belg.* 92 (1983) 39-47
- [64] Shefter E., Maunter H.G., *J. Am. Chem. Soc.* 89 (1967) 1249-1253
- [65] Schefter E., Maunter H.G., *J. Org. Chem.* (1962) 1249-1253
- [66] Leszczynski J., Lammertsma K., *J. Phys. Chem.* 95 (1991) 3128-3132
- [67] Lautié A., Hervieu J., Belloc J., *Spectrochimica Acta* (1983) 39A, 4, 367-372
- [68] Perez-Torrente J., Casado M., Ciriano M., Lahoz F., Oro L., *Inorg. Chem.* 35 (1996) 1782-1791
- [69] Rostkowska H., Szczepaniak K., Nowak M.J., Leszczynski J., KuBulat K., Person W.B., *J. Am. Chem. Soc.* 112 (1990) 2147-2160
- [70] Carlsson J., Drevin H., *J. Biochem.* 173 (1978) 723

- [71]Lapinski L., Nowak M.J., Fulara J., Les A., Adamowicz L., *J. Phys. Chem.* 96 (1992) 6250-6254
- [72]Leszczyński J., Lammertsma K., *J. Phys. Chem.* 95 (1991) 3128
- [73]Beak P., Covington J.B., *J. Am. Chem. Soc.* 100 (1978) 3961-3962
- [74]Shukla M. K., Leszczynski J., *J. Phys. Chem. A* 108 (2004) 10367-10375
- [75]Schoenberg A., Mostafa A., *J. Chem. Soc.* (1943) 275
- [76]Goyal R. N., Singh U. P., Abdullah A.A., *Bioelectrochemistry* 67 (2005) 7-13
- [77]Gagne R., Koval C.A., Lisensky G.C., *Inorg. Chem.* 19 (1980) 2854-2855
- [78]Chen J., Jiang T., Wei G., Mohamed A.A., Homrighausen C., Krause Bauer J. A., Bruce A.E., Bruce R.M., *J. Am. Chem. Soc.* 121 (1999) 9225-9226
- [79]Jiang T., Wei G., Turmel C., Bruce A.E., Bruce R.M., *Metal Based Drugs* 1 (1994) 419-431
- [80]Mabbott G. A., *J. Chem. Educ.* 60 (1983) 697-701
- [81]Kier L.B., *J. Pharma. Sci.* 70 (1981) 930-933
- [82]Wang X., Yang N., Wan Q., *Electrochimica Acta* 52 (2006) 361-368
- [83]Stern D. A., Laguren-Davidson L., Frank D. G., Cui J. Y., Lin C., Lu F., Salaita G.N., Walton N., Zapfen D.C., Hubbard A.T., *J. Am. Chem. Soc.* 111 (1989) 877-891

Chapter 4

***Syntheses, photochemistry and electrochemistry
of neutral binuclear gold complexes with phosphine and
bridging N-heterocyclic dithiolate ligands***

4.1 Introduction

As seen in chapter 1 of this thesis, derivatives of gold(I) are numerous and may contain a wide range of σ -donor ligands, such as derivatives of acetylene, pyridine, thiols, etc... We will concentrate in this introduction only on known gold phosphine thiolate complexes where the thiolate has a N-heterocycle substituent. Table 4.1 presents a synopsis of these compounds as well as their photoluminescent properties when available. These compounds have mainly been synthesized to study the effect of aurophilicity, hydrogen bonding and ligand variations on their crystal structure, or for medical purposes. Some of them were recently tested for anti-cancer activities; the results were poorer than those for their platinum analogues [1]. But this class of compounds presents interesting anti-microbial activity, as demonstrated by the study of Nomiya [2, 3]. A few luminescence studies have been performed.

Gold complexes present a rich photoluminescence, originating from various transition types, mainly LMCT, MC, MLCT. The electronic properties of the ligands and variation in aurophilicity can be used to tune the emission wavelength. Due to its high relative atomic mass, gold enhances spin-orbit coupling and therefore can induce phosphorescence.

Gold(I) acts a Lewis acid and has in particular an affinity for nitrogen and atoms of the chalcogen group (except oxygen). This is outlined in several works on $[\text{Au}_2(\mu\text{-S}^{\wedge}\text{N})(\mu\text{-P}^{\wedge}\text{P})]$, in which the bridging phosphine is linked to the thiolate through both Au-N and Au-S bonds (figure 4.1) [4, 5, 6].

The strategy for this study was to use the N-heterocycles studied in chapter 3 as bridging ligands to form annular, or open ring, binuclear gold(I) complexes. The van der Waals radius for gold being 170 pm, it is accepted that aurophilicity can appear when the gold(I)-gold(I) distance is shorter than 340 pm. The 1,3 relative positions of the two thiol groups should put an inherently longer distance between the two gold atoms. By eliminating possible gold-gold interaction, stabilisation of the $6p_{\sigma}$ orbital and destabilisation of $5d_{\sigma^*}$ through aurophilicity are not possible and we hope to get an emission with a high energy (short wavelength). The rigidity of the thiolate ligands, and the ring structure should reduce the vibrational non-radiative decay of the excited state and therefore enhance the photoluminescence. Luminescence of

gold phosphine thiolates is often attributed to a MLCT or metal-metal to ligand charge transfer (MMLCT) from the gold to the thiolate, with a possible contribution of an intraligand charge transfer or a metal-centred transition. The N-heterocycle ligands we used can be functionalised to change the electron density on the sulphur and therefore tune the luminescence.

A new series of gold phosphine dithiolates is presented and their photoluminescence properties studied. For each thiolate, the influence on the luminescence of the existence and length of the hydrocarbon chain between the two phosphines (between 1 and 4 carbon atoms) will be shown, as well as the influence of the nature of the thiolate for complexes of the same phosphine. Finally an electrochemical study has been carried out and we will conclude on their potential use as the emitting dopant in OLEDs.

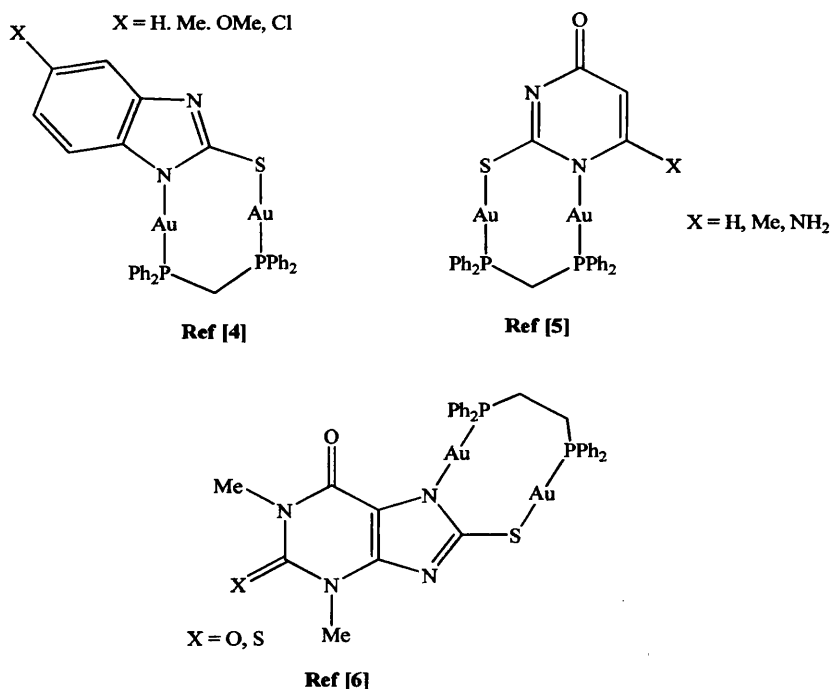


Figure 4.1: $[\text{Au}_2(\mu\text{-S}^{\wedge}\text{N})(\mu\text{-P}^{\wedge}\text{P})]$ examples

Thiol	Gold precursor	Emission (λ_{\max} , nm)	
Thioguanine	[AuCl(PPh ₃)], [AuCl(PEt ₃)]	(-)	[7]
2,6-Dithioxantine	[AuCl(PPh ₃)], [AuCl(PEt ₃)]	(-)	[7]
Benzimidazolethiol	[Au ₂ (CF ₃ CO ₂) ₂ (dppm)]	Neutral: 485-535	[4]
2-Mercaptopyridine	[AuCl(PPh ₃)], [AuCl(PEt ₃)], [AuCl(PCy ₃)]	(-)	[8]
2-Mercaptopyridine	[Au ₂ Cl ₂ (dppe)], [Au ₂ Cl ₂ (dppp)], [Au ₂ Cl ₂ (dppb)], [Au ₂ Cl ₂ (dppet)]	(-)	[9]
2-Mercaptopyridine	[Au ₂ Cl ₂ (dppf)]	(-)	[10]
2-Mercaptopyridine	[AuCl(P(<i>p</i> -CF ₃ C ₆ H ₄) ₃)], [AuCl(PPh ₃)]	(-)	[11]
2-Mercaptopyridine	[Au ₂ Cl ₂ (dppm)], [Au ₂ Cl ₂ (dpph)]	dppm: 496 & 660 dpph: 482	[12]
2-Mercaptopyridine	[Au ₂ Cl ₂ (dppm)], [Au ₂ Cl ₂ (dppe)]		[13]
2-Mercaptopyridine	[AuCl(PPh ₂ (Py))]	77 K (glass): 432 77 K (solid): 544 Solution: 437, 520	[14]
2-Mercaptopyridine	[AuCl(TPA)]	(-)	[1] [15]
(2-Pyridyl)methanethiol	[Au ₂ Cl ₂ (dppe)], [Au ₂ Cl ₂ (dppp)], [Au ₂ Cl ₂ (dppb)], [Au ₂ Cl ₂ (dppet)]	(-)	[9]
2-(2-Pyridyl)ethanethiol	[Au ₂ Cl ₂ (dppe)], [Au ₂ Cl ₂ (dppp)], [Au ₂ Cl ₂ (dppb)], [Au ₂ Cl ₂ (dppet)]	(-)	[9]
8-Mercaptotheophylline (purine derivative)	[AuCl(PPh ₃)], [Au ₂ Cl ₂ (dppm)]	(-)	[6]
8-Mercaptothiothylline (purine derivative)	[AuCl(PPh ₃)], [Au ₂ Br ₂ (dppe)]	(-)	[6]
2-Amino-5-mercapto- 1,3,4-thiadiazole	[AuCl(PPh ₃)], [AuCl(PMe ₃)] [AuCl(P(CH ₂ CH ₂ CN) ₃)] [Au ₂ Cl ₂ (dppm)], [Au ₂ Cl ₂ (dppe)], [Au ₂ Cl ₂ (dppet)], [Au ₂ Cl ₂ (dpph)]	{P(CH ₂ CH ₂ CN) ₃ }: 523 (dpph): 548	[16] [17]

(Table 4.1: List of known gold phosphine compounds with a N-heterocycle thiolate.

to be continued next page)

1,3,4-Thiadiazole-2,5-dithiol	[AuCl(PPh ₃)], [AuCl(PMe ₃)], [AuCl(PPh ₂ Py)], [Au ₂ Cl ₂ (dppf)], [Au ₂ Cl ₂ (dpph)]	(-)	[18]
6-Amino-2-mercaptobenzothiazole	[AuCl(P(CH ₂ CH ₂ CN) ₃)], [Au ₂ Cl ₂ (dpph)]	{P(CH ₂ CH ₂ CN) ₃ }: 545 (dpph): 560	[17]
Thiouracil	[Au ₂ Cl ₂ (dppm)]	483 (tribochromism)	[20]
2,4-Dimercaptopyrimidine	[AuCl(PPh ₃)]	(-)	[7]
4-Amino-2-mercaptopyrimidine	[AuCl(L)], with L = PMe ₃ , PEt ₃ , PPh ₃ , PPh ₂ Py [Au ₂ Cl ₂ (dppm)], [Au ₂ Cl ₂ (dppf)]	(-)	[21]
2-Mercaptopyrimidine	[AuCl(PPh ₃)], [AuCl(PEt ₃)], [AuCl(Cy ₃)]	(-)	[8]
2-Mercaptopyrimidine	(TPA)AuCl	(-)	[1] [15]
4,6-Dimethyl-2-mercaptopyrimidine	[AuCl(PPh ₃)]	(-)	[22]
Quinoline-8-thiol	[AuCl(PPh ₃)]	477	[23]

Table 4.1: List of known gold phosphine compounds with a N-heterocycle thiolate.

4.2 Syntheses of binuclear gold(I) phosphine thiolate complexes

First will be described the synthesis of the precursor gold complexes. Then the syntheses and characterisation of the binuclear gold(I) phosphine thiolate complexes will be presented. The crystal structures obtained for two compounds (**4a** and **4f**) will be described.

DCM, acetone, diethyl ether, DMF were purchased from Aldrich and used without further purification. Water was distilled three times before use.

4.2.1 Introduction

The classic procedure to obtain a gold(I) phosphine thiolate is to deprotonate the thiol with a base (NaOMe [24], KOH [25], triethylamine [26]) and then mix the resulting solution with a chlorogold(I) phosphine complex.

4.2.2 Synthesis of precursors

4.2.2.1 Dithiol ligands

2,6-Dimercaptopyridine, 2,6-dimercaptopyridine, 2,6-dimercaptopyridine were synthesized according to the procedures described in chapter 3. 1,3-Dimercaptobenzene, 4-Chloro-1,3-dimercaptobenzene, and 5,6-Diamino-2,4-dimercaptopyrimidine were purchased from Sigma Aldrich and used as received.

4.2.2.2: Syntheses of the gold(I) precursors used

The following chlorogold(I) phosphine complexes have been used: [AuCl(PPh₃)], [Au₂Cl₂(dppm)], [Au₂Cl₂(dppe)], [Au₂Cl₂(dppp)] and [Au₂Cl₂(dppb)]. These compounds have been synthesized according to the literature procedure [7,27]. The ³¹P and ¹H NMR spectra were recorded in CDCl₃ and the data are presented in table 4.2. The results are in accordance with the literature [28].

Product	¹ H NMR	³¹ P NMR
[AuCl(PPh ₃)]	7.4-7.5 (m)	33.3
[Au ₂ Cl ₂ (dppb)]	1.7 (br, 4H, CH ₂ -CH ₂ -CH ₂), 2.3 (br, 4H, CH ₂ -CH ₂ -P) 7.4-7.5 (m, 20H, phenyl ring)	30.7
[Au ₂ Cl ₂ (dppp)]	1.8 (br, 2H, CH ₂ -CH ₂ -CH ₂), 2.7 (br, 4H, CH ₂ -CH ₂ -P), 7.4-7.5 (m, 20H, phenyl ring)	26.9
[Au ₂ Cl ₂ (dppe)]	2.6 (b, 4H, CH ₂ -CH ₂ -P), 7.4 (m, 12H), 7.5 (m, 8H, phenyl ring)	31.9
[Au ₂ Cl ₂ (dppm)]	3.5 (t, 2H, P-CH ₂ -P), 7.35 (q, 8H), 7.45 (t, 4H, phenyl ring) 7.55 (t, 8H, phenyl ring)	24.0

Table 4.2: ¹H and ³¹P NMR peaks for the chlorogold(I) phosphine complexes used

4.2.2.3 Other gold(I) precursors synthesised

1,3-Bis(diphenylphosphino)benzene (bdp) has been synthesized according to the literature [29]. It has been used to give the new gold complex 1,3-bis(chlorogolddiphenylphosphino)benzene by the following procedure.

To a cold water solution (10 mL) of thiodiethanol (1 mL), a aqueous solution (10 mL) of KAuCl_4 (177 mg, 0.43 mmol) was added dropwise. When the solution was clear, a EtOH:acetone (1:1) solution of bdp (97 mg, 0.215 mmol) was added and the mixture stirred for 6 hours. The solution was warmed to room temperature, 100 mL water was added and the product was filtered off, washed with water and diethyl ether. The white product (129 mg, 0.14 mmol, yield 65%) obtained was dried under vacuum.

$^1\text{H NMR}$: single broad multiplet at 7.50 ppm.

$^{31}\text{P NMR}$: 33.2

bdp has a phosphorus NMR peak at -5.3 ppm. The shift to 33.2 ppm in the spectrum of the gold derivative (a value similar to $\delta(^{31}\text{P})$ of PPh_3AuCl) confirmed the gold connection to the phosphine.

Other attempts to produce bis(chlorogolddiphenylphosphino)benzene derivatives are described in appendix B.

4.2.3 Syntheses of gold(I) complexes

The gold(I) complexes synthesised belong to the general class of binuclear gold phosphine thiolates. Only one new mononuclear gold(I) complex has been synthesised and will be described first. After this the synthesis of binuclear gold(I) complexes will be described. The syntheses are presented according to the nature of the phosphine (bidentate or monodentate). In all the syntheses the quantities of reagents were such that the Au:S ratio was 1:1.

4.2.3.1 Formation of mononuclear gold(I) complex triphenylphosphine(2,6-dithiolato-pyridine)gold(I) (4f)

4.2.3.1.1 Synthesis

Under an inert atmosphere of nitrogen, a solution of 2,6-Dimercaptopyridine (10^{-3} mol) and MeONa (10^{-3} mol) dissolved in MeOH (10 mL) was mixed with a DCM (10 mL) solution of $[\text{AuCl}(\text{PPh}_3)]$ (10^{-3} mol) and allowed to react for 2 h in a flask protected from light. The resulting suspension was filtered through diatomaceous earth; the solvent was removed by evaporation under reduced pressure and the resulting yellow powder dried overnight under vacuum. Small dark-red crystals of **4f** were obtained by slow diffusion of diethyl ether into a concentrated DCM solution of the powder.

4.2.3.1.2 Analyses

Due to the small amount of material obtained (10 to 15 crystals), characterisation has been limited to the crystal structure.

4.2.3.1.3 Crystal structure of $[\text{Au}(\text{S}_2\text{C}_5\text{H}_4\text{N})(\text{PPh}_3)]$ (4f)

Fine yellow crystals of **4f** were obtained by slow diffusion of diethyl ether into a DCM solution of **4f**. The crystal structure is shown figure 4.1; crystal data and refinement parameters are reported in table 4.3. Relevant distances and angles are reported in table 4.4.

The product crystallises in a triclinic space group and each unit cell contains two molecules. They face each other head to tail, linked to each other by hydrogen bonding between the thione of one and the protonated nitrogen of the other (see figure 4.1(A)). The distance between the pyridine ring of one molecule and one of the phenyl groups of the other is about 380 pm. This distance could be short enough to allow π - π stacking [30] (see figure 4.2(B)), but as in similar compounds [11] the corresponding distance is shorter by 58 pm it would seem that the disposition of the two rings is influenced by steric effects. The distance between the gold atoms of the molecules forming the hydrogen bonded dimer is 768.1 pm, and the shortest gold-gold distance between gold atoms belonging to different dimers is 560.5 pm. As all of these distances are greater than twice the van der Waals radius of gold, there is no

gold-gold interaction in this crystal structure. Generally gold(I) has a linear coordination geometry but this can be disturbed by other interactions such as aurophilicity. In triphenylphosphine(2-mercaptopyridine)gold(I) (GTT), the coordination geometry is not linear due to a N-Au interaction [8], but this is prevented in our system by the protonation of the nitrogen of the heterocycle. The absence of a gold-gold interaction is further supported by the quasi linearity found for the gold(I) coordination.

The Au-S distance (231.9 pm) and Au-P distance (226.5 pm) are similar to those found in related compounds [8, 24, 31, 32, 33, 34]. For the non-coordinate sulphur, the C-S distance is 170.6 pm, similar to that for a thione, whereas the longer C-S distance (175 pm) for the other sulphur atom indicates that this atom is coordinated to the gold(I) in its thiolate form. The dihedral angle between the pyridine ring and the triphenylphosphine moiety of **4f** (35.64°) is larger than for GTT (14.0°) [8]. In GTT, a weak N-Au interaction has been discovered. As expected for this protonated pyridine ring, the long Au-N distance of 333.5 pm is greater than the sum of the van der Waals radii for Au-N (325 pm) [35] and therefore no interaction is possible between these atoms.

Distance (pm)	Angle ($^\circ$)
Au-S: 231.9(3)	P-Au-S: 178.5(1)
Au-P: 226.5(2)	Au-S-C 104.0(1)
Au-N: 333.5(4)	<u>Dihedral</u>
C-S: 175.0(2)	Au-S-C-N: 35.6(2)
C=S: 170.6(2)	
S \cdots HN: 251.0(2) (Hydrogen bond)	

Table 4.3: Selected distances and angles obtained from the crystal structure of **4f**

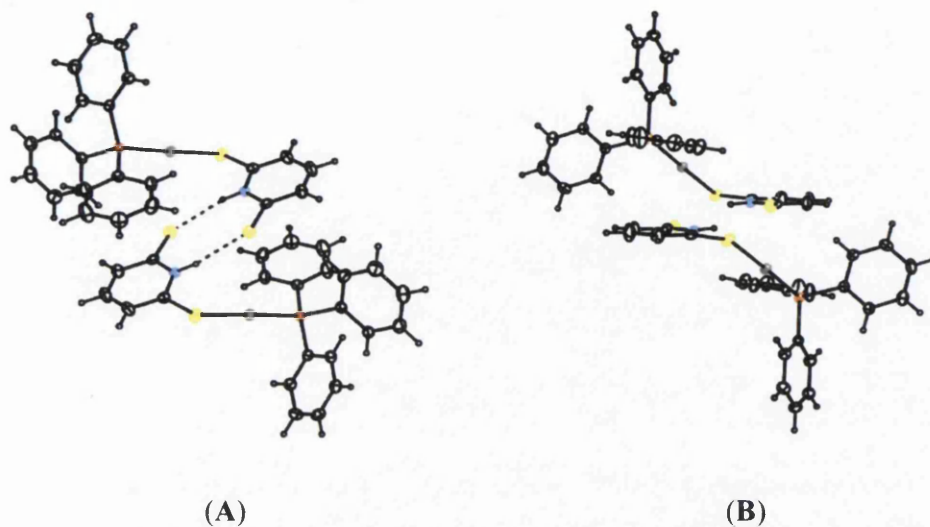


Figure 4.1: Representation of intermolecular hydrogen-bonds for **4f** dimer (A) and ring stacking for **4f** dimer (B). Sulphur atoms are in yellow, phosphorus in orange, nitrogen in blue and gold in grey.

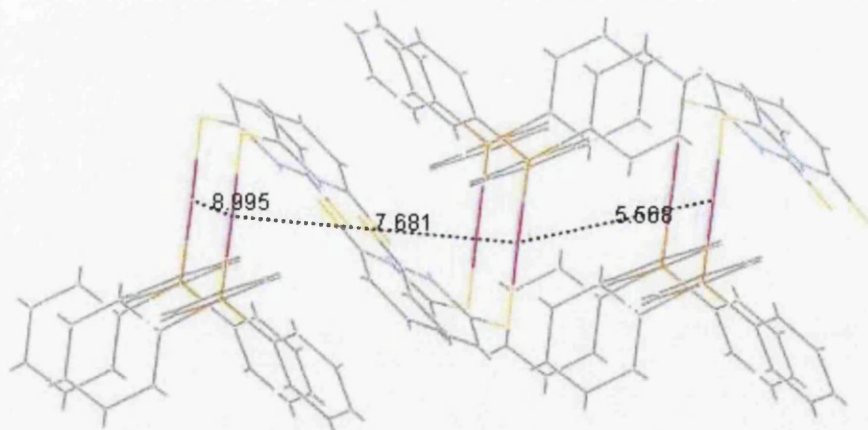


Figure 4.2: Representation of the different gold-gold distances in **4f**. Sulphur atoms are in yellow, phosphorus in orange, nitrogen in blue and gold in purple

Empirical formula	C ₂₃ H ₁₉ AuNPS ₂
Formula weight	601.45
Temperature (K)	149(2)
Crystal system	triclinic
Space group	P1
<i>a</i> /Å	8.995(1)
<i>b</i> /Å	10.875 (2)
<i>c</i> /Å	12.643(2)
α°	109.30(1)
β°	109.23(1)
γ°	96.32(1)
Volume/Å ³	1068.3(3)
Z	2
<i>D</i> _{calc} (g cm ⁻³)	1.714
Absorption coefficient(mm ⁻¹)	7.16
<i>F</i> (000)	580
Crystal dimensions (mm)	0.35 × 0.18 × 0.14
Reflections collected	11479
Independent reflections	5150 (<i>R</i> _{int} = 0.043)
θ Range for data collection(°)	3.8-28.3.
Absorption correction	multi-scan ABSPACK in CrisAlisPro RED
<i>T</i> _{min} / <i>T</i> _{max}	0.342/1.000
Reflection with $I \geq 2\sigma(I)$	4636
No. of parameters	257
Final R values [$I \geq 2\sigma(I)$]	0.043, <i>wR</i> ₂ ^a = 0.018
ρ_{fin} (min/max) (e.Å ⁻³)	-0.77/1.73

^a: $wR_2 = \{[w(F_o^2 - F_c^2)^2]/[w(F_o^2)^2]\}^{1/2}$, $w = 1/[\sigma(F_o^2) + (ap)^2 + bp]$, $p = (F_o^2 + 2F_c^2)/3$
a,b 0.021, 0.856

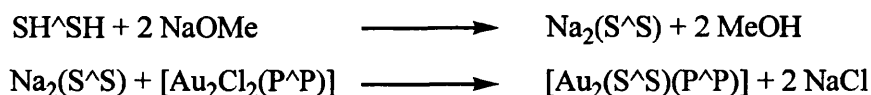
Table 4.3: Crystal data and structure refinement for C₂₃H₁₉AuNPS₂ (**4f**)

4.2.3.2 Formation of binuclear gold(I) complexes

In this section the syntheses of cyclic $[\text{Au}_2(\mu\text{-S}_{2a})(\mu\text{-P}^{\wedge}\text{P})]$ or open ring $[\text{Au}_2(\mu\text{-S}_{2b})(\text{PPh}_3)_2]$ compounds ($\mu\text{-P}^{\wedge}\text{P} = \text{PPh}_2(\text{CH}_2)_n\text{PPh}_2$, $n = 1,2,3,4$ and $\text{H}_2\text{S}_{2a} = \text{DMP}$, ADMN, DMPA, 24PYRI, 46PYRI and NPYRI; $\text{H}_2\text{S}_{2b} = \text{H}_2\text{S}_{2a}$ plus DMB and Cl-DMB) are described. Compounds **1a** [7] and **7a** [27] have already been reported in the literature.

4.2.3.2.1 Syntheses for all dithiolate ligands except ADMN

The thiolate was first deprotonated via a strong base (MeONa) and then reacted with the chlorogold phosphine complex. (when triethylamine was used as base ^1H NMR spectra indicated that it remained complexed with the product).



4.2.3.2.1.1 With chloro(triphenylphosphine)gold(I)

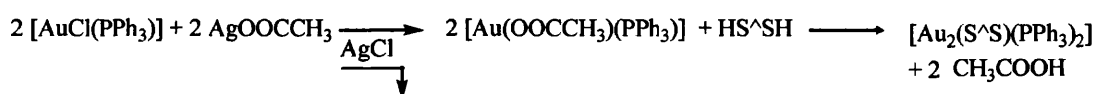
Under an inert atmosphere of dry nitrogen, one equivalent of the desired dithiol ($\approx 10^{-3}$ mol) and MeONa ($\approx 2 \times 10^{-3}$ mol) were mixed for 30 minutes in MeOH (10 mL) in a 50 mL two necked flask protected from light. Then, chloro(triphenylphosphine)gold(I) ($\approx 2 \times 10^{-3}$ mol) dissolved in dichloromethane (10 mL) was added to the solution and the mixture was left stirring for 2 h. The resulting suspension was filtered through diatomaceous earth to remove NaCl precipitated during reaction. The filtrate was concentrated to 5 mL by evaporation under reduced pressure and diethyl ether was added (10 mL). The resulting precipitate was collected via filtration and dissolved again in DCM (5 mL). Diethyl ether was added slowly and the resulting precipitate collected via filtration and dried overnight under vacuum.

4.2.3.2.1.2 With chlorogold(I) complexes of bridging diphosphines

Under an inert atmosphere of dry nitrogen, the desired dithiol ($\approx 10^{-3}$ mol) and MeONa ($\approx 2 \times 10^{-3}$ mol) were mixed for 30 minutes in MeOH (10 mL) in a 50 mL two necked flask protected from light. Then, the desired binuclear chlorogold phosphine complex ($\approx 10^{-3}$ mol) dissolved in dichloromethane (10 mL) was added to the solution and the mixture was left stirring for 2 h. The resulting suspension was filtered through diatomaceous earth to remove NaCl. The filtrate was concentrated to 5 mL by evaporation under reduced pressure. Diethyl ether (10 mL) was added and the resulting precipitate collected via filtration. This was dissolved again in DCM (5 mL) and diethyl ether added slowly. The resulting precipitate was collected via filtration and dried overnight under vacuum.

4.2.3.2.2 Syntheses with ADMN as dithiolate ligand

The ADMN ligand has a carboxylic acid group on the ring, which will be deprotonated by the use of a strong base. Therefore a different method has been used, in which the chlorogold phosphine complex was reacted first with silver acetate. The gold-acetate formed reacted with ADMN to give the desired product.



4.2.3.2.2.1 With chloro(triphenylphosphine)gold(I)

This reaction was carried out protected from light and under an inert atmosphere of dry nitrogen. Chloro(triphenylphosphine)gold(I) ($\approx 2 \times 10^{-3}$ mol) was dissolved in a DCM solution (10 mL) of AgOOCCH₃ ($\approx 2 \times 10^{-3}$ mol) and the mixture left stirring for 30 minutes. The precipitate of AgCl was removed by filtration through diatomaceous earth which was washed with an additional 5 mL DCM to ensure collection of all the filtrate. The filtrate was added to a methanolic, MeOH (5 mL), solution of ADMN ($\approx 10^{-3}$ mol) and the mixture was left stirring for 2 h. The solution was concentrated to 5 mL by evaporation under reduced pressure; the resulting precipitate was collected by filtration and dried overnight under vacuum.

4.2.3.2.2 With chlorogold(I) complexes of bridging diphosphines

These reactions were carried out protected from light and under an inert atmosphere of dry nitrogen. The binuclear chlorogold(I) phosphine complex ($\approx 10^{-3}$ mol) was added to a AgOOCCH_3 ($\approx 2 \times 10^{-3}$ mol) DCM solution (10 mL). The mixture was left stirring for 30 minutes. The precipitate of AgCl was removed by filtration through diatomaceous earth which was washed with 5 mL DCM. The filtrate was added to a methanolic, MeOH (5 mL), solution of ADMN ($\approx 10^{-3}$ mol) and the mixture was left stirring for 2 h. The solution was concentrated to 5 mL by evaporation under reduced pressure and the resulting precipitate was collected by filtration and dried overnight under vacuum. The products were separated on a silica column with DCM as eluent, the second band being the desired product.

4.2.3.2.3 Characterisation of the open ring complexes

$[\text{Au}_2(\mu\text{-}2,4\text{-S}_2\text{C}_4\text{H}_2\text{N}_2)(\text{PPh}_3)_2]$ (1a):

$^1\text{H NMR}$ (CDCl_3): 7.76 (d, 1H), 7.55 (m, 12H), 7.40 (m, 18H), 6.95 (d, 1H)

$^{31}\text{P NMR}$ (CDCl_3): 38.2 (s)

MS (FAB): 1060 [M]

IR (cm^{-1}): 1602 (vw), 1532 (m), 1498 (m), 1480 (m), 1435 (m), 1386 (m), 1371 (m), 1295 (m), 1185 (m), 1144 (m), 1099 (m), 997 (w), 804 (m), 743 (m), 710 (s), 690 (vs), 535 (s), 497 (s)

These results are consistent with the literature [7].

$[\text{Au}_2(\mu\text{-}4,6\text{-S}_2\text{C}_4\text{H}_2\text{N}_2)(\text{PPh}_3)_2]$ (2a):

$^1\text{H NMR}$ (CDCl_3): 8.33 (s, 1H), 7.72 (s, 1H), 7.5-7.4 (m, 30H)

$^{31}\text{P NMR}$ (CDCl_3): 37.9 (s)

MS (ES^+): 1061 $[\text{M}+\text{H}]^+$

[Au₂{μ-2,4-S₂C₄N₂(NH₂)₂}(PPh₃)₂](**3a**):¹H NMR (CDCl₃): 7.52 (m, 12H), 7.37 (m, 18H), 4.30 (s, 2H), 3.20 (s, 2H)³¹P NMR (CDCl₃): 37.4 (s)

MS (FAB): 1092 [M]

IR (cm⁻¹): 3450 (vw, NH₂), 1618 (w), 1537 (m), 1480 (w), 1434 (s) 1324 (w),
1290 (w), 1180 (w), 1100 (s), 998 (w), 847 (w), 744 (vs), 709 (vs), 690
(vs) 536 (vs), 507 (vs), 498 (vs).[Au₂(μ-2,6-S₂C₅H₃N)(PPh₃)₂](**4a**):¹H NMR (CDCl₃): 7.54 (m, 12H), 7.42 (m, 18H), 7.12 (2H, d, J±8Hz),
6.92 (1H, t, J±8Hz)³¹P NMR (CDCl₃): 38.3 (s)MS (ES⁺): 1060 [M+H]⁺IR (cm⁻¹): 1535 (s), 1478 (m), 1434 (s), 1397 (s), 1310 (w), 1148 (w), 1130 (s),
1100 (s), 1023 (w) 996 (m), 778 (s), 740 (s), 710 (s), 690 (vs), 538 (vs),
512 (vs), 495 (vs), 448 (s)

After slow diffusion of diethyl ether into a concentrated DCM solution of **4a**, some white crystals were obtained and subjected to study by X-ray crystallography, the results of which are given in section 4.2.3.2.5.

[Au₂(μ-2,6-S₂C₅H₂NCOOH)(PPh₃)₂](**5a**):¹H NMR (CDCl₃): 14.1 (s, 1H), 10.92 (s, 1H), 8.32 (d, 1H), 7.5 (30H, m),
6.85 (d, 1H)³¹P NMR (CDCl₃): 38.2 (s)MS (ES⁺): 1104 [M+H]⁺IR (cm⁻¹): 3500-3200 (m, OH), 1716 (m, C=O), 1650 (w), 1547 (s), 1480 (m), 1435
(s, O-H), 1399 (s), 1288 (s, C-O), 1251 (m), 1223 (w), 1210 (w), 1144
(w), 1131 (s), 1099 (s), 998 (m), 1026 (w), 851 (m), 739 (vs), 709 (vs),
686 (vs), 531 (vs), 496 (vs), 434 (vs), 413 (vs)

The ¹H NMR spectrum proves that this complex is in the protonated form.

[Au₂(μ-2,6-S₂C₄H₂N₂)(PPh₃)₂] (6a):¹H NMR (CDCl₃): 8.37 (s, 2H), 7.45 (m, 30H)³¹P NMR (CDCl₃): 36.6 (s)MS (FAB): 1060 [M+H]⁺[Au₂(μ-1,3-S₂C₆H₄)(PPh₃)₂] (7a):¹H NMR (CDCl₃): 7.95 (s, 1H), 7.40 (m, 30H), 7.20 (d, 2H, J ±4Hz),
6.75 (t, 1H, J ±4Hz)³¹P NMR (CDCl₃): 38.6 (s)MS (FAB): 1059 [M+H]⁺

These results are similar to the literature [27].

[Au₂(μ-1,3-S₂C₆H₃NCl)(PPh₃)₂] (8a):¹H NMR (CDCl₃): 8.20 (s, 1H), 7.40 (m, 30H), 7.10 (d, 1H, J ±8Hz),
6.90 (d, 1H, J ±8Hz)³¹P NMR (CDCl₃): 38.4 (s)MS (FAB): 1093 [M+H]⁺**4.2.3.2.4 Characterisation of the closed ring complexes**

These are grouped according to the dithiolate ligand used.

a) With DMP:[Au₂(μ-2,6-S₂C₅H₃N)(μ-dppm)] (4b):¹H NMR (CDCl₃): 7.65 (b), 7.35 (b), 7.12 (b), 6.91 (b), 3.78 (b)³¹P NMR (CDCl₃): 35.1 (s)MS (FAB): 920 [M+H]⁺IR (cm⁻¹): 2980 (w), 2600 (w), 2495 (w), 1534 (s), 1480 (m), 1434 (s), 1398 (s),
1170 (w), 1130 (s), 1099 (s), 1035 (w) 998 (m), 777 (s), 737 (s), 722 (s),
689 (vs), 523 (vs), 509 (vs), 471 (vs), 462 (s)

[Au₂(μ-2,6-S₂C₅H₃N)(μ-dppe)] (4c):¹H NMR (CDCl₃): 7.63 (b, 8H), 7.44 (b, 13 H), 6.92 (b, 2H), 2.83 (b, 4H)³¹P NMR (CDCl₃): 36.6 (s)MS (FAB): 934 [M+H]⁺IR (cm⁻¹): 2980 (w), 1535 (s), 1482 (m), 1435 (s), 1398 (s), 1170 (w), 1130 (s),
1102 (s), 1028 (w) 998 (m), 783 (s), 737 (s), 722 (s), 690 (vs), 518 (vs),
480 (vs), 435 (s)[Au₂(μ-2,6-S₂C₅H₃N)(μ-dppp)] (4d):¹H NMR (d₆-DMSO): 7.74(m, 8H), 7.60 (m, 12H), 7.13 (t, 1H), 6.88 (d, 2H),
2.88 (b, 4H), 2.05 (b, 2H)³¹P NMR (CDCl₃): 32.5 (s)MS (FAB): 948 [M+H]⁺IR (cm⁻¹): 2400 (w), 1533 (s), 1482 (m), 1435 (s), 1400 (s), 1150 (w), 1125 (s),
1106 (s), 1027 (w) 995 (m), 955 (s), 780 (s), 750 (m), 722 (s), 691 (vs),
516 (vs), 488 (s), 463 (s), 438 (s)[Au₂(μ-2,6-S₂C₅H₃N)(μ-dppb)] (4e):¹H NMR (CDCl₃): 7.58 (m, 8H), 7.42 (m, 12H), 6.92 (m, 3H), 2.74 (b, 4H),
1.7 (b, 4H)³¹P NMR (CDCl₃): 32.3 (s)MS (FAB): 962 [M+H]⁺IR (cm⁻¹): 2603 (w), 2497 (w), 1534 (s), 1479 (m), 1435 (s), 1397 (s), 1170 (w),
1146 (m), 1129 (s), 1102 (s), 1036 (w) 998 (m), 845 (w), 784 (s), 737 (s),
691 (vs), 519 (vs), 486 (s), 435 (s)

b) With ADMN $[Au_2(\mu-2,6-S_2C_3H_2NCOOH)(\mu-dppm)]$ (**5b**): 1H NMR (d_6 -DMSO): 7.82 (m, 8H), 7.45 (m, 13H), 6.65 (d, 1H), 4.72 (t, 2H) ^{31}P NMR (d_6 -DMSO): 30.2, 28.9 (AB system, $J = \pm 63$ Hz)MS (ES+): 964 [M+H]⁺IR (cm^{-1}): 3300-3400 (w), 2982 (w), 2444 (w), 1682 (s, C=O), 1548 (s), 1512 (m), 1482 (m), 1435 (s), 1390 (m), 1296 (m) 1247 (w), 1146 (m), 1099 (s), 998 (m), 866 (w), 791 (s), 766 (s), 739 (vs), 687 (vs), 524 (vs), 507 (vs), 475 (s) $[Au_2(\mu-2,6-S_2C_3H_2NCOOH)(\mu-dppe)]$ (**5c**): 1H NMR (d_6 -DMSO): 7.80 (m, 12H), 7.49 (m, 9H), 6.98 (b, 1H), 2.90 (b, 4H) ^{31}P NMR (d_6 -DMSO): 37.0 (s)IR (cm^{-1}): 3300-3400 (w), 2984 (w), 2448 (w), 1710 (s, C=O), 1546 (s), 1514 (m) 1477 (m), 1434 (s), 1405 (m), 1290 (m) 1247 (w), 1100 (s), 997 (m), 867 (w), 790 (w), 736 (s), 689 (vs), 520 (vs), 502 (vs), 475 (s) $[Au_2(\mu-2,6-S_2C_3H_2NCOOH)(\mu-dppp)]$ (**5d**): 1H NMR (d_6 -DMSO): 7.74(m, 8H), 7.62 (m, 12H), 7.14 (t, 1H), 6.92 (d, 2H), 2.88 (b, 4H), 2.05 (b, 2H) ^{31}P NMR (d_6 -DMSO): 33.5MS (ES+): 992 [M+H]⁺Melting point ($^{\circ}C$): 173 ± 1 $^{\circ}C$ IR (cm^{-1}): 3300-3400 (w), 2915 (w), 2581 (w), 1714 (s, C=O), 1541 (s), 1475 (m), 1434 (s), 1407 (m), 1288 (m) 1250 (w), 1104 (s), 998 (m), 867 (w), 789 (w), 744 (s), 690 (vs), 523 (vs), 499 (vs), 475 (s)

c) With DMPA $[Au_2(\mu-2,6-S_2C_4H_2N_2)(\mu-dppm)]$ (6b): 1H NMR (CDCl₃): 7.89 (s, 2H), 7.72, 7.45, 7.37 (m, 20H), 4.72 (t, 2H) ^{31}P NMR (CDCl₃): 34.6MS (FAB): 921 [M+H]⁺IR (cm⁻¹): 3375 (vw), 3050 (vw), 1624 (vw), 1542 (vw), 1463 (m), 1436 (s),
1373 (m), 1167 (m) 1136 (s), 1100 (s), 1026 (w), 998 (m), 823 (m),
780 (m), 723 (s), 738 (s), 689 (vs), 523 (s), 510 (s), 477 (s), 449 (s). $[Au_2(\mu-2,6-S_2C_4H_2N_2)(\mu-dppp)]$ (6d): 1H NMR (CDCl₃): 7.95 (s, 2H), 7.72, 7.55 (m, 20H), 2.86 (b, 4H), 2.08 (b, 2H) ^{31}P NMR (CDCl₃): 42.0MS (FAB): 949 [M+H]⁺IR (cm⁻¹): 3375 (vw), 3050 (vw), 1618 (w), 1542 (m), 1479 (m), 1435 (s),
1373 (w), 1326 (m), 1293 (m), 1162 (w) 1133 (s), 1100 (s),
1026 (w), 998 (m), 848 (m), 743 (m), 710 (s), 691 (vs), 537 (s), 512 (s),
479 (s), 449 (s). $[Au_2(\mu-2,6-S_2C_4H_2N_2)(\mu-dppb)]$ (6e): 1H NMR (CDCl₃): 7.95 (s, 2H), 7.72, 7.55 (m, 20H), 2.86 (b, 4H), 2.08 (b, 2H) ^{31}P NMR (CDCl₃): 32.0MS (FAB): 949 [M+H]⁺IR (cm⁻¹): 3360 (vw), 3050 (vw), 1619 (w), 1542 (m), 1480 (m), 1435 (s),
1326 (m), 1293 (m), 1182 (w) 1133 (s), 1100 (s), 1026 (w), 998 (m),
848 (m), 744 (m), 710 (s), 692 (vs), 537 (s), 510 (s), 479 (s), 449 (s).

d) With 24PYRI $[Au_2(\mu-2,4-S_2C_4H_2N_2)(\mu-dppm)]$ (1b):

1H NMR (CDCl₃): 7.80 (d, 1H), 7.55 (m, 8H), 7.32 (m, 12H), 6.70 (d, 1H),
3.65 (t, 2H)

^{31}P NMR (CDCl₃): 27.3, 26.5 (AB system with J = 55 Hz)

MS (FAB): 921 [M+H]⁺

IR (cm⁻¹): 1532 (m), 1499 (m), 1433 (m), 1386 (m), 1372 (m), 1294 (m), 1187 (m),
1149 (m), 1098 (m), 997 (w), 814 (m), 772 (m), 721 (s), 738 (s), 688 (vs),
521 (s), 510 (s), 455 (s), 419 (s).

 $[Au_2(\mu-2,4-S_2C_4H_2N_2)(\mu-dppe)]$ (1c):

1H NMR (CDCl₃): 7.80 (d, 1H), 7.55 (m, 8H), 7.40 (m, 12H), 6.90 (d, 1H),
2.75 (s, 4H)

^{31}P NMR (CDCl₃): 42.9 (s)

MS (FAB): 935 [M+H]⁺

IR (cm⁻¹): 1533 (m), 1499 (m), 1435 (m), 1387 (m), 1372 (m), 1295 (m), 1187 (m),
1147 (m), 1103 (m), 998 (w), 804 (m), 744 (m), 725 (s), 690 (vs), 520 (s),
485 (s)

 $[Au_2(\mu-2,4-S_2C_4H_2N_2)(\mu-dppp)]$ (1d):

1H NMR (CDCl₃): 7.81 (d, 1H), 7.58 (m, 8H), 7.37 (m, 12H), 6.89 (d, 1H),
2.57 (s, 4H), 2.14 (s, 2H)

^{31}P NMR (CDCl₃): 41.4

MS (FAB): 949 [M+H]⁺

IR (cm⁻¹): 1530 (m), 1497 (m), 1435 (m), 1385 (m), 1369 (m), 1292 (m), 1184 (m),
1144 (m), 1101 (m), 998 (w), 802 (m), 740 (m), 687 (vs), 516 (s), 480 (s)

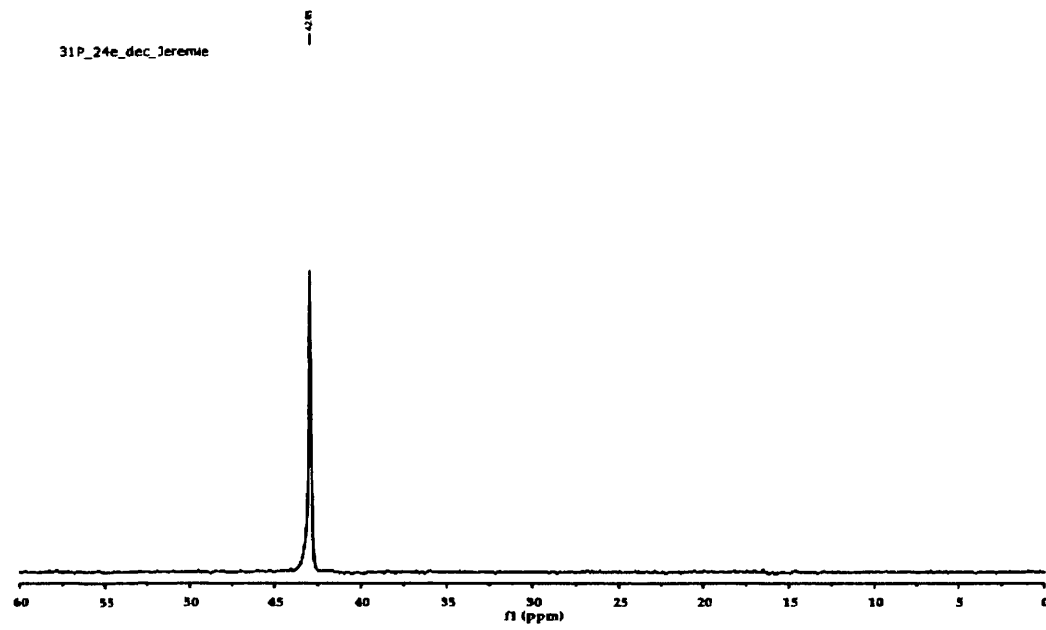


Figure 4.2: ^{31}P NMR spectrum of **1c**: note the single peak (compare to figure 4.3)

$[\text{Au}_2(\mu\text{-}2,4\text{-S}_2\text{C}_4\text{H}_2\text{N}_2)(\mu\text{-dppb})]$ (**1e**):

^1H NMR (d_6 -DMSO): 7.91 (s, 1H), 7.72 (m, 8H), 7.50 (m, 12H), 6.91 (s, 1H),

2.73 (b, 4H), 1.72 (b, 4H)

^{31}P NMR (d_6 -DMSO): 42.3

MS (FAB): 963 $[\text{M}+\text{H}]^+$

IR (cm^{-1}): 1533 (m), 1499 (m), 1435 (m), 1385 (m), 1371 (m), 1295 (m), 1189 (m),

1147 (m), 1103 (m), 998 (w), 805 (m), 741 (m), 690 (vs), 519 (s), 487 (s)

f) With NPYRI $[Au_2\{\mu-2,4-S_2C_4N_2(NH_2)_2\}(\mu-dppm)]$ (**3b**):

1H NMR (d_6 -DMSO): 7.80 (m, 8H), 7.45 (m, 12H), 5.95 (s, 2H), 4.65 (t, 2H),
3.80 (s, 2H)

^{31}P NMR (d_6 -DMSO): 29.8, 28.6 (AB system, $J = \pm 60$ Hz)

MS (FAB): 951 $[M+H]^+$

IR (cm^{-1}): 3330 (vw, NH_2), 1613 (w), 1539 (m), 1482 (w), 1435.7 (s) 1333 (w),
1188 (w), 1101 (s), 998 (w), 851 (w), 740 (vs), 723 (vs), 690 (vs) 525 (vs),
512 (vs), 479 (vs).

 $[Au_2\{\mu-2,4-S_2C_4N_2(NH_2)_2\}(\mu-dppe)]$ (**3c**):

1H NMR (d_6 -DMSO): 7.80 (m, 8H), 7.50 (m, 12H), 5.95 (b, 2H),
4.10 (b, 2H), 2.95 (b, 4H)

^{31}P NMR (d_6 -DMSO): 42.1, 38.1

MS (FAB): 965 $[M+H]^+$

IR (cm^{-1}): 3360 (vw, NH_2), 1607 (w), 1540 (m), 1482 (w), 1435 (s) 1329 (w),
1180 (w), 1104 (s), 998 (w), 851 (w), 740 (vs), 727 (vs), 691 (vs), 519
(vs), 491 (vs).

 $[Au_2\{\mu-2,4-S_2C_4N_2(NH_2)_2\}(\mu-dppp)]$ (**3d**):

1H NMR (d_6 -DMSO): 7.75 (m, 8H), 7.45 (m, 12H), 5.90 (s 2H),
4.05 (s, 2H), 2.85 (b, 4H), 1.95 (b, 2H)

^{31}P NMR (d_6 -DMSO): 40.8, 41.3

MS (FAB): 979 $[M+H]^+$

IR (cm^{-1}): 3330 (vw, NH_2), 1621 (w), 1542 (m), 1482 (w), 1435 (s) 1321 (w),
1188 (w), 1102 (s), 998 (w), 847 (w), 746 (vs), 725 (vs), 692 (vs) 527 (vs),
517 (vs), 488 (vs).

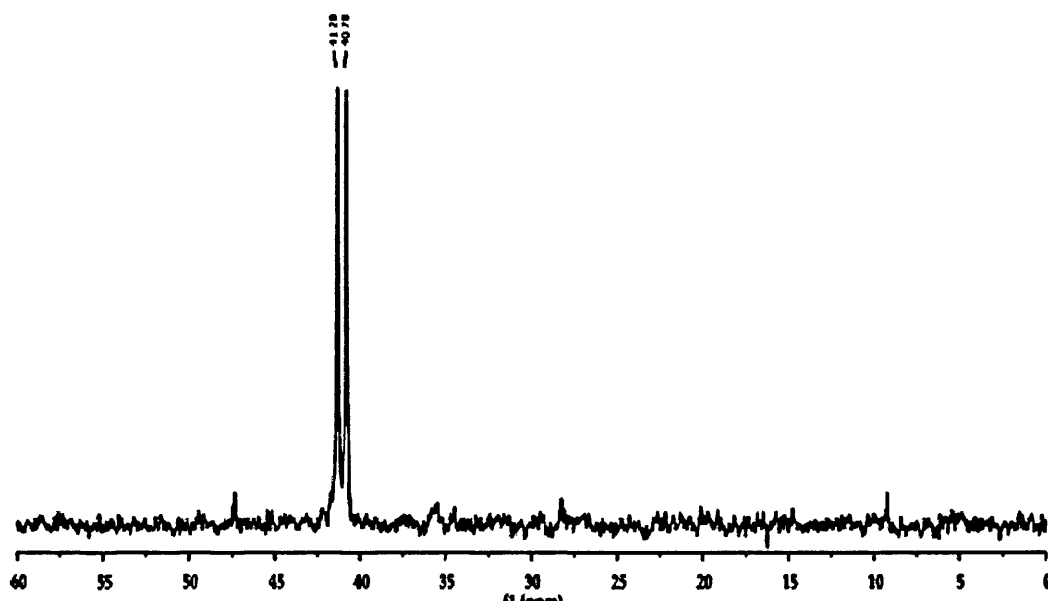


Figure 4.3: ^{31}P NMR spectrum of **3d**, note the double peak

The doublet in the ^{31}P NMR spectra of complexes belonging to the **3** series is generally absent in the spectra of complexes belonging to the **1** series. The two phosphorus atoms are chemically inequivalent in both series, but the electron-donating effect of the two amino-groups in **3** seems to emphasize the effect of asymmetry on their ^{31}P NMR spectra.

$[\text{Au}_2\{\mu\text{-}2,4\text{-S}_2\text{C}_4\text{N}_2(\text{NH}_2)_2\}\{\mu\text{-dppb}\}]$ (**3e**):

^1H NMR (d_6 -DMSO): 7.75 (m, 8H), 7.50 (m, 12H), 5.95 (s, 2H),
4.05 (s, 2H), 2.75 (s, 4H), 1.72 (s, 4H)

^{31}P NMR (d_6 -DMSO): 40.5, 39.7

MS (FAB): 993 $[\text{M}+\text{H}]^+$

IR (cm^{-1}): 3350 (vw, NH_2), 1621 (w), 1541 (m), 1480 (w), 1435 (s) 1325 (w),
1181 (w), 1100 (s), 998 (w), 847 (w), 743 (vs), 691 (vs), 537 (vs), 517
(vs), 496 (vs).

4.2.3.2.5 Crystal structure of $[\text{Au}_2(\mu\text{-2,6-S}_2\text{C}_5\text{H}_3\text{N})(\text{PPh}_3)_2]$ (**4a**)

The crystals were obtained by slow diffusion of diethyl ether into a concentrated DCM solution of **4a**. Despite a number of attempts at recrystallisation, the crystal quality was not good enough to obtain really good resolution of the structure. The data obtained do however allow us to describe the structure of the four molecules forming the asymmetric unit. The unit cell is formed by eight of these asymmetric units. A representation of one of the four molecules forming the asymmetric unit is given in figure 4.4. The final “R” value is too high for the structure to be reported in a crystallography study; even so, the results are interesting for consideration here. The crystal data and refinement are presented in table 4.5.

As we have four molecules in the asymmetric unit with very similar geometries, they will be treated as one molecule. The distances and angles reported in table 4.4 are calculated as an average of the corresponding value for each molecule. The error given is equal to two standard deviations.

First it is noticeable that the two triphenylphosphinegold moieties are each connected to the thiolate through one sulphur atom but are structurally distinct. Atoms belonging to the first type will be labelled (OUT) and the ones belonging to the second (IN). The Au-S distance (229 ± 2 pm for (IN), and 226 ± 4 pm for (OUT)) and Au-P distance (226.5 ± 0.8 pm for (IN) and 224 ± 2 pm for (OUT)) are similar to those usually found for this kind of compound [8, 31, 32, 33, 34]. One of the triphenylphosphine gold(I) moieties is out of the pyridine plane by 45° , the other by -14° . S-Au-P angles ($172.4 \pm 0.6^\circ$ for (IN), $177.2 \pm 0.8^\circ$ for (OUT)) are disturbed from the ideal linear geometry of gold(I). The C-S distances (172 ± 2 pm for (IN) and 174 ± 8 pm for (OUT)) are longer than the C=S distance ($169.2(2)$ pm) found for the thione in 2-Mercaptopyridine in the solid state [36]. As seen in chapter 3, DMP can be present as a thione-thiol or a di-thiol. The C-S bond length suggests that DMP is functioning as a dithiolate ligand in **4a**.

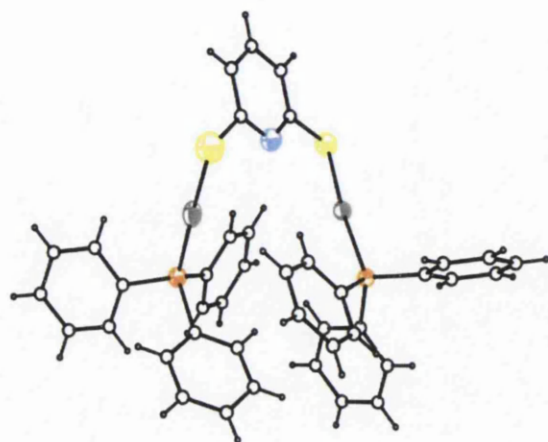
Distances (pm)	Angles (°)
Au–Au: 495 ± 5	S–Au–P(OUT): 177.2 ± 0.8 S–Au–P(IN): 172.4 ± 0.6
Au–S (IN) : 229 ± 2 (OUT): 226 ± 4	<u>Dihedral</u> N–C–S–Au(OUT): 43.9 ± 2.2 N–C–S–Au(IN): -14.0 ± 2.6
Au–P (IN) : 226.5 ± 0.8 (OUT): 224 ± 2	
S–C (IN) : 172 ± 3 (OUT): 174 ± 8	
S–N (IN) : 321 ± 5 (OUT): 328 ± 3	

Table 4.4: Selected crystal structure bond distances and angles of **4a**

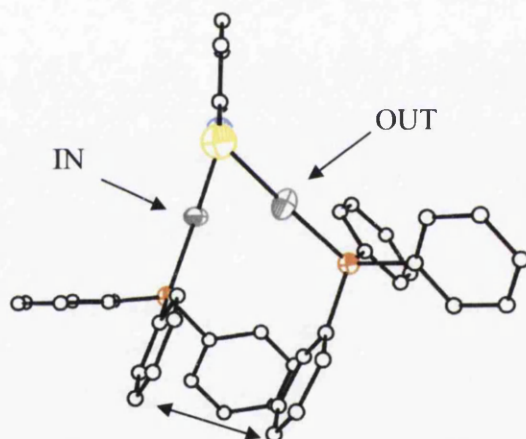
Secondly, the gold-gold distance (495 ± 5 pm) is far greater than the sum of the gold van der Waals radii (340 pm), so there is no intramolecular gold-gold interaction in the crystal.

Thirdly, $d_{\text{Au(IN)-N}}$ is $321.8 (\pm 6)$ pm which is shorter than the sum of their van der Waals radii [8]. Hence there is a gold-nitrogen interaction for the phosphinegold moiety in the plane, which could be responsible for the slight deviation from the ideal linear geometry about the Au atom. But no direct nitrogen-gold bonds are detectable, confirming the higher affinity of gold for sulphur than nitrogen.

And finally, one phenyl group of each phosphinegold moiety interacts with another through π - π stacking (see figure 4.3(B)). In triphenylphosphine(2-thiolatopyridine)gold(I) the phosphinegold moiety is out of the plane by 14.4° [8]. In **4a** (IN) the phosphinegold moiety has the same dihedral angle, but for (OUT) the dihedral angle is far greater at $43.9 \pm 2.2^\circ$. This larger value could be explained by the interaction between the two triphenylphosphines and the bulkiness of the two groups.



(A)



Phenyl facing each other

(B)

Figure 4.4: (A) Representation of compound **4a**, (B) Representation of compound **4a** with the pyridine ring perpendicular to the representation view (hydrogen atoms have been omitted for clarity). In both pictures, gold atoms are in grey, nitrogen atom in blue, phosphorus atoms in orange and sulphur atoms in yellow.

Empirical formula	C ₄₁ H ₃₃ Au ₂ NP ₂ S ₂
Formula weight	1026.46(1)
Temperature (K)	275
Crystal system	Monoclinic
Space group	C2/c
<i>a</i> /Å	29.121(1)
<i>b</i> /Å	29.0870(1)
<i>c</i> /Å	34.9750(1)
α /°	90.00
β /°	91.56(1)
γ /°	90.00
Volume/Å ³	29614.33(1.68)
Z	32
<i>D</i> _{calc} (g cm ⁻³)	1.8418
Absorption coefficient (mm ⁻¹)	16.79
<i>F</i> (000)	15136
Crystal dimensions (mm)	0.80 × 0.24 × 0.12
Reflections collected	29279
Independent reflections	23699 (<i>R</i> _{int} = 0.25)
θ Range for data collection(°)	
Absorption correction	multi-scan ABSPACK in CrisAlisPro RED
<i>T</i> _{min} / <i>T</i> _{max}	0.161/1.000
Reflections with <i>I</i> ≥ 4σ(<i>I</i>)	23699
No. of parameters	473
Final <i>R</i> values [<i>I</i> ≥ 4σ(<i>I</i>)]	0.23, <i>wR</i> ₂ ^a = 0.565
ρ _{fin} (min/max) (e.Å ⁻³)	

$$^a: wR_2 = \{[w(F_o^2 - F_c^2)^2] / [w(F_o^2)^2]\}^{1/2}, w = 1 / [\sigma(F_o^2) + (ap)^2 + bp], p = (F_o^2 + 2F_c^2) / 3$$

a, b 0.2, 0

Table 4.5: Crystal data and structure refinement for C₄₁H₃₃Au₂NP₂S₂ (**4a**)

4.2.4 Discussion

A crystal structure for **7a** has been reported by Laguna's group [27]. The characterisation of **1a** is also reported elsewhere [7]. The spectroscopic data obtained for these compounds in this work are in accordance with the results disclosed in the literature.

The deprotonation of the dithiol by a strong base like MeONa in a DCM:MeOH solution induces a nucleophile attack on the chlorogold(I) phosphine complex followed by the displacement of the chloride and formation of NaCl. When a diphosphine is used, several possible types of final product are possible. Puddephatt [37-40] and others [41, 42] have shown that there can be an equilibrium between type A and type B (figure 4.5). Mass spectrometry should allow us to distinguish these types.

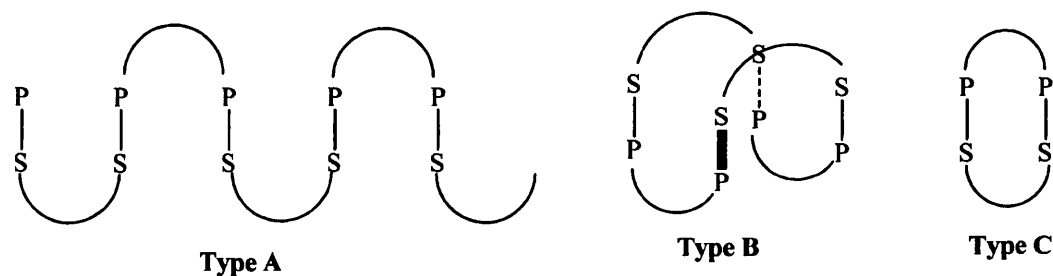


Figure 4.5: Connection possibilities for diphosphine/dithiolate complexes

4.2.4.1 NMR studies

Up to three triphenylphosphinegold moieties can coordinate to the deprotonated dithiol 1,2-Dimercaptobenzene, as shown by Laguna or Schmidbaur [27, 43]. This is mainly due to the aurophilic interactions and the close proximity of the two sulphur atoms. Peaks attributed to the phosphine ligand and to the thiolate ligand appear in every ^1H NMR spectrum. For the open ring series, the relative values of ^1H NMR peak integration are consistent with a double substitution of the dithiol. For the closed ring compounds, the relative values of peak integration are consistent with a phosphine/thiol ratio of 1/1. The ratio of phosphine/thiol used in the synthesis has led to the desired product.

The ^{31}P NMR peaks are shifted to lower field when the chlorine atom on the phosphinegold moiety is substituted by the thiolate (see table 4.4). The values

obtained lie in the 30-38 ppm range which is consistent with that found in the literature for similar gold phosphine thiolate complexes. No ^{31}P peaks were detected in the region for a phosphinegold moiety connected to a nitrogen ligand (20-27 ppm) [5, 6]. This means that the unique binding site for the phosphinegold moiety on a nitrogen-containing heterocyclic dithiol is the sulphur atom; no contribution from the nitrogen atom in the ring is detectable, even for the shortest bridging diphosphine dppm.

$[\text{Au}_4(1,2\text{-dimercaptobenzene})_2(\text{dppm})_2]$ are type B molecules and their $^{31}\text{P}\{1\text{H}\}$ NMR spectra present an AA'BB' system with two peaks at 35.4 and 25.3 ppm [44]. Their mass spectrometry shows clearly the presence of the two Au_2 units. With the support of the mass spectrometry data, and the presence of only one peak in the ^{31}P NMR spectra of complexes with dppm and symmetric dithiolate ligands, we can conclude that all the complexes with dppm (**1b-6b**) are annular (type C). An AB pattern is observed in the phosphorus NMR spectra of compounds with a dppm bridge and an asymmetric dithiolate ligand. The peak intensity ratio between the inner and outer peaks has been checked and is consistent with an AB pattern. DFT calculation (see chapter 5) and the crystal structure of **4a** show that the two S-Au-P branches are out of the plane of the N-heterocycle, so in the case of an asymmetric N-heterocycle, the two phosphorus atoms are not rigorously NMR equivalent, which explains the AB pattern observed.

The phosphorus spectra of binuclear gold complexes of NPYRI with diphosphine bridges have two peaks. The asymmetry of the pyrimidine ring by itself is not enough to break the NMR equivalence, as the 24PYRI derivatives show only one phosphorus peak. The equivalence between the two phosphorus nuclei could be broken by the effect on the electron distribution in the molecule of the electron-donating amino-groups. Recently $[\text{Au}_2(\mu\text{-dppm})]$ has been connected to some asymmetric 2-mercaptobenzimidazoles by Lee [4] and the ^{31}P NMR spectra of these complexes show a doublet which is also attributed to the asymmetry of the monothiolate ligand.

Complexes with a bridging diphosphine seem to be of the type C (annular) according to the ^{31}P NMR spectra.

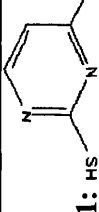
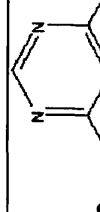
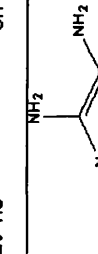
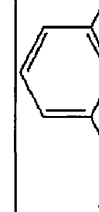
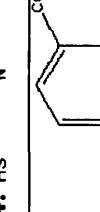
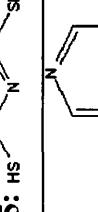
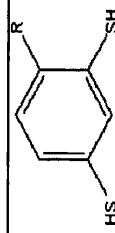
	a: PPh ₃	b: dppm	c: dppe	d: dppp	e: dppb
1: HS  24PYRI	38.2	AB system 27.3, 26.5 J = 55 Hz	43	41.8	41
2: HS  46PYRI	37.9	X	X	X	X
3: HS  NPYRI	37.4	AB system 29.8, 28.6 J = 60 Hz	42.1, 38.1	41.3, 40.8	40.5, 39.7
4: HS  DMP	38.3	35.1	36.6	32.5	32.3
5: HS  ADMIN	38.2	AB system 30.2, 28.9 J = 63 Hz	37.0	33.5	X
6: HS  DMPA	38.1	34.1	X	42.0	32.0
7 (H); 8 (Cl):  R = H, Cl	38.4 (X = H) 38.7 (X = Cl)	X	X	X	X

Table 4.6: ³¹P NMR peaks obtained for binuclear complexes synthesised in this work

4.2.4.2 Mass spectrometry

For all the compounds (1-8) the FAB mass spectrometry technique gave a peak corresponding to the mass (m/z) of the protonated molecule. FAB is the mass spectrometric technique providing the best results for this class of compounds.

For all annular compounds, no higher mass peak could be detected; the $[M+H]^+$ peak dominates the spectra and no type B or type A species have been detected.

For open ring compounds, the FAB mass spectra gave a peak at the m/z of the desired compound but also peaks at: 459 $[\text{AuPPh}_3]^+$, 721 $[\text{Au}(\text{PPh}_3)_2]^+$, 1409 $[\text{S}(\text{AuPPh}_3)_3]^+$ and also one at higher mass corresponding to $[M+(\text{AuPPh}_3)]^+$. This pattern is observed for all of the eight compounds synthesised. Similar peaks have been reported in numerous studies of FAB or electrospray mass spectrometry with mono- or di-thiolate derivatives of triphenylphosphinegold [27, 45-49], and they are generally attributed to possible fragmentation by-products.

Overall the mass spectrometry results confirm that we have only type C closed ring molecules, and for the open ring system, it supports the information provided by the ^1H NMR spectra that only two triphenylphosphinegold groups are connected to the dithiolate.

4.2.4.3 IR spectroscopy

Each IR spectrum had bands corresponding to both the thiolate and the desired phosphine. The $\nu(\text{NH})$ vibrational band for a protonated pyridine (pyridinium) is at around $3312\text{-}3167\text{ cm}^{-1}$ [47]. In a series of gold 2-thiol pyridines, Puddephatt found this vibration to be at 3241 , 3204 or 3154 cm^{-1} [24]. These vibrations are absent in all of our IR spectra except those for the NPYRI series. The NPYRI series show peaks around 3450 cm^{-1} which are attributed to the vibration of NH bonds belonging to the amino-groups rather than the pyrimidine ring [47]. Therefore we can be sure that we do not have any protonated species. The vibrational band of SH, which is at around 2500 cm^{-1} is also absent from the spectra, reinforcing the conclusion of a S-Au bond.

4.2.4.4 Possible reasons which drive the reaction toward annular compounds

When 1,3-Dimercaptobenzene or 4-Chloro-1,3-dimercaptobenzene have been used with different binuclear chlorogold complexes of bridging diphosphines, a precipitate was formed in the solution which could not be dissolved in any solvent used. A possible route to synthesise the desired product would have been to react $[\text{Au}_2(\text{S}^-\text{S})(\text{AsPPh}_3)]$ on the diphosphine, as Laguna has done for $[\text{Au}_2(1,2\text{-dithiolatobenzene})(\text{dppe})]$ [44].

When a N-heterocyclic dithiol with the nitrogen in-between the two thiol groups is used, the major final product is an annular binuclear gold compound. We can understand this by reference to the following argument. After one gold atom of a binuclear chlorogold complex of a bridging diphosphine has reacted with a deprotonated thiol, the other gold atom can react with a thiol belonging to another molecule (inter-molecularly) or with the unreacted thiol of the ligand already attached (intra-molecularly). In the N-heterocycle dithiol, the "N-C-S" region is more electron rich than an equivalent C-C-S region due to the possible delocalisation of the electron and the non-bonding pair present on the nitrogen. Therefore the "N-C-S" region attracts the unreacted gold atom to give intramolecular substitution rather than intermolecular substitution (see figure 4.6) and the annular derivative is formed. As an insoluble product thought to be of polymeric nature (type A) is obtained when 1,3-dimercaptobenzene is used (or 4-chloro-1,3-dimercaptobenzene), the chelating effect by itself is not sufficient to explain the high selectivity towards the annular form.

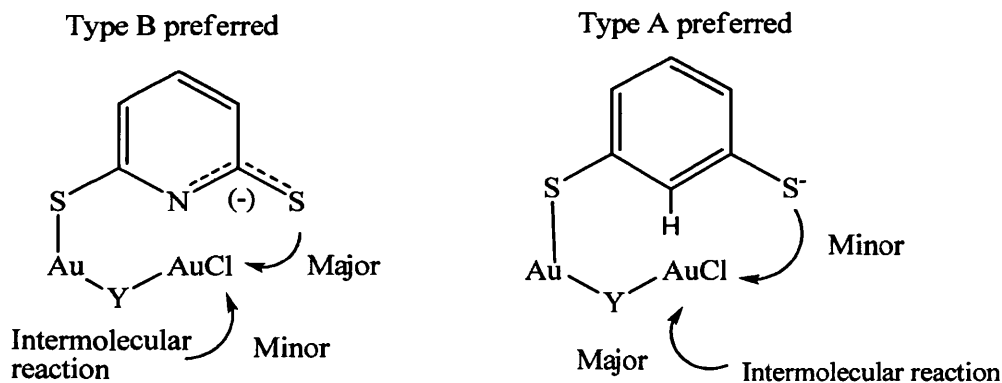


Figure 4.6: Hypothetical intermediate in the substitution mechanism which could explain the selectivity of the reaction towards a final product of type B or type A

4.2.5 Conclusions from synthetic work

We can conclude that in this series of complexes of binuclear gold phosphine N-heterocyclic-dithiolates, the two ligands are connected to the metal center through a S-Au-P bond. The nitrogen atom of the heterocycle is not protonated (except for **5a**).

There is no indication of any N-Au bonding in these compounds.

For complexes with bridging ligands, the mass spectrometric and ^{31}P NMR data are consistent with an annular structure.

4.3 Photoluminescence studies

A large number of organogold compounds have been synthesised in the literature. The aim of most of these studies has been to understand the effect of aurophilicity on molecular structure. However, a growing number of recent studies have focused on the photoluminescence properties of organogold compounds for a number of technological applications including: chemo-sensing [49-52], OLEDs [53-56], and sensors for volatile organic solvents [57, 58].

Here we limit discussion of the photochemistry of gold complexes to that of interest for this work, *i.e.* gold phosphine thiolates.

In 1993, Bruce and Bruce [59] characterised the phosphorescence of a series of binuclear gold phosphine complexes with dithiolate $[\text{Au}_2(\mu\text{-S}(\text{CH}_2)_3\text{S})\{\mu\text{-PPh}_2(\text{CH}_2)_n\text{PPh}_2\}]$ ($n = 2\text{-}5$) or monothiolate ligands $[\text{Au}_2(4\text{-SC}_6\text{H}_4\text{Me})\{\mu\text{-PPh}_2(\text{CH}_2)_n\text{PPh}_2\}]$ ($n = 2\text{-}5$). Their emission was attributed to $[\text{S}\rightarrow\text{Au}]$ LMCT excited state [59]. Meanwhile Fackler's group synthesised and photochemically studied a series of mononuclear gold phosphine thiolates with 1,3,5-triaza-7-phosphaadamantane (TPA) or triphenylphosphine as phosphine to give a small cone angle of 102° (for TPA), and hence minimize the steric hindrance for any weak aurophilicity [26]. The luminescence of this class of compounds was influenced by:

- 1) the ligands, as a more electron-withdrawing thiolate will blue shift the emission;
- 2) the gold-gold intermolecular interaction which will destabilise the filled $5d_z^2$ gold orbitals and stabilise the empty $6p_z$ gold orbitals (z being the axes going through the two metal atoms);
- 3) the absence of phenyl groups on the phosphine facilitate the study by removing the possibility of any LLCT.

The aurophilicity reduces the HOMO-LUMO gap (see point 2 and figure 4.7), resulting in a red shift of the emission. Therefore a metal-metal to ligand charge transfer is generally thought to be the dominant transition in the luminescence of most of these compounds. But there may also be some intraligand transitions between π and π^* orbitals of a triphenylphosphine. The electron-withdrawing effect of substituents on the thiolate can bring the orbital energy levels of the phosphine ligand, the thiolate ligand, and the metal close together and therefore the ordering of the orbitals may be altered.

A clear example of the effect of aurophilicity on the photoluminescence is illustrated by a diphosphine-bridged binuclear gold complex which when bonded to a benzocrown ether thiolate acts as chemo-sensor. When a metal ion is encapsulated in the crown, then the two gold atoms are close enough to interact and this gives a red shift in the emission due to the switch from a $[S \rightarrow Au]$ LMCT to a $[S \rightarrow Au \cdots Au]$ ligand to metal-metal charge transfer excited state [49-51].

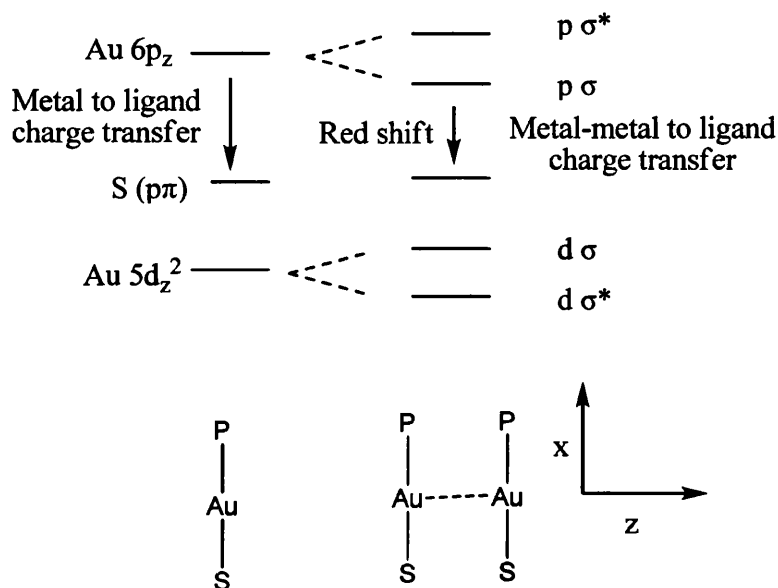


Figure 4.7: Effect of the gold-gold interaction on the luminescence

Recently, Yam's group produced a number of complexes containing phosphinegold moieties connected to a thiolate ligand derived from thiocarbamide, having a blue luminescence at room temperature in solution and green phosphorescence at 77 K. Here the emission is attributed to intraligand donor-acceptor transfer, probably mixed with some LMCT [31].

In gold phosphine thiolates, the origin of the luminescence has been shown to be quite varied and not particularly well defined: it can be a ligand to metal-metal charge transfer or LMCT, with some mixing with intra ligand or metal centred charge transfer depending on the ligand used. The existence of π orbitals on a phosphine phenyl ring could produce LLCT from $S(\pi)$ to $Ph(\pi^*)$ [45]. To complicate the situation even more, binuclear gold compounds can give luminescent aggregates at 77 K or room temperature through either the gold-gold interaction [4, 60] or π

stacking [61]. So the precise origin of the emission in any new gold phosphine thiolate compounds is still difficult to predict *a priori*.

Eisenberg and co-workers have carried out photoluminescence studies on some mononuclear gold phosphine 2-mercaptopyridine derivatives [14]. They observed a complex photochemistry with unclear assignments of the emission bands. Tzeng studied the binuclear gold complexes of 2-mercaptopyridine connected to dppm or dpph [12] and conclude that emission in the solid state or in solution originates from a [S→Au] transition.

In the photochemical analysis of the compounds reported here we will first describe the electronic absorption of the complexes, according to the type of N-heterocycle used. Then the photoluminescence results obtained in different media (glass at 77 K, room temperature solution, room temperature solid state) will be presented.. Then, a discussion of the effect on the photoluminescence of the phosphine, the presence or absence of a closed ring, and the thiolate ligands will be given.. The results from the DFT calculation discussed in detail in chapter 5 provide useful information for the interpretation of the experimental results.

4.3.1 Absorption spectroscopy

The electronic absorption spectra were measured in DCM:MeOH (1:1) solution; the values of the maximum absorption wavelengths (λ_{\max}) with their associated absorption coefficients (ϵ_{\max}) are reported in tables 4.7 to 4.9. For clarity, the results have been grouped according to the thiolate ligand. The absorption coefficients were calculated using the least squares method on Beer-Lambert plots for concentrations between $1\text{-}50 \times 10^{-5} \text{ mol dm}^{-3}$. The Beer-Lambert plots shows a linear regression along the range of concentration used, showing the absence of aggregation of the species present at these concentrations. (Due to the small amount of **4f** obtained, no Beer-Lambert study has been carried out for this compound.)

Our compounds have some features in common in their electronic absorption spectra: a high energy band at wavelength around 250 nm, then two bands at $\approx 264 \text{ nm}$ and $\approx 274 \text{ nm}$, and a series of lower energy absorption bands. Discussion of these low energy bands will be arranged according to the nature of the ring supporting the two thiolate groups: first benzene, then pyrimidine, then pyrazine and finally the pyridine ring.

All the chlorogold(I) phosphine precursors show absorption bands below 300 nm. The two absorption bands at 267 nm and 278 nm of $[\text{AuCl}(\text{PPh}_3)]$ have been attributed to a $[\text{n} \rightarrow \pi^*]$ transition and to a $[\pi \rightarrow \pi^*]$ transition respectively on PPh_3 [59]. We found a similar set of bands for all our binuclear gold products in the same region (268 nm and 274 nm) and therefore we attribute them also to the same transitions.

4.3.1.1 Complexes with a benzene-ring thiolate (**7a** and **8a**)

Absorption spectra are depicted in figure 4.8 and measurements summarised table 4.7. These two complexes have the same shape of absorption spectrum. Brown *et al.* assigned the two bands at 290 nm and 360 nm of a series of mono gold phosphine thiolates to LMCT $[\text{S} \rightarrow \text{Au}]$ [62]. The mononuclear complex $[\text{Au}(\text{SPh})(\text{PPh}_3)]$ has the same absorption maxima [63] and these have also been attributed to LMCT transitions. By analogy, the two bands at 288 and 330 nm are therefore assigned to LMCT $[\text{S} \rightarrow \text{Au}]$. Compound **8a** has an electron-withdrawing chloro-group, and therefore we would have expected a slight blue shift in the absorption bands of **8a**

compared with **7a**. This effect seems to be lost in this compound, perhaps because of the broad and unresolved absorption bands.

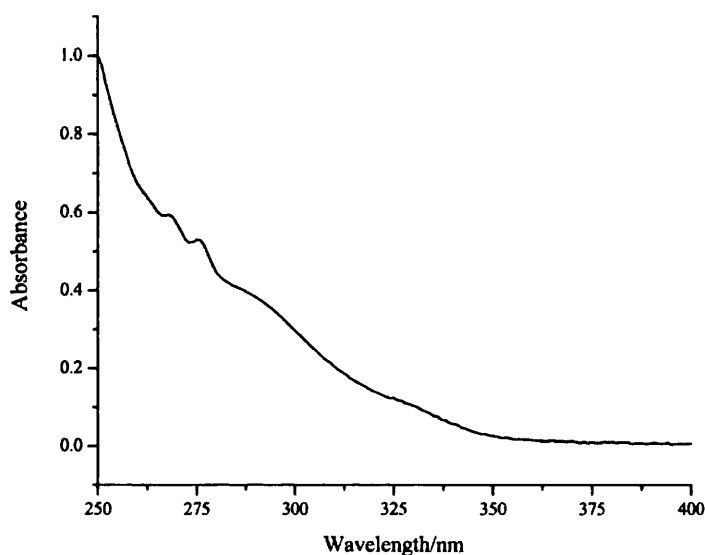


Figure 4.8: Room temperature absorption spectrum of **7a** in DCM:MeOH (1:1)

DMB	λ_{\max} in nm (ϵ_{\max} in $\text{dm}^3 \text{mol}^{-1} \text{cm}^{-1}$)	Cl-DMB	λ_{\max} in nm (ϵ_{\max} in $\text{dm}^3 \text{mol}^{-1} \text{cm}^{-1}$)
7a	236 (67000 \pm 3000) 274 (24000 \pm 1300) 288 (20000 \pm 1000) 330 (4300 \pm 200)	8a	236 (61000 \pm 2800) 274 (27000 \pm 1000) 288 (22000 \pm 700) 330 (4700 \pm 150)

Table 4.7: Maximum absorption wavelength (λ_{\max}) and absorption coefficients (ϵ_{\max}) for compounds with DMB and Cl-DMB as dithiolate ligand, in DCM:MeOH(1:1)

4.3.1.2 Compounds with a pyrimidine thiolate

Representative absorption spectra are given in figures 4.9 to 4-11 and measurements are summarised in table 4.8.

Most complexes, except those with dppm as the phosphine ligand, present similar spectra with bands at ≈ 286 nm, and ≈ 330 nm for the 24PYRI series (and for **2a**, 46PYRI connected to two triphenylphosphine gold units), with corresponding bands red shifted at ≈ 304 nm and ≈ 356 nm for NPYRI. These bands are too low in energy to be MC transitions. They could be ILCT (localised on the pyrimidine ring), LLCT ($S(\pi) \rightarrow \text{Ph}(\pi^*)$), MLCT, or LMCT transitions. NPYRI has two electron-donating

amino-substituents and when compare to its unsubstituted analogue 24PYRI, the red shift in absorption observed tends to eliminate the possibility of a MLCT transition.

24PYRI	λ_{\max} in nm (ϵ_{\max} in $\text{dm}^3 \text{mol}^{-1} \text{cm}^{-1}$)	NPYRI	λ_{\max} in nm (ϵ_{\max} in $\text{dm}^3 \text{mol}^{-1} \text{cm}^{-1}$)
1a	274 (54000 \pm 2000) 292 (62000 \pm 2000) 324 (25800 \pm 700) 366 (2300 \pm 100)	3a	276 (22100 \pm 800) 304 (14100 \pm 500) 348 (12700 \pm 400)
1b	234 (26300 \pm 900) 280 (11000 \pm 500) (shoulder) 338 (3900 \pm 200) 376 (330 \pm 30)	3b	268 (25700 \pm 700) 294 (15000 \pm 400) 356 (11100 \pm 400)
1c	274 (22000 \pm 700) 283 (21400 \pm 600) 328 (9000 \pm 200) 380 (310 \pm 80)	3c	274 (23200 \pm 800) 300 (14500 \pm 600) 346 (10800 \pm 500)
1d	236 (36500 \pm 700) 286 (16500 \pm 400) 330 (8300 \pm 200) 380 (300 \pm 20)	3d	274 (16000 \pm 800) 302 (11800 \pm 600) 348 (8600 \pm 400)
1e	274 (29200 \pm 700) 284 (28300 \pm 700) 328 (8700 \pm 600) 380 (280 \pm 90)	3e	274 (20500 \pm 900) 302 (11800 \pm 500) 344 (8800 \pm 400)
46PYRI	λ_{\max} in nm (ϵ_{\max} in $\text{dm}^3 \text{mol}^{-1} \text{cm}^{-1}$)	46PYRI	λ_{\max} in nm (ϵ_{\max} in $\text{dm}^3 \text{mol}^{-1} \text{cm}^{-1}$)
2a	274 (20000 \pm 1500) 285 (17000 \pm 1200) 324 (28600 \pm 1500)	2b	268 (14400 \pm 800) 322 (7500 \pm 500) 358 (6200 \pm 300)

Table 4.8: Maximum absorption wavelength (λ_{\max}) and absorption coefficient (ϵ_{\max}) for compounds with the dithiolate ligand having a pyrimidine ring, in DCM/MeOH(1:1)

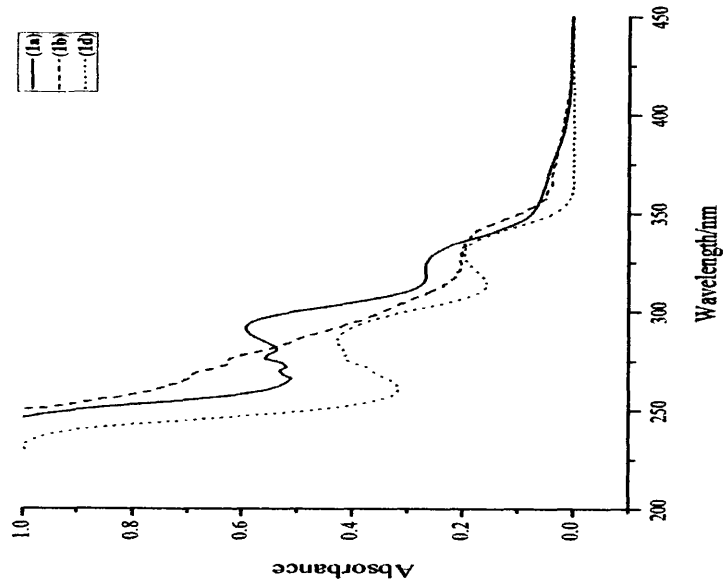


Figure 4.9: Normalised room temperature absorption spectra for **1a** (plain), **1b** (dash) and **1d** (dot) in DCM:MeOH (1:1)

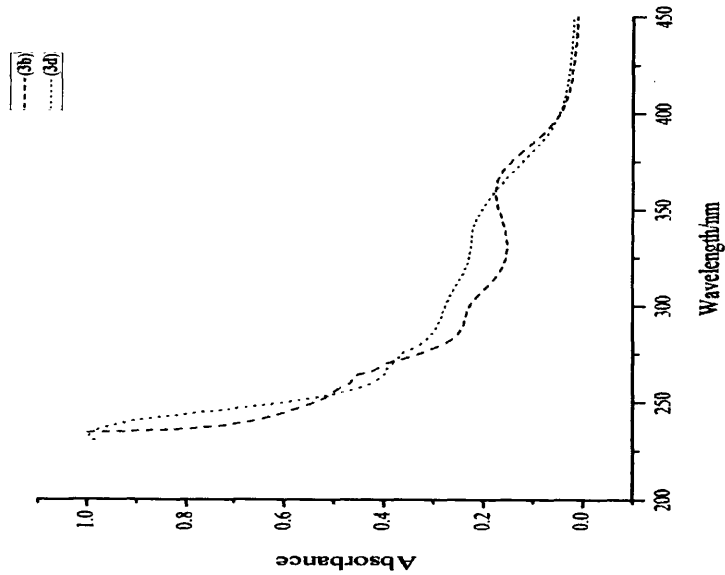


Figure 4.10: Normalised room temperature absorption spectra for **3b** (dash) and **3d** (dot) in DCM:MeOH (1:1)

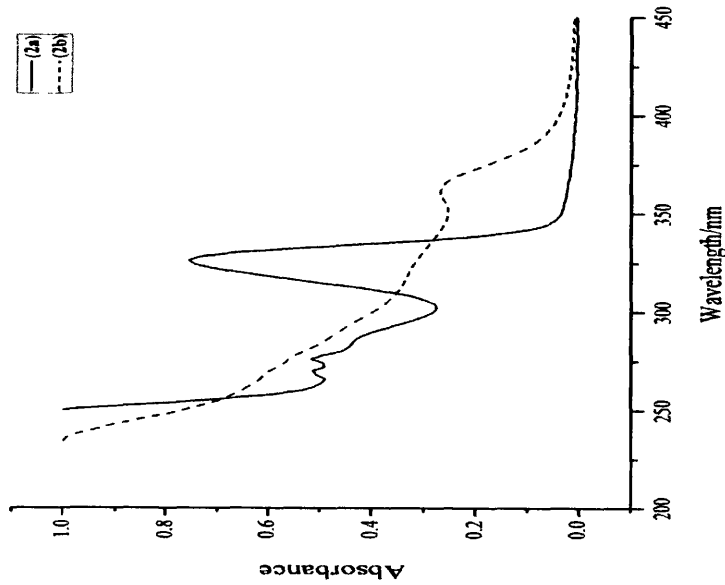


Figure 4.11: Normalised room temperature absorption spectra for **2a** (plain) and **2b** (dash) in DCM:MeOH (1:1)

It is not surprising that the two dimercaptopyrimidine isomers of these gold phosphine derivatives present the same absorption pattern, but the difference in absorption coefficients is intriguing.

A LMCT [S→Au] or [ligand→Au] transition would explain the red shift in absorption observed between NPYRI and 24PYRI and is consistent with the wavelength observed. ILCT is still possible as the free deprotonated ligand absorption spectra (see part 3.3.1.3) present bands in the same spectral region.

In the 24PYRI complexes, the extinction coefficients of the 380 nm bands are far lower than in the deprotonated ligands, and this may suggest a “forbidden” transition, perhaps of triplet nature.

dppm possesses two diphenylphosphino-groups linked by a methylene group. This relatively short linkage compared with the other phosphines could bring the two gold atoms closer, and perhaps close enough to induce a weak gold-gold interaction

4.3.1.3 Compounds with a pyridine thiolate

Absorption spectra are depicted in figures 4.13 and 4.14 and measurements summarised in table 4.10. The absorption spectrum of **4b** has no clear absorption maxima. When a second derivative is calculated using the Origin 8.0 program (see figure 4.12), some minima can be seen at high energy, but at low energy, noise prevents a clear attribution of absorption maxima. Compounds **4c**, **4d** and **4e** also show absorption spectra with broad and ill-defined absorption bands.

All compounds of this series have some high energy absorption bands around 260-274 nm which are attributed to ($n \rightarrow \pi$) and ($\pi \rightarrow \pi^*$) transitions localised on the phenylphosphine ligands, and also some low energy absorption bands, around 340 nm and 380 nm for the DMP series and at 345 nm and 395 nm for the ADMN series. The 340-345 nm bands do not correspond to any free ligand absorption, but the lower energy bands do and could therefore be attributed to ligand-based transitions.

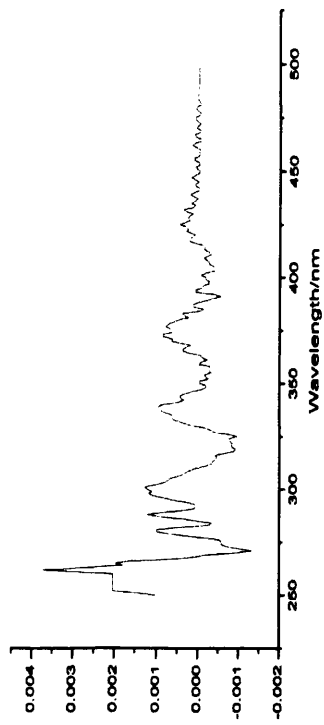


Figure 4.12: Second derivative for the absorption spectrum of complex **4b**

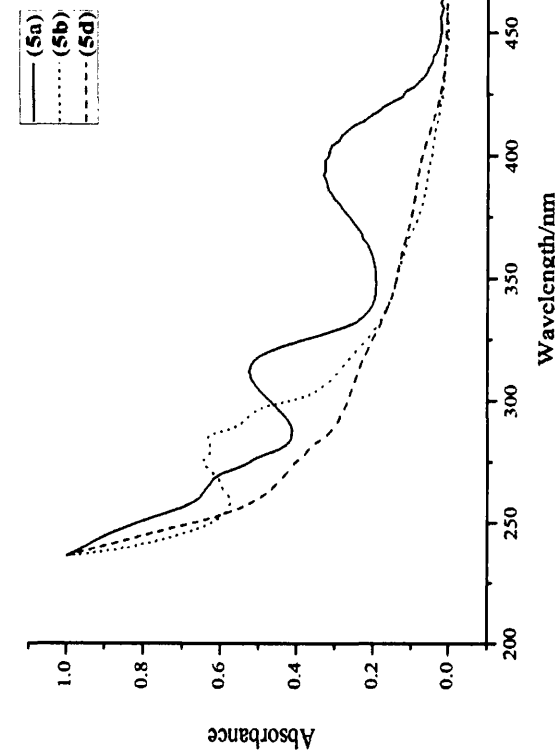
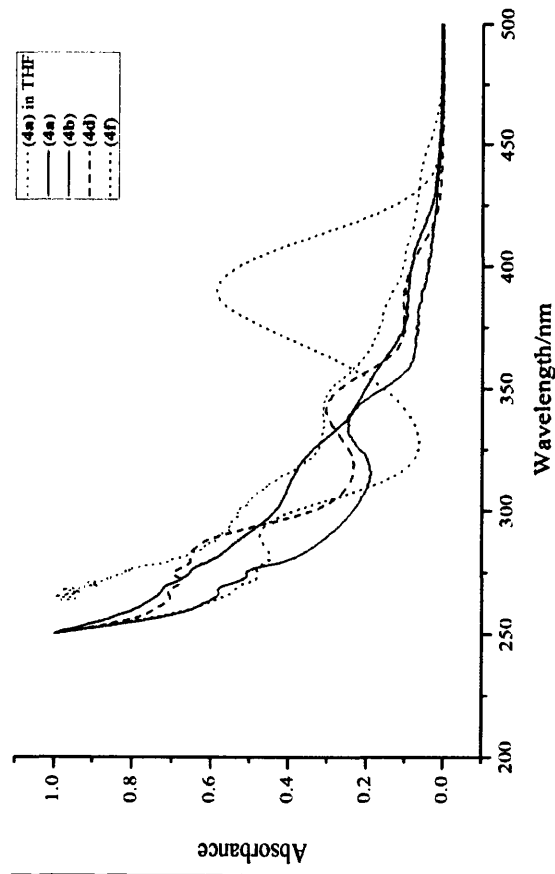


Figure 4.13: Absorption spectra for **4a** (plain red), **4b** (plain black), **4d** (dash black) and **4f** (dot black) in DCM:MeOH (1:1), for **4a** in THF (dot red)

Figure 4.14: Absorption spectra for **5a** (plain), **5b** (dot) and **5d** (dash) in DCM:MeOH (1:1)

Compound **5a** has a different spectral shape to all the other complexes, with an intense band at 398 nm and no bands present in the 350 nm region. The ^1H NMR spectrum shows that the compound is in the protonated form. This leads us to a study of the influence of a protonating agent on the absorption and luminescence properties of **4a**.

Influence of protonating or deprotonating species on compounds of the DMP series

When a drop of CF_3COOH was added to a solution of **4a**, the absorption spectrum was similar to that of **5a**, with an intense band at 384 nm and no bands in the 350 nm region (see figure 4.15). Even a solution made with crystals of compound (**4a**), for which protonation was observed by neither diffraction X-ray nor ^1H NMR spectroscopy, showed a weak absorbance peak at 385 nm in DCM:MeOH (1:1), which disappeared when some base (tetrabutylammonium hydroxide, 20% in MeOH) was added.

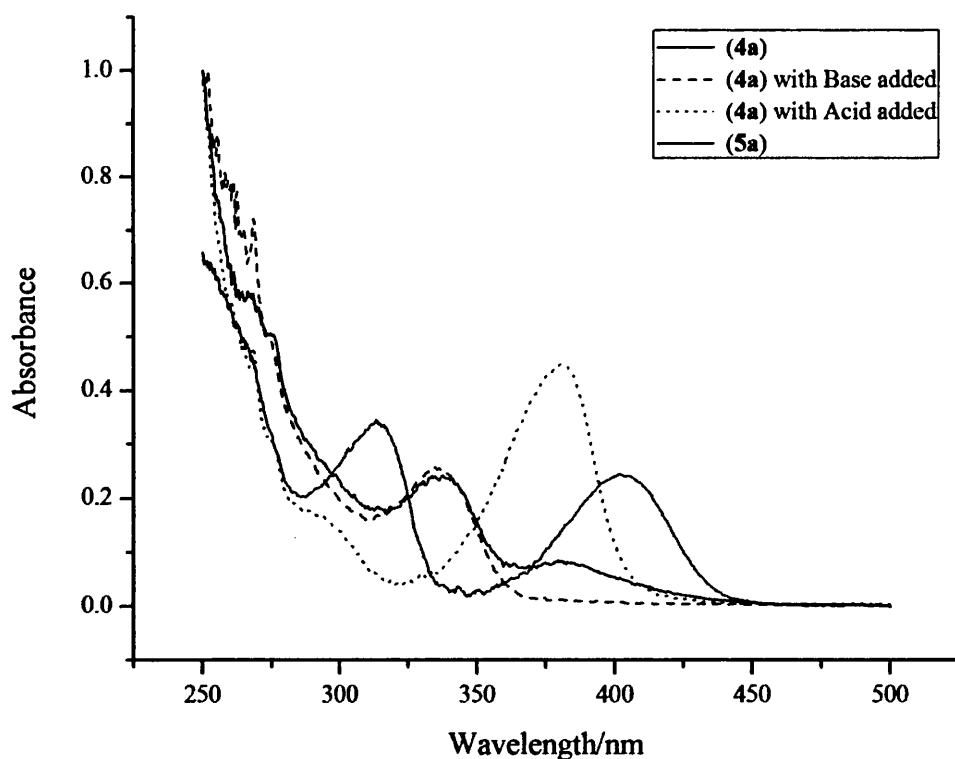


Figure 4.15: Normalised absorption in DCM:MeOH (1:1) of **4a** (black) starting material (plain), with some base added (dash), with some acid added (dot) and of **5a** (red)

Transitions involved in the absorption

The difference in electronegativity on Pauling's scale between gold and sulphur indicates the S-Au bond is polarised with a negative charge localised on the sulphur and a positive charge localised on the gold. A LMCT [S→Au] transition transfers an electron to the gold, and therefore reduces the polarity of the bond.

The transition at 340-350 nm for these complexes seems to be a LMCT, as for the pyrimidine complexes studied in this work, and similar compounds reported in the literature [12]. The band at 390 nm or 400 nm (for DMP or ADMN series respectively) could be a LMCT originating from the whole thiolate ligand

Being a mononuclear gold complex, **4f** is considered separately. The bands at 268 and 274 are attributed to the triphenylphosphine. The free ligand DMP absorbs at 290 nm and 380 nm. So the band at 290 nm could be attributed to a LMCT [S→Au] [14] and/or ILCT. The blue shift from 318 nm (for [Au(Spy)(PPh₂Py)] in DCM [14]) to 290 nm for our analogue could be due to both the more polar solvent used in our study and the electron-withdrawing effect of the thione on the pyridine ring (the mesomeric effect), both suggestive of a LMCT transition. Based on the absorption of the free ligands, the 390 nm band is probably an ILCT transition based on the thione moiety.

The solvent effect on the absorbance is in accordance with the LMCT attribution: in less polar THF the bands at 336 nm and 380 nm are red-shifted to 346 nm and 400 nm respectively, meaning that the excited state is less polarised than the ground state. As mentioned at the beginning of this section, the LMCT will reduce the polarity of the S-Au bond.

DMP	λ_{\max} in nm (ϵ_{\max} in $\text{dm}^3 \text{mol}^{-1} \text{cm}^{-1}$)	ADMN	λ_{\max} in nm (ϵ_{\max} in $\text{dm}^3 \text{mol}^{-1} \text{cm}^{-1}$)
4a	234 (66300 \pm 3000) 274 (26500 \pm 1000) 336 (13800 \pm 800) 380 (3800 \pm 400)	5a	274 (22600 \pm 1000) 314 (30500 \pm 1500) 398 (22400 \pm 500)
4b	274 (32900 \pm 800) 318 \pm 3 (21100 \pm 500) 354 \pm 3 (broad shoulder) 396 \pm 5 (2500 \pm 200)	5b	274 (38000 \pm 1200) 312 \pm 3 (28000 \pm 1000) 354 \pm 3 (12400 \pm 800) 404 \pm 3 (4500 \pm 400)
4c	274 (15500 \pm 700) 341 (6800 \pm 400) 392 (1650 \pm 150)	5c	274 (22000 \pm 1100) 302 (20700 \pm 1000) 345 (15400 \pm 600) 398 (8100 \pm 500)
4d	274 (11200 \pm 500) 335 (5400 \pm 300) 390 (1500 \pm 200)	5d	278 (12100 \pm 300) 302 (9700 \pm 200) 344 (5100 \pm 200) 395 (4100 \pm 100)
4e	274 (11800 \pm 500) 336 (5500 \pm 400) 392 (1000 \pm 90)	4f	274 ^a 290 ^a 390 ^a

^a: due to the small amount of product available no extinction coefficients were measured

Table 4.10: Maximum absorption wavelength (λ_{\max}) and absorption coefficients (ϵ_{\max}) for compounds with DMP and ADMN as dithiolate ligand, in DCM/MeOH (1:1)

4.3.1.4 Compounds with a pyrazine thiolate

Absorption spectra are shown in figure 4.16 and measurements summarised in table 4.9.

They show three peaks around 290 nm, \approx 376 nm and \approx 430 nm. By comparison with literature values, and with the pyrimidine series described previously, the two high energy bands are attributed to LMCT [S \rightarrow Au] transition.

The low energy absorption band around 430 nm appears in the free ligand absorption spectra. This absorption maximum varies according to the phosphine used, so it can not be a pure intraligand charge transfer which would be insensitive to these substitutions. A LMCT from the ligand itself to the gold atom is possible and would explain the red shift in maximum absorption when dppm is used as phosphine ligand because the two gold atoms are brought closer together. The first two transitions have the origin of their ground state localised more on the sulphur, whereas the lower energy transition has a ground state delocalised over all the thiolate ligand.

DMPA	λ_{\max} in nm (ϵ_{\max} in $\text{dm}^3 \text{mol}^{-1} \text{cm}^{-1}$)
6a	276 (12100 \pm 400) 295 (4800 \pm 200) (shoulder) 376 (3000 \pm 100) 442 (1900 \pm 100) (shoulder)
6b	274 (14200 \pm 500) 310 (9500 \pm 400) 382 (4200 \pm 200) 436 (1200 \pm 100) (shoulder)
6d	274 (24300 \pm 600) 286 (20300 \pm 500) 376 (7500 \pm 300) 428 (2500 \pm 200) (shoulder)

Table 4.9: Maximum absorption wavelength (λ_{\max}) and absorption coefficient (ϵ_{\max}) for compounds with DMPA as dithiolate ligand in DCM/MeOH (1:1)

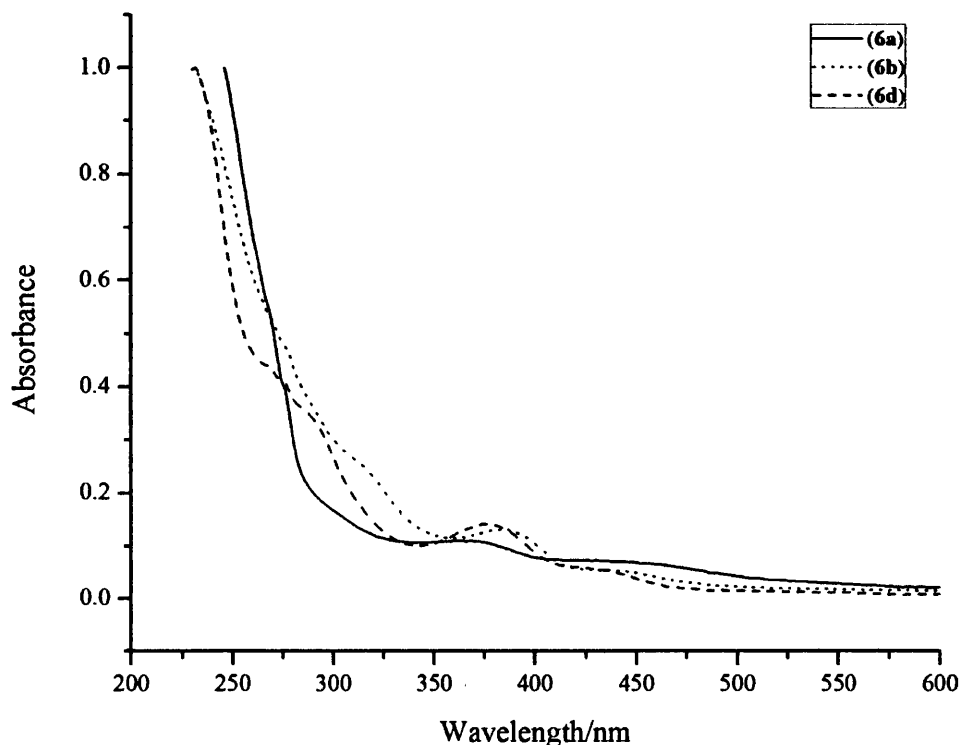


Figure 4.16: Room temperature absorption spectra for **6a** (plain), **6b** (dot) and **6d** (dash), in DCM:MeOH (1:1)

4.3.1.5 General conclusions from the absorption study

No aggregation was detectable in the Beer-Lambert study at the concentrations used. These compounds have in common an intraligand transition based on the phosphine at 268 nm and 275 nm, and a LMCT [S→Au] transition in the 330-360 nm region with the exact position depending on the thiolate ligand. Some mixing with a LMCT arising from the ligand instead of the sulphur, or with some metal-centred transition, is not excluded.

The low energy absorption bands appearing for some compounds above 380 nm could also originate from a LMCT based on the whole thiolate ligand, a suggestion which is supported by the TD-DFT calculations described in chapter 5.

4.3.2 Photoluminescence studies

Photoluminescence studies have been carried out in solution at room temperature and 77 K, and in the solid state at room temperature. Results will be presented according to the dithiolate ligands of the compounds. Then the data will be compared across all compounds studied to determine the influence of the dithiolate ligand and of the phosphine ligand.

4.3.2.1 Experimental

All the low temperature measurements were done at 77 K. The solvent used was a mixture of DCM:MeOH (1:1) which gives an optically transparent glass without any cracking. Solutions of the desired compound were put in a 3 mm diameter NMR tube, which was immersed in a Dewar containing liquid nitrogen. The absorbances of the solutions used were all below 0.2 in a 1 cm quartz cell at the excitation wavelength. The 77 K quantum yields were all measured using 330 nm excitation with the phosphorescence emission of benzophenone ($\Phi_p = 0.9$ in a polar solvent [64]) as reference. All spectra were corrected for the photomultiplier response and the lamp profile, and are shown normalised. As expected, 77 K excitation spectra are shifted compared to the room temperature absorptions. Low temperature time-resolved studies have been carried out using the device described section 2.3.2.1. Different energy pulses were used by changing the source voltage to check the absence of double photon absorption; the slits of the monochromator were set at 8 nm. The solid state measurements were obtained using a solid state attachment in which the sample is held between two round transparent quartz plates, and using slit of 6 nm width for both excitation and emission monochromators.

4.3.2.2 Binuclear gold phosphine series with 24PYRI as dithiolate

Binuclear gold phosphine complexes of 2,4-dimercaptopyrimidine are all luminescent at 77 K in a DCM:MeOH (1:1) glass and in the solid state at room temperature. No noticeable luminescence was detected in nitrogen purged DCM:MeOH (1:1) solution at room temperature. The behaviour of compounds **1c**, **1d** and **1e** will first be described then that of **1a** and **1b**.

In a glass at 77 K, compounds with the longer chain between the two phosphines **1c**, **1d** and **1e**, all give the same emission pattern (see figure 4.17 as example) with three

emission bands at 390 nm, 410 nm and 430 nm which appear for any excitation wavelength. The emission is long lived which indicates that it originates from a forbidden transition, and is therefore considered to be phosphorescence.

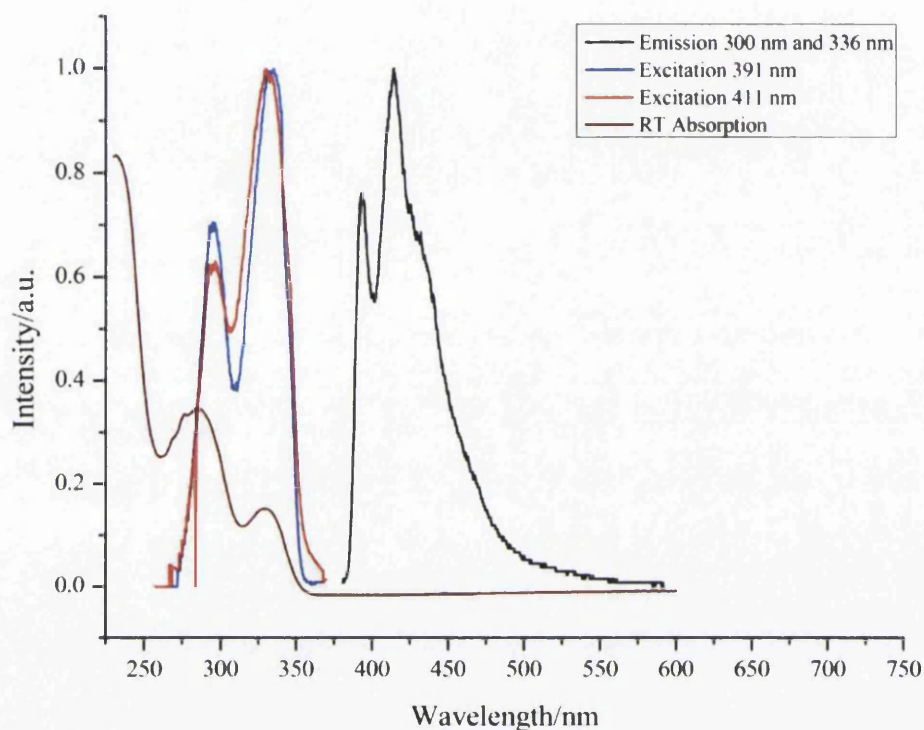


Figure 4.17: Excitation and emission spectra for compound **1c** in a DCM:MeOH (1:1) glass at 77 K: normalised excitation (blue for 391 nm and red for 411 nm) and emission spectra (black), room temperature absorption spectrum (brown)

Phosphine intraligand CT or thiolate-based CT as an origin of the emission can be discarded for the following reasons.

- 1) Variation in the emission spectra for different phosphines is not as great as would be expected if the emission was from the phosphine ligand.
- 2) Different gold phosphine thiolates with tricyclohexanylphosphine [25, 49, 60] or TPA [26] instead of a phenyl-substituted phosphine also emit despite the absence of the benzene rings.
- 3) 24PYRI emits at 488 nm and 516 nm in this solvent at 77 K. (see chapter 3).
- 4) The excitation spectra show no bands at wavelength lower than 290 nm, where the π orbital based on the phosphine absorbs.

A MC triplet origin of the luminescence is not excluded, but cannot by itself explain the variation in the emission spectra. In gold compounds with a reducing ligand such as thiolate the lowest excited state is expected to be of a LMCT nature [65], and the excitation spectra show clearly that the emission originates from absorptions at 300 nm and 336 nm previously attributed to a LMCT [S→Au] charge transfer.

Gated spectra at 10 μ s between 395 nm and 500 nm match quite well the corresponding emission spectra of compounds **1c**, **1d** and **1e**. At any emission wavelength, deconvolution of the time-resolved curves gives a good fit to a double exponential decay. Normalised spectra at different emission wavelengths show that emission across the 400 to 440 nm range has the same kinetics, but the kinetics change at longer wavelength (see figure 4.18). This difference is difficult to explain. The origin of the double exponential decay is unclear, as all analysis seems to indicate that only one species is present. However a double exponential decay was also observed by Fackler in the solid state luminescence of a series of mononuclear gold phosphine thiolates [26] and this was attributed to the presence of both a LMCT transition and an intraligand transition involving π orbitals of the phosphine.

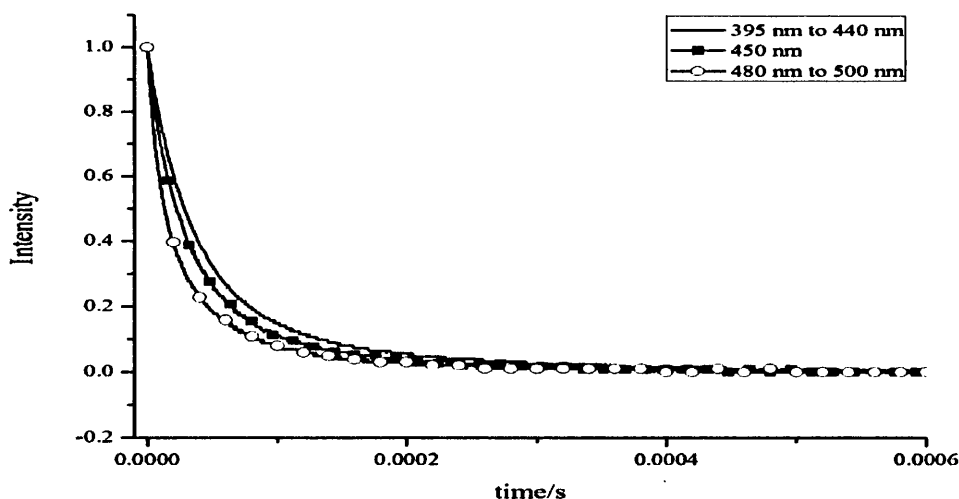


Figure 4.18: Normalised time-resolved spectra for **1e** between 395 nm and 440 nm (no figure), at 450 nm (filled figures) and between 480 and 500 nm (hollow figures)

24PYRI	77 K λ_{max} (nm)	77 K lifetime (μs) (excitation 355 nm)	77 K quantum yield ^(a)
1a	386		0.66
	420	13.9 (\pm 1.4) 90%	
	475	6.2 (\pm 1.8) 10%	
1b	385		0.38
	409		
	430	12 (\pm 1) 25%	
	516	3.2 (\pm 0.2) 75%	
1c	394	77 (\pm 5) 80%	0.82
		18 (\pm 1) 20%	
	410	77 (\pm 4) 66%	
		6 (\pm 0.5) 33%	
	430	68 (\pm 3) 74%	
	3.5 (\pm 0.3) 26 %		
1d	395	6.5 (\pm 0.3) 22%	0.82
		2.1 (\pm 0.3) 76%	
	411	5.6 (\pm 0.3) 30%	
		1.9 (\pm 0.2) 70%	
	433	5.7(\pm 0.3) 30%	
	1.8 (\pm 0.2) 70%		
1e	394		0.9
	412	180 (\pm 10) 20%	
		32 (\pm 2) 80%	
	431	180 (\pm 10) 20%	
		32 (\pm 2) 80%	

Table 4.10: 77 K photochemical properties of gold phosphine thiolates with 24PYRI as ligand

^(a) reference to benzophenone having $\Phi_{\text{P}} = 0.9$

Compounds **1a** and **1b** have emission patterns (see figures 4.19 and 4.20) different from those of the compounds with a longer chain between the phosphine groups. When considering **1a**, the 10 nm red shift for these bands is consistent with the LMCT origin of emission described previously, as the triphenylphosphine moiety is a less effective σ donor its their bridged diphosphine analogues. The lifetime measured at 420 nm for **1a** is over the microsecond range, so we assume that the radiative deactivation process here is phosphorescence.

The new features are found in the low energy region and consist of a band at 475 nm for **1a** and 516 nm for **1b**. The large gap between the emission and the excitation spectra, and the lifetime in the microsecond range for the 516 nm band for **1b**, indicate phosphorescence. For **1a**, the excitation spectra corresponding to this low energy emission wavelength show a shoulder at lower intensity which appears in the room temperature absorption spectra as a very weak band ($\epsilon_{\max} = 2300$); this shoulder is absent in the excitation spectra for the emission bands of higher energy. In **1b**, this absorption band appears also with an even weaker absorption coefficient (ϵ_{\max} around 600). Possible explanations for this new emission are the following.

- 1) Aggregation has occurred at low temperature through the aurophilic interaction, and this is responsible for a phosphorescent luminescence in this region through metal-metal centred emission of a [d \rightarrow p] origin [60]. The aggregation phenomenon is linked directly to the type of ligand used.
- 2) As explained before, dppm will sterically pull the two gold atoms closer. The gold-gold distance will be reduced and aurophilicity can appear. And the emission could then originate from a LMMCT excited state. This explanation is valid just for **1b** though.
- 3) A last possibility would be that the nitrogen of the hetero cycle and the gold interact. This interaction is possible for **1b** through the steric effect of the dppm, and is seen in the crystal structure of **4a**, the pyridine analogue of **1a**. This interaction could enhance an [Au \rightarrow ligand] radiative deactivation.

Although a possibility we consider aggregation improbable as no such phenomenon is observed at the same concentration with longer chain diphosphines, and the bulkiness of dppm is not that different from that of the dppe or dppb analogues. A

LMMCT is also unlikely as it will not explain the band observed for **1a**. Therefore we suggest the enhancement of a gold to ligand transition through a weak Au-N interaction as the most probable reason for this emission.

Emission quantum yields are high, presumably because the ring and the rigid ligand reduce non-radiative pathways arising from molecular torsion.

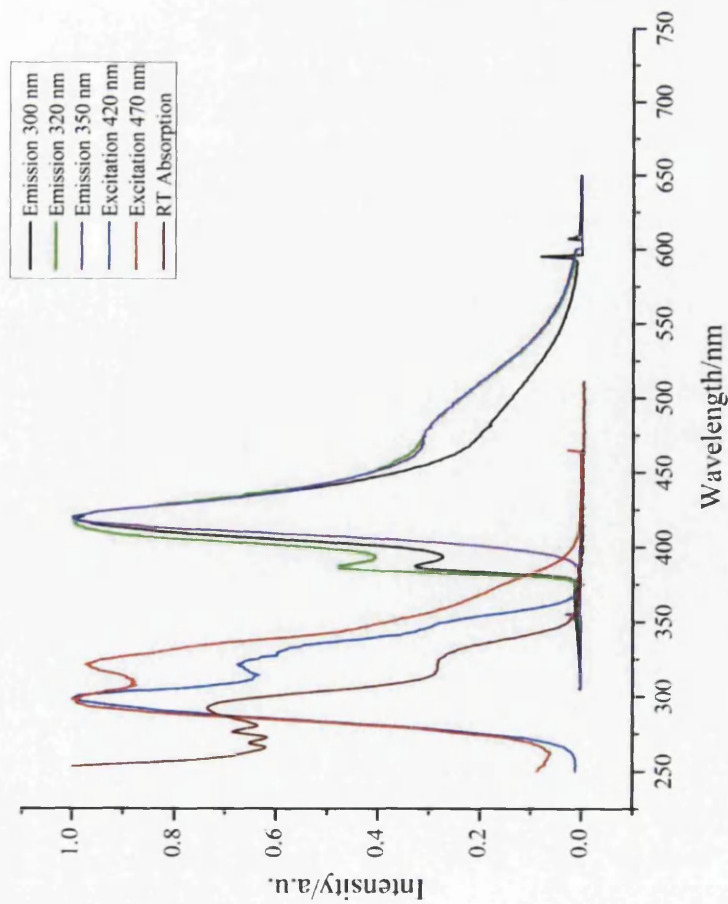


Figure 4.19: Emission and excitation spectra of compound **1a** in a DCM:MeOH (1:1) glass at 77 K: normalised excitation spectra at 420 nm (blue) and 470 nm (red), and emission spectra at 300 nm (black), 320 nm (green), and 350 nm (violet); room temperature absorption spectrum (brown)

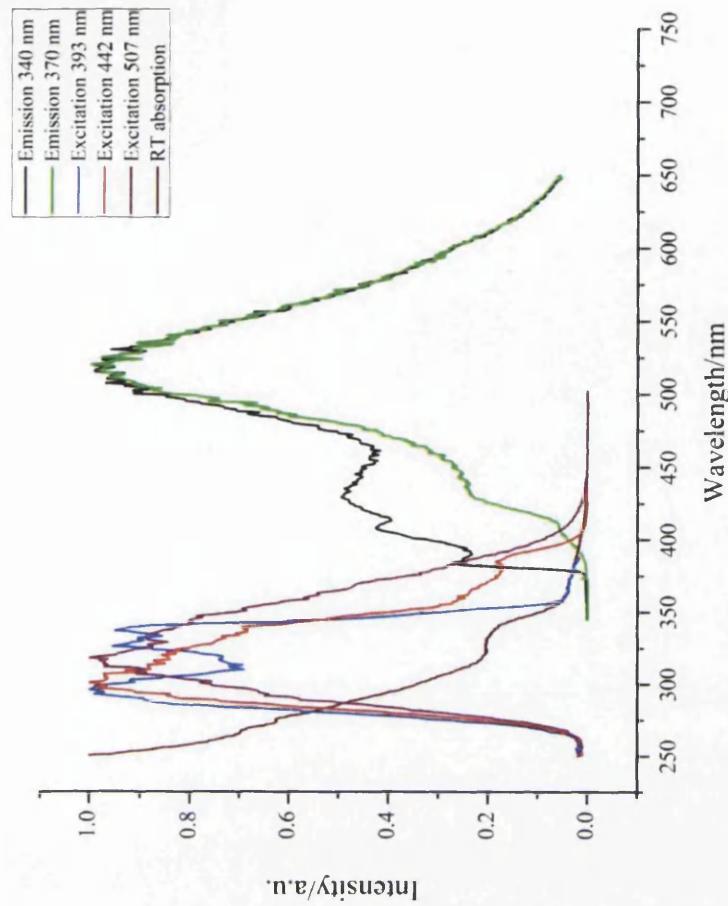


Figure 4.20: Emission and excitation spectra of compound **1b** in a DCM:MeOH (1:1) glass at 77K: normalised excitation spectra at 393 nm (blue), 442 nm (red), and 507 nm (violet); emission spectra at 340 nm (black) and 370 nm (green); and room temperature absorption spectrum (brown)

All these compounds seem to emit in a glass at 77 K through a highly efficient phosphorescence process originating from LMCT excited state mixed with possible MC emission.

The compounds are non-luminescent in a nitrogen-purged DCM:MeOH (1:1) solution at room temperature. The non-phosphorescence in solution is not an unusual result for gold phosphine thiolates [12, 26]. However, the use of a non-protic solvent such as THF or DCM would be worthwhile in further studies.

At room temperature in the solid state, a bright green emission is seen upon excitation at 330 nm or 370 nm (see figure 4.21). The large shift between the excitation and emission spectra lets us assume that this is a phosphorescent emission. The excitation spectra correspond to the absorption bands in solution assigned to LMCT transitions. The emission maxima change according to the phosphine present so the emission could not be originating from the thiolate ligand; therefore we attribute the origin of the emission to be the excited state $^3[\text{S} \rightarrow \text{Au}]$, possibly mixed with $^3[\text{ligand} \rightarrow \text{Au}]$ [49]. As the emission bands are quite broad (FWHM of 100 nm or greater) and ill defined because of the noisy signal it is hard to determine precisely any trend in the emission spectra. Nevertheless, **1b** emission is slightly red shifted which could be due to the enhancement of the $[\text{Au} \rightarrow \text{ligand}]$ process described before.

Compound	1a	1b	1c	1d	1e
λ_{max} (nm)	490 (± 5)	530 (± 5)	510 (± 5)	-	510 (± 5)

Table 4.11: Room temperature emission in the solid state for complexes with 24PYRI as ligand. The spectrum of **1d** was not measured, because of the small amount of compound available.

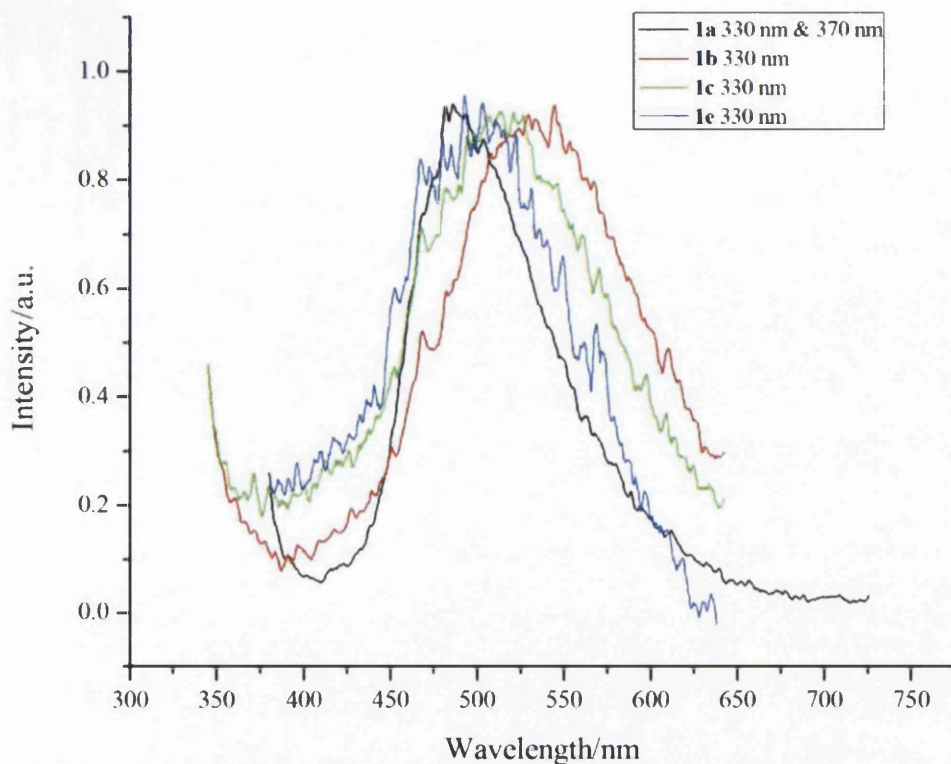


Figure 4.21: Room temperature solid state emission for compounds of the 24PYRI series

4.3.2.3 Binuclear gold phosphine series with NPYRI as dithiolate

The 77 K emission and excitation spectra are given in figures 4.22 and 4.23, and the data are summarised in table 4.12.

This class of compounds emits in a glass made of DCM:MeOH (1:1) at 77 K. The emission is a broad band with a full-width-at-half-maximum (FWHM) around 90 nm; no vibrational bands are observed. Except for compound **3b** which has dppm as a bridging diphosphine, no change in the emission bands is observed when the excitation wavelength changes. Compared to their 24PYRI analogues, their emission is red shifted by + 90 nm on average. The two amino-groups are electron donors, and will destabilize the HOMO and therefore reduce the HOMO-LUMO energy gap. This red shift in emission confirms our previous assignment of the emission to originate from a $[S \rightarrow Au]$ excited state.

The large gap between the excitation and emission spectra and the sub-millisecond lifetime of the excited state allow us to attribute these emissions to phosphorescence. Their phosphorescence quantum yields are lower than those of their 24PYRI

analogues, probably due to the non-radiative pathway possibility offered by vibration of the two amino-groups on the heterocyclic ring. The gated time-resolved study analysis shows that the same kinetics are followed across the emission band. The decay seems to follow two first order pathways as the curves fit a double exponential. We can reasonably suppose that a [Au→S] and a [Au→ligand] transition are responsible for the dual emissive pathways.

NPYRI	77 K λ_{\max} (nm)	77 K Lifetime (μs) (excitation 355 nm)	77 K quantum yield ^(a)
3a	540	700 (± 5) 47% 120 (± 2) 49%	0.31
3b	446 525	309 (± 10) 40% 30 (± 2) 58% 420 (± 12) 38% 67 (± 4) 60%	0.45
3c	(407, 435, weak) 528	475 (± 10) 34% 102 (± 4) 65%	0.38
3d	(412, 440 weak) 518	517 (± 37) 50% 130 (± 14) 50%	0.50
3e	(412, 440 weak) 530	694 (± 10) 35% 165 (± 3) 65%	0.38

Table 4.12: 77 K photochemical properties of gold phosphine thiolates with NPYRI as ligand.

^(a) reference to benzophenone having a $\Phi_p = 0.9$

As seen for the 24PYRI series, these compounds also do not present any noticeable emission in a DCM:MeOH (1:1) solution at room temperature.

The solid state emission was too low in intensity to be measured.

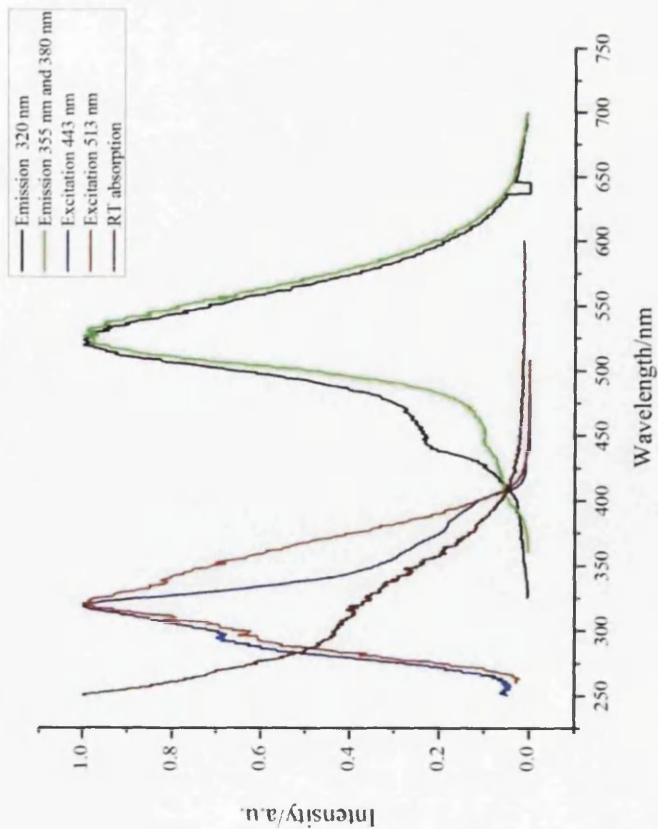


Figure 4.22: Emission and excitation spectra of compound **3b** in a DCM:MeOH (1:1) glass at 77 K: normalised excitation spectra at 443 nm (blue) and 513 nm (red); emission spectra at 320 nm (black), 355 nm and 380 nm (green); and room temperature absorption spectrum (brown)

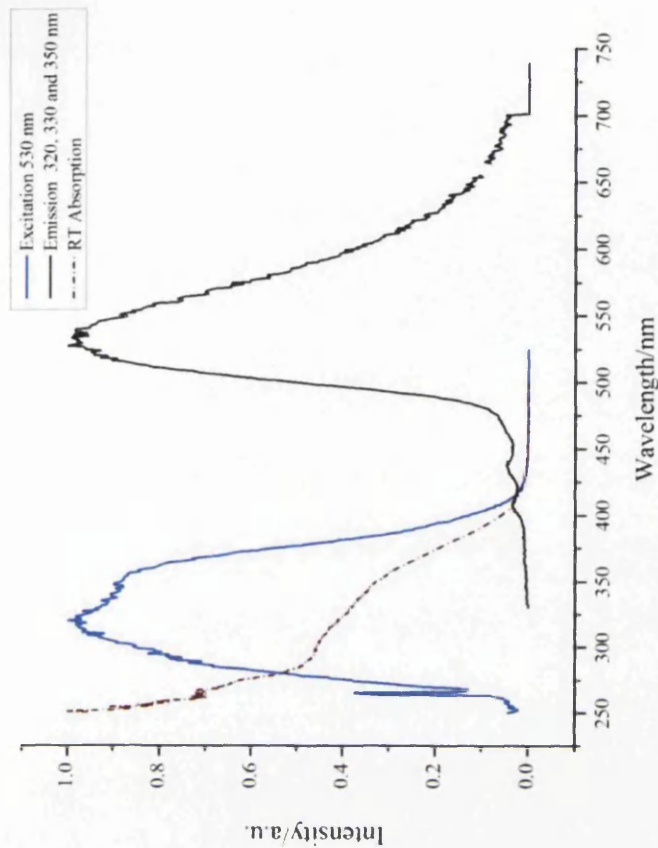


Figure 4.23: Emission and excitation spectra of compound **3c** in a DCM:MeOH (1:1) glass at 77 K: normalised excitation spectrum (blue); normalised emission spectrum (black); and room temperature absorption spectrum (brown)

4.3.2.4 Binuclear gold phosphine series with 46PYRI as dithiolate

The interesting feature of these compounds is the absence of nitrogen in the heterocycle between the two sulphur binding sites, but with a thiolate bridging ligand which should have a similar charge effect on the sulphurs as 24PYRI. The emission and excitation spectra at 77 K are depicted in figures 4.24 and 4.25, and the results are summarised in table 4.13.

The 77 K excitation spectra for both compounds have the same shape as the absorption spectra at room temperature with a maximum at 330 nm for **2a** and 360 nm for **2b**. For both compounds a band at 403 nm (**2a**) and 415 nm (**2b**) is present as a shoulder in the 77 K emission spectra. Due to the close proximity in energy to the band in the excitation spectra this emission could be fluorescence. However the spectra are dominated by two more intense bands at 438 nm (**2a**) and 505 nm (**2b**) which are shifted sufficiently from their corresponding excitation spectra to be considered to be phosphorescence. Quantum yields are relatively high at around 0.4. The relative red shift in emission of **2b** compared to **2a** could be explained following the same arguments as before, *i.e.* a shorter gold-gold distance or a gold-nitrogen interaction. The red shift seems to confirm once more the attribution of this emission to a triplet state originating from a LMCT [S→Au] excitation [49].

46PYRI	77 K λ_{\max} in nm	77 K quantum yield	Room temperature solid state λ_{\max} in nm
2a	403 (shoulder) 438 474 (shoulder)	0.42 (± 0.08)	520
2b	415 (shoulder) 443 505	0.44 (± 0.08)	522

Table 4.13: Photochemical properties of gold phosphine thiolates with 46PYRI as ligand

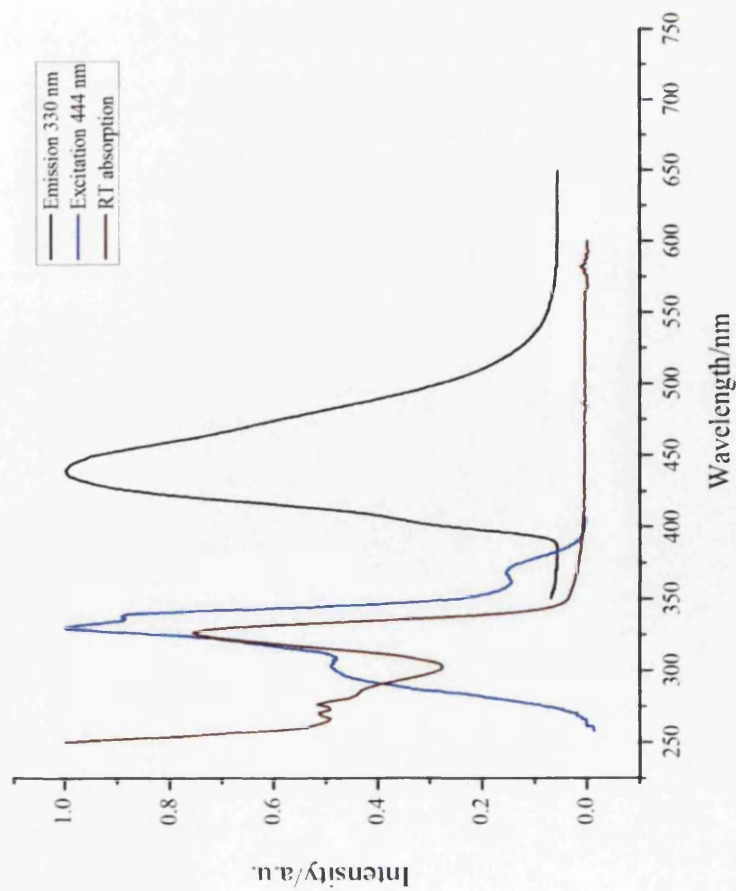


Figure 4.24 Compound **2a** in a DCM:MeOH (1:1) glass at 77 K: normalised excitation spectrum at 444 nm (blue); normalised emission spectrum at 330 nm (black); and room temperature absorption spectrum (brown)

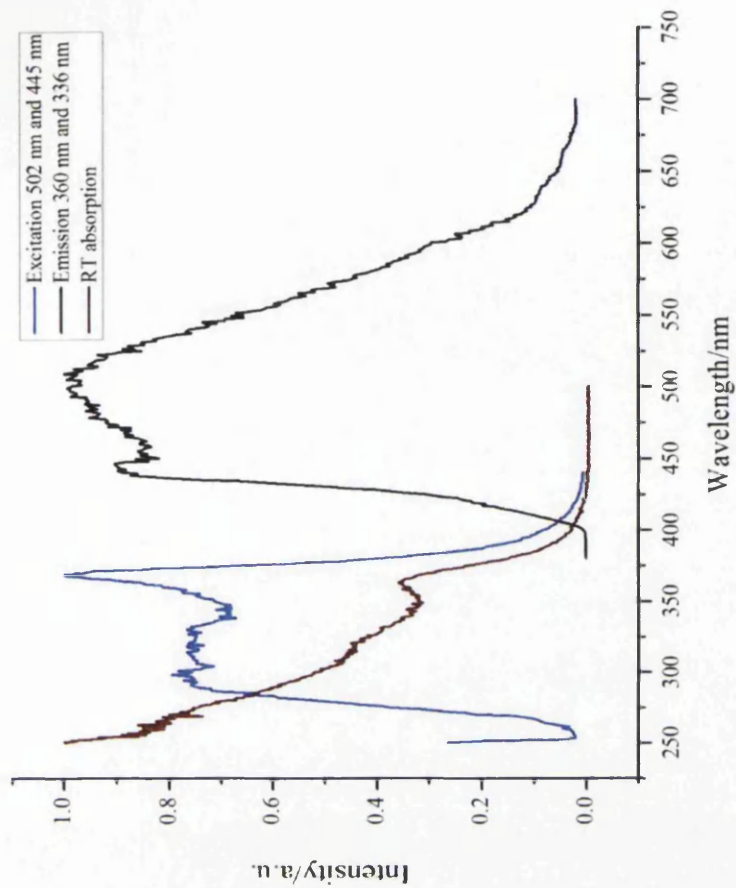


Figure 4.25: Compound **2b** in a DCM:MeOH (1:1) glass at 77 K: normalised excitation spectrum at 502 nm and 445 nm (blue); normalised emission spectrum at 360 and 336 nm (black); and room temperature absorption spectrum (brown)

In DCM:MeOH (1:1) solution no noticeable luminescence was observed, even when nitrogen purged.

When excited at 330 nm in the solid state at room temperature (figure 4.26), these compounds emit around 520 nm with a broad (FWHM = 150 nm for **2a** and 175 nm for **2b**) poorly defined band. The excitation spectra follow the low energy part of the room temperature solution absorption spectra and there is a large gap between the two spectra. Therefore this emission can possibly be attributed to originate from a LMCT $^3[S \rightarrow Au]$ excited state [49]. Possible mixing with a MC state is not excluded. The signals are too noisy to draw further conclusion on the origin of the emission.

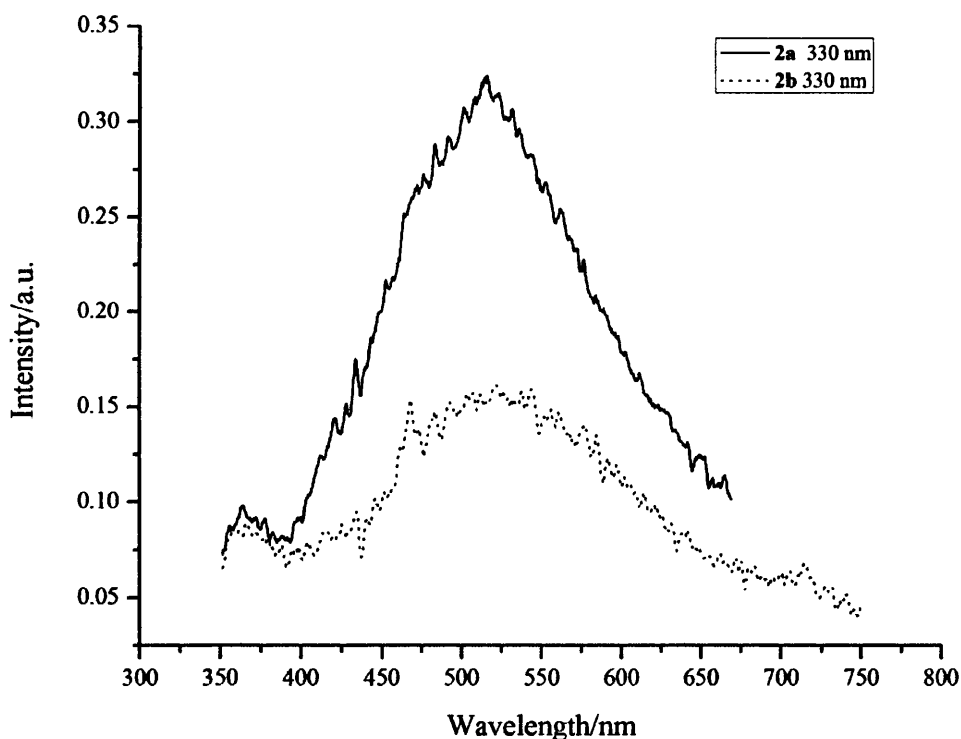


Figure 4.26: Normalised room temperature solid state emission spectra for **2a** (plain) and **2b** (dot)

4.3.2.5 Binuclear gold phosphine series with DMPA as dithiolate

The emission and excitation spectra at 77 K are depicted in figures 4.27 to 4.29. The results are summarized in table 4.14. In this series, the emission maximum of the free ligand is similar to the emission maximum of the gold derivative, therefore the 77 K DMPA emission in a DCM:MeOH (1:1) glass excited at 380 nm has been shown on the figures as a dotted curve to aid discussion.

The compounds in a glass made of DCM:MeOH (1:1) at 77 K emit brightly in the yellow. The emission spectra of compounds **6a** and **6d** are very similar to the one of the free deprotonated ligand DMPA. But their excitation spectra at any emission wavelength are different and are clearly separated from the emission spectra by 30 nm for **6a** and **6d**. This shift indicates the possibility of phosphorescence-like emission, confirmed for **6a** by time-resolved measurements. Furthermore, their emission band is not exactly of the same width as that for the ligand (FWHM of 55 nm for DMPA, 80 nm for **6a** and 60 nm for **6d**). So the relative closeness of the emission spectra of the species seems to be coincidental. Neither free ligand impurities nor IL charge transfer from the pyrazine ring are responsible for the emission. This is further supported by the fact that derivative **6b** has an emission band red shifted by 20 nm compared with DMPA. The high energy band emission has an excitation profile which indicates it originates from a LMCT [S→Au] excited state [49] with possible mixing with a MC excited state. The low energy band at 550 nm appearing for both compounds **6a** and **6b** originate from excitation spectra with a tail in the 400 nm region. This could be due to aggregation or a weak N-Au interaction. Another possibility which will be developed further in the next part, when discussing the DMP analogues, is the presence of a protonated species in solution.

Time-resolved studies have been carried out for **6a** at 77 K. Gated spectra between 470 nm and 510 nm show a good fit with the emission spectra, and the deconvolution of the time-resolved data fits a double exponential. Two first order kinetic processes are involved in the radiative deactivation in the emission range 470 - 510 nm, one very long lived (1.35 ms) and the other one shorter lived (277 μ s). The emission lifetimes at 580-590 nm also corresponds to two first order processes but with different kinetics, which might be explained by protonation of the compounds.

DMPA	77 K λ_{max} in nm (lifetime in μs)	77 K quantum yield	RT solid state λ_{max} in nm
6a	495 (1350 \pm 60 (45%), 277 \pm 20 (53%)) 577 (12.7 \pm 0.2 (50%), 170 \pm 1 (50%))	0.9 (\pm 0.1)	554 nm
6b	520 550 570	0.9 (\pm 0.1)	551 nm
6c	498	0.8 (\pm 0.11)	560 nm

Table 4.14 Photochemical properties of gold phosphine thiolates with DMPA as ligand

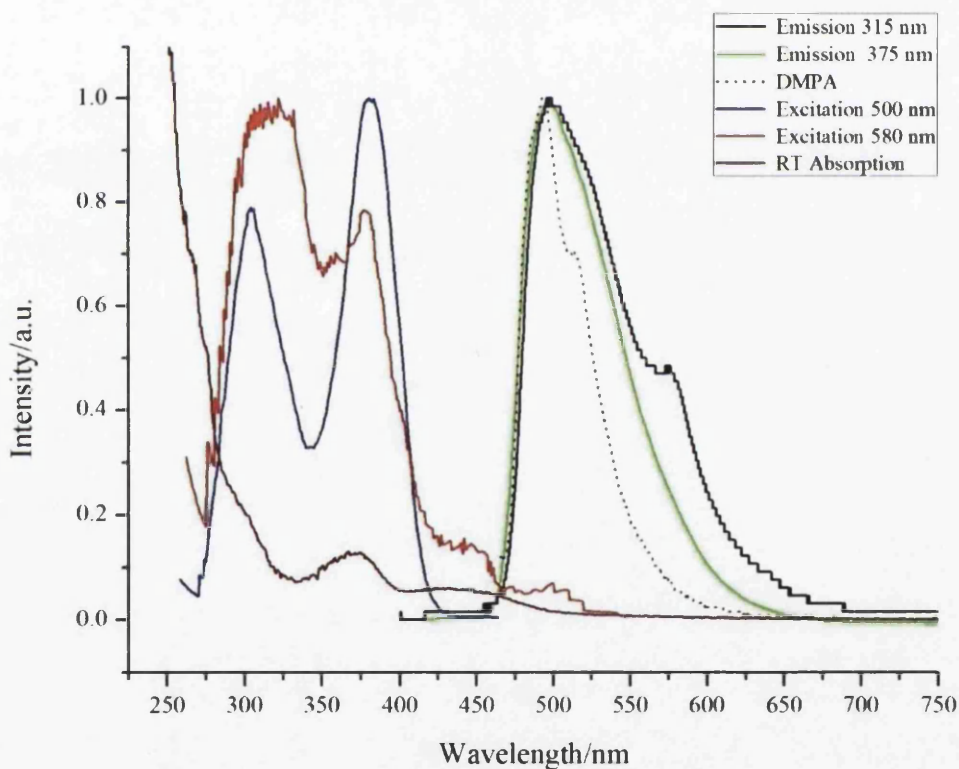


Figure 4.27: Compound **6a** in a DCM:MEOH (1:1) glass at 77 K: normalised excitation spectra for 500 nm (blue) and 580 nm (red); normalised emission spectra with excitation at 315 nm (black) and 375 nm (green); room temperature absorption spectrum (brown); and 77 K emission spectrum of the sodium salt of DMPA with excitation at 380 nm (dotted)

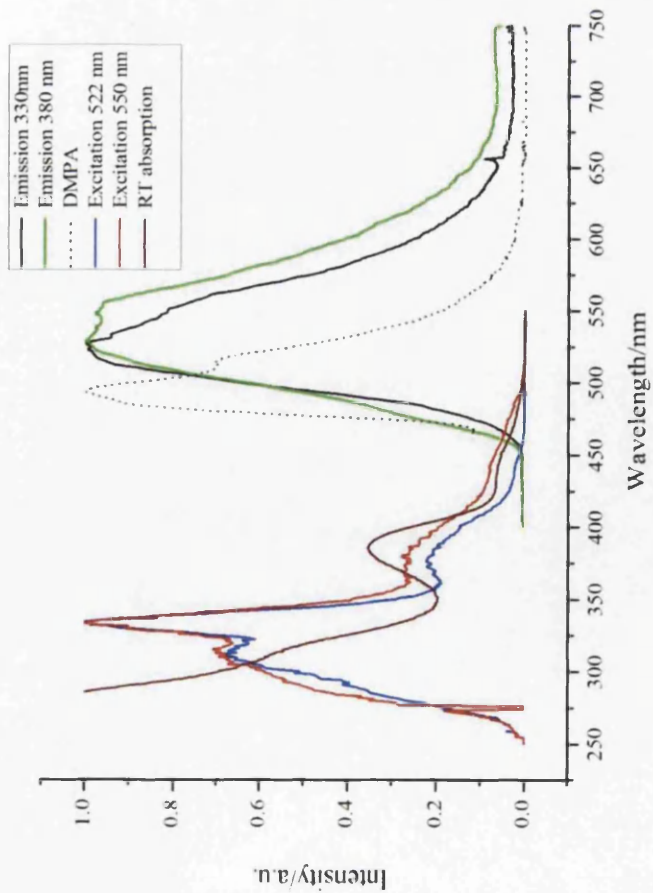


Figure 4.28: Emission and excitation spectra of compound **6b** in a DCM:MeOH (1:1) glass at 77 K: normalised excitation spectra (522 nm blue, 550 nm red); normalised emission spectra (excitation at 330 nm (black), 380 nm (green)); r.t. absorption spectrum (brown); and 77 K emission spectrum of the sodium salt of DMPA with excitation at 380 nm (dotted)

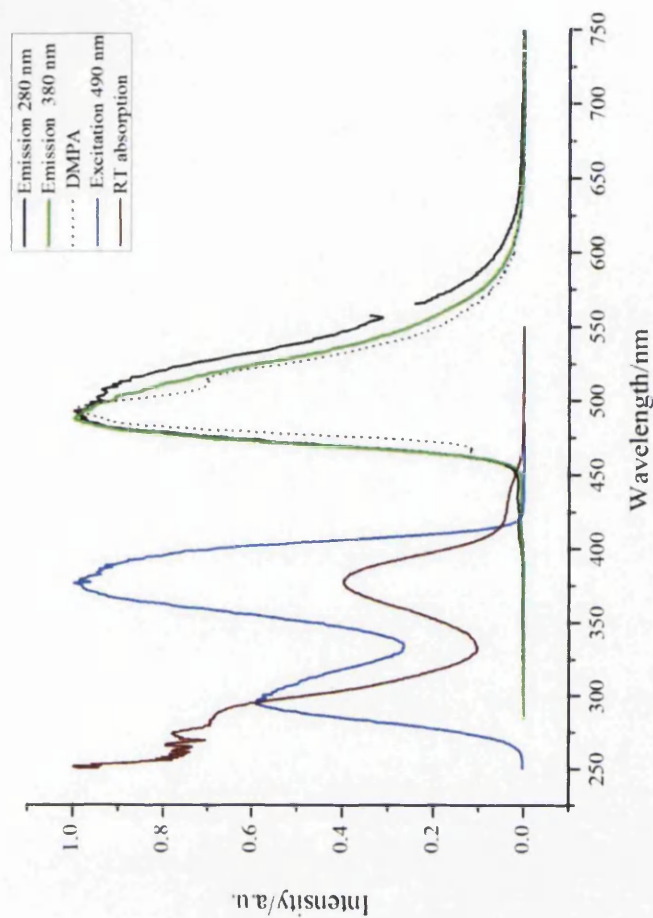


Figure 4.29: Emission and excitation spectra of compound **6d** in a DCM:MeOH (1:1) glass at 77 K: normalised excitation spectrum 490 nm (blue); normalised emission spectra (excitation at 280 nm (black), 380 nm (green)); r.t. absorption spectrum (brown); and 77 K emission spectrum of the sodium salt of DMPA with excitation at 380 nm (dotted)

In a DCM:MeOH (1:1) solution, no noticeable emission was detected even when nitrogen purged.

Room temperature solid state emission (see fig 4.30) feature an emission maximum between 551 and 560 nm, for all excitation wavelengths used. Even if there is a slight difference in emission maximum between **6b** and **6d**, the signal is too noisy to conclude anything about the shifts. However the **6a** emission maximum is nevertheless clearly red-shifted by 8 nm, which indicates that the less electron donating triphenylphosphine red shifts the emission. The emission probably arises from a LMCT excited state. The large shift between the emission and excitation spectra allow us to conclude for a phosphorescent emission, probably arising from a LMCT [S→Au] transition [26, 49], although possible mixing with a MC transition is not excluded.

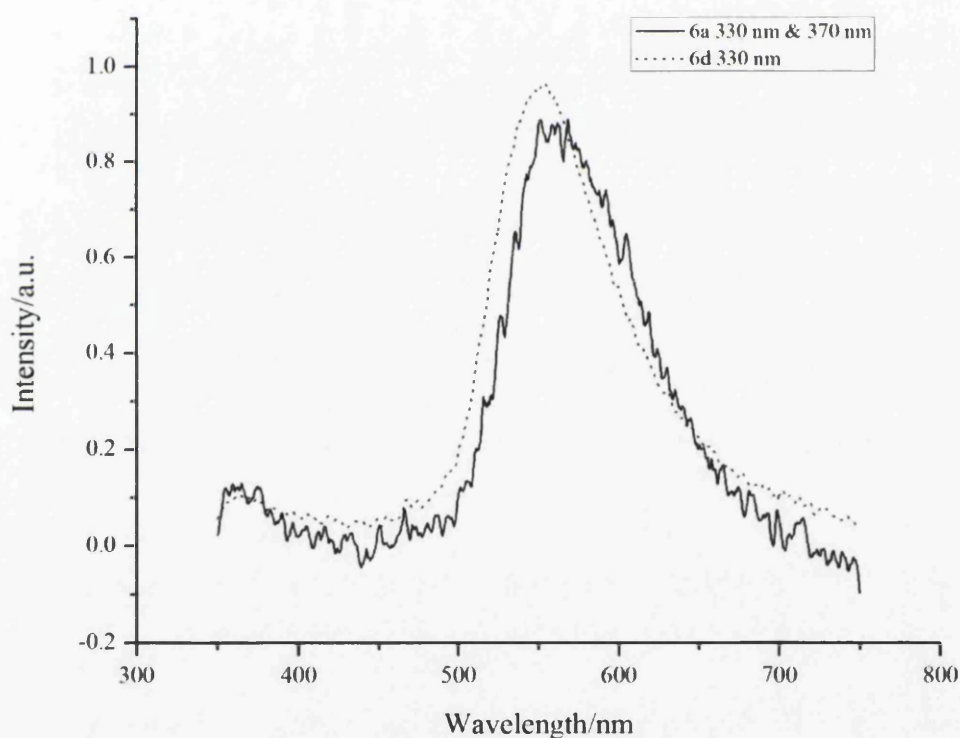


Figure 4.30 RT solid state emission for **6a** (plain) and for **6d** (dot) excited at 330 nm

4.3.2.6 Binuclear gold phosphine series with DMP as dithiolate

The emission and excitation spectra at 77 K are depicted in figures 4.31 to 4.37. The results at 77 K are summarised in table 4.15. The room temperature emission results are summarised in table 4.16.

In this series, the emission spectra at 77 K were different at different excitation wavelengths. As the crystal structure has been obtained for **4a**, a thorough study of this compound has been conducted and the results obtained will be presented in the following paragraphs before discussion of the rest of the series. Its photochemistry is complex: when excited at 320 nm, **4a** emits with a high energy band at 408 nm and a maximum emission at lower energy at 454 nm, with two additional bands at 433 nm and 485 nm. When excited at 380 nm, only one emission peak at 454 nm appears. Excitation spectra for the 408 nm and 454 nm bands show two transitions at 290 nm and 334 nm, while the excitation spectrum for the 454 nm band shows an additional band at 380 nm (see figure 4.31).

It was noticed in the ^1H NMR spectrum of the **4a** equivalent **5a** (complex with ADMN) that the species was protonated and the 77 K emission was the same for all excitation wavelengths. Therefore we added some trifluoroacetic acid to an aliquot of a DCM:MeOH (1:1) solution of **4a**, and some tetrabutylammonium hydroxide (20% v/v) in MeOH to another aliquot, and obtained their room temperature absorption and 77 K emission spectra.

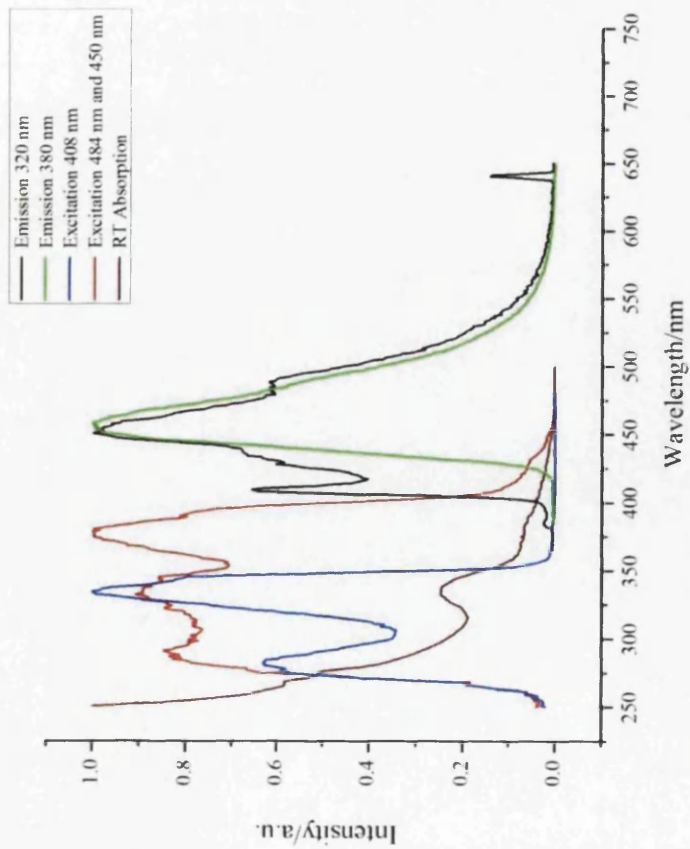


Figure 4.31: Emission and excitation spectra of compound **4a** in a DCM:MeOH (1:1) glass at 77 K: normalised emission spectra at 320 nm (black) and at 380 nm (green); normalised excitation spectra at 408 nm (blue), at 450 nm and 484 nm (red); and room temperature absorption spectra (brown)

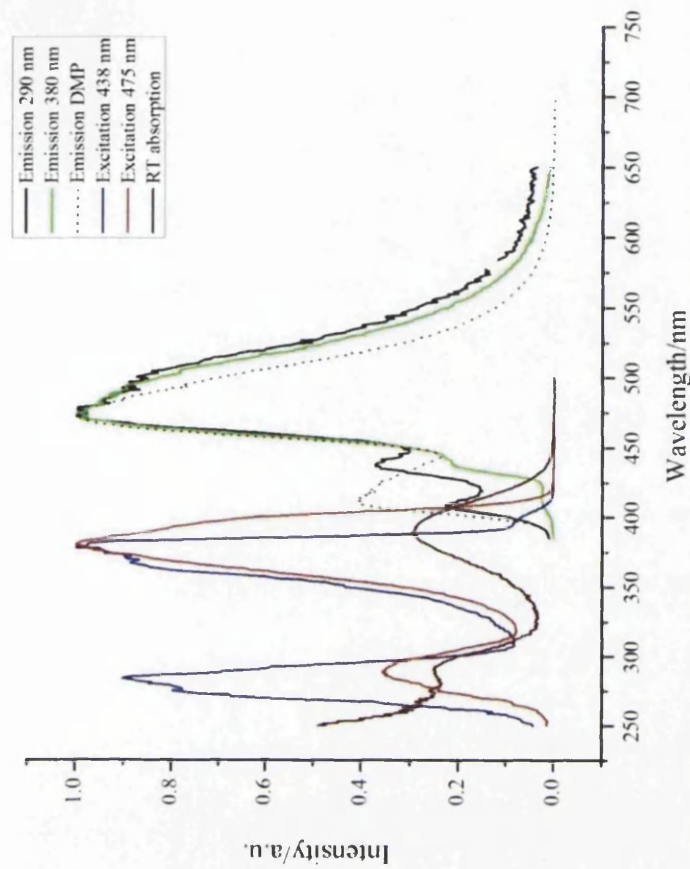


Figure 4.32: Emission and excitation spectra of compound **4f** in a DCM:MeOH (1:1) glass at 77 K: normalised emission spectra at 290 nm (black) 380 nm (green); normalised excitation spectra at 438 nm (blue) and 475 nm (red); room temperature absorption spectrum (brown); 77 K emission spectrum of free ligand DMP in DCM:MeOH (1:1) excited at 380 nm (dot)

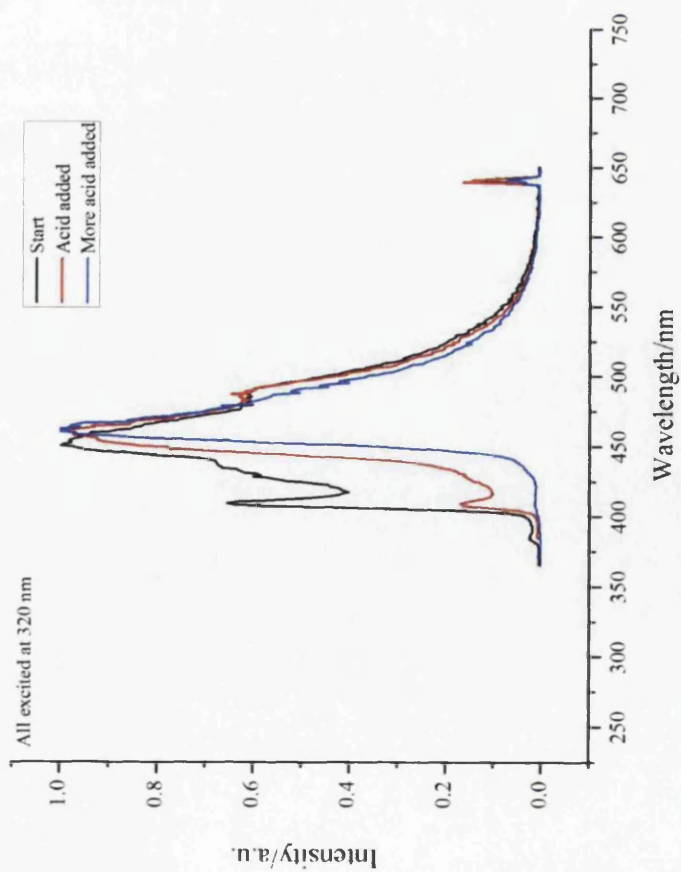


Figure 4.32A: 77 K normalised emission spectra at 320 nm of **4a** in DCM:MeOH(1:1) with different portions of trifluoroacetic acid added: start (black); with 10 μL (red); with 110 μL (blue)

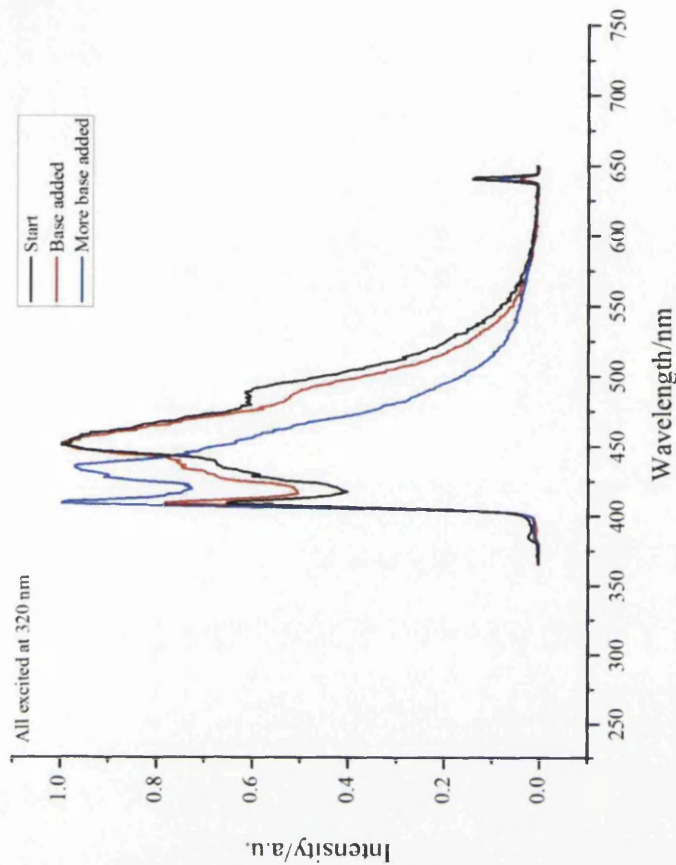


Figure 4.32 B: 77 K normalised emission spectra at 320 nm of **4a** in DCM:MeOH(1:1) with different portions of tetrabutylammonium hydroxide in methanol (20% v/v) added: start (black); with 10 μL (red); with 110 μL (blue)

Normalised emission spectra of **4a** at 77 K in DCM:MeOH (1:1) with protonating or deprotonating agents are presented in figures 4.32A and 4.32B. When acid is added, the band at 454 nm sharpens and is slightly red shifted to 460 nm, and the emission peaks at 485 nm, 408 nm and 435 nm all disappear. When base is added, the two bands at 408 nm and 435 nm become predominant and the bands at 454 nm and 485 nm are still present but are much diminished in the absorption “tail”.

The protonation dependence of emission of the thiolate ligand suggests it may play a major role in the emission process.

(Note that the mononuclear gold triphenylphosphine complex DMP (**4f**) has also been isolated and its photochemistry studied. Its maximum emission is at 475 nm with two higher energy emission bands at 342 nm and 308 nm, the relative intensity of which change according to the excitation wavelength. The maximum emission band of **4f** is not detectable in the **4a** emission spectra and is therefore discarded as a possible impurity.)

DMP annular gold complexes **4b**, **4c**, **4d**, **4e** are also emissive in a DCM:MeOH(1:1) glass at 77 K (see figures 4.33 to 4.35). The emission bands of **4b** at 506 nm and 475 nm are red-shifted compared to those of other compounds of the series, and this follows the trend observed with the other thiolate ligands. The rest of the complexes emit around 440 nm when excited at 330 nm and at 470 nm when excited at 380 nm. The excitation spectra for these two bands show that they originate from the same excitation bands but with different contributions. The long lifetime of the emission measured for **4a**, **4f** and **4d** suggests that it is phosphorescence.

DMP	77 K, λ_{\max} (nm)	77 K lifetime (μs)	Quantum yield
4a	408 ^a	10 (± 1) ^(*)	0.5 (± 0.2)
	433 ^a		
	454 ^{a,b}		
	485 ^{a,b}		
4b	475 ^{a,b}		0.7 (± 0.15)
	506 ^{a,b}		
	543 ^{a,b}		
4c	452 ^a		0.8 (± 0.2)
	460 ^b		
4d	411 ^a	133 (± 1) 60 % 28 (± 2) 40% 120 (± 1) 52 % 10 (± 0.8) 48%	0.7 (± 0.1)
	446 ^a		
	478 ^b		
4e	418 ^a		0.6 (± 0.2)
	436 ^a		
	473 ^b		
4f	408 ^c	135 (± 12) 70 % 22 (± 7) 30%	0.6 (± 0.1)
	437 ^c		
	473 ^{b,c}		
	495 ^{b,c}		

Table 4.15: Photochemical properties of gold phosphine thiolates with DMP as ligand at 77 K

^{a)} excitation at 320 nm

^{b)} excitation at 380 nm

^{c)} excitation at 290 nm

^(*): the results obtained are of poor quality because they were obtained with the weaker laser pulse of the flash photolysis apparatus in Coimbra. They can fit a double exponential as well as a single one but both fits give poor residuals.

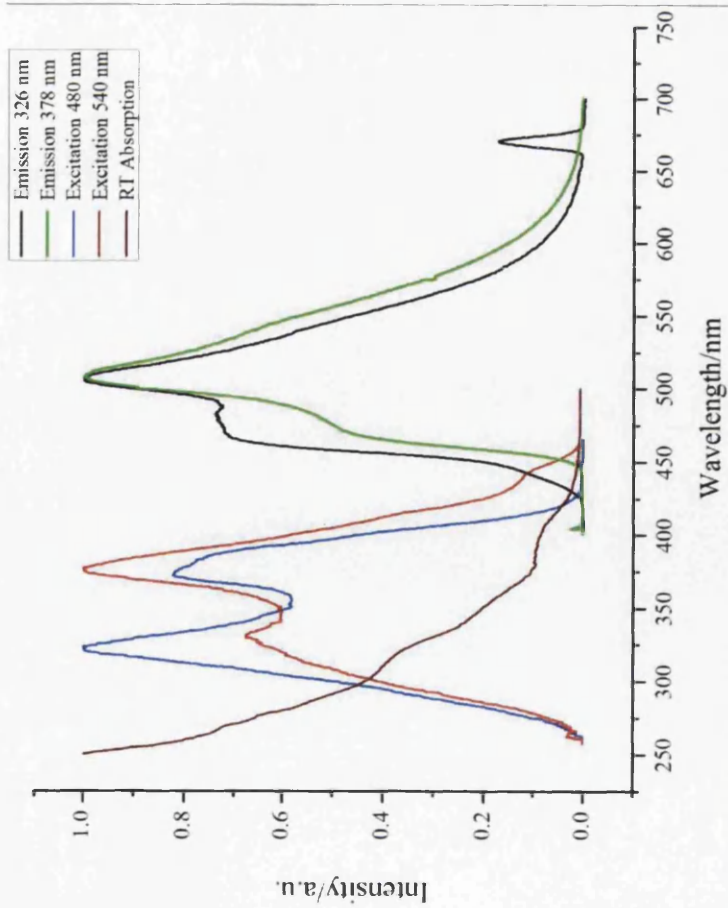


Figure 4.33: 77 K normalised emission spectra of **4b** in DCM:MeOH (1:1) at 326 nm (black) and 378 nm (green), normalised excitation spectra at 480 nm (blue) and 540 nm (red); room temperature absorption spectrum (brown)

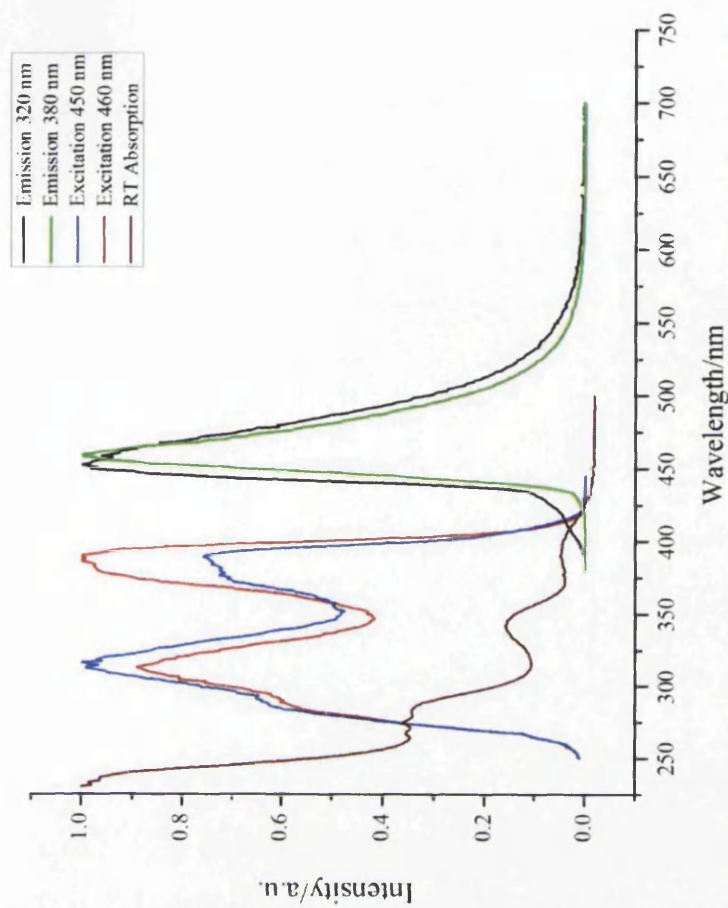


Figure 4.34: 77 K normalised emission spectra of **4c** in DCM:MeOH (1:1) at 320 nm (black) and 380 nm (green); normalised excitation spectra at 450 nm (blue) and 460 nm (red); room temperature absorption spectrum (brown)

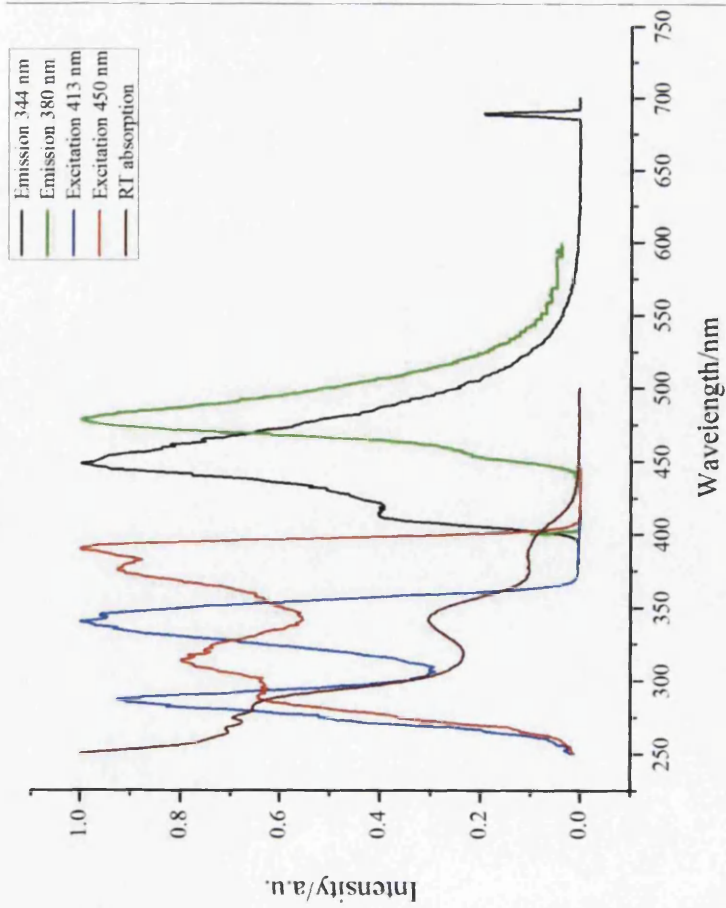


Figure 4.35: 77 K normalised emission spectra of **4d** in DCM:MeOH (1:1) at 344 nm (black) and 380 nm (green); normalised excitation spectra at 408 nm (blue) and 450 nm (red); room temperature absorption spectrum (brown)

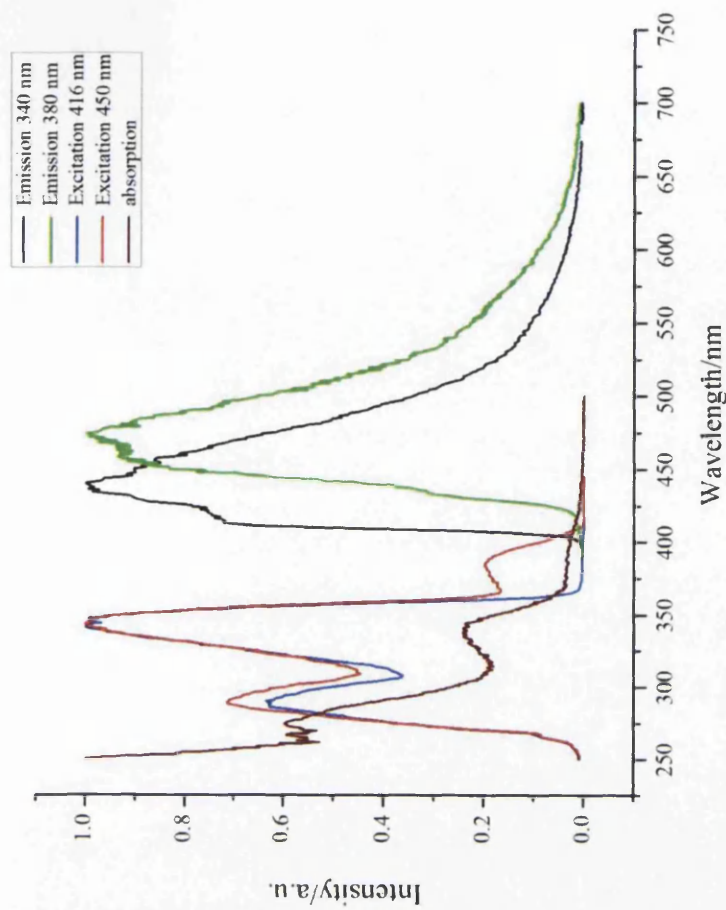


Figure 4.36: 77 K normalised emission spectra of **4e** in DCM:MeOH (1:1) at 340 nm (black) and 380 nm (green); normalised excitation spectra at 416 nm (blue) and 450 nm (red); room temperature absorption spectrum (brown)

These complexes are the only ones in this study to emit in nitrogen-purged DCM:MeOH (1:1) solution at room temperature. Figure 4.37 gives an illustration of this emission with **4a** as an example. This emission is quenched by oxygen; there is a large shift between the excitation spectra and the emission spectra; and time-resolved measurements for **4b** and **4c** give lifetimes in the microsecond range. We can therefore attribute this emission to phosphorescence. Due to the slight red shift when either dppm or PPh₃ are the phosphine ligands we attribute this emission to be from a ³[S→Au] state [26, 49].

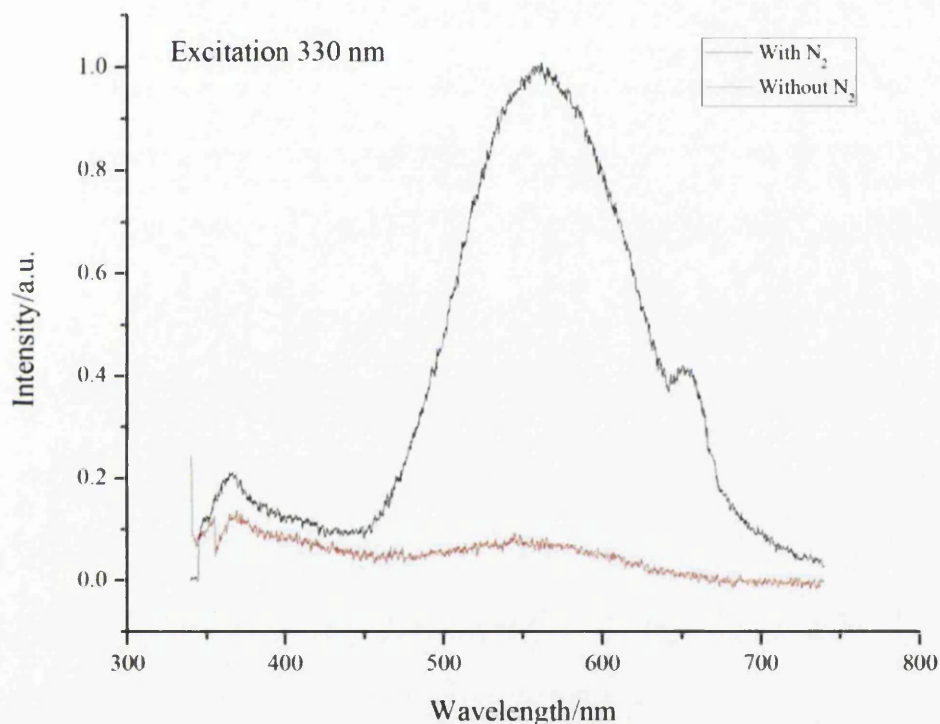


Figure 4.37: Room temperature emission for an excitation at 330 nm of **4a** under nitrogen (black) or under air (red). The peak at 660 nm under nitrogen is an artefact due to light scattering.

RT emission	4a	4b	4c	4d	4e
λ_{max} (nm)	557	560	550	552	550
Lifetime (μs)	(-)	0.42 (\pm 0.04) 25% 1.3 (\pm 0.08) 75%	0.13 (\pm 0.01) 25% 0.80 (\pm 0.05) 75%	(-)	(-)

Table 4.16: Solution phase room temperature emission maxima for excitation at 330 nm. Time-resolved data are only available for **4b** and **4c**.

Finally the solid state room temperature emission of this series will be described (see figure 4.38). The emission maximum varies with the type of phosphine used, eliminating the possibility of a ligand-based emission. As the lifetime is in the microsecond range for **4e** and **4d** in the solid state, and all the compounds of the series have a large shift between their emission and excitation spectra, we attribute their emission to phosphorescence. The gated spectra at 0.75 μs follow nicely the emission spectrum of **4d**. The time-resolved study shows again two kinds of process involved in the luminescence. The short lived one has been attributed, as in the literature [26], to intraligand transitions involving π and π^* orbitals of the triphenylphosphine whereas the long lived one is associated with a LMCT from the sulphur of the ligand to the gold.

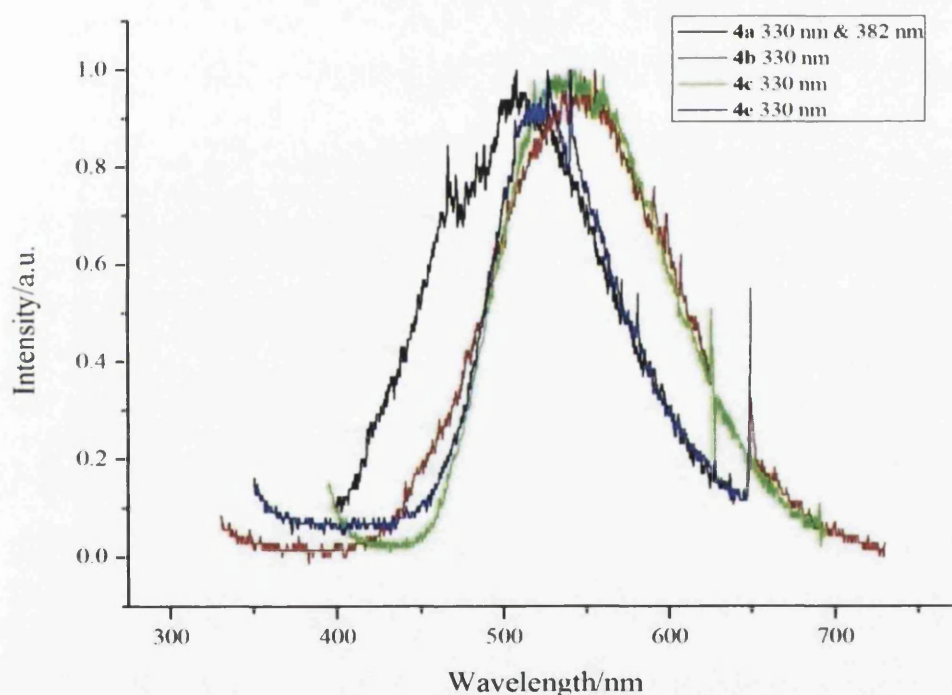


Figure 4.38: Room temperature solid state emission for an excitation at 330 nm of complexes with DMP as a thiolate ligand

Complex	4a	4b	4c	4d	4e
λ_{max} (nm)	510	545	535	525	525
Lifetime (μs)				0.7 (\pm 0.07) 67% 5.9 (\pm 0.18) 28%	1.0 (\pm 0.07) 50% 6.9 (\pm 0.2) 50%

Table 4.17: Room temperature solid state emission for complexes with DMP as thiolate ligand

4.3.2.7 Binuclear gold phosphine series with ADMN as dithiolate

The emission and excitation spectra at 77 K are depicted in figures 4.39 to 4.41 and results at 77 K are summarised in table 4.18. The solid state room temperature emission results are summarised in table 4.19.

The complexes emit at 77 K in the 490-470 nm region. The long emission lifetime measured for **5a** and **5b** in this wavelength area and the relatively large shift between emission and excitation spectra allow us to assign this emission to phosphorescence. We can, by analogy, reasonably attribute the emission of complexes **5c** and **5d** to phosphorescence too. Emission does not originate from the thiolate for the following reasons.

- 1) The emission of the free ligand, ADMN, emission and that from the gold compounds do not match.
- 2) The emission maximum changes with the phosphine used.

The excitation spectra show the LMCT origin of the excited state. When compared with the DMP series, the emission is red shifted by *ca.* 10 nm or more. The same red shift is observed in the emission of the free ligands. So the emission is likely to be a gold to ligand phosphorescence originating from a $^3[\text{S} \rightarrow \text{Au}]$ or $^3[\text{L} \rightarrow \text{Au}]$ excited state [26, 49]. The 77 K quantum yields are higher for the closed ring system than for the open one, non-emissive vibrational deactivation being more efficient in the latter.

ADMN	77 K λ_{max} (nm)	77 K lifetime (μs)	77 K quantum yield
5a	490	1800 (\pm 200) 40%	0.4
	518	270 (\pm 50) 60% (*)	
5b	470	120 (\pm 1) 52%	0.8
	502		
5c	480		0.85
	513		
5d	461		0.8
	474		

Table 4.18: 77K photochemical properties of gold phosphine thiolate complexes with ADMN as thiolate

(*): measurements made with a weaker laser pulse from the flash photolysis system in Coimbra, giving a noisy signal and a large error value.

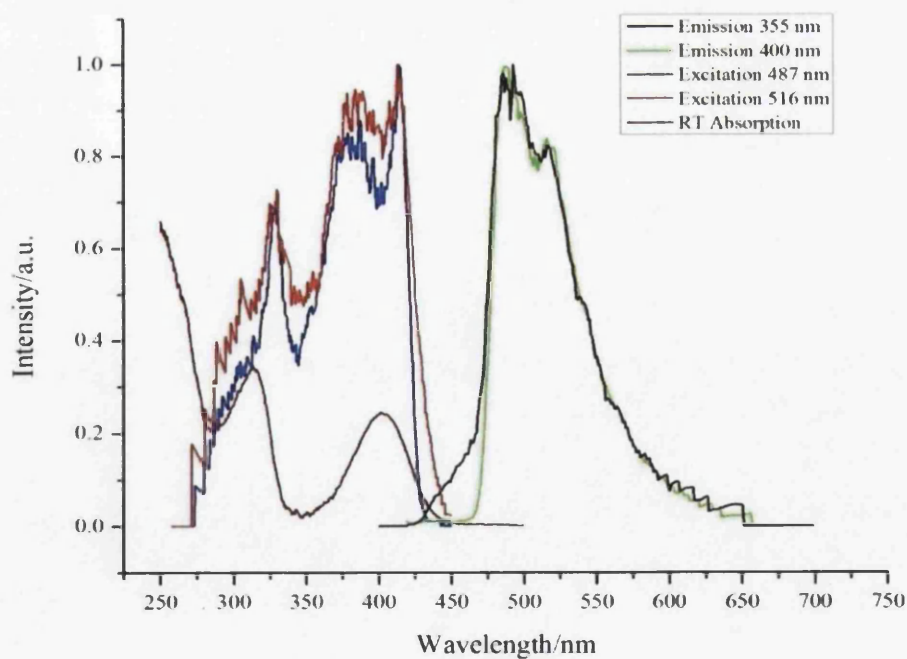


Figure 4.39: 77 K normalised emission spectra of **5a** in DCM:MeOH (1:1) at 355 nm (black), and 400 nm (green); normalised excitation spectra at 487 nm (blue) and 516 nm (red); and room temperature absorption spectrum (brown)

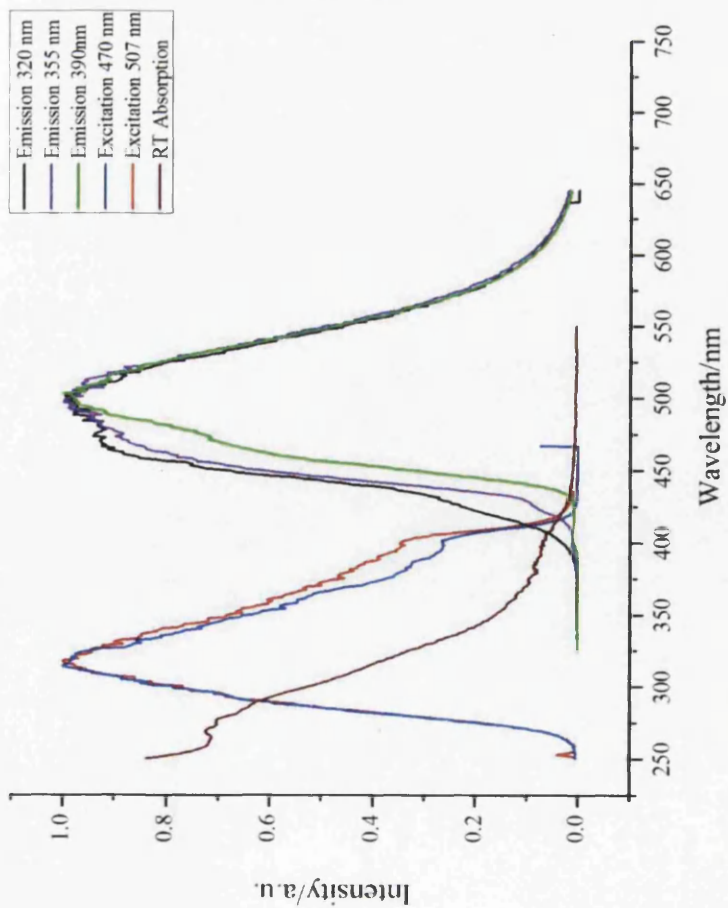


Figure 4.40: 77 K normalised emission spectra of **5b** in DCM:MeOH (1:1) at 320 nm (black), 355 nm (violet) and 390 nm (green); normalised excitation spectra at 470 nm (blue) and 507 nm (red); room temperature absorption spectrum (brown)

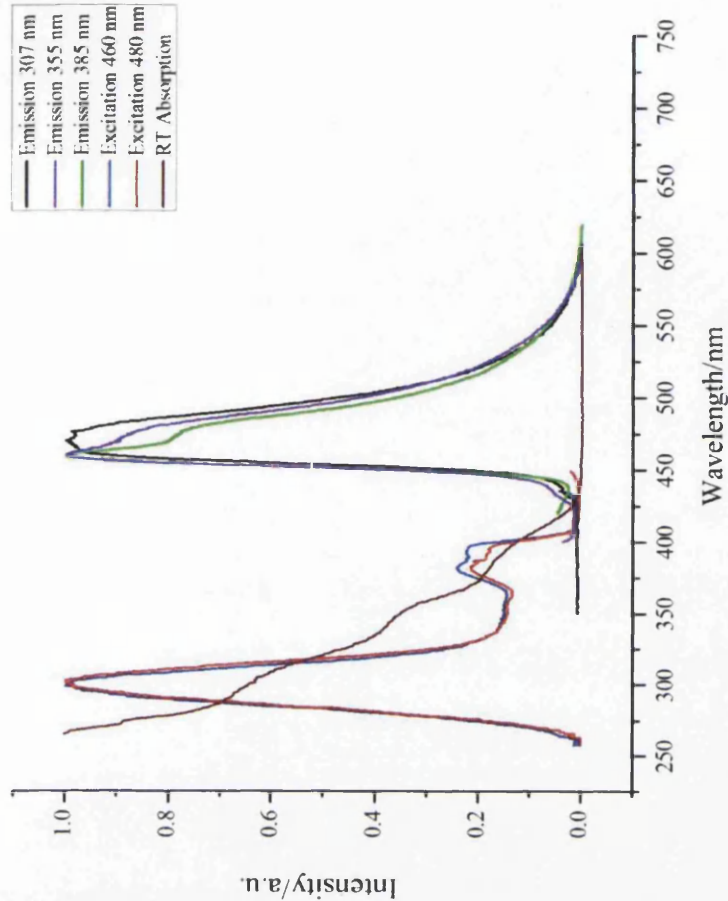


Figure 4.41: 77 K normalised emission spectra of **5d** in DCM:MeOH (1:1) at 307 nm (black), 355 nm (violet) and 385 nm (green); normalised excitation spectra at 460 nm (blue) and 480 nm (red); room temperature absorption spectrum (brown)

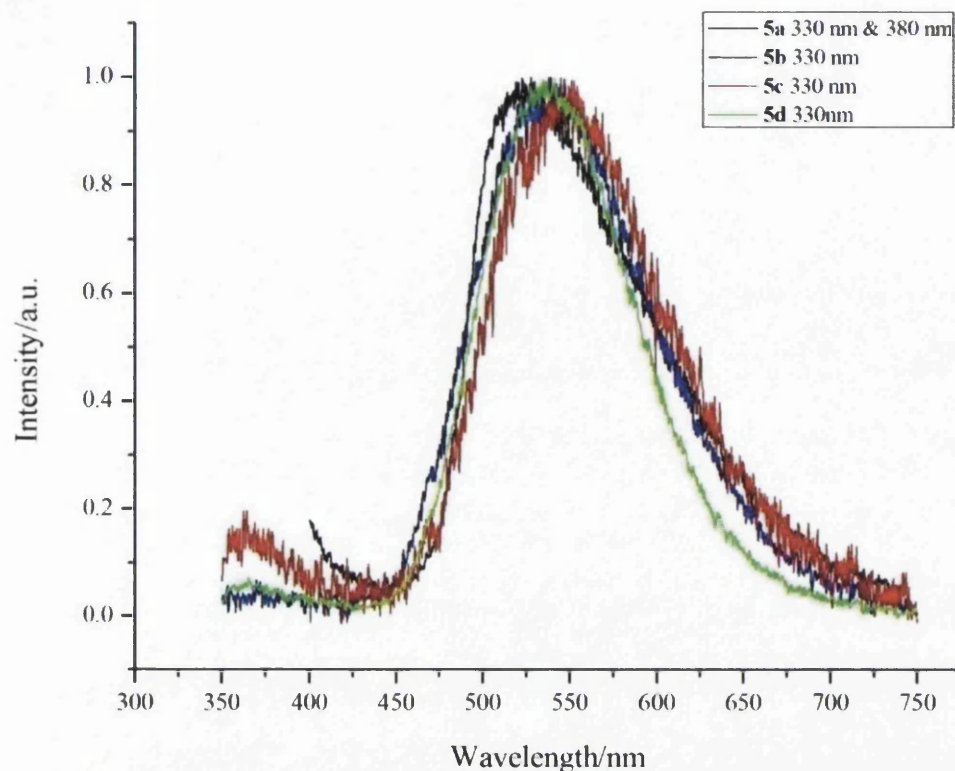


Figure 4.42: Room temperature solid state emission for complexes with ADMN as thiolate ligand

The complexes are all emissive in the solid state, with emission maxima at ca. 535 nm for **5b**, **5c**, **5d** and at 520 nm for **5a**. The emission is broad, with a FWHM around 120 nm. We assign this emission to phosphorescence because of the large shift between the emission and the excitation maxima. In similar emitting complexes, this emission has been attributed to a LMCT transition [26, 49].

Complex	5a	5b	5c	5d
λ_{\max} (nm)	520	535	535	535

Table 4.19: Room temperature solid state emission for complexes with ADMN as thiolate ligand

4.3.2.8 Binuclear gold phosphine series with DMB or Cl-DMB as dithiolate

The emission and excitation spectra at 77 K are depicted in figures 4.43 and 4.44. Results at 77 K are summarised in table 4.20.

DMB complexes emit at higher energy than their chloro-substituted analogues (426 nm and 438 nm respectively). The red shift in emission with the chloro-substituent has also been observed in the mononuclear gold(I) equivalent studied by Fackler [26] in the solid state at 77 K. For both complexes, their excitation spectra show only one peak around 330 nm corresponding to a LMCT [S→Au]. The shift between the excitation and emission spectra indicate that the emission is phosphorescent in nature, as it is for the mononuclear gold analogues [26].

DMB	77 K λ_{max} (nm)	77 K quantum yield
7a	426	0.66
Cl-DMB	77 K λ_{max} (nm)	77 K quantum yield
8a	438	0.60

Table 4.20: 77K photochemical properties of gold phosphine thiolate complexes with DMB or Cl-DMB as thiolate

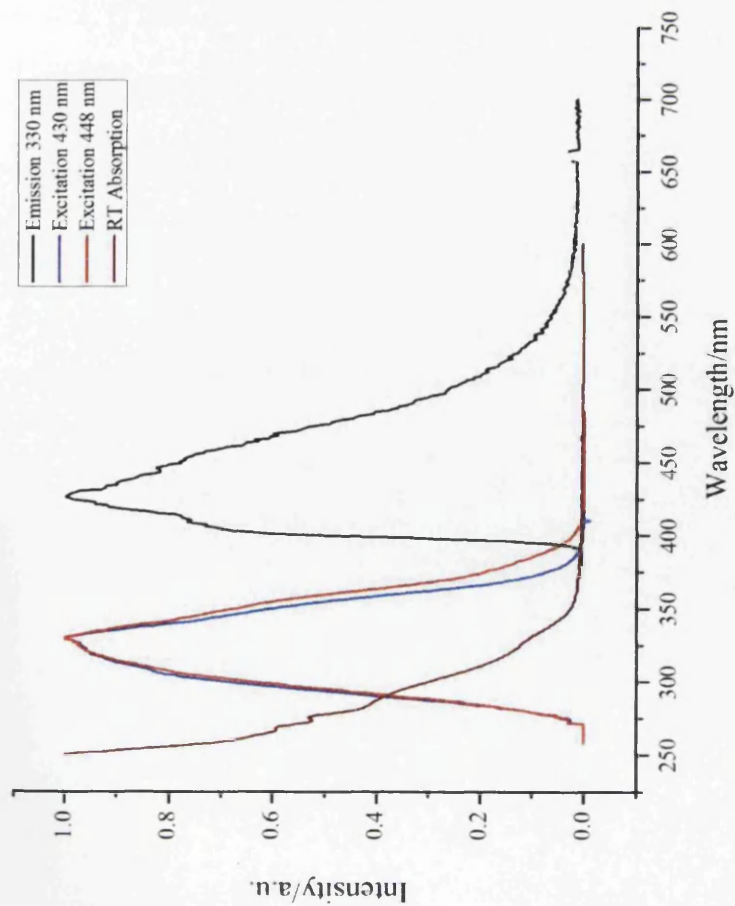


Figure 4.43: 77 K normalised emission spectrum of **7a** in DCM:MeOH (1:1) at 330 nm (black); normalised excitation spectra at 430 nm (blue) and 448 nm (red); room temperature absorption spectrum (brown)

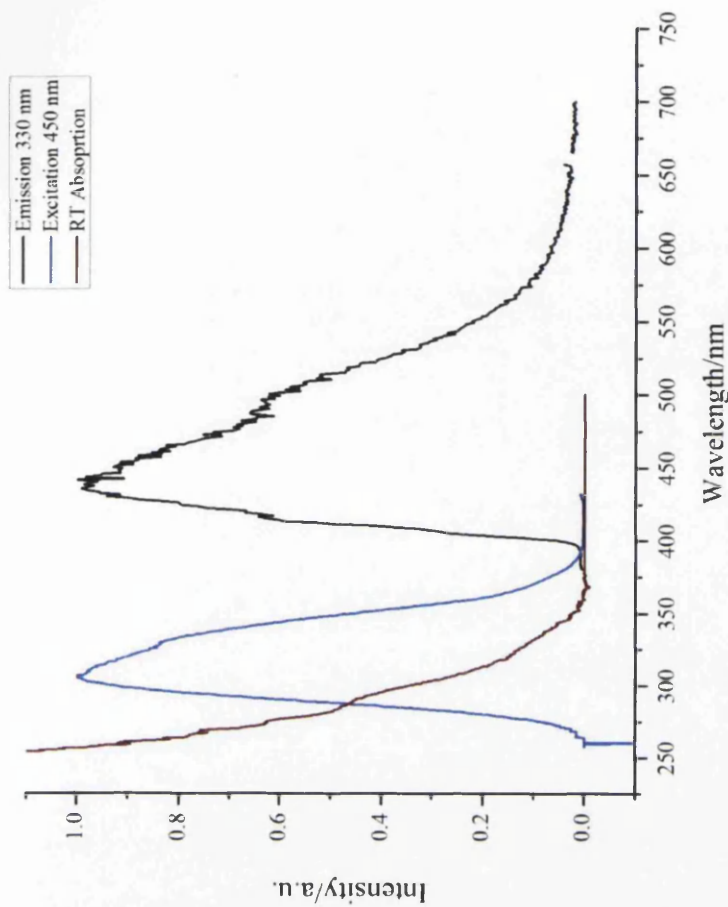


Figure 4.44: 77 K normalised emission spectrum of **8a** in DCM:MeOH (1:1) at 330 nm (black); normalised excitation spectrum at 450 nm (blue); room temperature absorption spectrum (brown)

4.3.3 Discussion

Table 4.21 provides a summary of emission maxima at 77 K.

4.3.3.1 Influence of the phosphine (length, charge)

77K measurements:

Triphenylphosphine is more electron-withdrawing than its bidentate diphosphine analogues, such as dppm for example, and will render the gold atom less electron rich. The general red shift observed in the longest wavelength emission band is consistent with a LMCT origin of the emission. dppm, dppe, dppp and dppb should have more or less similar electronic effects on the gold atom. Variation in the emission may then be due to steric effects. dppm has a shorter linkage (only one methylene group) compared with the other diphosphines, and therefore could bring the two gold atoms closer, and perhaps close enough to induce some weak aurophilicity. There is also the possibility of some weak gold-nitrogen interactions which may affect the energy of the LMCT emission.

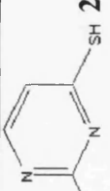
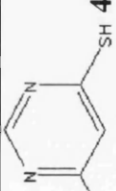
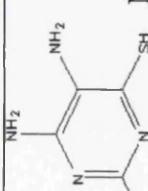
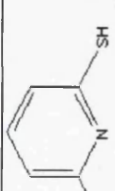
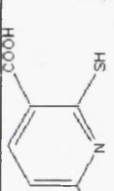
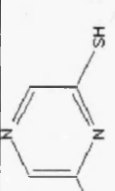
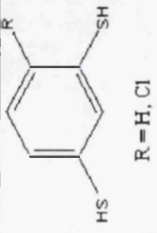
Emission	a: PPh ₃	b: dppm	c: dppe	d: dppp	e: dppb
1:  24PYRI	420, 475	430 & 516	410 & 430	411 & 433	412 & 432
2:  46PYRI	438	443 & 505	X	X	X
3:  NPYRI	530, 550	525	528	518	530
4:  DMP	455	480 & 506	460	478	473
5:  ADMIN	490	502	480 & 514	461 & 474	x
6:  DMPA	495	520	x	498	x
7 (H); 8 (Cl):  7 (H); 8 (Cl) R = H, Cl	426 (DMB, 7) 438 (Cl-DMB, 8)	x	x	x	x

Table 4.21: Synopsis of the maximum emission wavelength at 77 K when excited at wavelength > 360 nm

4.3.3.2 Influence of the thiolate

77 K measurements:

The complexity of the 77 K emission pattern and the time-resolved measurements show that different emission processes are present. The orbital of the phosphine ligand and the thiolate ligand seem to be close in energy and variation in the electron-withdrawing or electron-donating group on the thiolate will enhance one or other type of transition. The electron withdrawing group COOH will stabilise the HOMO localised on the pyridine ring and therefore promote an emission more based on the thiolate ligand, whereas the electron donating group NH₂ in NPYRI will promote a LMCT transition. Protonation of the DMP ligand will also promote an emission based on the ligand. When no substituent is present, the nature of the emissive state is mixed, and the electron having been excited can originate from the sulphur or more likely from the whole thiolate ligand. In any case, the origin of the luminescence is a LMCT excited state, with the possibility of some mixing with a MC transition.

The presence of a nitrogen atom in the heterocycle between the two thiolate groups produces a red shift in the emission at 77 K.

Room temperature measurements:

The only complexes which emit in DCM:MeOH (1:1) solution at room temperature are those of the DMP series. There is no clear explanation why this is the only cases, some measurements in another non-protic solvent (DCM or THF) could be useful to check the influence of the solvent on the quenching process.

All of the complexes emit in the solid state at room temperature. There is no definitive evidence found in the emission data for any gold-gold interaction. The emission maxima vary slightly with the phosphine used. The emission is attributed to a LMCT ³[S→Au], with possible mixing with a MC transition.

4.3.4 Conclusion from photochemical studies

The absorption spectra of the complexes have two kinds of bands. The high energy bands at 290-300 nm are attributed to transitions based on the π and π^* orbitals of the phosphine, whereas the low energy bands (> 320 nm) are attributed to a LMCT transition, the orbital being localised either on the sulphur or the whole thiolate ligand, with some possible mixing with a MC transition.

The emission of these complexes is complex in its origin but is predominantly phosphorescence. The most probable origin is a $^3[\text{S} \rightarrow \text{Au}]$ excited state, with some mixing with thiolate-based emission. The DFT calculations reported later support this interpretation. By changing the electronic structure of the dithiolate ligands, we can tune the emission wavelength and possibly change the transitions responsible for the emission. Electron donating groups on the thiolate such as amino groups red-shift the emission and also promote the LMCT origin of the emission, whereas an electron withdrawing group will promote a ILCT origin of the emission. The presence of the nitrogen in-between the two sulphur atoms also causes a red shift in the emission.

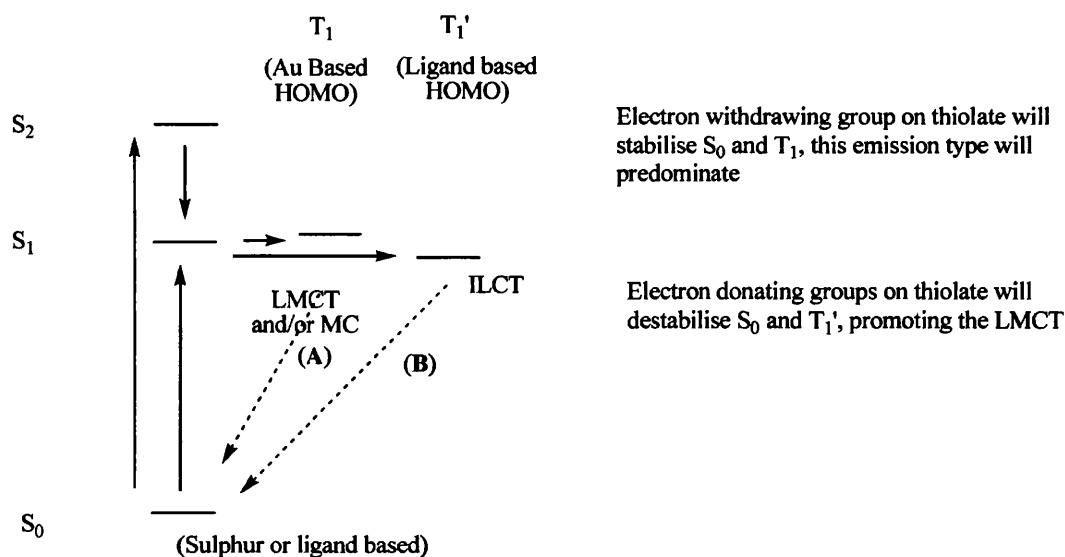


Figure 4.45: Jablonski diagram showing the possible transitions in the complexes

4.4 Electrochemistry

Measurements were done in nitrogen purged DCM, as the gold complexes are poorly soluble in MeCN. No values were collected for NPYRI gold complexes due to their poor solubility in DCM or MeCN. Variation in scan rate did not change the results and reported results were obtained with a scan rate of 0.25 V s^{-1} .

Mononuclear gold phosphine thiolates show irreversible electrochemistry in solution [66-73]. The oxidation leads to the formation of a thiyl radical which can dimerise into a disulfide bridge or react with the solvent. The following process has recently been proposed [73] to explain the first oxidation step and the irreversibility of the electrochemical process:

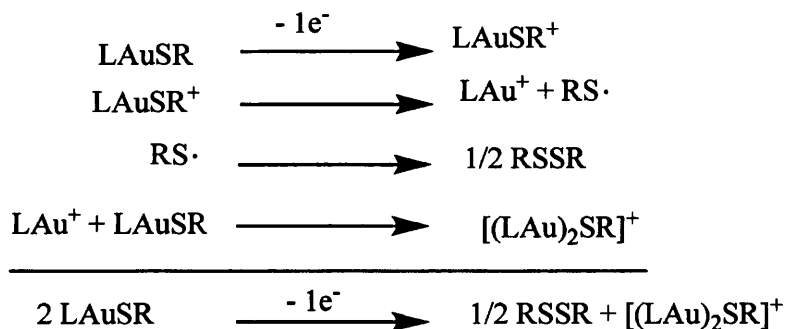


Figure 4.46: Mechanism for the oxidation of a gold (I) thiolate to a disulfide (L being a non-thiolate ligand such as Cl or a phosphine, R being an hydrocarbon fragment)

We had thought that formation of a free radical might be inhibited by using a bridging bidentate ligand and by having two gold centres which could electrochemically communicate to stabilise the oxidised species. However, the electrochemistry is irreversible on oxidation for all our complexes, annular or not. This irreversibility prevents any direct calculation of the number of electrons involved in the electrochemical process. It was noticed that the oxidised ferrocene reacts with an oxidation species produced by the gold complexes as its reversible reduction peak appears only if a large amount of ferrocene is added to the solution, we can assume that the thiyl radical is reacting with the ferrocinium cation. As we were interested mainly in checking the possible reversibility of the oxidation of these classes of compounds, no further quantitative analyses were carried out.

4.5 Conclusion

A new series of 28 binuclear phosphinegold N-heterocyclic dithiolates have been synthesised and characterised. In making this range of compounds both the thiolate ligand and the phosphine ligands have been systematically changed. It has been shown that gold is bonded to the thiolate exclusively through sulphur atoms and that no intermolecular or intramolecular gold-gold interactions are present.

The photochemistry of these compounds is complex and varies according to the properties of the thiolate or phosphine used. In a glass at 77 K, the emission wavelengths range from 420 nm (with 24PYRI) to 530 nm (with NPYRI), with the excited state having a lifetime in the 12-50 μ s range. In this medium they are all good emitters as the lowest quantum yield is about 0.4 and it can reach 0.9, notably with the DMPA ligand. The emission mainly originates from a LMCT triplet state or ligand based triplet state enhanced by the gold heavy atom effect. Electron withdrawing or donating groups based on the thiolate will change the nature of the emission. Electron withdrawing groups will enhance the ligand based origin of the emission whereas electron donating groups will enhance the LMCT origin. The DFT calculations presented in the following chapter help to complement this interpretation. All of the complexes studied show irreversible electrochemistry in solution.

Only compounds with DMP phosphoresce at room temperature in DCM:MeOH (1:1) solution. The emission is in the 540 nm region, from an excited state radiatively deactivated by two processes in the microsecond range ($\approx 0.4 \mu$ s and $\approx 1.5 \mu$ s). The compounds phosphoresce in the solid state at room temperature in the 500-560 nm range. The presence of a protonated species (except for 5a) was not being detectable in the ^1H NMR and therefore discarded.

Reference for Chapter 4

- [1] Miranda S., Vergara E., Mohr F., de Vos D., Cerrada E., Mendía E., Laguna M., *Inorg. Chem.* 47 (2008) 5641-5648
- [2] Nomiya K., Yamamoto S., Noguchi R., Yokoyama H., Kasuga N. C., Ohya K., Kato C., *J. Inorg. Biochem.* 95 (2003) 208-220
- [3] Nomiya K., Noguchi R., Ohsawa K., Tsudam K., Oda M., *J. Inorg. Biochem.* 78 (2000) 363-370
- [4] Schneider J., Lee Y., Perez J., Brennessel W.W., Flaschenriem C., Eisenberg R., *Inorg. Chem.* 47 (2008) 957-968
- [5] Lee Y.A., Eisenberg R., *J. Am. Chem. Soc.* 125 (2003) 7778-7779
- [6] Colacio E., Roqerosa A., Ruiz J., Roman P., Gutierrez-Zorrilla J.M., Vegas A., Martinez-Ripoll M. *Inorg. Chem.* 30 (1991) 3743-3749
- [7] Stocco G., Gattuso F, Isab A.A., Shaw C.F. III, *Inorg. Chim. Acta* 209 (1993) 129-135
- [8] Cookson P.D., Tiekink E.R.T., *J. Chem. Soc. Dalton Trans.* (1993) 259-263
- [9] Onaka S., Yaguchi M., Yamauchi R., Ozeki T., Ito M., Sunahara T., Sugiura Y., Shiotsuka M., Nunokawa K., Horibe M., Okazaki K., Iida A., Chiba H., Inoue K., Imai H., Sako K., *J. Organomet. Chem.* 690 (2005) 57-68
- [10] Canales F., Gimeno M.C., Jones P.G., Laguna A., Sarroca C., *Inorg. Chem.* 36 (1997) 5206-5211
- [11] Nunokawa K., Onaka S., Tatematsu T., Ito M., Sakai J., *Inorg. Chim. Acta* 322 (2001) 56-64
- [12] Tzeng B., Liao J., Lee G., Peng S., *Inorganica Chimica Acta* 357 (2004) 1405-1410
- [13] Bardali M., Connely N.G., Gimeno M.C., Jones P.G., Laguna A., Laguna M., *J. Chem. Soc. Dalton Trans.* (1995) 2245-2250
- [14] Hao L., Mansour M.A., Lachicotte R.J., Gysling H.J., Eisenberg R., *Inorg. Chem.* 39 (2000) 5520-5529
- [15] Vergara E., Miranda S., Mohr F., Cerrada E., Tiekink E.R.T., Romero P., Mendia, A., Laguna M., *Eur. J. Inorg. Chem.* (2007) 2926-2933
- [16] Tzeng B., Schier A., Schmidbaur H., *Inorg. Chem.* 38 (1999) 3978-3984
- [17] Tzeng B.C., Huang Y.C., Wu W.M, Lee S.Y., Lee G.H., Peng S.M., *Cryst. Growth Des.* 4 (2004) 63-70

- [18] Wilton-Ely J.D.E.T., Schier A., Mitzel N.W., Schmidbaur H., *Inorg. Chem.* 40 (2001) 6266-6271
- [19] Uson Bonati F., Burini A., Pietroni B.R., Giorgini E., Bovio B., *J. Organomet. Chem.* 344 (1988) 119-135
- [20] Lee Y.A., Eisenberg R., *J. Am. Chem. Soc.* 125 (2003) 7778-7779
- [21] Wilton-Ely J.D.E.T., Schier A., Mitzel N.W., Nogai S., Schmidbaur H., *J. Organomet. Chem.* 643-644 (2002) 313-323
- [22] Lang E.S., Fernandes Jr R.M., Lemos S.S., Lang L.C., Burrow R.A., *Acta Cryst. Sect E* 58 (2002) m469 -m470
- [23] Tzeng B.C., Chan C.K., Cheung K.K., Che C.M., Peng S.M., *Chem. Commun.* (1997) 135-136
- [24] Jia G., Puddephatt R.J., Vittal J.J., *Polyhedron* 16 (1992) 2009-2014
- [25] Li C., Lu X., Wong K.M., Chan C., Zhu N., Yam V.W., *Inorg. Chem.* 43 (2004) 7421-7430
- [26] Forward J., Bohmann D., Fackler Jr J.P., Staples R.J., *Inorg. Chem.* 34 (1995) 6330-6336
- [27] Gimeno M.C., Jones P. G., Laguna A., Laguna M., Terrobae R., *Inorg. Chem.* 33 (1994) 3932-3938
- [28] Puddephatt J., *J. Chem. Soc Dalton Trans.* (2000) 521
- [29] Christina H., McFarlane E., McFarlane W., *Polyhedron* 7 (1998) 1875-1881
- [30] Miranda S., Vergara E., Mohr F., de Vos D., Cerrada E., Mendía E., Laguna M., *Inorg. Chem.* 47 (2008) 5641-5648
- [31] Ho S.Y., Cheng E.C., Tiekink E.R.T., Yam V.W., *Inorg. Chem.* 45 (2006) 8165-8174
- [32] Harker C.S.W., Tiekink E.R.T., Whitehouse M.W., *Inorg. Chim. Acta* 181 (1991) 23-30
- [33] Henderson W., Nicholson B.K., Tiekink E.R.T., *Inorg. Chim. Acta* 359 (2006) 204-214
- [34] Forward J.M., Fackler Jr. J.P., Assefa Z., in "Optoelectronic Properties of Inorganic Compounds", Plenum Press, New York, 1998
- [35] Hunks W.J., Jennings M.C., Puddephatt R.J., *Inorg. Chem.* 38 (1999) 5930-5931
- [36] Koizumi T., Tsutsui K., Tanaka K., *Eur. J. Org. Chem.* 23 (2003) 4528-4532
- [37] Hunks W.J., Jennings M.C., Puddephatt R.J., *Inorg. Chim. Acta* 359 (2006) 3605-3616

- [38] Brandys M.C., Puddephatt R.J., *J. Am. Chem. Soc.* 123 (2001) 4839-4840
- [39] Burchell T.J., Eisler D.J., Jennings M.C., Puddephatt R.J., *Chem. Commun.* (2003) 2228-2229
- [40] Hunks W.J., Jennings M.C., Puddephatt R.J., *Chem. Commun.* (2002) 1834-1835
- [41] Cha S.H., Kim J.U., Kim K.H., Lee J.L., *Chem. Mater.* 19 (2007) 6297-6303
- [42] Awaleh M.A., Baril-Robert F., Reber C., Badia A., Brisse F., *Inorg. Chem.* 47 (2008) 2964-2974
- [43] Ehlich H., Schier A., Schmidbaur H., *Organometallics* 21 (2002) 2400-2406
- [44] Terroba R., Fernandez E.J., Hursthouse M.B., Laguna M., *Polyhedron* 17 (1998) 2433-2439
- [45] Bardaji M., Calhorda M.J., Costa P.J., Jones P.G., Laguna A., Perez M.R., Villacampa M. D., *Inorg. Chem.* 45 (2006) 1059-1068
- [46] Gimeno M.C., Jambrina E., Fernandez E.J., Laguna A., Laguna M., Jones P.G., Merchan F.L., Terroba R., *Inorganica Chimica Acta* 258 (1997) 71-75
- [47] Bardaji M., Laguna M., Perez M.R., *Organometallics* 21 (2002) 1877-1881
- [48] Ferrer M., Reina R., Rossell O., Seco M., Segales G., *J. Organomet. Chem.* 515 (1996) 205-211
- [49] Yam V.W., Chan C.L., Li C.K., Wong K.M., *Coord. Chem. Rev.* 216-217 (2001) 173-194
- [50] Yam V.W., Li C.K., Chan C.L., *Angew. Chem. Int. Ed.* 37 (1998) 2857-2858
- [51] Li C.W., Lu X.X., Wong K.M., Chan C.L., Zhu N., Yam V.W.-W., *Inorg. Chem.* 43 (2004) 7421-7430
- [52] Lagunas M.C., Fierro C.M., Pintado-Alba A., la Riva H., Betanzos-Lara S., *Gold Bull.* 40 (2007) 135-141
- [53] Fave C., Cho T.Y., Hissler M., Chen C.W., Luh T.Y., Wu C.C., Reau R., *J. Am. Chem. Soc.* 125 (2003) 9254-9255
- [54] Ma Y., Zhu X., Shen J., Chao H.Y., Che C.M., *Applied Phys. Lett.* 74 (1999) 1361-1363
- [55] Ma Y., Che C.M., Chao H. Y., Zhou X., Chan W.H., Shen J., *Adv. Mater.* 11 (1999) 852-857
- [56] Evans R.C., Douglas P., Winscom C.J., *Coord. Chem. Rev.* 250 (2006) 2093-2126

- [57] Mansour M.A., Connick W.B., Lachicotte R.J., Gysling H.J., Eisenberg R., *J. Am. Chem. Soc.* 120 (1998) 1329-1330
- [58] Luquin A., Elosua C, Vergara E., Estalla J, Cerrada E., Bariain C., Matias I.R., Garrido M., Laguna M., *Gold Bull.* 40 (2007) 225-233
- [59] Narayanaswamy R. , Young M.A., Parkhurst E., Ouellette M., Kerr M.E, Ho D.M., Elder R.C., Bruce A.E., Bruce M.R.M., *Inorg. Chem.* 32 (1993) 2506-2517
- [60] Tang S.S., Chang C.P., Lin I.J.B., Liou L.S., Wang J.C., *Inorg. Chem.* 36(1997) 2294-2300
- [61] Hao L., Lachicotte R.J., Gysling H.J., Eisenberg R., *Inorg. Chem.* 38 (1999) 4616-4617
- [62] Brown D. H., McKinlay G., Smith W. E., *J. Chem. Soc. Dalton Trans.* (1977) 1874-1878
- [63] Uson R., Laguna A., Laguna M., *Inorg. Synth.* 26 (1989) 85-91
- [64] Murrov S.L., Carmichael I., Hug G.L. in "Handbook of photochemistry, second edition", 1993
- [65] Vogler A., Kunkely H., *Coord. Chem. Rev.* 219-221 (2001) 489-507
- [66] Ahmed L.S., Clegg W.C., Davies D.A., Dilworth J.R., Elsegood M.R.J., Girffiths D.V., Horsburg L., Miller J.R., Wheatley N., *Polyhedron* 18 (1999) 593-600
- [67] Hansch C., Leo A., Taft R.W., *Chem. Rev.* 91(1991) 165-182
- [68] Battisti A., Bellina O., Diversi P., Losi S., Marchetti F., Zanello P., *Eur. J. Inorg. Chem.*, (2007) 865-875
- [69] Chen J., Jiang T., Wei G., Mohamed A.A., Homrighausen C., Krause Bauer J.A., Bruce A.E., Bruce M.R.M., *J. Am. Chem. Soc.* 121 (1999) 9225-9226
- [70] Mohamed A.A., Bruce A.E., Bruce M.R.M., *Met.-Based Drugs* 6 (1999) 233-239
- [71] Mohamed A.A., Abdou H.E., Chen J., Bruce A.E., Bruce M.R.M., *Comments Inorg. Chem.* 23 (2002) 321-325
- [72] Mohamed A.A., Chen J., Bruce A.E., Bruce M.R.M., Krause Bauer J.A., Hill D.T., *Inorg. Chem.* 42 (2003) 2203-2205
- [73] Chen J., Mohamed A.A., Abdou H.E., Krause Bauer J.A., Fackler Jr J.P., Bruce A.E., Bruce M.R.M., *Chem. Commun.* (2005) 1575-1576

Chapter 5

***Computational studies of some N-heterocyclic dithiols
and their binuclear gold(I) phosphine complexes***

5.1 Introduction

Computational power provides scientists with a new, fast and increasingly reliable way of studying chemical processes via simulation of molecular geometry, orbitals, and energies [1, 2]. Improvement in computer capacity has increased the number of atoms in molecules which can be studied such that now even small polymers (up to 250 atoms) or complex biological systems can be studied in a reasonable time [1, 2]. Different molecular properties can be calculated, such as: dipole moment, relative energy, charge distribution, and the energies of molecular orbitals. The influence of different variables (such as pressure or temperature) on thermochemical properties can also be predicted. Reaction pathways can be calculated, and electron or proton affinity can be estimated with good accuracy. This “*in silico*” revolution provides us with a huge amount of valuable data and in some cases can help to understand the behaviour of complicated systems. However, we note with caution that this is still a complementary tool which cannot yet replace experimentation and direct observation and measurement.

With regards to the work described in the previous chapters, the following were defined as the aims of this modelling study.

a) Calculations were done on the dithiols to determine:

- 1) the ground state molecular geometry;
- 2) the most stable tautomer in different environments;
- 3) the IR spectra of the most stable tautomers;
- 4) the localisation of the LUMO and HOMO;
- 5) the energy and the localisation of the transitions when excited by light.

b) Calculations were done on different gold(I) compounds to determine:

- 1) the geometry of the molecules and the gold-gold distance;
- 2) the localisation of the LUMO and HOMO, the relative energies of the different excited states and their orbital localisation.

Once the aims of the calculations are defined, then the choice of method and basis set can be made. The choice of the method and basis set is a delicate question of balance between computing time and accuracy of the results.

5.1.1 Description of the basis set

The basis set is the mathematical description of the orbitals within a system used to perform the theoretical calculation. A large basis set will have less constraint on the localisation of the electrons in space and will give a better description of the orbitals. Each basis set is a combination of basis Gaussian functions which vary in type and numbers. The basis set will assign a certain basis function to each atom of a molecule in an approximation of its atomic orbitals.

A split valence basis set will add more basis functions to an atom, increasing the sizes but not the shape, of the valence orbitals (*i.e.* 6-31G) [1]. To allow the shape to change, a polarized basis has to be used. This polarized basis set will add orbitals with angular momentum higher than that required just to describe the valence shell orbital (*e.g.* with 6-31G(d,p), d orbitals will be added to a heavy atom, and p orbitals to hydrogen atoms) [1]. Another level of complexity is to add some diffuse function on the atom. They are large sized versions of the s- or p-type function and therefore allow electrons to occupy a larger region of space: (6-31G+(d,p)). This diffuse function is particularly interesting in the case of excited state optimisation or ionic species [1].

For heavy atoms beyond the third row of the periodic table, it is better to use the effective core potential method (ECP) where the inner shell is treated approximately as frozen in space and the electrons of the outer shell are moving. Furthermore, relativistic effects which are important in these atoms are included in this treatment. LanL2DZ [29] is a commonly used basis set for this type of atom. For a more detailed review of the basis set, the reader is referred to references 1 and 2.

5.1.2 Description of methods used in computational chemistry

Electronic structural methods can be of *ab initio* or semi-empirical types. They describe the procedures used to perform the calculations for modelling the molecular system.

For optimisation purposes and energy calculations, the simplest level is the Hartree-Fock Self-Consistent Field (HF) level of theory [18], which neglects any electron-electron interactions in the calculations. Then we have the density field function

(DFT/B3LYP) using the Becke-style theory implemented with the Lee-Yang-Parr correlation functions [20,21]. Another level is the Møller-Plesset (MP) [19] perturbation theory which takes into account electron correlation. The perturbations can be taken up to the fourth order (MP4). Configuration interaction-singlet (CIS) and time-dependent DFT (TD-DFT) have been developed to simulate excited states. Numerous other methods have been developed. A detailed description of the different methods and their mathematical description is outside the scope of this thesis, but for further reading see references 1 and 2, 18 to 22.

5.2 Computational studies of some N-heterocyclic dithiols

5.2.1 Introduction

The discovery of thiouracil as a constituent base of RNA, together with the biological activity of N-heterocycles thiols, has triggered numerous studies on N-heterocycles thiol tautomerism. [10-17, chapter 3]. To understand better the experimental results obtained in chapter 3, computational simulations of the N-heterocycles dithiolate have been done with the following aims in mind:

1. to determine which is the more stable tautomer in different media, (gas phase, MeOH, cyclohexane);
2. to simulate the IR spectra;
3. to identify the HOMO and LUMO of these species.

5.2.2 Geometry optimisation and the most stable tautomer

To determine which isomer is thermodynamically stable in the gas phase, the geometrical structure of the molecule was first optimised using the HF level of theory. The hypothetical presence of hydrogen bonding between the thiol and the nitrogen of the heterocycle determined which basis set was required, since for this interaction a diffuse function has to be used. A preliminary study was used to determine which basis set would be the best to give reliable data in a convenient time. We used the DMP ligand in both its dithiol and thiol-thione forms, and the computational times required are reported in table 5.1.

	Method and basis set	Time
Test A	HF/6-31G	0 h 11 mins
Test B	HF/6-31G(d)	0 h 40 mins
Test C	HF/6-311+G(d,p)	4 h 03 mins
Test D	HF/6-311+G(2d,2p)	10 h 30 mins

Table 5.1: Comparison of the computing time necessary to reach a stable geometry for the DMP dithiol isomer (Test D took 1 day 7 hours for the thiol-thione form)

Not surprisingly, the larger the basis set, the longer the calculation. Test A and test B were run more for comparative purposes on the optimisation time. Test D and test C gave a very similar final geometry, and no major difference in the IR, or orbital

localisation, was observed. So the computing time using the basis set in test D is far too long for the precision obtained in the results required. The basis set used in Test C is sufficient to get the most stable isomer and to obtain reliable results on the IR and localisation of the HOMO-LUMO.

All the structures were optimised using the HF level of theory with the basis set 6-311+G(d,p). To assess that the molecule stands in a local minimum of the potential energy curve and not in a saddle point, an IR simulation at the same level of theory and with the same basis set was systematically performed. Peaks of the IR spectrum are calculated using second derivatives of the energy with respect to nuclear positions, therefore one or more negative values are a sign of an optimised structure which is not in a local minimum. An estimation of the zero point energy (ZPE) corrections was obtained and scaled by the empirical factor 0.925 obtained by Scott and Radom [4]. Note that the scale found for the basis set HF/6-311G(d,p) was used. The difference in scaling with the basis set having a diffuse function should be minimal [4].

The optimised structure at the HF level was then used to calculate the single point energy with two other methods (DFT/B3LYP/6-311+G(d,p) and MP2/6-311+G(d,p)) which include electron correlation effects. All these results are for isolated molecules in the gas phase. To describe better their properties in solution, the model using the Self-Consistent Reaction Field (SCRF) was used. The solvent is considered as a continuum of uniform dielectric field, and the solute is placed inside a cavity within this field. The different methods used with SCRF determine the size and shape of the cavity. The simplest model is a sphere of a given radius; the most complex one defines the cavity as the isodensity surface of the molecule, which should be determined by iterative processes. The method used for our computation was a polarisable continuum model (PCM), which defines the cavity as the union of interlocking atomic spheres, and which is commonly used [5, 53].

5.2.2.1 Determination of the most stable tautomer of 2,4-dimercaptopyrimidine (24PYRI)

24PYRI has been studied for a long time because of interest in its biological and pharmacological activities, and tautomerism seems to be a key process in the mutation occurring during DNA duplication.

To assess the validity of the initial input files and the calculations, replication of the calculations done in the work of Yanez *et al.* [3] was run and these gave the same final energy at the MP2 level as this previous study. This confirms that the dithione is the most stable tautomer in the gas phase [31, 33].

5.2.2.2 Determination of the most stable tautomer of 4,6-dimercaptopyrimidine (46PYRI) in different media

The three possible tautomers are depicted in figure 5.1 and the results of the energy calculation in the gas phase are reported in table 5.2. Results for the energy calculations from the optimisation taking into account the solvent effect are summarised in table 5.3. Note that for 46PYRI only, calculations with different basis sets and levels of theory give different orders of stability of isomers so results from a number of calculations are presented.

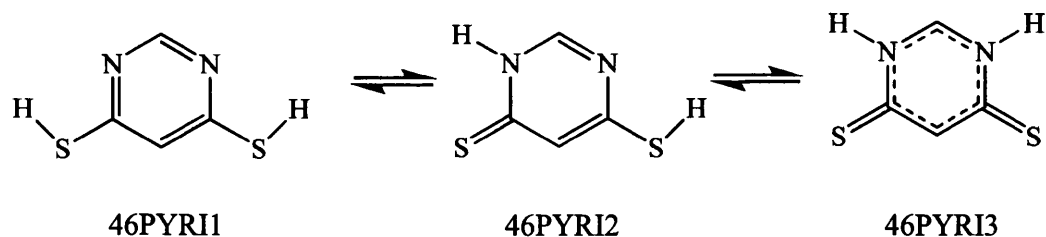
A crystal structure of the dithione has been reported in chapter 3 and this provided a useful reference to check the geometry optimisation of 46PYRI. The bond distances calculated by structural optimisation are in good agreement with those from the crystal structure, differing by only ± 3 pm. The computed geometry tends to allocate shorter distances than are seen in the crystal structure. This can be understood in terms of perturbation by crystal packing and interaction with other molecules in the solid state, which cause the symmetry in the bond distances calculated by the *ab initio* method to disappear (see figure 5.2).

At the HF level of theory, the most stable tautomer is the dithiol 46PYRI1 in the gas phase, but at the DFT level of calculation, 46PYRI2 is the lowest energy tautomer (table 5.2). The very small difference in energy ($0.16 \text{ kcal mol}^{-1}$) between the two most stable tautomers suggests that they both may exist in equilibrium in solution (an analysis of the potential energy curve between the two tautomers could help to

determine the activation energy of the equilibrium). The MP2 level of theory, with either a small basis set or a large one gives the same result as the HF calculations. So it seems that the DFT level of theory is not a good method of computation for this molecule.

If the geometry optimisation calculations are run by taking into account the dielectric constant of the solvent, the dithione, 46PYRI3, is the most stable tautomer in a polar solvent whereas the monothione, 46PYRI2, is the most stable isomer in a non-polar solvent. The large energy difference between the two forms suggests that the equilibrium will be shifted towards the formation of essentially only one species in solution, although the species present will be different in polar and apolar solvents.

According to the calculation, 46PYRI is a dithione in a polar solvent, and is in the monothione form in an apolar solvent. However it seems to be a dithiol in the gas phase. 24PYRI is experimentally determined to be a dithione in a isolated matrix [13]. As its isomer 46PYRI is predicted to be in the dithiol form by our *ab initio* calculations, it could be very interesting to study this compound in a isolated matrix to confirm our result.

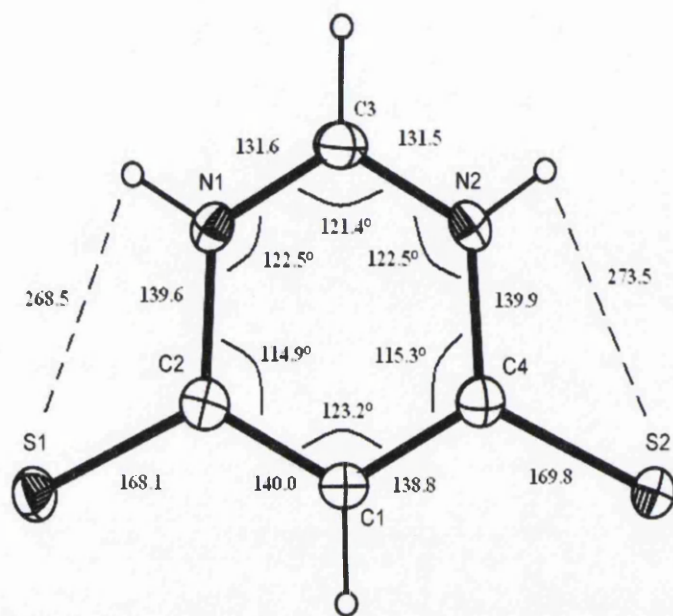
**Figure 5.1:** Tautomers of 46PYRI

	46PYRI1	46PYRI2	46PYRI3
Total energy HF	-1057.832051	-1057.831546	-1057.810343
ZPE	0.080725	0.084777	0.0878
$\Delta E_{(HF)}$	0	2.7	17.7
Total energy DFT	-1060.833744	-1060.837750	-1060.826048
$\Delta E_{(DFT)}$	0	-0.16	8.9
Total energy MP2/6-31G(d)	-1058.780852	-1058.782508	-1058.768298
$\Delta E_{(MP2/6-31G(d))}$	0	1.3	12.0
Total energy MP2/6-311+G(d,p)	-1058.980431	-1058.977381	-1058.959171
$\Delta E_{MP2/6-311+G(d,p)}$	0	4.3	17.4

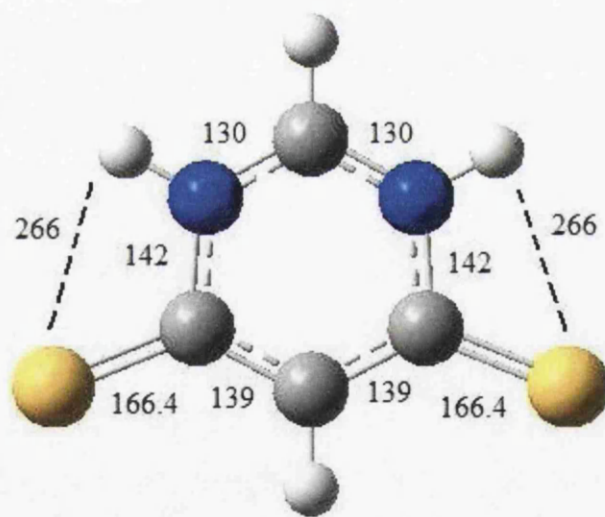
Table 5.2: Total energy (Har.) calculated at the HF/6-311+G(d,p), B3LYP/6-311+G(d,p), MP2/6-31G(d) and MP2/6-311+G(d,p) level, ZPE (Har.) without scale factors calculated at the HF/6-311+G(d,p) level, and relative energy with respect to the most stable tautomer at the two levels of theory, taking into account the ZPE scaled by 0.925 (in kcal mol⁻¹) for 46PYRI tautomers

	Total energy MeOH	ZPE	ΔE	Total energy Cyclohexane	ZPE	ΔE
46PYRI1	-1057.849266	0.078546	8.7	-1057.84031	0.079805	0
46PYRI2	-1057.864326	0.082699	1.7	-1057.846147	0.083924	-1.3
46PYRI3	-1057.87021	0.086191	0	-1057.832195	0.087528	9.6

Table 5.3: Total energy (Har.) and ZPE correction (Har.) without scale factors calculated at the HF/6-311+G(d,p) level, relative energy with respect to the most stable tautomer taking into account the ZPE scaled by 0.925 (in kcal mol⁻¹) for 46PYRI tautomers using SCRF = CPCM with MeOH and cyclohexane



A



B

Figure 5.2.: Structure, bond distances (pm) and angles ($^{\circ}$) of 46PYRI3

A) from X-ray diffraction

B) from the optimisation at the HF/6-311+G(d,p) level

5.2.2.3 Determination of the most stable tautomer of 2,6-dimercaptopyrazine (DMPA) in different media

The three possible tautomers are depicted in figure 5.3 and the results of the energy calculation for the gas phase reported in table 5.4. Energies calculated by taking into account the solvent effect via PCM are reported in table 5.5.

The structure optimisation gives angles and bond distances consistent with those found in the crystal structure of analogous N-heterocyclic thiols or thiones [15]. The difference in total energy (taking into account the ZPE) of the different tautomers demonstrates the higher stability of the dithiol DMPA1 in the gas phase. If the DMPA3 thiol group is in the plane of the pyridine, then the calculated IR spectrum contains a band having a negative value corresponding to a vibration localised on this thiol. By putting it out of the plane, a local minimum (all IR bands having positive values) is reached. This is the only case in this study where the thiol group has to be out of the plane to obtain a stable conformation.

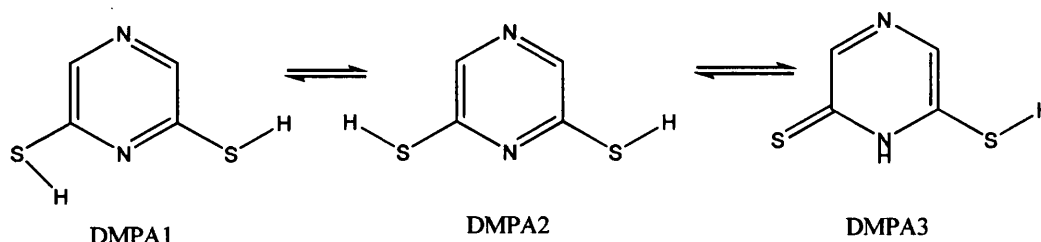


Figure 5.3: Tautomers of DMPA

	Total energy HF	ZPE	$\Delta E_{(HF)}$	Total energy MP2	$\Delta E_{(MP2)}$
DMPA1	-1057.813158	0.079928	0	-1058.968656	0
DMPA2	-1057.81158	0.080008	1.0	-1058.967025	1.1
DMPA3	-1057.805366	0.083696	7.1	-1058.959655	7.8

Table 5.4: Total energy (Har.) calculated at the HF/6-311+G(d,p) level and MP2/6-311+G(d,p) level, ZPE correction (Har.) without scale factors calculated at the HF/6-311+G(d,p) level, and relative energy with respect to the most stable tautomer at the two level of theory, taking into account the ZPE scaled by 0.925 (in kcal mol⁻¹) for DMPA tautomers

When the solvent effect is taken into account, the thione is the most stable form in a high dielectric polar protic solvent, and the dithiol DMPA1 is the most stable in the apolar solvent cyclohexane. These results are similar to the ones previously obtained in this work. The equilibrium between DMPA1 and DMPA3 in cyclohexane tends to be shifted towards the formation of the dithiol only as suggested by the large energy gap between the two forms (4.1 kcal mol⁻¹).

If the two species are considered in equilibrium in solution, by using the standard formula to estimate an equilibrium constant

$$K = e^{\frac{-\Delta E}{RT}} \quad \text{Equation 5.1}$$

with ΔE being the difference in energy between the two species in J·mol⁻¹, R the ideal gas constant and T the temperature in Kelvin (taken as 298 K) we can calculate the proportion of each species present. In methanol the equilibrium has an equilibrium constant of 0.36 suggesting a mixture in solution of DMPA3 (74%) and DMPA1 (26%). As all the studies in the literature and in this work show that the thiones are predominant in polar solvents, it would be reasonable to find that the equilibrium is shifted in MeOH towards the formation of DMPA3 exclusively.

	Total energy MeOH	ZPE	ΔE	Total energy Cyclohexane	ZPE	ΔE
DMPA1	-1057.831198	0.077809	0.6	-1057.821605	0.079071	0
DMPA2	-1057.83169	0.078084	0.5	-1057.820691	0.079285	0.7
DMPA3	-1057.836013	0.081934	0	-1057.818751	0.083030	4.1

Table 5.5: Total energy (Har.) and ZPE correction (Har.) without scale factors calculated at the HF/6-311+G(d,p) level, relative energy taking into account the ZPE scaled by 0.925 (in kcal mol⁻¹) for DMPA tautomers using SCRF = CPCM with MeOH and cyclohexane

5.2.2.4 Determination of the most stable tautomer of 2,6-dimercaptopyridine (DMP) in different media

The three structure-optimised tautomers are depicted in figure 5.4. The results of the energy calculation in the gas phase at different levels of theory are reported in table 5.6; the results for the calculation, taking into account solvent effects via the polarisable continuum model (PCM), are reported in table 5.7.

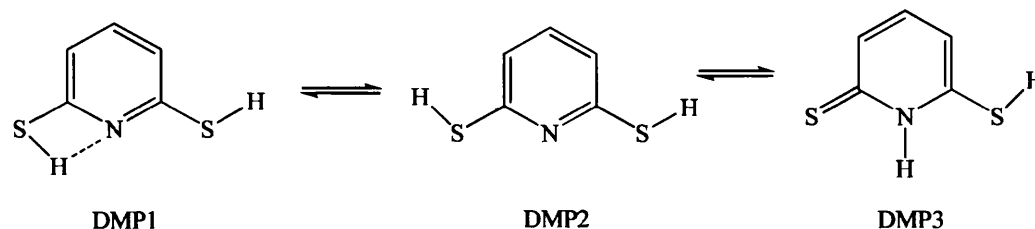


Figure 5.4: Tautomers of DMP

	Total energy HF	ZPE	$\Delta E_{(HF)}$	Total energy MP2	$\Delta E_{(MP2)}$
DMP1	-1041.825173	0.092505	0	-1042.949296	0
DMP2	-1041.823125	0.092590	1.3	-1042.947091	1.4
DMP3	-1041.820075	0.096384	5.5	-1042.940643	7.7

Table 5.6: Total energy (Har.) calculated at the HF/6-311+G(d,p) level and MP2/6-311+G(d,p) level, ZPE correction (Har.) without scale factors calculated at the HF/6-311+G(d,p) level, and relative energy with respect to the most stable tautomer at the two levels of theory, taking into account the ZPE scaled by 0.925 (in kcal mol⁻¹) for DMP tautomers

	Total energy MeOH	ZPE	ΔE	Total energy Cyclohexane	ZPE	ΔE
DMP1	-1041.843044	0.090375	4.3	-1041.833429	0.091666	0
DMP2	-1041.843488	0.090646	4.2	-1041.832158	0.091821	0.88
DMP3	-1041.853929	0.094659	0	-1041.834628	0.095734	1.6

Table 5.7: Total energy (Har.) calculated at the HF/6-311+G(d,p) level, ZPE correction (Har.) without scale factors calculated at the HF/6-311+G(d,p) level, and relative energy with respect to the most stable tautomer taking into account the ZPE scaled by 0.925 (in kcal mol⁻¹) for DMP tautomers using SCRF = CPCM with MeOH and cyclohexane

The geometry optimisation gives a C-S distance of 177 pm for the thiol and 167 pm for the thione, which are consistent with values found in the crystal structures of analogous compounds [5].

The most stable tautomer in the gas phase, as well as in nonpolar solvents is the dithiol in which one of the mercapto groups is H-bonded to the N atom of the ring. In a polar solvent, the most stable tautomer is the thione DMP3. This is in agreement with the results obtained in the literature from experimental observations, or *ab initio* calculations, for 2-mercaptopyridine which show that only the thione is present in polar solvents [6-10], and only the thiol form is present in a non-polar solvent or in the gas phase [11-12]. Fu *et al.* have demonstrated recently [5] the role of a protic solvent in the tautomerism process. The C=S acceptor and N-H donor hydrogen bonding sites can form a stable complex with the solvent, which hindered a direct intramolecular tautomerisation, but opens up a new solvent assisted tautomerisation route. According to the calculation given here, the dithione DMP3 is more stable by 4.3 kcal mol⁻¹ than the dithiol DMP1. For comparison, the thione 2-mercaptopyridine is stabilised in water by 3.6 kcal·mol⁻¹ [5]. The PCM method does not take into account the possible hydrogen bonding of protic solvents, but just considers the dielectric constant of the solvent. Therefore the result that DMP1 is slightly less stable than DMP2 in MeOH cannot be explained by a protic effect in our case, but rather by considering that DMP2 has a higher dipole moment than DMP1 (4.5 D and 3.1 D respectively).

By using equation 5.1, we can estimate the tautomer proportions. In MeOH, thione DMP3 is predominant at 99.9% compared with DMP1 or DMP2. In cyclohexane, DMP1 is predominant at 87 %, with DMP2 at 11% and DMP3 at 2%. So we can reasonably suggest that only the dithione (DMP3) is present in a protic polar solvent and only the dithiol (DMP1) is present in a non-polar solvent.

5.2.2.5 Determination of the most stable tautomer of 2,6-dimercaptonicotinic acid (ADMN) in different media

The five possible tautomers studied are depicted in figure 5.5 and the results of the energy calculation in the gas phase are reported in table 5.8.

The crystal structure described in chapter 3 was of the sodium salt of mono-deprotonated ADMN and therefore no comparison with the computational geometry optimisation of the neutral ADMN is possible. In all the structures the carboxylic acid group is in the plane of the pyridine ring. In some case a structure with it out of the plane could be optimised to a true minimum, but the total energy of this conformation is higher than the planar one. The five tautomers studied have been selected to represent the network of possible intramolecular hydrogen bonding possible. With any level of theory used for the computation (HF or MP2) on an isolated molecule, the most stable tautomer is ADMN5, i.e. the dithiol having its two thiol groups involved in intramolecular hydrogen bonding.

The carboxylic acid group plays a determining role in the stability of the different tautomers by its OH donor or C=O acceptor hydrogen bond effects. Also both thione tautomers (ADMN2 and ADMN4) are less stable than ADMN5. The hydrogen donor in ADMN2 is -OH, while -SH is the hydrogen donor in ADMN4. The hydrogen carried by the hydroxyl group can move by tautomerism along the carboxylic acid group, whereas the one in the thiol group is fixed and can only participate in the hydrogen bond. This could explain why ADMN2 is 4.2 kcal mol⁻¹ at the HF level (3 kcal mol⁻¹ at the MP2 level) less stable than ADMN4 in the gas phase. ADMN1 and ADMN5 are close in energy. To pass from one conformation to the other, the molecule should pass through an intermediate like ADMN3. The calculation suggests that in the gas phase ADMN is present in the dithiol form only.

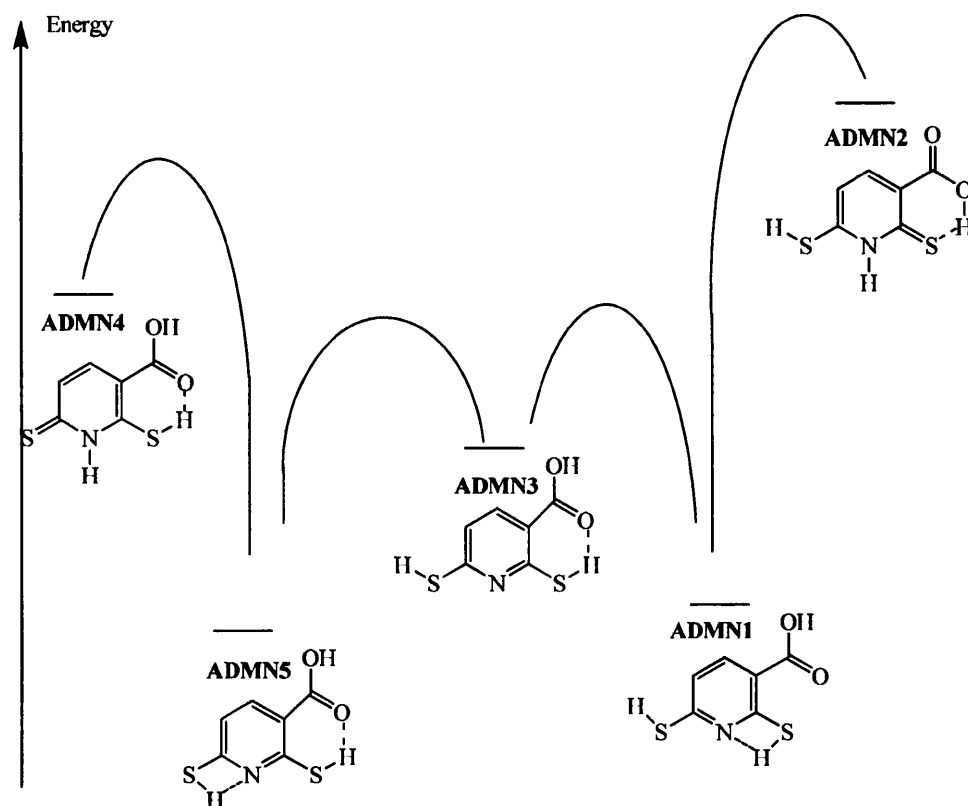


Figure 5.5: Relative energies of the ADMN tautomers. Dotted lines represent the possible hydrogen bond interactions which were not introduced in the initial structure.

	Total energy HF	ZPE	$\Delta E_{(\text{HF})}$	Total energy MP2	$\Delta E_{(\text{MP2})}$
ADMN1	-1229.497611	0.109715	0.9	-1231.132315	0.6
ADMN2	-1229.491095	0.113116	6.9	-1231.134117	6.8
ADMN3	-1229.496770	0.109669	1.4	-1231.139461	1.4
ADMN4	-1229.498135	0.113497	2.7	-1231.139133	3.8
ADMN5	-1229.498971	0.109661	0	-1231.141727	0

Table 5.8: Total energy (Har.) calculated at the HF/6-311+G(d,p) level and MP2/6-311+G(d,p) level, ZPE correction (Har.) without scale factors calculated at the HF/6-311+G(d,p) level, and relative energy taking into account the ZPE scaled by 0.925 (in kcal mol⁻¹) for ADMN tautomers

Structural optimisation of the ADMN tautomers taking into account the solvent effect through PCM would be time-consuming when using the large basis set 6-311+G(d,p). From the results obtained previously in this chapter, the use of a smaller basis set will provide reliable results of the relative stability of tautomers in a shorter time (3 hours instead of 11 hours). Therefore the basis set 6-31+G(d) was used for the results reported in table 5.9.

	Total energy MeOH	ZPE	ΔE	Total energy Cyclohexane	ZPE	ΔE
ADMN1	-1229.373823	0.107482	2.3	-1229.357517	0.109324	0.1
ADMN2	-1229.376846	0.111677	2.8	-1229.354858	0.113093	4
ADMN3	-1229.369981	0.107552	4.8	-1229.3550267	0.109272	1.6
ADMN4	-1229.381120	0.111372	0	-1229.361157	0.113069	0
ADMN5	-1229.369760	0.107388	4.8	-1229.3539088	0.109569	2.5

Table 5.9: Total energy (Har.) and ZPE correction (Har.) without scale factors calculated at the HF/6-31+G(d) level, relative energy with respect to the most stable taking into account the ZPE scaled by 0.925 (in kcal mol⁻¹) for ADMN tautomers using SCRF = CPCM with MeOH and cyclohexane

In MeOH, ADMN4 is the tautomer with the lowest total energy and therefore the most stable. As its difference in energy from the other tautomers is greater than 2 kcal mol⁻¹, it should be the only species present in significant concentration in a solvent with a high dielectric constant.

In cyclohexane, thione ADMN4 has the lowest total energy. The difference in energy taking into account the ZPE shows that the dithiol ADMN1 and ADMN4 have almost the same total energy ($\Delta E = 0.1$ kcal mol⁻¹). Hoff *et al.* [32] justify the stabilisation of the thione tautomer in cyclohexane by the large dipole difference between 2-mercaptopyridine and pyridine-2-thione (2-3 times greater). The difference in calculated dipole moment between ADMN4 and ADMN1 (7.1 D and 5.4 D respectively) is too low to explain why the thione is stabilised in cyclohexane. At this level of theory, it is not possible to conclude which tautomeric form is

thermodynamically dominant in cyclohexane. Since the difference in energy was so small, a larger basis set was then used to optimise the structure in cyclohexane. A larger basis set will provide a more accurate stabilisation energy. It has been shown that to have a reliable approximation of the stabilisation energy for 2-mercaptopyridine a large basis set taking into account electron correlation should be used, and the ZPE should be included in the total energy calculation [32]. To get better results in cyclohexane, the basis set previously used (6-311+G(d,p)) was implemented to optimise the ADMN2 and ADMN4 structures with the solvent effect and to get the corresponding ZPE. The difference in energies and ZPE are shown in table 5.10. The difference in ZPE is the same for the two basis sets. The difference in non ZPE-corrected energy drops by $0.8 \text{ kcal mol}^{-1}$ when a larger basis set is used. Dithiol ADMN1 is the most stable tautomer according to this calculation.

	6-31+G(d)	6-311+G(d,p)
ΔE without ZPE (kcal mol^{-1})	2.3	1,5
ΔZPE (kcal mol^{-1})	-2.4	- 2.4
ΔE including ZPE (kcal mol^{-1})	0.1	- 0.7

Table 5.10: Effect of the basis set on the difference in stabilisation energy and ZPE between ADMN1 and ADMN4 run at the HF level of theory with CPCM = cyclohexane (the ZPE is corrected by a factor of 0.925 when included in the total energy calculation).

To check this shift in the most stable tautomer, a MP2/6-311+G(d,p) single point energy (and CPCM) calculation was run on all of the structures optimised previously at the HF/6-311+G(d,p) level and their differences in energy including the ZPE calculated at the HF/6-311+G(d,p) level are reported in table 5.11. The results are conclusive regardless of the level of theory used: ADMN1 dithiol is the most stable tautomer in cyclohexane. At the MP2 level, it is clear that the tautomeric equilibrium is displaced toward the thiol forms, with ADMN1 being the most stable.

	Total energy Cyclohexane HF/6-311+G(d,p)	ZPE	ΔE_H F	Total energy Cyclohexane MP2/6-311+G(d,p)	ΔE_{MP2}
ADMN1	-1229.511573	0.108378	0	-1231.153503	0
ADMN2	-1229.508743	0.112212	4.0	-1231.148648	5.3
ADMN3	-1229.509216	0.108401	1.5	-1231.150667	1.8
ADMN4	-1229.514038	0.112205	0.7	-1231.151487	3.5
ADMN5	-1229.510658	0.108292	0.5	-1231.152281	0.7

Table 5.11: Total energy (Har.) and ZPE correction (Har.) without scale factors calculated at the XX/6-311+G(d,p) level (XX = HF or MP2), relative energy with respect to the most stable taking into account the ZPE calculated at HF/6-311+G(d,p) scaled by 0.925 (in kcal mol⁻¹) for ADMN tautomers using CPCM = cyclohexane

This study in cyclohexane could raise some doubts about the validity of the basis set used for the calculation in MeOH. Therefore an optimisation using HF/6-311+G(d,p) has been performed on ADMN1 and ADMN4 and a similar difference of corrected energy (1.7 kcal mol⁻¹) has been obtained, validating that ADMN4 is the most stable tautomer in a polar solvent.

5.2.2.6 Conclusion on the geometry optimisation

The geometry optimisations done at the HF/6-311+G(d,p) level of theory give structures having bond distances similar to the ones found in the solid state for thiones or thiols and therefore could be considered to give reliable information on the relative stability of the tautomers. As has already been underlined [32], these comparisons are strongly dependent upon taking into account the ZPE in the energy calculation, and the use of a relatively high level basis set. This is particularly important for ADMN in a polar solvent because of the higher number of possible intramolecular hydrogen bonds. Despite giving the correct most stable tautomer in the gas phase or in MeOH, the 6-31+G(d) level has been proven to be too weak for estimating this correctly in cyclohexane. A 6-311+G(d,p) level with the HF level of theory is required to get a reliable result for this solvent.

The compounds studied show the strong media influences generally observed for N-heterocycle thiol-thione tautomerism.

For structures with a pyridine or and pyrazine ring the following general observations can be made.

- 1) The thiol form is the more stable in the gas phase or in solvents with a low polarity or no protic effect.
- 2) The thione form is the more stable in a protic solvent or in a solvent of high polarity. The possibility of intermolecular hydrogen bonds is a key feature in pushing the equilibrium towards the thione.

In the crystal structure of 46PYRI, which has a pyrimidine ring, the molecules are linked through hydrogen bonding, which could explain why the only tautomer detected in the crystal structure of 46PYRI is the dithione.

5.2.3 Studies of infrared spectra

The infrared bands were calculated on all the optimised structures previously reported to assess whether the energy corresponding to this geometry is a local minimum on the potential energy curve. The level of theory used in this calculation was HF/6-311+G(d,p); no imaginary values in the harmonic frequency analysis were found, indicating that we are at a local minimum. The frequencies of the vibrational bands should be corrected for systematic shortcomings of the quantum-mechanical methodology, mainly to correct for anharmonicity [17], and the value suggested by Scott and Radom [4] of 0.925 was used.

To be able to compare the results obtained in the calculation with empirical measurements, we would need to isolate the molecule in an inert frozen matrix of argon, as has been done by Lapinski *et al.* [14-17] for 2-mercaptopyridine, 2-thiopurine, 2-mercaptopyridazine or 2-mercaptopyrimidine. This technique was not available to us.

The IR spectra reported in chapter 3 were measured in the solid state at room temperature, where bands are wider than those observed at low temperatures. By comparing these experimental measurements with those from the calculations, we hoped to determine the dominating tautomer. For ADMN, only the infrared spectrum of the sodium salt was measured so it will not be considered.

5.2.3.1 46PYRI infrared spectra

The IR frequencies for different tautomers are reported in table 5.13.

The vibrational bands around 430 cm^{-1} and 1240 cm^{-1} correspond to that calculated for $\nu_{\text{C=S}}$. These vibrational bands are present in the solid state spectrum. Also, most of the bands from the measurements in the solid state found a correspondence in the IR spectrum calculated for 46PYRI3. So from the comparison of the calculated values and the IR measured, 46PYRI3 is thought to be the most stable tautomer.

The crystal structure of 46PYRI shows the dithione being the only species present. The calculation at the HF/6-311+G(d,p) level for 46PYRI3 seems to give a decent approximation of the IR spectrum in the solid state and therefore we can assume that this level of theory is high enough to deduce the tautomer present in the solid state.

Measured ν cm ⁻¹	46PYRI1 ν cm ⁻¹ (intensity)	46PYRI2 ν cm ⁻¹ (intensity)	46PYRI3 ν cm ⁻¹ (intensity)
	250 (57)	231 (35)	
410			390 (45)
451		430 (25)	439 (98)
531			577 (34)
714		685 (74)	733 (96)
813	808 (106)	823 (132)	830 (226)
847	864 (22)		
970		973 (24)	964 (26)
1050			991 (799)
1180	1105 (25)	1193 (244)	1162 (88)
1202	1124 (48)		1198 (643)
1240		1241 (21)	1283 (25)
1358	1329 (110)	1446 (183)	1362 (463)
1385	1487 (157)		
1531	1591 (234)	1604 (837)	1517 (1004)
			1612 (230)
1579	1626 (650)	1670 (608)	1678 (1090)
2689	3100 (21)	3542 (100)	3525 (211)

Table 5.12: Infrared bands for 46PYRI in the solid state and evaluated for the different tautomers with HF/6-311+G(d,p). Values are corrected by 0.925.

5.2.3.2 DMPA infrared spectra

The infrared frequencies for different tautomers are reported in table 5.14.

Measured ν cm^{-1}	DMPA1 ν cm^{-1} (intensity)	DMPA2 ν cm^{-1} (intensity)	DMPA3 ν cm^{-1} (intensity)
449			
470			463 (20)
550	891 (19)		
827	915 (70)	888 (19)	711 (70)
850	941 (40)	930 (70)	889 (23)
996	1015 (108)	951 (36)	974 (170)
1134	1022 (34)	1023 (107)	1147 (202)
1173	1174 (50)	1175 (44)	1181 (132)
1383	1232 (142)		1319 (112)
1461	1429 (110)	1430 (100)	1482 (46)
1544	1603 (168)		
1639	1620 (24)	1603 (196)	1604 (497)
2900			3532 (93)
3198			
3342			

Table 5.13: Infrared bands for DMPA in the solid state and evaluated for the different tautomers with HF/6-311+G(d,p). Values are corrected by 0.925.

The measured infrared spectra does not fit at all any of the calculated vibrational frequencies for the dithiol DMPA1 or DMPA2. When compared with DMPA3, a correspondence can be found between the two. The band measured at 463 cm^{-1} corresponding to a $\nu_{\text{C=S}}$ vibration, has a match at 470 cm^{-1} in the calculated spectrum. According to these infrared simulations, DMPA is present as the thione form, DMPA3, in the solid state.

5.2.3.3 DMP infrared spectra

The infrared frequencies for different tautomers are reported in table 5.15.

Measured ν cm^{-1}	DMP1 ν cm^{-1} (intensity)	DMP2 ν cm^{-1} (intensity)	DMP3 ν cm^{-1} (intensity)
447			444 (26)
657			675 (26)
703			690 (31)
750	798 (59)	794 (60)	780 (63)
815	807 (39)	808 (47)	825 (38)
850			
870			932 (64)
973		952 (32)	975 (147)
1019	1082 (37)	1086 (25)	
1128	1173 (58)	1180 (40)	1134 (334)
1158	1186 (67)	1187 (63)	1154 (127)
1237	1220 (44)	1225 (52)	1244 (27)
	1446 (29)		
1360	1456 (169)	1456 (185)	1372 (40)
	1616 (144)	1615 (119)	1415 (45)
1568	1621 (267)	1621 (313)	1511(46)
			1608 (640)
			1654 (238)
2815			3810 (74)

Table 5.14: Infrared bands for DMP in the solid state and evaluated for the different tautomers with HF/6-311+G(d,p). Values are corrected by 0.925.

The measured infrared spectra does not fit the calculated infrared for the dithiols DMP1 or DMP2. But similarities can be found with DMP3. The measured band at 447 cm^{-1} corresponding to a $\nu_{\text{C-S}}$ vibration, has a match at 444 cm^{-1} in the calculated spectrum. According to these infrared simulations, DMP is present as the thione form, DMP3, in the solid state, as has already been found for the similar compound 2-mercaptopyridine [34].

5.2.4 HOMO-LUMO localisation and transition estimation via TDDFT

TDDFT studies using the basis set 6-31+G(d) have been reported to be a useful method to model the excited states and optical transitions of thiones. [23]. Therefore a single point energy TDDFT/B3LYP/6-31+G(d) calculation was run on the previously optimised structures at the HF/6-311+G(d,p) level. We will compare the results with the experimental results obtained in solution, which are given in chapter 3. TDFT calculations with the B3LYP/6-31+G(d) basis set have been run on the structure of the most stable tautomer previously determined. The orbitals illustration of the orbitals have been made via the program Gaussview, with an isodensity of 0.03.

The optical transitions calculated with TDDFT are also allocated an oscillator strength. A calculated very low or zero oscillator strength can be associated with:

- 1) a spin-forbidden transition (singlet to triplet) which will usually not be detected experimentally, or,
- 2) a spin allowed (singlet to singlet) but symmetry forbidden transition. Vibrational coupling can allow the experimental observation of this band. These vibrational couplings are not taken into account in TDDFT calculations.

5.2.4.1 TDDFT for 2,6-dimercaptopyridine (DMP)

TDDFT calculations performed on the DMP1 or DMP2 optimised structures do not give any singlet-singlet transition above 268 nm (see table 5.16). Despite being the most stable tautomers in the gas phase, their calculated transitions show that they do not fit the experimental values measured in a polar solvent, which confirms that these two species are not present in a DCM/MeOH (1:1) solution of DMP. However, for DMP3, calculation gives two bands with strong oscillator strengths at 367 nm and 281 nm, which originate from a $^1(\pi \rightarrow \pi^*)$ transition. The other calculated weak transitions could be due to some symmetry forbidden $^1(n \rightarrow \pi^*)$ transitions. In DCM/MeOH (1:1), two bands are observed experimentally but these are slightly red-shifted from the computational values. TDDFT calculation on the DMP3 optimised structure in MeOH was then performed in order to get a better representation of the molecular structure.

Transition/nm with (oscillator strength (f))		
DMP1	DMP2	DMP3
267 (0.0908)	267 (0.0845)	420 (0.0002)
234 (0.0034)	234 (0.0038)	367 (0.0876)
232.9 (0.1398)	233.8 (0.1400)	328 (0.0001)
232.7 (0.0003)	232.5 (0.0000)	322 (0.0002)
230.3 (0.0143)	228 (0.0165)	307 (0.0089)
		281 (0.3235)

Table 5.15: Singlet-singlet transitions and oscillator strengths, calculated with TDDFT/B3LYP/6-31+G(d) for DMP tautomers

The main transitions obtained using DMP3 optimised taking into account the solvent force field are presented in table 5.16. The gas phase optimised structure gives two transitions at 366 nm and 282 nm with oscillator strengths of 0.088 and 0.326 respectively. If the optimised structure taking into account the solvent is used for the calculation, these transitions are then red-shifted to 402 nm and 292 nm (oscillator strengths 0.068 and 0.329 respectively), see table 5.17. These values match quite well the observed transitions in solution: the calculated long wavelength absorption band is at 10 nm longer wavelength than that observed experimentally, and the higher energy absorption band is at the same wavelength.

Experimental		Calculated	
λ_{\max}/nm	ϵ_{\max} $\text{dm}^3 \text{cm}^{-1} \text{mol}^{-1}$	λ_{\max}/nm	Oscillator Strength (f)
292	10300 (± 400)	292	0.329
392	8100 (± 300)	402	0.068

Table 5.16: Comparison between absorption in DCM:MeOH (1:1) solution and TDDFT/B3LYP/6-31+G(d) calculated transitions for DMP3 taking into account the solvent influence ($f > 0.005$)

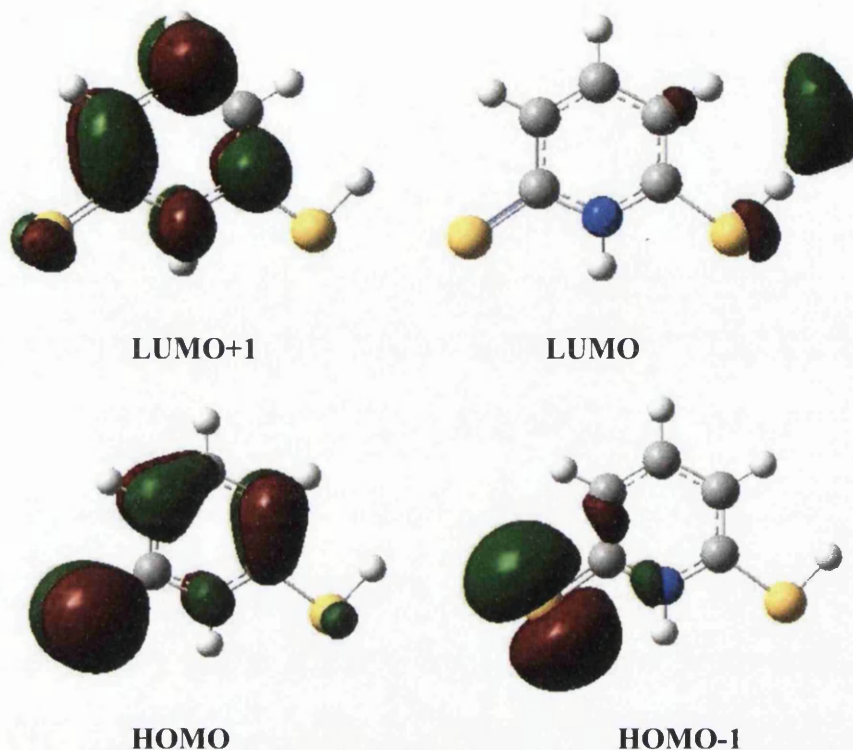


Figure 5.6: LUMO and HOMO molecular orbitals of DMP3

The LUMO and HOMO orbitals of DMP3 are depicted in figure 5.5. The HOMO is composed of a thione sulphur p orbital and π ring orbitals, while the HOMO-1 is composed quite exclusively of a thione sulphur p orbital. The LUMO is mainly located on the SH, while the LUMO+1 delocalised all over the molecule.

The short lifetime observed for this compound even at 77 K (see chapter 3) has been explained by the presence of the thiol substituent, which opens a vibrational non-radiative deactivation pathway. The localisation of the LUMO on the thiol nicely supports this hypothesis.

5.2.4.2 TDDFT for 2,6-dimercaptopnicotinic acid (ADMN)

TDDFT calculations have been performed on three ADMN optimised structure tautomers in the gas phase at the HF/6-311+G(d,p) level: two thiones (ADMN4 and ADMN2), and the most stable tautomer in the gas phase ADMN5 (see table 5.17). No computation has been done on the two other tautomers in the gas phase as they are not the most stable dithiol, and dithiol compounds are expected not to match the absorption spectra, as seen with DMP previously. As the absorption is measured in solution, the two thiones ADMN2 and ADMN4 have been optimised at the HF/6-311+G(d,p) level with CPCM = methanol, and a TDDFT/B3LYP/6-31+G(d) has been performed on these optimised structures and the transitions obtained compare with the experimental results (see table 5.18).

Transition/nm with (oscillator strength (f))		
ADMN2	ADMN4	ADMN5
387 (0.0752)	424 (0.0000)	306 (0.1090)
379 (0.0002)	371 (0.0002)	269 (0.1887)
322 (0.0000)	360 (0.0177)	265 (0.0004)
299 (0.0003)	312 (0.5103)	257 (0.2612)
293 (0.0001)	267 (0.0002)	
285 (0.2721)	261 (0.0106)	
268 (0.0239)	252 (0.0352)	

Table 5.17: Singlet-singlet transitions and oscillator strengths, calculated with TDDFT/B3LYP/6-31+G(d) for ADMN tautomers

The singlet-singlet transition evaluation does not show any bands above the 310 nm region for the dithiol ADMN5. However, the thione tautomers have bands around 387 nm and 322 nm ($f = 0.075$ and 0 respectively) for ADMN2 or 360 nm and 312 nm ($f = 0.0177$ and 0.5193 respectively) for ADMN4. As the experimental absorption spectrum has bands at 320 nm and 380 nm, ADMN2 or ADMN4 are the predominant species. However, since this calculation was done for isolated molecules, it was necessary to refine the calculation to take into account solvent effects; the results are presented in table 5.18.

Experimental		Calculated ADMN2		Calculated ADMN4	
λ_{\max}/nm	ϵ_{\max} $\text{dm}^3 \text{cm}^{-1} \text{mol}^{-1}$	λ_{\max}/nm	Oscillator Strength	λ_{\max}/nm	Oscillator Strength
274	9200 (± 200)	292	0.2252	274	0.0208
320	12700 (± 300)	332	0.0000	324	0.4885
390	12400 (± 300)	400	0.0001	387	0.0130
400	14300 (± 500)	414	0.0592	399	0.0002

Table 5.18: Comparison between absorption in DCM:MeOH (1:1) solution and TDDFT/B3LYP/6-31+G(d) calculated transitions performed on structures taking into account solvent influence (bands shown are those with $f > 0.005$ for ADMN4, and selected bands to match absorption spectra for ADMN2)

The new transitions of ADMN4, calculated when taking solvent into account, match quite well in position the experimental ones. The lowest energy calculated transition which has a very low oscillator strength, could be attributed to a $^1(n \rightarrow \pi^*)$ calculated transition. Calculated transitions for ADMN2 are globally close in position to the experimental ones, but two transitions (332 nm and 400 nm) have very low oscillator strength. They are attributed to a $^1(n \rightarrow \pi^*)$ transition, but the experimental 320 nm band has a high absorption coefficient ($> 10^4$). So ADMN2 alone is unlikely to be the species responsible for the absorption spectrum in MeOH:DCM (1:1). ADMN4 is a better candidate, but is still not a perfect match. Perhaps the real situation is a mix of both ADMN2 and ADMN4.

The calculated molecular orbitals for ADMN4 are shown in figure 5.7. It is noteworthy that the LUMO and LUMO+1 are very close in energy (eigenvalue 0.048 and 0.049) and therefore LUMO+2 will also be given in figure 5.7. The HOMO is localised on π orbitals of the C=S bond and the pyridine ring, whereas the HOMO-1 is only located on the C=S bond. LUMO and LUMO+1 will be treated together as they are so close in energy. The LUMO+1 is located partially on the π^* orbital of the ring but mainly on the C-O and OH bonds of the carboxylic acid group. The LUMO+2 is located on π^* orbitals of the pyridine ring. The partial localisation of the LUMO on the electron-withdrawing carboxylic acid group is not very surprising, it can also explain why no phosphorescence is observed, since non-radiative vibrational

deactivation should be important with the carboxylic acid group and may quench the lowest triplet state emission efficiently.

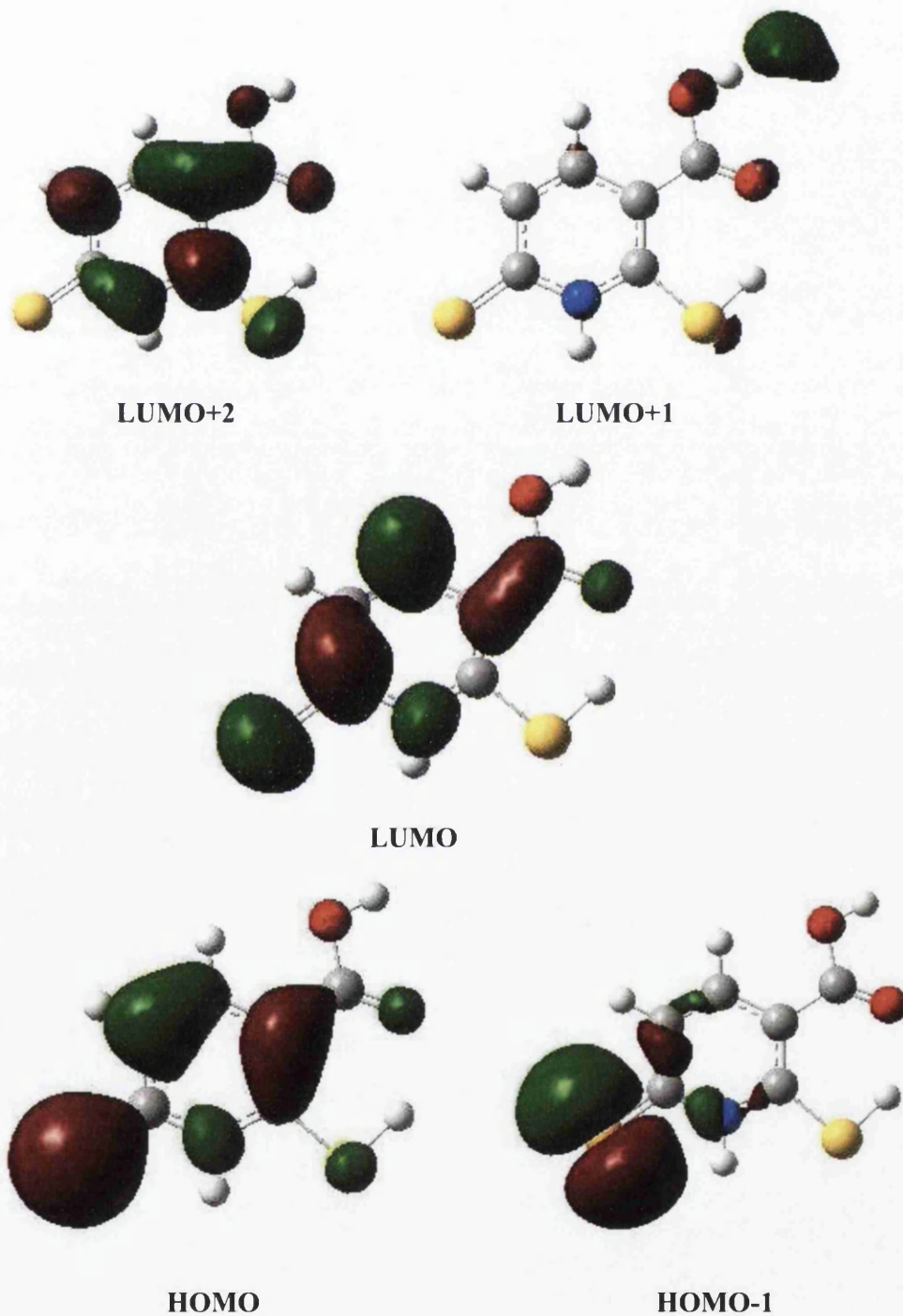


Figure 5.7: Orbitals of ADMN4

5.2.4.3 TDDFT for 2,6-dimercaptopyrazine (DMPA)

Note that the sodium salt of de-protonated DMPA has been used to obtain the absorption spectra, whereas the calculations have been carried out on the neutral DMPA.

Table 5.19 presents the transitions found by applying TDDFT to the structure optimised isolated molecule. The two dithiols DMPA1 and DMPA2 have no transition bands above 290 nm, whereas the thione tautomer, DMPA3, shows transitions at 297 nm and 376 nm with significant oscillator strength. The experimental absorption spectrum of de-protonated DMPA shows a very intense absorption peak around 433 nm, so it may be present in solution as the thione form.

Transition/nm with (oscillator strength (f))		
DMPA1	DMPA2	DMPA3
287 (0.0055)	286 (0.0056)	470 (0.0003)
284 (0.1193)	283 (0.1133)	376 (0.0758)
252 (0.0000)	279 (0.0000)	337 (0.0002)
		297 (0.0052)
		275 (0.2600)
		260 (0.0041)

Table 5.19: Singlet-singlet transitions and oscillator strengths calculated with TDDFT/B3LYP/6-31+G(d) for DMPA tautomers.

Despite being in a neutral state, DMPA3 is the species best matching the experimental absorption spectra and it is the most stable according to the energy calculations; its orbitals are depicted in figure 5.8.

Experimental		Calculated	
λ_{\max}/nm	ϵ_{\max} $\text{dm}^3 \text{cm}^{-1} \text{mol}^{-1}$	λ_{\max}/nm	Oscillator Strength
252	6000 (± 300)	253	0.0730
290	5700 (± 200)	283	0.3056
433	6200 (± 200)	391	0.1012

Table 5.20: Comparison between absorption bands in DCM:MeOH (1:1) solution and TDDFT/B3LYP/6-31+G(d) calculated transitions for DMPA3 taking into account the solvent influence (calculated transitions with $f > 0.005$ are shown)

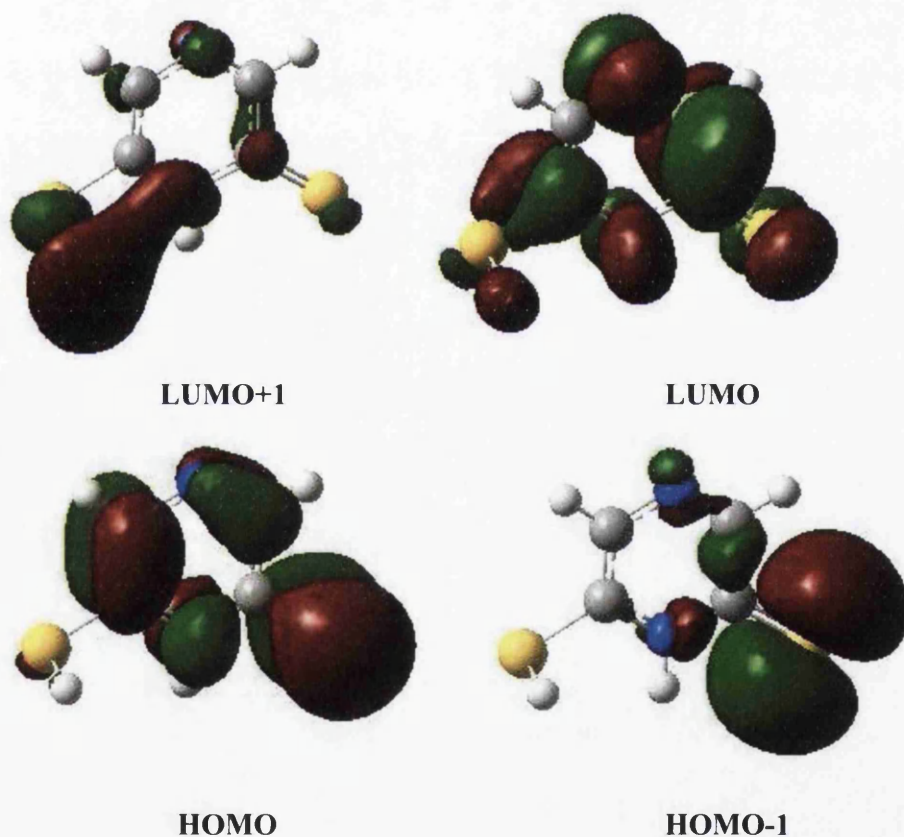


Figure 5.8: Orbitals of DMPA3

The HOMO is split between the C=S bond π orbital and the pyrazine ring π orbital. HOMO-1 is mainly localised on the C=S bond. The LUMO is delocalised all over the molecule whereas the LUMO+1 is mainly on the thiol substituent. As seen with ADMN and DMP, the localisation of the LUMOs on the “floppy” thiol is expected to quench effectively any radiative deactivation from a triplet state.

5.2.4.4 TDDFT for 4,6-dimercaptopyrimidine (46PYRI)

Table 5.21 shows the calculated transitions found by applying TDDFT to the structure optimised isolated molecule. The dithiols 46PYRI1 has no transitions above 256 nm, whereas the two thione tautomers, 46PYRI2 and 46PYRI3, show transitions at 285 nm and higher with significant oscillator strengths. We can, therefore, exclude the dithiol from being responsible for the experimental absorption spectrum, since this shows absorption bands up to 380 nm. However, the results are inconclusive regarding which thione tautomer is the origin of the absorption spectrum.

Transition/nm with (oscillator strength (f))		
46PYRI1	46PYRI2	46PYRI3
256 (0.0054)	405 (0.0001)	511 (0.0001)
253 (0.0000)	351 (0.0481)	472 (0.0000)
250 (0.0552)	348 (0.0001)	439 (0.0003)
234 (0.0032)	281 (0.3638)	384 (0.0000)
230 (0.0735)	259 (0.0046)	357 (0.1802)
227 (0.4267)	257 (0.0275)	328 (0.0028)
		303 (0.4212)
		294 (0.1628)

Table 5.21: Singlet singlet transition and oscillator strengths calculated using TDDFT/B3LYP/6-31+G(d) for 46PYRI tautomers without the solvent effect.

The TDDFT method was then applied to the optimised geometry, taking into account the solvent effect, for tautomers 46PYRI2 and 46PYRI3. The results are reported in table 5.22. In the 290-320 nm region, 46PYRI3 is predicted to have three intense bands at 302, 310 and 324 nm whereas 46PYRI2 should have only one band at 291 nm. The experimental spectrum in DCM:MeOH shows a broad band with a maximum at 380 nm and a number of weaker bands at lower wavelength (see figure 5.9). Although the match is far from perfect these data suggest 46PYRI3 as the dominant species present.

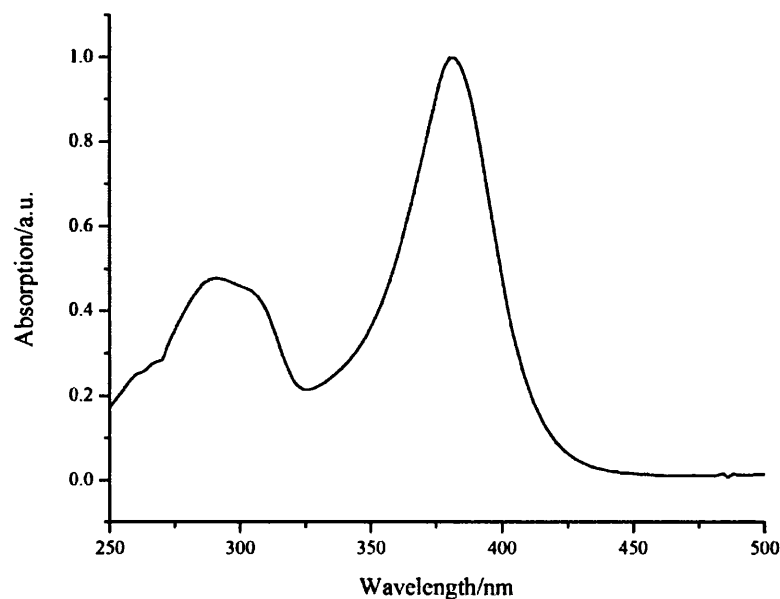


Figure 5.9: Absorption spectrum 46pyri in DCM:MeOH (1:1)

Experimental		Calculated 46PYRI2		Calculated 46PYRI3	
λ_{\max}/nm	ϵ_{\max} $\text{dm}^3 \text{cm}^{-1} \text{mol}^{-1}$	λ_{\max}/nm	Oscillator Strength	λ_{\max}/nm	Oscillator Strength
260	8000 (\pm 850)	253	0.2245	248	0.0954
290	13000 (\pm 1300)	269	0.0437	302	0.0097
310		291	0.3510	310	0.2856
380	30000 (\pm 3200)	389	0.0330	324	0.3751
				382	0.0593

Table 5.22: Comparison between absorption in DCM:MeOH (1:1) solution and TDDFT/B3LYP/6-31+G(d) calculated transitions for 46PYRI structures taking into account solvent influence ($f > 0.005$)

The HOMO for 46PYRI3 is localised on the π orbitals of the C=S bonds and the π orbitals of the pyrimidine ring. The HOMO-1 is mainly localised on the C=S bonds. The LUMO is mainly located on the C=S π^* anti-bonding orbitals with a contribution from the C-N π^* anti-bonding orbitals. The LUMO+1 is spread uniformly over the molecule. The LUMO+2 is located on the pyrimidine ring. No LUMO orbital seems to be associated with a floppy bond which will promote non-radiative decay. Therefore, if a triplet state is reached, it may well live long enough to give phosphorescence.

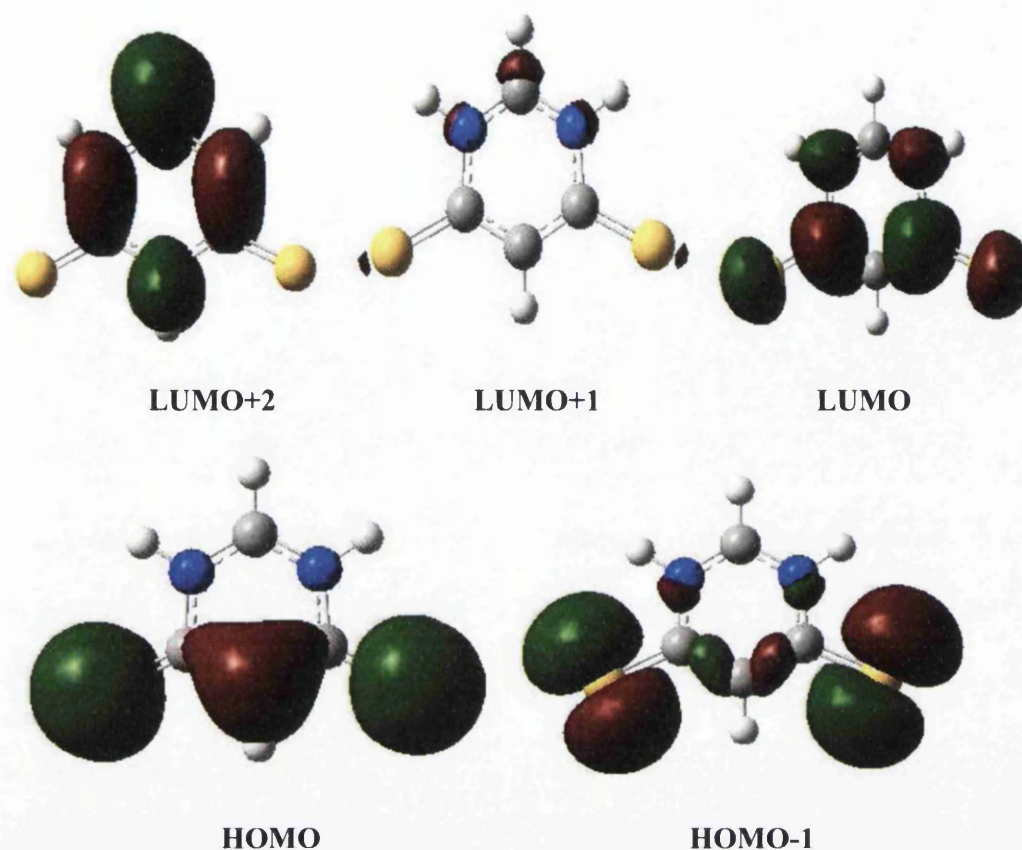


Figure 5.9: Orbitals of 46PYR13

5.2.4.5 Conclusions from TDDFT calculations

Thiols generally do not absorb above 300 nm, whereas thiones do. As all the compounds studied here absorb above 300 nm then thione rather than thiol structures are the most likely species present in solution. When used with the optimised structures and taking into account the solvent dielectric field, the TDDFT method gave positions and oscillator strengths of optical transitions which could generally be reasonably well correlated with those found experimentally, and which gave useful information to help determine which structure was present in solution.

In general the HOMO is localised partially on the C=S and the ring, whilst the HOMO-1 is localised on the C=S bond. When there is a -SH substituent or -COOH substituent present, the LUMO is partially or totally localised on it. When excited, the vibrational or proton exchange non-radiative pathway can therefore compete effectively with radiative pathways, and this may allow long lived phosphorescence to be quenched. However in the case of 46PYR1 the LUMO is mainly localised on the ring and no obvious vibrational deactivation can be predicted. Therefore the

triplet excited state of 46PYRI has a greater probability of deactivation through phosphorescence.

5.2.5 Conclusions from the *ab initio* simulation of N-heterocyclic dithiolates

Ab initio geometry optimisations have been run on different tautomeric forms of DMPA, ADMN, DMP and 46PYRI, considering them as isolated molecules or as inside a force field arising from the solvent dielectric constant. The relative energies obtained at different levels of calculation allow us to conclude that the dithiol tautomer is the most stable in the gas phase, or in a non-polar solvent (except 46PYRI where the monothione is predominant). The thione is the most stable form in a polar solvent

The crystallographic data for 46PYRI and the optimised structure of 46PYRI3 are in agreement.

Infrared bands have been calculated for each tautomer and the optical transitions simulated via TDDFT. Experimental measurements obtained in chapter 3 have been compared with those predicted from by *ab initio* calculations. Infrared comparisons allow us to confirm that it is the thione form which is adopted in the solid state. The TDDFT confirms the presence of thiones in solution and in some cases gives a good match to experimental absorption values.

Ab initio calculations can provide reliable and useful information on the properties of this class of compounds, provided they are run with a large basis set including at least one diffuse function and several split valence orbitals.

5.3 Computational studies of binuclear gold(I) phosphine N-heterocyclic dithiolate complexes

5.3.1 Introduction

Aurophilicity, and the relativistic effect explaining it, has been one of the causes for the study of gold derivatives in computational chemistry. The treatment of this weak interaction requires extra care: the relativistic effect should be adequately included, a polarisation function added and a correlated method should be used. Pyykkö has produced recently an extensive review on the state of the art of this subject [24,25] and studied the electron correlation effect on the calculations at different levels of theory [26, 44]. It appears that the best way to take into account all the effects of the gold atom is to use the effective core potential (ECP) method and a pseudo-potential. The pseudo-potentials developed by Hay and Wadt [29, 30] are commonly used, often implemented with a polarisation function of the 5d shell having $\alpha_F = 1.19$ [27] and $\alpha_F = 0.2$ for polarisability and aurophilicity [28].

This method has been used successfully by Pan to simulate the excited states of different annular binuclear gold(I) complexes as well as the influence of aurophilicity with bridging phosphine ligands [35], bridging phosphines and/or dithiolates [36, 49], phosphinothioethers [37] or two dithiolate ligands [46]. He also recently studied the effect of substituents on the luminescence and structure of binuclear gold(I) complexes [45].

Recently, the ECP method with DFT/B3LYP functionality and the LanL2DZ [29] basis set, to simulate the geometry and the localisation of the orbitals, has been used systematically by different groups: Laguna's group [38] or Lin's group [39] on gold-pyridine complexes, Che's group [40] with gold(I) and copper(I) phosphine thiolate complexes or Martinez to study some uracil-gold interactions [41]. Binuclear gold(I) phosphine thiolate complexes have also been studied [42, 43].

To save computing time the phenyl groups are replaced by hydrogen atoms or methyl groups [40, 43]. This replacement gives minor to no structural change and reasonable TDDFT calculation results [40, 43].

The molecular structures were optimized by DFT without symmetry constraints using the program GAMESS [47]. The calculations employed B3LYP and the basis set LanL2DZ with effective core potentials and valence basis set [29, 30, 48], augmented with two f-type polarization functions with the exponents 0.2 and 1.19 [44] to describe the valence electrons of gold. The 6-31G(d,p) basis sets were used for the expansion of the Kohn-Sham orbitals of sulphur, phosphorus, oxygen, nitrogen, carbon and hydrogen. At the final equilibrium geometry with minimum energy, the maximum $\partial E/\partial r$ gradient was 10^{-5} Hartree Bohr [47]. The energy Hessian was calculated for the resultant stationary points, and all were characterized as local minima (i.e., no imaginary frequencies). This program gives the representation of the HOMO and LUMO only. So we used a single energy point calculation using Gaussian3.0 on the optimised geometry with GAMESS, and DFT/B3LYP/LanL2DZ associated with NBO (natural bond orbital) was used to get the orbitals and the electronic charge carried by each atoms. TDDFT/B3LYP/LanL2DZ was used to calculate transitions.

The structure of $[\text{Au}_2(\text{SCH}_2\text{S})(\text{PH}_2\text{CH}_2\text{PH}_2)]$ has already been optimised by Pan [49] at the MP2/LanL2DZ level. He added a d-type function to S ($\alpha = 0.421$) and P ($\alpha = 0.34$) and an f-type function to Au ($\alpha = 0.2$) in the ECP calculations. As a check on our technique this molecule was optimised using our method and the distances obtained were compared to those obtained by Pan. Au-P and Au-S distance were the same, but the Au-Au distance was 20 pm longer in our case than either the experimental value or the *ab initio* distances calculated by Pan [49]. The influence of this error will be discussed later.

5.3.2 Structure optimisation

Two criteria have driven the selection of the molecules for this study:

- 1) the influence of the thiolate;
- 2) the influence of the methylene chain length between the two phosphine ligands.

Compounds **1b**, **2b**, **4b**, **5b**, **6b** and **4c** were selected for study. A representation of their optimised structures is given in figure 5.10 and relevant distances, angle and dihedral angles are reported in table 5.23.

All the Au-P and Au-S distances are in accord with values found in literature (226 pm and 230 pm respectively) [50, 51, 52]. All the gold-gold distances are far greater

than the sum of the gold van der Waals radii (340 pm) and therefore no aurophilic interaction is possible. The S-Au-P angles deviate slightly from the ideal gold(I) linear coordination mode, but by only a few degrees. Although, as mentioned in section 5.3.2, our method has a tendency to overestimate the gold-gold distance the S-Au-P angle would have to bend to an angle less than 170° to bring the two Au atoms close enough for any aurophilic interaction to be considered, and this has not been observed in any kind of gold(I) phosphine thiolate.

	1b	2b	4b	4c	5b	6b
<u>Distance (pm)</u>						
Au–Au	376.1	375.8	376.1	375.8	369.2	380.1
Au–P	228	230	228	228	229	228
Au–S	235	235	235	235	235	235
<u>Angle (°)</u>						
P–Au–S	175.7	169.7	176.2	173.1	177.1	175.4
	175.9	172.3	176.1	171.5	177.8	175.7
<u>Dihedral Angle</u>						
Au–S–C–N	13.4	41.9	14.0	14.5	13.1	12.3
	12.2	-17.9	14.5	15.6	14.3	14.3

Table 5.23: Representative geometrie parameters of the optimised structure of the six complexes studied, obtained using DFT/B3LYP/LanD2DZ

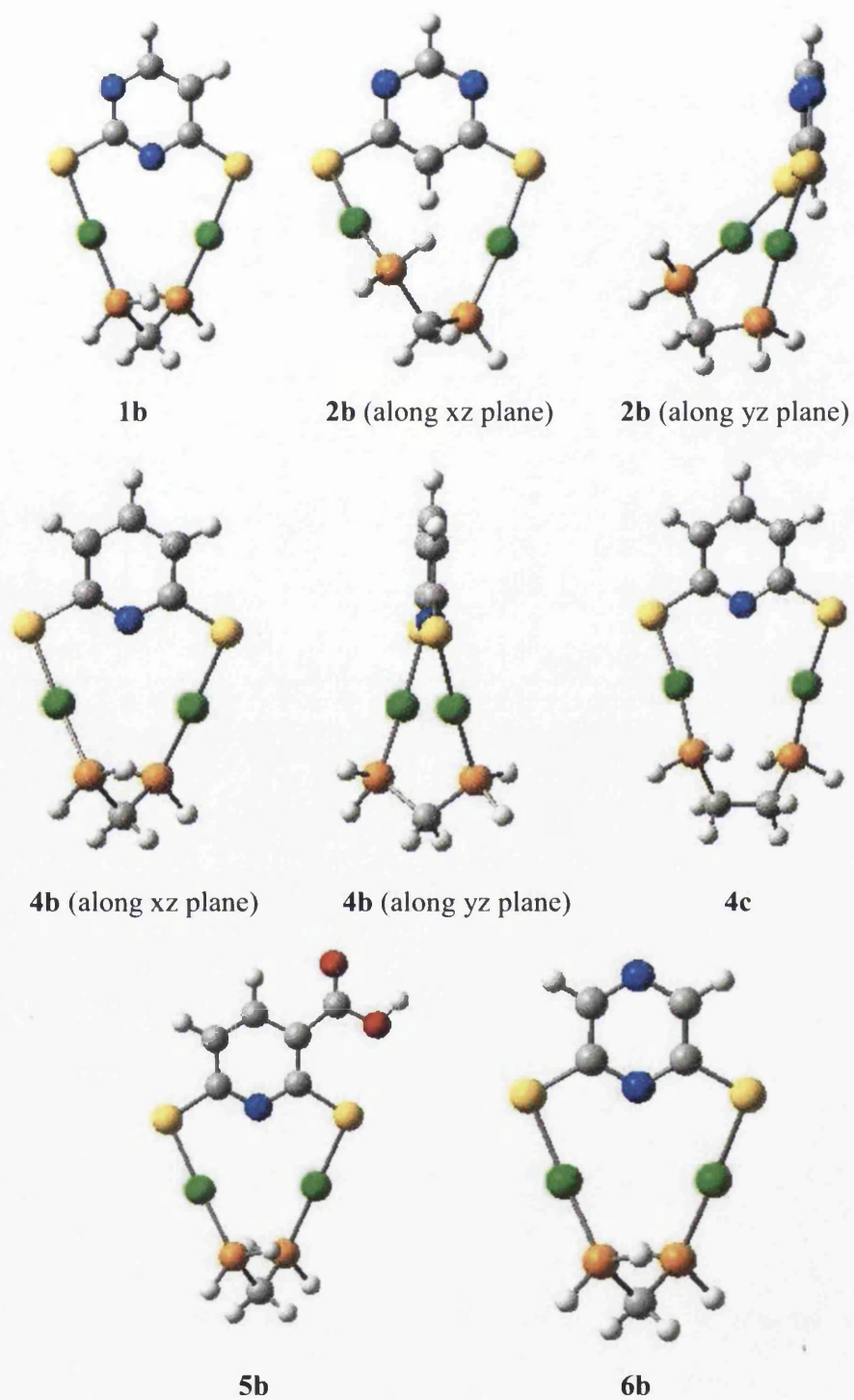


Figure 5.10: Optimised structures of binuclear gold(I) complexes, gold in green, sulphur in yellow, phosphorus in orange, nitrogen in blue, carbon in grey, hydrogen in white and oxygen in red

Most of the compounds have one S-Au-P branch each side of the plane formed by the N-heterocycle (see figure 5.10, **4b** along yz plane) but for **2b** the optimised structure has both branches on the same side. The starting geometry for all compounds is planar, so perhaps the presence of the hydrogen inbetween the two gold moieties in **2b** prevents the free movement of the S-Au-P branches through the plane during the optimisation. It would be interesting to check whether another stable structure with a S-Au-P branch on each side of the 46PYRI ring would be possible, by starting with a geometry closer to that geometry, but lack of time prevented us from carrying out such a study.

These optimised structures have bond distances and angles consistent with literature values and can be considered reliable representations. Therefore we can localise the HOMO and LUMO of the different species and also perform a TDDFT single point energy calculation to determine their optical transitions. The program used for structure optimisation can locate no orbitals other than the LUMO and HOMO. So a single point energy calculation using DFT and TDDFT with the function B3LYP and the basis set LanL2DZ was completed with Gaussian 3.0 to obtain orbitals for other energy levels also.

5.3.3 Localisation of the HOMO and LUMO

Figures 5.11 to 5.16 show the frontier orbitals for molecules **1b**, **2b**, **4b**, **4c**, **5b** and **6b** with a geometry optimised with the ECP method. For comparison purposes, **3b** was been optimised with DFT/B3LYP/LanL2DZ and the calculated orbital occupancy using this method is shown in figure 5-17. The energy levels of representative orbitals are shown in table 5.24.

Structure optimisation using DFT/B3LYP/LanL2DZ gives Au-S and Au-P bond lengths which are elongated by 13 pm and 15 pm respectively when compared with those obtained using the ECP method. Optimisation using DFT/B3LYP/LanL2DZ of the five other molecules gave a similar bond elongation. However, constitution of the frontier orbitals was independent of the method used. So the orbitals occupancies for **3b** are comparable with the others, despite perhaps having been poorly geometrically optimised.

	1b	2b	4b	4c	5b	6b
LU+3	-0.78	-1.11	-0.54	-0.50	-0.98	-0.86
LU+2	-1.17	-1.36	-0.94	-0.75	-1.19	-1.24
LU+1	-1.18	-1.60	-1.07	-0.81	-1.25	-1.30
LUMO	-1.80	-2.12	-1.64	-1.29	-1.81	-1.84
HOMO	-5.52	-5.85	-5.08	-4.94	-5.41	-5.39
HO-1	-5.90	-5.98	-5.64	-5.49	-5.85	-5.94
HO-2	-6.08	-6.32	-6.15	-6.00	-6.22	-6.15
HO-3	-6.80	-6.93	-6.65	-6.49	-6.77	-6.88

Table 5.24: Calculated energy (eV) of the orbitals for the binuclear gold complexes in the ground state

The HOMO and HOMO-1 of all the compounds are located on the thiolate ligand. The HOMO is formed of orbitals belonging to the C=S and to the N-heterocycle. Generally, AOs belonging to the nitrogen are absent from the HOMO. A small contribution from gold d orbitals can be observed.

The LUMO is located mainly on gold and phosphine orbitals. No orbital can be detected on the N-heterocycle, with the exception of **5b** in which the electron withdrawing carboxylic acid group contributes to the MO. The LUMO+1 is generally located all over the molecule notably on the N-heterocycle, except for **2b** and **3b**. The two electron donating amino groups in **3b** are probably responsible for the shift of the LUMO+1 towards the phosphine group in this case. In **5b**, the proportion of AO belonging to the N-heterocycle participating in LUMO+1 is more important than in any other compound, which might be explained by the electron withdrawing effect of the carboxylic acid substituent. Generally LUMO+2 is located on the gold and phosphine atoms, with a small contribution from the N-heterocycle.

From this study, the lowest energy absorption bands should be LMCT and LLCT in nature, from the sulphur to the gold-phosphine bonds, with some possible contribution of a gold MC transition. Similar results on gold phosphine thiolates have recently been obtained [42]. A higher transition S_2 , HOMO→LUMO+1, will be of mixed nature in most cases, ILCT and LMCT. When an electron-withdrawing group is present on the thiolate the probability of ILCT would be enhanced whereas an electron-donating group will reduce the ILCT probability and enhance the LMCT.

As described in chapter 4 these compounds have a complex photochemistry. Generally at 77 K, the emission spectra of these molecules have only one band when excited in the low energy region of their absorption spectra. When excited at higher energy, a new higher energy band, more or less intense appears. The time-resolved measurements proved, in the case of **1b**, that they correspond to two different transitions in which the excited states are not in equilibrium. The computational study suggests that the lowest energy emission arises from a LMCT excited state mixed with some MC, and this would correspond to the emission seen upon excitation into the low energy region of the absorption spectrum. However, excitation into a higher energy band, and population of higher energy levels such as LUMO+1, results in both LMCT and ILCT transitions.

The neutral ligand is present in its thione form in DCM:MeOH (1:1), according to the *ab initio* studies. However when bonded to the phosphinegold moieties, it is present as a derivative of the dithiol form, with Au instead of H, and the presence of the gold(I) atom may modify the emission. This could explain why the ILCT emission is shifted in the complex when compared with the ligand emission.

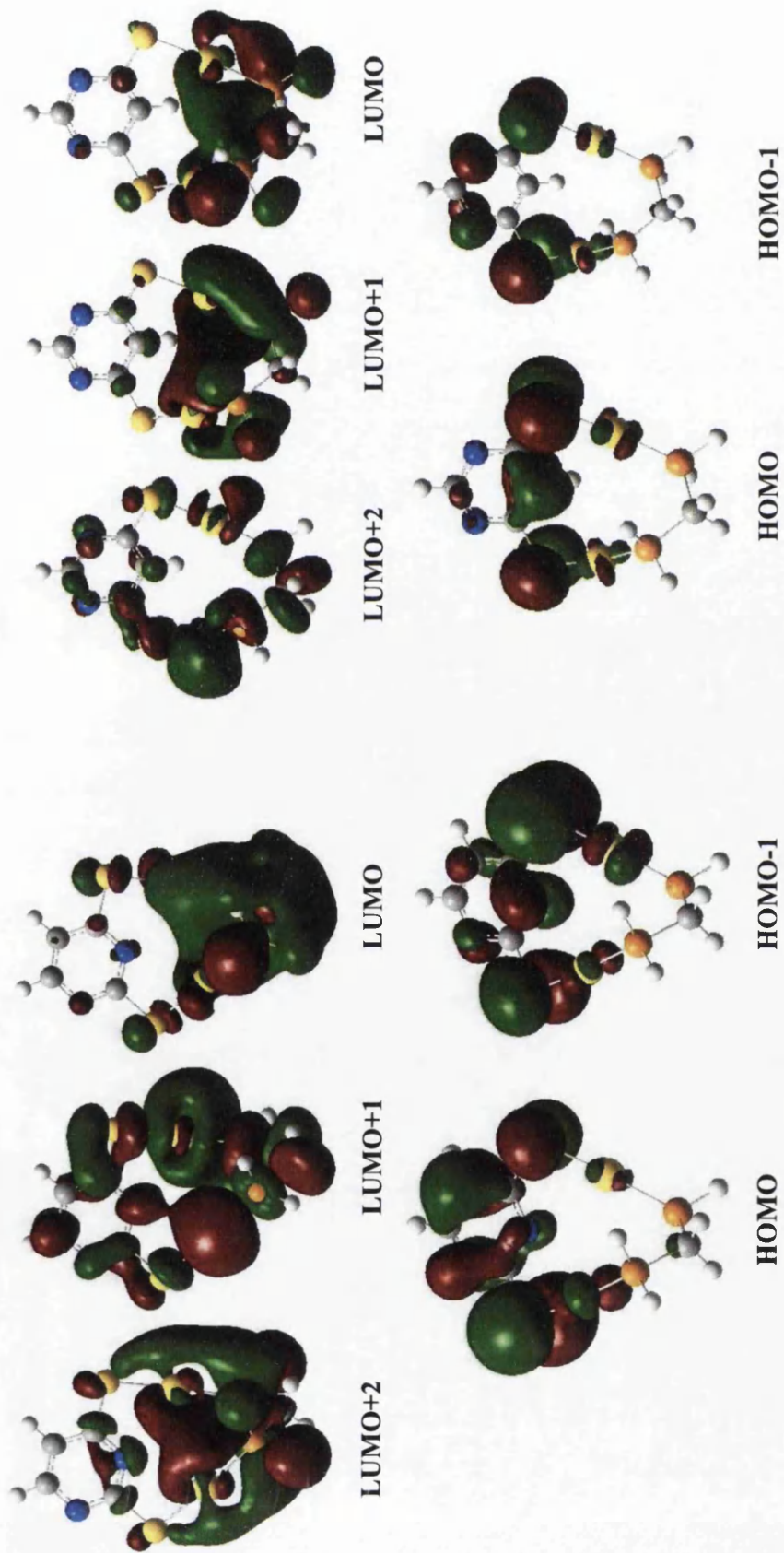


Figure 5.11: Representation of the frontier orbitals calculated at the B3LYP/LanL2DZ level for **1b**

Figure 5.12: Representation of the frontier orbitals calculated at the B3LYP/LanL2DZ level for **2b**

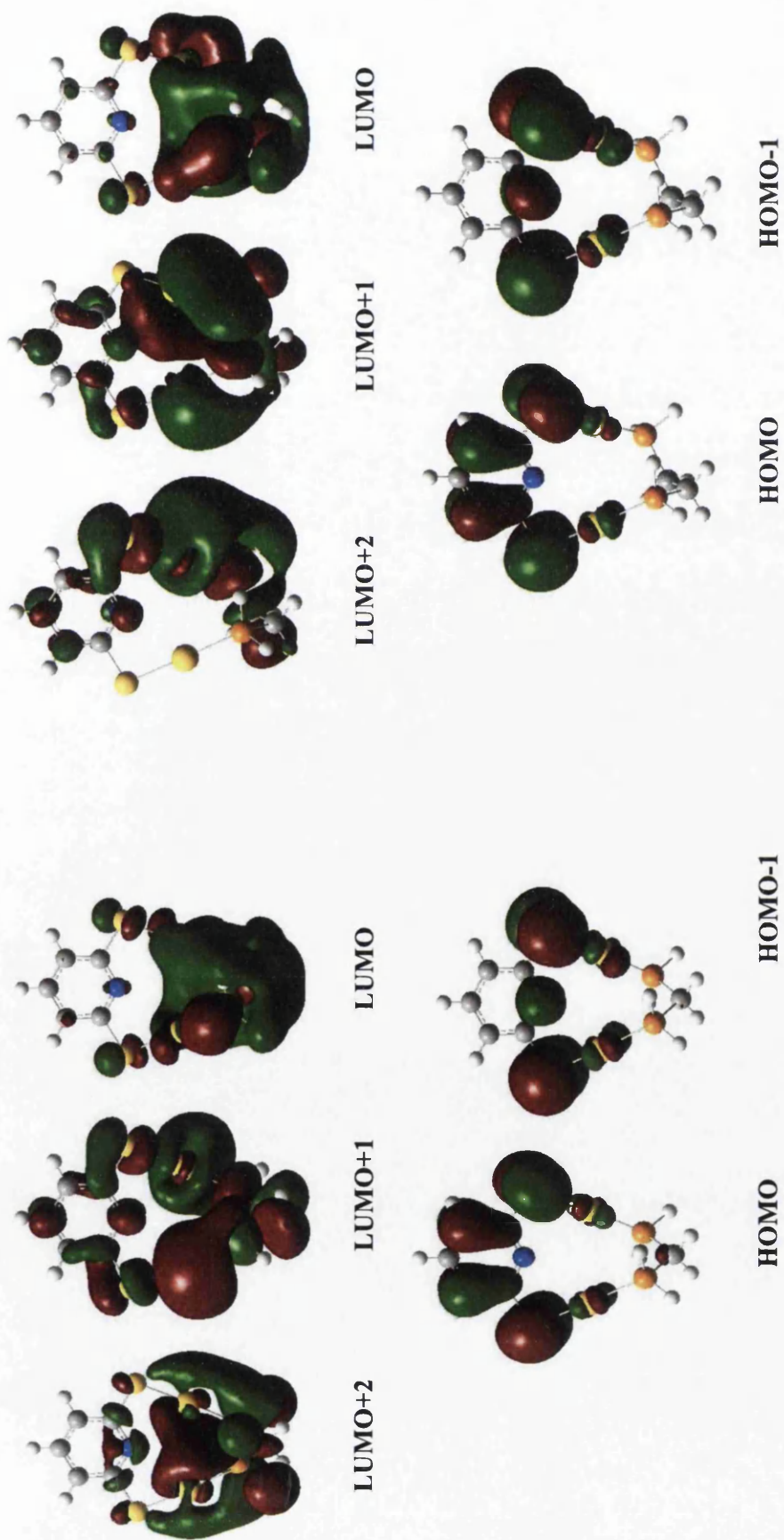


Figure 5.13: Representation of the frontier orbitals calculated at the B3LYP/LanL2DZ level for **4b**

Figure 5.14: Representation of frontier orbitals calculated at the B3LYP/LanL2DZ level for **4c**

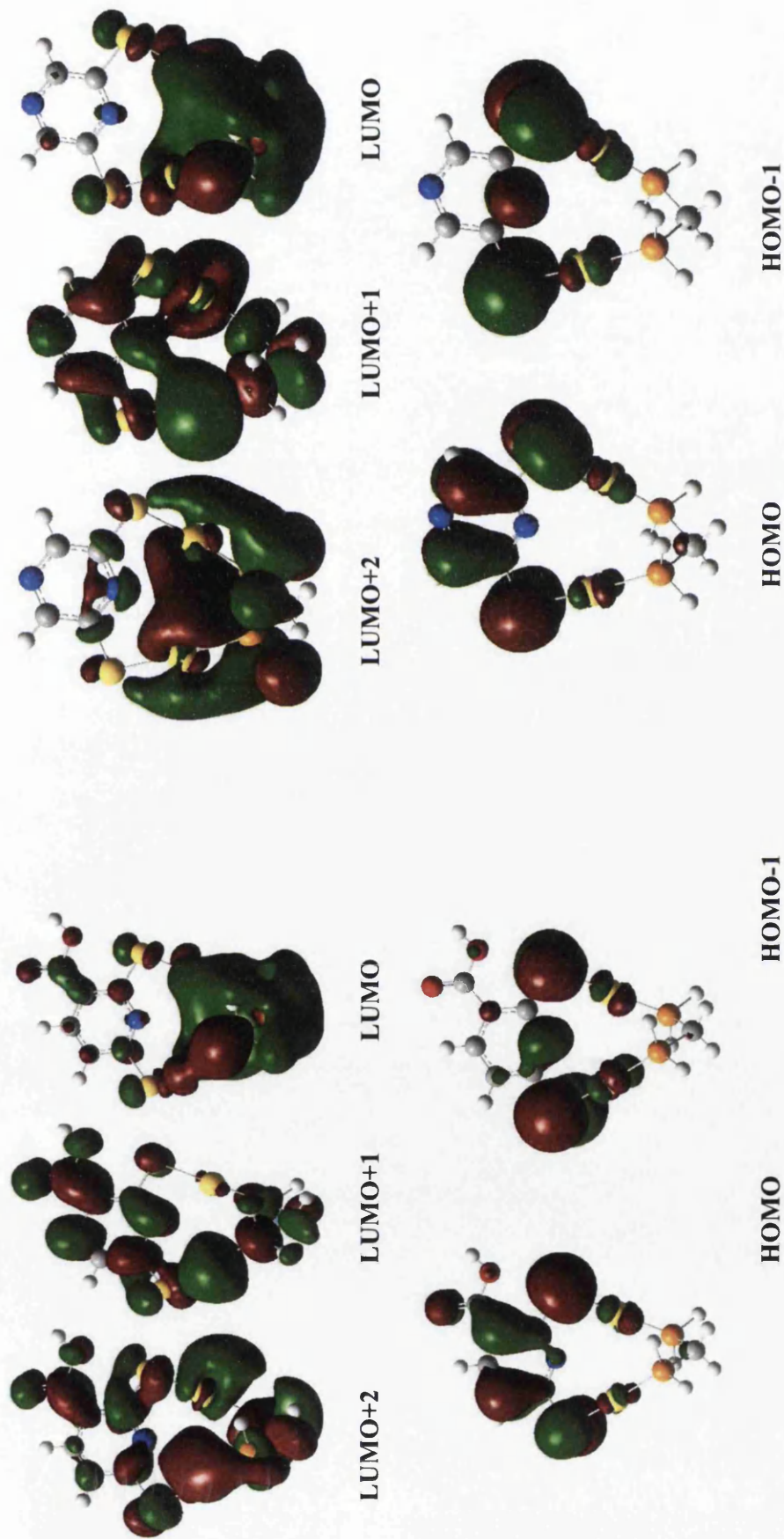


Figure 5.15: Representation of the frontier orbitals calculated at the B3LYP/LanL2DZ level for **5b**

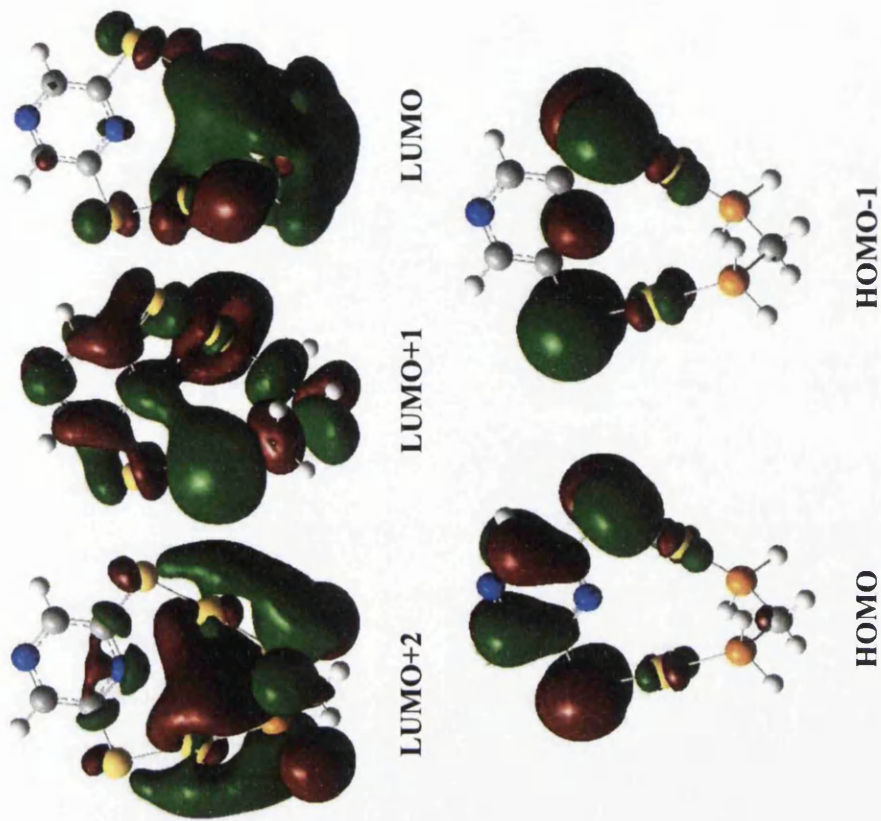


Figure 5.16: Representation of the frontier orbitals calculated at the B3LYP/LanL2DZ level for **6b**

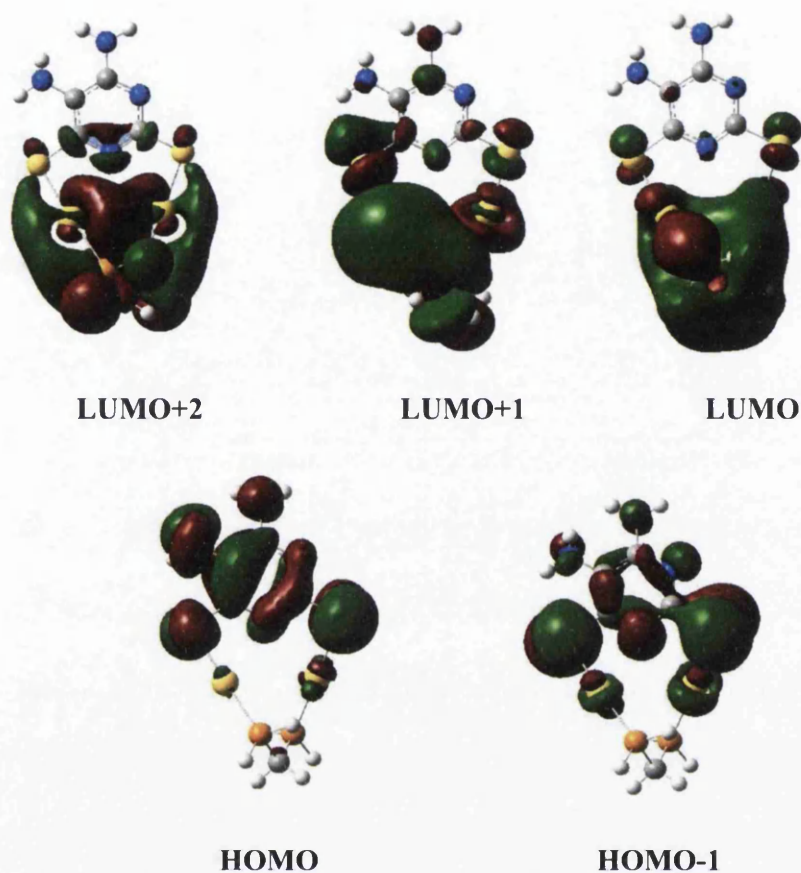


Figure 5.17: Representation of the **3b** frontier orbitals calculated at the DFT/B3LYP/LanL2DZ level

5.3.4 Relative charge calculation

The Mulliken charges carried by atoms are given in the output file of any calculation done with Gaussian. This estimation is quite rough and to have a better approximation, a natural bond orbital (NBO) calculation is preferable. The results of such a calculation in the ground state of our complexes are given in table 5.25 for gold, sulphur and phosphorus atoms.

	1b	2b	4b	4c	5b	6b
S	-0.256	-0.251	-0.280	-0.283	-0.257	-0.264
	-0.235	-0.236	-0.280	-0.283	-0.210	-0.266
Au	0.307	0.276	0.301	0.302	0.301	0.305
P	0.342	0.337	0.339	0.322	0.342	0.340

Table 5.25: Charge calculated through natural bond orbital population analysis.

The gold atoms carry a partial positive charge of *ca.* 0.303 each, except for **2b** where the charge is +0.276. The more electron rich thiolates are the two DMP rings (corresponding to the **4** and **5** series). Both sulphur atoms on **4b**, **4c** and **6b** carry the same charge due to the symmetry of the molecule. The asymmetry in **1b** and **5b** explains the difference in charge for the two sulphur atoms. The lower charge carried by **5b** compared with **4b** (or **4c**) is due to the presence of the electron-withdrawing carboxylic acid group. Considering the difference in charge between gold and sulphur atoms, their bond should have a quite weak ionic character.

5.3.5 Conclusion

Structure optimisation using ECP associated with a B3LYP function and a LanL2DZ function, can give a reliable molecular structure. The structures obtained confirm the absence of any intramolecular aurophilic interaction. Examination of molecular orbitals gives a good insight into the nature of the HOMO and LUMO and this was used to help rationalise the luminescence behaviour of these compounds. Notably, the influence on the LUMO of electron-donating or -withdrawing substituents on the thiolate groups, can be understood, and the possibility of both ILCT and LMCT excited states has been confirmed.

5.4 General conclusions from *ab initio* studies

The optimised structures of the dithiols have been compared with both literature data and the crystal structure obtained for 46PYRI. The IR and UV-VIS absorption bands have also been compared and a reasonably good match has been found for the thione forms of the N-heterocycles studied. The data all support the predominance of only one tautomer, the thione, in solution.

For the gold complexes the absence of any aurophilic interaction has been confirmed and the nature of the LUMOs and HOMOs determined. The insight thus obtained helps understand the photophysics of these molecules.

While computational methods are very useful it is essential to take care with both data input and interpretation before drawing any conclusions. As many calculated values as possible should be compared with experimental data as a check before too much is made of the data provided by this powerful tool. The gold complexes should be optimised with the ECP method with B3LYP and LanL2DZ. It is essential to have two f-type functions for the gold atoms, to take into account the relativistic effect.

This *ab initio* technique could be a powerful tool to help predict the influence of structure and substituents on molecular properties without having to synthesize the whole series of compounds of interest. This gives a precious gain in time and energy by allowing researchers to focus on those molecules most likely to have the properties required for the particular application in hand. But experiments will always be the final test for a hypothesis or theory.

Reference for Chapter 5

- [1] Foresman J.B., Frisch A., in "Exploring Chemistry with Electronic Structure Methods" 2nd edition, Gaussian Inc., Pittsburgh, PA, 1996
- [2] Jalbout A.F., Nazari F., Turker L., *J. Mol. Struct. (Theochem)* 671 (2004) 1-21
- [3] Lamsabhi M., Alcami M., Mo O., Bouab W., Esseffar M., Abboud J. L.-M., Yanez M., *J. Phys. Chem. A* 104 (2000) 5122-5130
- [4] Scott A.P., Radom L., *J. Phys. Chem.* 100 (1996) 16502-16513
- [5] Fu A., Li H., Du D., *J. Mol. Struct. (Theochem)* 767 (2006) 51-60
- [6] Beak P., *Acc. Chem. Res.* 10 (1977) 186-192
- [7] Beak P., Covington J.B., *J. Am. Chem. Soc.* 100 (1978) 3961-3962
- [8] Beak P., Covington J.B., Smith S.G., White J.M., Zeigler J.M., *J. Org. Chem.* 45 (1980) 1354-1362
- [9] Katritzky A.R., Jug K., Oniciu D.C., *Chem. Rev.* 101 (2001) 1421
- [10] Schank A., Dereppe J.M., Meerssche M.V., *Bull. Soc. Chim. Belg.* 92 (1983) 199-206
- [11] Stoyanov S., Stoyanova T., Akrivos P.D., Karagiannidis P., Nikolov P., *J. Heterocycl. Chem.* 33 (1996) 927-933
- [12] Beak P., Covington J.B., White J.M., *J. Org. Chem.* 45 (1980) 1347-1354
- [13] Leszczynski J., Lammertsma K., *J. Phys. Chem.* 95 (1991) 3128-3132
- [14] Rostkowska H., Lapinski L., Nowak M.J., *J. Phys. Chem. A* 107 (2003) 804-809
- [15] Nowak M.J., Lapinski L., Rostkowska H., Les A., Adamowicz L.J., *J. Phys. Chem.* 94 (1990) 7406-7414
- [16] Nowak M.J., Lapinski L., Fulara, J., Les A., Adamowicz L.J., *J. Phys. Chem.* 95 (1991) 2404-2411
- [17] Lapinski L., Nowak M.J., Kolos R., Kwiatkowski J.S., Leszczynski J., *Spectrochim. Acta A* 54 (1998) 685-693
- [18] Pople J.A., Nesbet R.K., *J. Chem. Phys.* 22 (1954) 571-575
- [19] Moller C., Plesset M.C., *Phys. Rev.* 46 (1934) 618
- [20] Parr R.G., Yang W., in "Density-functional Theory of Atoms and Molecules" Oxford University Press, Oxford, 1989
- [21] Becke A.D., *Phys Chem. A* 38 (1988) 3098
- [22] Dolg M., in "Modern Methods and Algorithms of Quantum Chemistry", 2nd Edition, J. Grotendorst, p507-540, 2000
- [23] Petiau M., Fabian J., *J. Mol. Struct. (Theochem)* 538 (2001) 253-260

- [24] Pyykkö P., *Inorg. Chim. Acta* 358 (2005) 4113-4130
- [25] Pyykkö P., *Angew. Chem. Int. Ed.* 43 (2004) 4412-4456
- [26] Pyykkö P., Zhao Y.-F., *Angew. Chem. Int. Ed.* 30 (1991) 604-605
- [27] Pyykkö P., Runeberg N., Mendizabal F., *Chem. Eur. J.* 3 (1997) 1451-1457
- [28] Li J., Pyykkö P., *Chem. Phys. Lett.* 197 (1992) 586-590
- [29] Hay J., Wadt W.R., *J. Chem. Phys.* 82 (1985) 270-283
- [30] Hay J., Wadt W.R., *J. Chem. Phys.* 82 (1985) 299-310
- [31] Stanovnik B., Tisler M., Katritzky A.R., Denisko O.V., *Adv. Hetero. Chem.* 91 (2006) 1-134
- [32] Moran D., Sukcharoenphon K., Puchta R., Schaefer III H. F., Schleyer P., Hoff C. D., *J. Org. Chem.* 67 (2002) 9061-9069
- [33] Meng F., *J. Mol. Struct. (Theochem)* 806 (2007) 159-164
- [34] Lautié A., Hervieu J., Belloc J., *Spectrochimica Acta* (1983) 39A, 4, 367-372
- [35] Pan Q.J., Zhang H.X., Fu H.G., Yu H.T., *Eur. J. Inorg. Chem.* (2006) 1050-1059
- [36] Pan Q.J., Zhang H.X., *J. Phys. Chem. A* 108 (2004) 3650-3661
- [37] Pan Q.J., Zhang H.X., *Inorg. Chem* 43 (2004) 593-601
- [38] Fernandez E.J., Laguna A., Lopez-de-Luzuriaga J.M., Monge M., Montiel M., Olmos M.E., Perez J., Rodriguez-Castillo M., *Gold Bull.* 40 (2007) 172-184
- [39] Lin J.C.Y., Tang S.S., Sekhar Vasam C., You W.C., Ho T.W., Huang C.H., Su B.J., Huang C.Y., Lee C.S., Hwang W.S., Chang A.H.H., Lin I.J.B., *Inorg. Chem.* 47 (2008) 2543-2551
- [40] Li C.H., Kui S.C.F., Sham I.H.T., Chui S.Y., Che C., *Eur. J. Inorg. Chem.* (2008) 2421-2428
- [41] Valdespino-Saenz J, Martinez A., *J. Phys. Chem. A* 112 (2008), 2408-2414
- [42] Bardaji M., Calhorda M.J., Costa P.J., Jones P.G., Laguna A., Perez M.R., Villacampa M.D., *Inorg. Chem.* 45 (2006) 1059-1068
- [43] Costa P.J., Calhorda M.J., *Inorg. Chim. Acta.* 359 (2006) 3617-3624
- [44] Mendizabal F., Pyykkö P., *Inorg. Chem.* 37 (1998) 3018-3025
- [45] Pan Q.J., Fu H.G., Yu H.T., Zhang H.X., *Chem Phys. Letters* 426 (2006) 257-262
- [46] Guo Y.R., Pan Q.J., Fang G.Z., Liu Z.M., *Chem Phys. Letters* 413 (2005) 59-64
- [47] Schmidt M.W., Baldrige K.K., Boatz J.A., Elbert S.T., Gordon M.S., Jensen J.H., Koseki S., Matsunaga N., Nguyen K.A., Su S.J., Windus T.L., Dupuis M., Montgomery J.A., *J. Comput. Chem.* 14 (1993) 1347

- [48] Hay J., Wadt W.R., *J. Chem. Phys.* 82 (1985) 284-298
- [49] Pan Q.J., Zhang H.X., *J. Chem. Phys.* 119 (2003) 4346-4352
- [50] Narayanaswamy R., Young M.A., Parkhurst E., Ouellette M., Kerr M.E., Ho D.M., Elder R.C., Bruce A.E., Bruce M.R.M., *Inorg. Chem.* 32 (1993) 2506-2517
- [51] Jones B.J., Yuan J., Narayanaswamy R., Young M.A., Elder R.C., Bruce A.E., Bruce M.R.M., *Inorg. Chem* 34 (1995) 1996-2001
- [52] Davila R.M., Elduque A., Grant T., Staples R.J., Fackler Jr. J.P., *Inorg. Chem.* 32 (1993) 1749-1755
- [53] Shukla M.K., Leszczynsky J., *J. Chem. Phys. A* 108 (2004) 10367-10375

Chapter 6

Conclusions

The aim of this work was to synthesise and characterise a series of novel binuclear gold phosphine thiolate complexes with a view to evaluating their potential as triplet emitters for use in OLEDs. Annular dinuclear gold(I) complexes with a rigid dithiolate ligand, and generally a bridging diphosphine were selected for synthesis. A series of twenty five new gold(I) complexes have been successfully characterised with different N-heterocyclic dithiolates. For each dithiolate, different phosphines have been used to create open ring systems, or annular systems of 10 to 13 atoms. The selectivity of the syntheses towards the annular structure may have been promoted by the presence of the nitrogen atom in the ring between the two thiol groups. All of these gold complexes emit in the solid state or in a frozen glass. However, RT emission in solution is measurable only for complexes with DMP as dithiolate.

6.1 Future work on the new dithiols synthesised

Two new dithiols have been synthesised, and their luminescence characterised along with that of other known N-heterocyclic compounds. The most stable tautomer in the solid state is the thione form. Thiones have been identified as possible emitters for OLED application. However, the absence of luminescence in the solid state from the compounds synthesised here remove them from the list of potential luminescent materials.

The new compounds synthesised here, i.e. dimercaptopyrazine and dimercaptonicotinic acid are worthy of further study since complexes with other metals *e.g.* Ru [1], Pt [2], Os [3] metals may show interesting luminescent properties. It could be also worthwhile to synthesise their copper, silver, rhenium or palladium derivatives [4] and to see if they are emitters.

Both compounds are also interesting additions to the group of materials showing thiol–thione tautomerism in either, or both, ground and excited states. ADMN, which has more extended hydrogen bonding possibilities, may prove an interesting subject with which to study the role of hydrogen bonding in tautomerism.

6.2 Future work with the binuclear gold(I) complexes synthesised

The photochemistry of these compounds is complex. It has been shown not only that the emission wavelength can be tuned according to the ligand used, but also that the nature of the excited states involved in luminescence can change depending on the ligand. In these complexes, luminescence seems to arise from a ILCT or LMCT triplet excited state; they all phosphoresce in the solid state or in a glass at 77 K. The relative rigidity of the annular complexes and the rigidity of the dithiolate lead to high quantum yield at 77 K. An electron withdrawing group seems to promote a ILCT excited state while an electron-donating group seems to promote a LMCT.

The following approaches may be useful in future work with the aim of achieving a blue luminescence.

- 1) A dithiolate possessing an electron-donating group will reduce the HOMO-LUMO energy gap, the excited state being a LMCT. To counterbalance this effect we can render the gold atom more electron-rich by reducing the π -backbonding to the phosphine, *i.e.* by using a less π -acidic phosphine than a phenylphosphine derivative, such as TPA or a cyclohexylphosphine.
- 2) An electron-withdrawing group will stabilise the LUMO based on the thiolate in the case of a LMCT. The use of a less π -acidic phosphine will also blue-shift the emission originating from a LMCT and this will be added to the electron-withdrawing effect of the thiolate. But as ILCT is also promoted, the emission properties of the ligand may require careful study before being able to draw any firm conclusions.

As the MO energy levels are close lying in the case of gold(I) phosphine thiolate complexes, the order of the MO energy levels can shift with a very slight change in the electron density/properties of the ligand.

The electrochemical irreversibility of potential phosphorescent emitters has been used as an argument to exclude from consideration those compounds which will probably be unstable towards the charge recombination processes occurring in OLEDs. However as the electrochemistry is obtained in solution, numerous side reactions (notably with the solvent or other by-products formed by the redox process) can take place which will not necessarily occur in the solid state or in an OLED device. Therefore solution electrochemical irreversibility should not be taken as a

definitive reason for exclusion, although reversible redox chemistry can be taken as a good indicator.

The thiolates used are similar to molecules present in biological systems, especially 24PYRI which is a parent of the DNA base uracil. Gold(I) complexes have been used in different medical applications, notably as anti-rheumatic medicines, but some research shows the possibility of their development as cytotoxic agents for cancer cells. The combination of a thiolate ligand of similar structure to biological molecules, the annular structure of the complexes, and the presence of two gold(I) atoms, provides intriguing features for further studies of biological activity. And with this in mind the water solubility of such complexes could be increased by using water soluble phosphines such as TPA.

6.3 Future *ab initio* calculations

Ab initio calculation has proven to be helpful in understanding the localisation of the HOMO and LUMO on the molecules and in evaluating the energies of different thiol/thione tautomers in different environments. It is nevertheless necessary to check the results obtained by reference to experimental data, as the results from computation depend on the basis set and the method used. Computational methods for the estimation of emission wavelength are still not precise, but they are useful in helping understand the origin of the luminescence and the effect of the ligand structure on luminescence properties. Some calculations to simulate the geometrically optimised excited state of the gold compounds could be useful.

References for Chapter 6

- [1] Kannan S., Sivagamasundari M., Ramesh R., Liu Y., *J. Organometallic Chem.* 693 (2008) 2251-2257
- [2] Koshiyama T., Omura T., Kato M., *Chem. Lett.* 33 (2004) 1386-1387
- [3] Adams R.D., Barnard T., Rawlett A., Tour J.M., *Eur. J. Inorg. Chem.* 4 (1998) 429-431
- [4] Raper E.S., *Coord. Chem. Rev* 61. (1985) 115-184

APPENDICES

Appendix A: List of chemicals used and purification if needed

Triethylamine (boiling point = 90°C) was distilled over CaH₂ before use. Anhydrous NH₄Cl was purified by sublimation under nitrogen and stored under nitrogen.

All other products were used as received, without further purification.

Air-sensitive chemicals, perchlorate salts, and lithium aluminium hydride were stored under nitrogen in a desiccator.

Chemical	Supplier	Grade
Acetone	Fisher	AR
Acetonitrile	Fisher	HPLC
Ammonium chloride	Sigma-Aldrich	99.5%
1,2-Benzenedithiol	Sigma-Aldrich	96%
1,3-Benzenedithiol	Fluka	99.9%
Benzophenone	Sigma-Aldrich	Spectroscopic
1,2-Bis(dicyclohexylphosphino)benzene	Sigma-Aldrich	97%
Bis(dicyclohexylphosphino)methane	Sigma-Aldrich	98%
Bis(diphenylphosphino)butane	Sigma-Aldrich	97%
Bis(diphenylphosphino)ethane	Sigma-Aldrich	98%
Bis(diphenylphosphino)methane	Sigma-Aldrich	98%
Bis(diphenylphosphino)propane	Sigma-Aldrich	97%
1-Bromo-3,4-difluorobenzene	Acros	98%
α -Bromo-3,4-difluorotoluene	Acros	98%
4-Chloro-1,3-benzenedithiol	Acros	98%
1-Chloro-3,4-difluorobenzene	Acros	98%
Chlorodiphenylphosphine	Sigma-Aldrich	98%
Chloroform	Fisher	Reagent grade
Cis-1,2-bis(diphenylphosphino)ethene	Acros	98%
Deuterated chloroform stabilized with 0.5 wt. % silver foil	Sigma-Aldrich	99.8%
Deuterated dimethylsulfoxide	Sigma-Aldrich	99.8%
Diatomaceous earth	Sigma-Aldrich	
1,3-Dichloroisoquinoline	Sigma-Aldrich	97%

Dichloromethane	Fisher	Reagent
2,4-Dichloropyrimidine	Sigma-Aldrich	97%
4,6-Dichloropyrimidine	Sigma-Aldrich	97%
2,6-Dichloroisonicotonic acid	Sigma-Aldrich	98%
2,6-Dichloronicotinic acid	Sigma-Aldrich	97%
2,6-Dichloro-3-nitropyridine	Sigma-Aldrich	92%
2,6-Dichloro-4-nitropyridine	Sigma-Aldrich	97%
2,6-Dichloropyrazine	Sigma-Aldrich	99%
2,4-Dichloropyridine	Sigma-Aldrich	97%
2,6-Dichloropyridine	Fluka	98.5%
Diethylthiocarbamoyl chloride	Sigma-Aldrich	95%
Diethyl ether	Fisher	Reagent
Diethyl ether	Sigma-Aldrich	Anhydrous, 99.9%
1,2-Difluorobenzene	Acros	98%
1,3-Difluorobenzene	Acros	98%
1,2-Difluoro-4-iodobenzene	Acros	98%
1,3-Difluorotoluene	Acros	98%
2,4-Dihydroxypyridine	Sigma-Aldrich	97%
Dimethyl acetylenedicarboxylate	Sigma-Aldrich	99%
Dimethylformamide	Fluka	
Dimethylsulfoxide	Fluka	Purum \geq 99%
Ethanol	Fisher	
Ethanolamine	Sigma-Aldrich	Reagent
Ethylene glycol	Sigma Aldrich	Reagent
Gold(III) chloride trihydrate	Sigma-Aldrich	
Hexamethyldisilazane	Fluka	98%
Isopentane	Aldrich	99%
1,3-Isoquinolinediol	Sigma-Aldrich	
Lawesson's reagent	Sigma-Aldrich	97%
Lithium aluminium hydride	Fluka	97%
Methanol	Fisher	
Nitrogen	BOC	Anhydrous

Appendix A

Potassium perchlorate	Sigma-Aldrich	98%
Potassium <i>tert</i> -butoxide	Fluka	97%
Potassium tetrachloroaurate(III)	Alfa Aesar Sigma-Aldrich	98%
2,4-Quinolinediol	Fluka	
Rhodamine B	Kodak	Laser Grade
Silica 60A particle size	Fisher	35-70 microns
Silver acetate	Sigma-Aldrich	98%
Silver hexafluorophosphate	Sigma-Aldrich	98%
Silver perchlorate	Sigma-Aldrich	99.9%
Silver tetrafluoroborate	Sigma-Aldrich	98%
Silver trifluoroacetate	Sigma-Aldrich	99%
Sodium (in oil)	Lancaster	99%
Sodium hydrosulfide hydrate	Sigma-Aldrich	
Sodium methoxide	Fluka	97%
Tetrabutylammonium bromide	Sigma-Aldrich	98%
Tetrabutylammonium hydroxide	Sigma-Aldrich	20% in MeOH
Tetrahydrofuran	Fisher	99%
Tetrahydrothiophene	Sigma-Aldrich	99%
Thioacetamide	Sigma-Aldrich	98%
2,2'-Thiodiethanol	Fluka	98.5%
Toluene	Fisher	
Trifluoroacetic acid	Sigma-Aldrich	
Triphenylphosphine	Fluka	98.5%
Water	Fisher	HPLC

Appendix B: Attempts to synthesise different dimercaptopyridines

The phosphinegold(I) thiolates have a luminescence originating from a Au→S (MLCT) transition. A more electron-withdrawing thiolate will shift the luminescence towards higher energy. Therefore the synthesis of 2,6-dimercaptopyridine ligands with different substituents was attempted.

Different methods were explored:

- 1) synthesis of dichloropyridines and substitution of the halogen via NaSH in DMF;
- 2) synthesis from dihydroxy derivatives using P₂S₅, or thiourea (NH₂)₂C=S.

The molecules aimed for are listed in figure B-1 and the reactions attempted are summarised in scheme B-1.

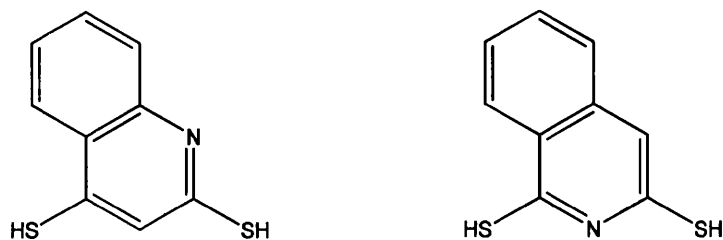
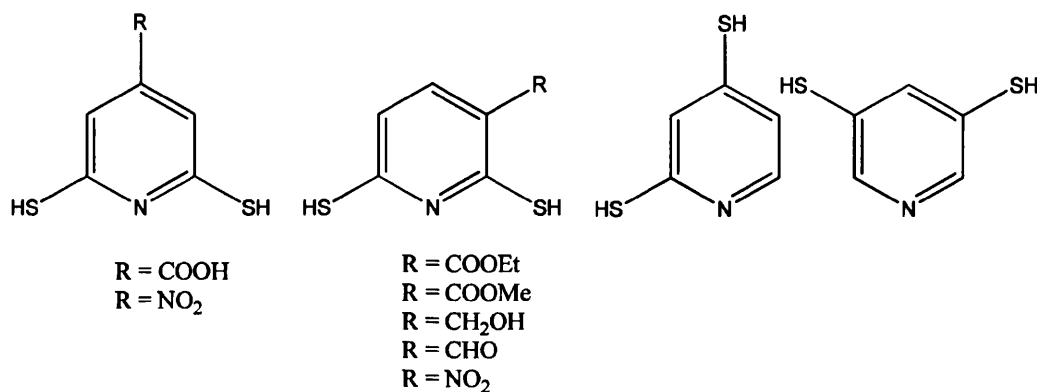


Figure B-1: Molecules for which synthesis was attempted

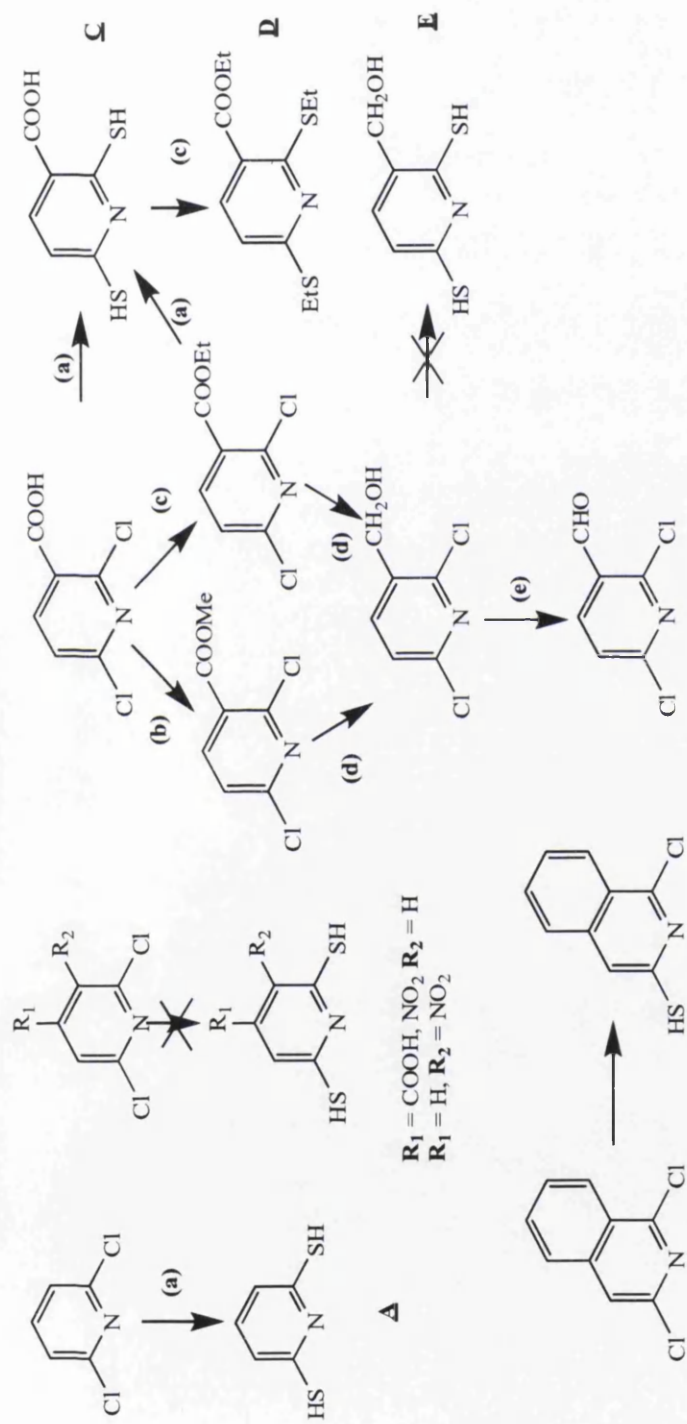
B.1 Reactions with dichloropyridine derivatives

As 2,6-dimercaptonicotinic acid has been synthesized in this work, we tried to synthesise its corresponding ester, alcohol and aldehyde derivatives. The dichloropyridine starting material had to be synthesised and then reacted with NaSH in boiling DMF.

Starting with a mixture of dichloronicotinic acid and TMOA (or TEOA) the corresponding ester was synthesized. Reduction of either ester with LiAlH_4 and anhydrous AlCl_3 in boiling dry diethyl ether under dry N_2 gives the alcohol. This was oxidised with MnO_2 to give the aldehyde. All these chlorinated derivatives have already been synthesised and characterised in the literature [1-3].

The substitution of this series of dichloropyridines with NaSH uses extreme conditions of a very polar solvent and high temperature, and it was found that the two esters produced dimercaptonicotinic acid, while the alcohol and the aldehyde derivatives gave an unidentified product.

The action of TMOA or TEOA on dimercaptonicotinic acid alkylates both the carboxylic acid group and the two mercapto-groups, illustrating their nucleophilicity.



- (a)** NaSH, 8 h, boiling DMF
(b) 24 h, TMOA (trimethylorthoacetate), boiling toluene
(c) 24 h, TEOA (triethylorthoacetate), boiling toluene
(d) LiAlH_4 , AlCl_3 , dry diethyl ether
(e) MnO_2 , 2h, methanol

Scheme B-1: Reaction scheme for the different reactions attempted

B.2 Dichloropyridine syntheses and characterisation

B.2.1. 2,6-Dichloronicotinic acid ethyl ester [B1]

One equivalent of triethylorthoacetate (TEOA) was mixed with one equivalent of 2,6-dichloronicotinic acid for 24 h in boiling toluene. The solvent was removed by evaporation under reduced pressure and the resulting oil was left overnight; this gave white crystals of the desired product which was characterised by ^1H NMR spectroscopy and X-ray diffraction. The structure has already been reported, and no further analysis was done.

^1H NMR ($\text{d}_4\text{-MeOH}$): 8.2 (d, 1H), 7.4 (d, 1H), 4.3 (q, 2H, $\text{CH}_2\text{-CH}_3$), 1.3 (t, 3H, $\text{CH}_2\text{-CH}_3$)

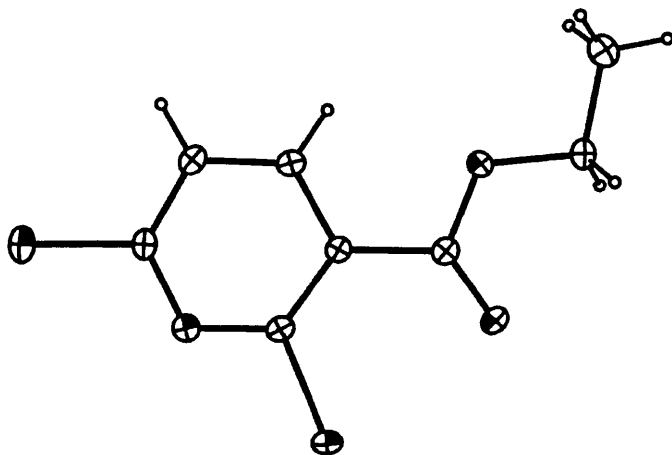


Figure B-2: Crystal structure of 2,6-dichloronicotinic acid ethyl ester

B.2.2 2,6-Dichloronicotinic acid methyl ester [B2]

One equivalent of trimethylorthoacetate (TMOA) was mixed with one equivalent of 2,6-dichloronicotinic acid for 24 h in boiling toluene. The solvent was removed by evaporation under reduced pressure and the resulting oil was left overnight; this gave white crystals of the desired product, which was characterised by ^1H NMR spectroscopy and X-ray diffraction. The structure has already been reported, and no further analysis was done.

^1H NMR (CDCl_3): 8.1 (d, 1H), 7.2 (d, 1H), 3.9 (s, 3H, CH_3)

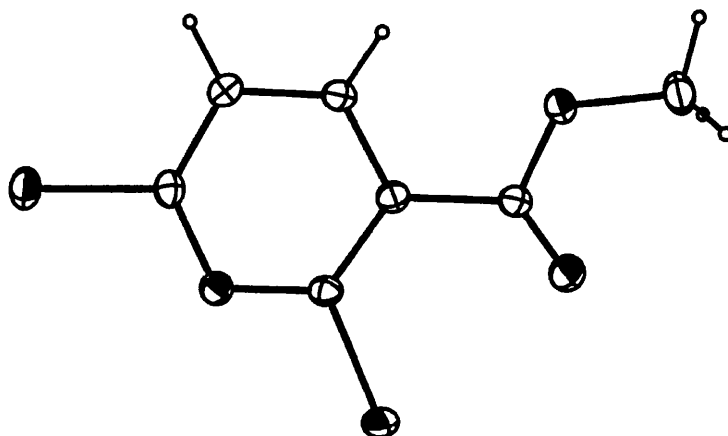


Figure B-3: Crystal structure of 2,6-dichloronicotinic acid methyl ester

B.2.3 2,6-Dichloro-5-(hydroxymethyl)pyridine [B3]

By mixing one of the esters formed before with lithium aluminium hydride and anhydrous aluminium trichloride in dry diethyl ether, the ester group was reduced to an alcohol. After 2 h of reaction, diethyl ether was removed by evaporation under reduced pressure and the alcohol isolated and characterised by ^1H NMR spectroscopy.

^1H NMR (CDCl_3): 7.8 (d, 1H), 7.2 (d, 1H), 4.7 (s, 2H, CH_2OH), 2.5 (s, 1H, CH_2OH)

B.2.4 2,6-Dichloronicotinaldehyde [B4]

A mixture of manganese dioxide and 2,6-dichloro-5-(hydroxymethyl)pyridine was left to react in methanol for 2 hours the solution was filtered through diatomaceous earth and the solvent removed under vacuum. The resulting white powder was identified by ^1H NMR spectroscopy as 2,6-dichloro-nicotinaldehyde.

^1H NMR (CDCl_3): 10.3 (s, 1H, CHO), 8.1 (d, 1H), 7.3 (d, 1H)

B.3 Different attempts to synthesise dithiol compounds

B.3.1 Reactions of dichloropyridine derivatives with NaSH

All of the dichloropyridines described above were reacted with NaSH in boiling DMF to attempt to substitute the halogen for a thiol. From the ester derivatives, we obtained only dimercaptionicotinic acid. From the alcohol or aldehyde derivatives, a yellow insoluble product was obtained. When 2,6-dichloropyridine with a nitro group in position 4 or 5, or with a carboxylic acid group in position 4, was used as starting material, a red insoluble compound was obtained.

B.3.2 Reaction of trialkylorthoacetate with dimercaptionicotinic acid

Two new compounds have been synthesised:

B.3.2.1 2,6-Bis(ethylthio)nicotinic acid ethyl ester [B5]

One equivalent of triethylorthoacetate was mixed with one equivalent of 2,6-dimercaptionicotinic acid for 24 h in boiling toluene. The solvent was removed by evaporation under reduced pressure and the residue left overnight to give a yellow oil of 2,6-bis(ethylthio)nicotinic acid ethyl ester which was characterised by ^1H NMR spectroscopy.

^1H NMR: 7.88 (d, 1H), 6.76 (d, 1H), 4.37 (q, 2H, OCH_2CH_3),
3.12 (h, 4H, SCH_2CH_3), 1.28 (m, 9H, CH_2CH_3)

B.3.2.2 2,6-Bis(methylthio)nicotinic acid methyl ester [B6]

One equivalent of trimethylorthoacetate was mixed with one equivalent of 2,6-dimercaptionicotinic acid for 24 h in boiling toluene. The solvent was removed by evaporation under reduced pressure and the residue left overnight to give a yellow oil of 2,6-bis(methylthio)nicotinic acid methyl ester which was characterised by ^1H NMR spectroscopy.

^1H NMR: 7.88 (d, 1H), 6.76 (d, 1H), 3.93 (s, 3H, OCH_3), 3.02 (s, 3H, SCH_3)

B.3.3 Reaction with dihydropyridines

All attempts at the synthesis from thiourea and 2,6-dihydroxy-5-(hydroxymethyl)-pyridine just gave an insoluble product.

B.3.4 Reactions with quinoline or isoquinoline derivatives

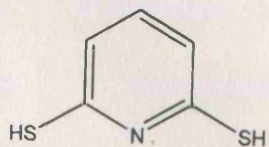
Reaction of ten equivalents of NaSH with dichloroquinoline in hot DMF resulted only in mono-substitution. Further reactions of the mono-chlorinated derivative with P_2S_5 or more NaSH with a longer reaction time left the mono-chlorinated material unchanged.

Action of P_2S_5 on dihydroxyquinoline or dihydroxyisoquinoline gave a brown insoluble product.

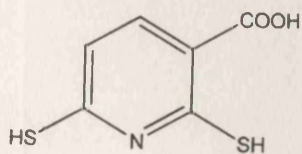
References for appendix B

- [1] Trujillo J.I., Gopalan A.S., *Tet. Lett.* 34 (1993) 7355-7358
- [2] Newkome G.R., Lee H.W., *J. Org. Chem.* 47 (1982) 2800-2802
- [3] Mutterer F., Weis C.D., *Helvetica Chim. Acta* 212 (1976) 229-240

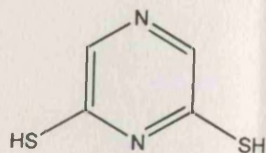
Drawing and abbreviations associated with the molecules studied.



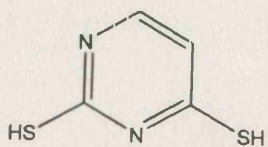
2,6-dimercaptopyridine
DMP



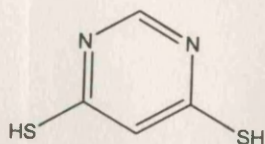
2,6-dimercaptopyridine-3-carboxylic acid
ADMN



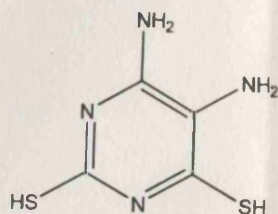
2,6-dimercaptopyrazine
DMPA



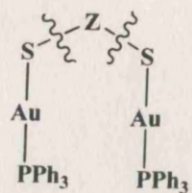
2,4-dimercaptopyrimidine
24PYRI



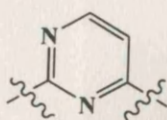
4,6-dimercaptopyrimidine
46PYRI



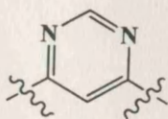
5,6-diamino-2,4-dimercaptopyrimidine
NPYRI



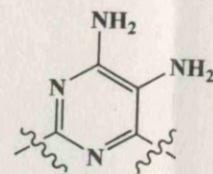
Z =



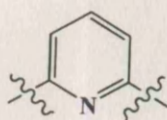
1a



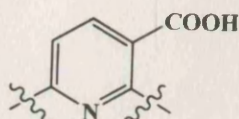
2a



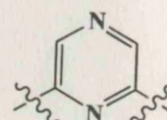
3a



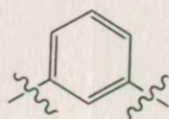
4a



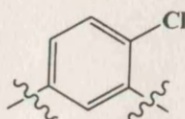
5a



6a



7a



8a